The Integration of InP/InGaAsP Ridge Waveguide Structures with Dielectric Waveguides on Silicon

by

Edward R. Barkley

Submitted to the Department of Electrical Engineering and Computer Science
in partial fulfillment of the requirements for the degree of

Doctor of Philosophy in Computer Science and Engineering

at the

MASSACHUSETTS INSTITUTE OF TECHNOLOGY
[February 2007]
September 2006

Author .....
Department of Electrical Engineering and Computer Science
Sept 29, 2006

Certified by .....
Clifton G. Fonstad
Vitesse Professor of Electrical Engineering
Thesis Supervisor

Accepted by .....
Arthur C. Smith
Chairman, Department Committee on Graduate Students

The Integration of InP/InGaAsP Ridge Waveguide Structures with Dielectric Waveguides on Silicon

by

Edward R. Barkley

Submitted to the Department of Electrical Engineering and Computer Science
on Sept 29, 2006, in partial fulfillment of the
requirements for the degree of
Doctor of Philosophy in Computer Science and Engineering

Abstract

Chip-to-chip optical interconnect technology, which is being explored as a potential replacement for copper chip-to-chip interconnects at data transmission rates exceeding 10 Gb/s, is one of several technologies that could be enabled by the monolithic integration of III-V optoelectronic devices on a silicon integrated circuit.

Two significant capabilities required to achieve this monolithic integration were addressed: the assembly of III-V device structures on silicon and the fabrication of the waveguides that perform the intra-chip routing of the optical signal to and from these integrated device structures. These waveguides, consisting of a silicon oxynitride core (n = 1.6) and a silicon dioxide cladding (n = 1.45) were deposited via plasma-enhanced chemical vapor deposition (PECVD). The integrated InP/InGaAsP structures were fabricated using an existing novel technique for preparing very thin (on the order of 5 μm thick) substrate free rectangular structures (approximately 145 μm wide by 300 μm long) with cleaved facets. Using a pick-and-place method, the InP/InGaAsP structures were assembled in 6 μm deep rectangular wells formed by etching through the waveguide stack. The resulting configuration of the integrated devices in the wells facilitated end-fire coupling with the silicon oxynitride waveguides.

Transmission spectrum measurements for this configuration verified the desired end-fire optical coupling through the integrated InP/InGaAsP device structures with a total coupling loss of 17.75 dB. This loss was shown through measurements and finite difference time domain (FDTD) simulations to be a function of integrated device misalignment, silicon oxynitride waveguide design, length of the gaps between the etched well edges and the device facets, and the well etch properties. Based on FDTD simulations and device misalignment statistics, it was shown that realistic, feasible improvements in the device alignment coupled with the use of higher index contrast waveguides could lower the coupling loss to 3.25 dB.

Thesis Supervisor: Clifton G. Fonstad
Title: Vitesse Professor of Electrical Engineering

Acknowledgments

I would just like to thank all of the people that have helped me along the way. I would like to start by thanking my wife, Korey, who has been so supportive when I've needed support and motivating when I've needed a push. I also want to thank my Mom and Dad and my sisters Lori and Jen, and my brothers-in-law, Greg and Andy.

I would like to thank my supervisor, Prof. Fonstad, whose guidance over these last seven years has resulted in a truly enriching, educational experience. The research group, including James Perkins, Joe Rumpler, Wojtek, Henry Choy, Shaya Famenini, Sheila Prasad, and Vivian Lei have all helped in so many ways, from providing technical insight, lab insight, and perhaps most importantly of all, comic relief. My good friends James and Joe were always there to make me laugh, to make me feel insane for some of the inside jokes that I found to be hilarious, to make me the subject of various postings on my door, etc., etc.

A special thanks to my thesis committee, Prof. Boning and Prof. Ram. Their influence on my experience extended beyond simply serving on my committee. Prof. Boning helped me specifically with a journal article based, in part, on his work. Prof. Ram, through the Center for Integrated Photonics (CIPS), got me interested and involved in the research and entrepreneurship communities, which helped to expand my scope..

So many people have helped me with various aspects of this project and they are too many to include here. The most noteable are the people at MTL, specifically Dan Adams, Paul Tierney, Vicky Diadiuk, Kurt Broderick, Eric Lim, Paudley Zamora, Bob Bicchieri, and Kurt Broderick (just to name a few). A special thanks, too, to the Building 13-ers: Conor, Seth, Dave D, Travis, Bill, Janice, Prof. Orlando, Yakov, Alexei, and Ivan. My good friend Dave Berns has made the daily life at MIT not only bearable, but enjoyable. Our discussions ranged from technical to personal and it was Dave's influence and friendship that got me through some very difficult times.

I would also like to thank Ali Motamedi, Milos Popovic, Jeff Chen, and Peter

Rakich. Without these four people, I would not yet be finished. Their knowledge of optics combined with their patience and willingness to help resulted in my quick transition from knowing only Maxwell's Equations, to being capable of taking real measurements with real devices in a real lab and being capable of simulating and understanding the coupling problems.

A special thanks to everyone else ... who will be annoyed that they have been referred to simply as "everyone else." My apologies, but I start work tomorrow, and I have to get home now and get on with my life! So I'll just say Thank You for your help!

Contents

List of Figures

List of Tables

Chapter 1

Introduction

The miniaturization of silicon microelectronics has been driven by the overwhelming economic and functional benefits of scaling. As the size of a transistor, the fundamental microelectronic device, is reduced, the transistor switching time is reduced and the systems that employ these transistors become more dense, less expensive, and capable of performing tasks of ever increasing complexity. The result of some sixty years of such development is the affordable, powerful silicon microelectronic integrated circuits (ICs) that have enabled the present mobile digital information age.

Integral to the success of the digital microelectronic revolution is the semiconductor material silicon, whose fundamental material properties make it the ideal semiconductor for low power, high speed logic and memory applications. While reduction of the size of the individual transistors is important, the technology of planar wafer-based microfabrication, which permits the dense integration of these components together on a single integrated circuit, is equally vital. Over the past sixty years, continuous improvements have been made to this microfabrication technology, and these improvements have allowed for manufacturers to push the limits of scaling and integration.

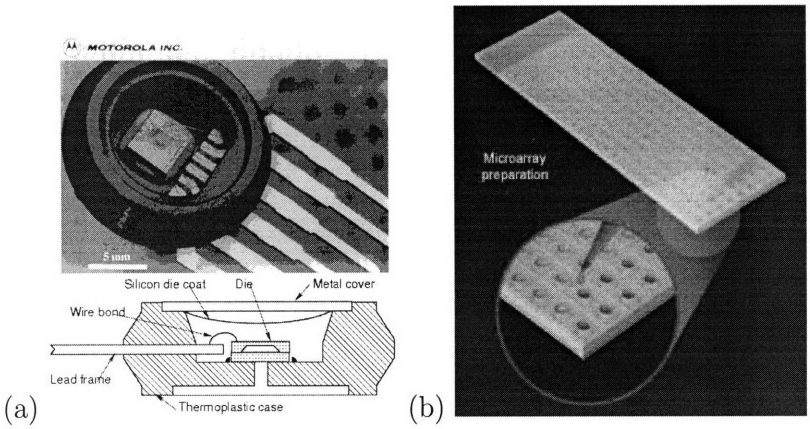

Figure 1-1: Examples of successful application of scaling and integration: (a) A packaged integrated pressure sensor developed by Motorola and a schematic cross-section showing the key components of the sensor [1]. (b) A microarray used for DNA study [2].

Beyond Microelectronics

Due to recognition of the successful application of silicon microfabrication technology within the field of electronics, the technology has been applied to other fields as well. For example, successful application of scaling and integration to sensor technology in the late 70's led to the development of integrated pressure sensors which play a role in improved automotive fuel economy [1]. The pressure sensor, shown in Figure 1-1, is integrated on a single silicon chip with electrodes that enable electronic control and readout.

In the field of microbiology, the development of DNA microarrays (often made from silicon) which allow for the orderly arrangement and study of thousands of DNA samples (see Figure 1-1) , has accelerated the pace of genomics research [2].

These are just two of the many examples of devices that make use of wafer-based microfabrication technology for something other than the standard microelectronic integrated circuit. These examples are given to make the point that silicon is an important material for technologies reaching well beyond CMOS microelectronics. Because silicon is so prevalent, a technology that can extend the utility of silicon by giving silicon some new functionality or capability, has the potential to impact a wide

array of applications.

The Limitations of a Single Material

While silicon is certainly a versatile material, it is not without limitations. Depending on the application or device, there are other materials which may be better suited for the task. One such device is the semiconductor laser, a component that is used in systems ranging from common DVD players to high speed fiber optic communication systems. These lasers are typically made from III-V semiconductors such as gallium arsenide (GaAs) and indium phosphide (InP). Silicon is not the ideal material with which to make a laser because of a fundamental material property that makes electro-optical conversion in silicon an inefficient process[1]. For years, however, researchers have been attempting to make a continuous wave silicon laser. This work was ultimately a success[2], however at this point, these silicon lasers have very limited efficiency. But the fact that such an effort was even undertaken, when room temperature operation of semiconductor lasers was achieved in 1970 [5] with the gallium arsenide (GaAs) material system, speaks to both the prevalence of silicon and a particular limitation of the semiconductor wafer based microfabrication process.

Wafer based microfabrication is a planar process that begins with a wafer of high purity crystalline material called the substrate. Any devices created during the microfabrication are limited in makeup to a small set of materials that are compatible with the substrate material. So even though a semiconductor laser is not new technology, the massive research effort of making a laser from the indirect bandgap material, silicon, is still relevant. This is because of the challenges associated with attempts to combine the GaAs material used to make the semiconductor laser from 1970 with silicon[3].

[1]The process of converting electrons into photons is a fundamentally inefficient process in silicon relative to certain III-V semiconductors. This is because silicon is an indirect bandgap material (see Reference [3]).

[2]Researchers at Intel Corporation have developed a silicon laser based on the Raman effect ([4]). These lasers convert light of one wavelength, called the pump wavelength, to light of a longer wavelength. This is called optical pumping as opposed to electrical pumping in which electrons are converted to light in the laser.

[3]Actually, there have been successful attempts to combine GaAs with Si, most notably the efforts

Overcoming the Limitation

It is this limitation with which this thesis is concerned. A new technique has been developed to fabricate lasers from InP, a material well suited for lasing at the telecom compatible wavelength of 1550 nm, and to integrate these lasers on a silicon substrate in such a way that they are intimately connected to the silicon chip. This thesis deals specifically with the design, fabrication, and testing of optical waveguides, the purpose of which is to facilitate this intimate connection between the integrated lasers and the silicon chip.

1.1 Motivation for III-V's on Silicon

Coupled with the ever increasing data processing capacity of silicon CMOS microelectronics, is an increased demand on the data handling components of digital microelectronic systems; currently, copper interconnects. In order for the system to function properly, the copper interconnects that transport the data between the various processing units must be capable of handling the increased data transmission rates. As microprocessor speeds increase, the metal interconnects suffer higher frequency dependent loss due to the skin effect and dielectric absorption [8]. At higher frequencies, the tolerances on impedance discontinuities for a given maximum allowable reflection become smaller as well. While potential future improvements in dielectric materials and processing techniques can alleviate some of these problems, a data rate of 10 Gb/s is typically cited as the maximum feasible data rate for all but the shortest chip-to-chip copper-based interconnects [9]. In order to maintain the current pace of performance enhancement, an alternative interconnect is required.

Optical interconnects (which use light, rather than the manipulation of electrons to transmit data) have been examined as a potential solution to the copper intercon-

discussed in References [6] and [7]. To be more precise, the limitation with these solutions is that they are typically very specific to the exact III-V material that is being combined with silicon. The exact technique used to combine GaAs with silicon, for example, cannot be used to combine InP with silicon. One of the advantages of the technique proposed in this work is that the same approach can be applied to the integration of many different III-V semiconductor materials on silicon.

nect problem. Optical interconnects already exist for communication channels with lengths greater than 1 m, as illustrated in Figure 1-2. Optical interconnects have the advantage over copper interconnects in terms of available channel bandwidth, and they don't suffer from electromagnetic interference and large signal attenuation, as do copper interconnects. That said, optical interconnects first were examined over twenty years ago [10] as an alternative to standard copper interconnects, for the very same reasons. So why have they not yet taken over? The reason for this is that the performance benefits aren't yet realized relative to copper at the current data transmission rates at chip-to-chip interconnect lengths. The crossover point, in terms of data transmission rate at a given interconnect length (and vice versa), where optical interconnects start to outperform copper interconnects in terms of power and latency was examined recently in Reference [11]. The analysis shows that at high enough rates, (greater than 10 Gb/s) there is a performance benefit for interconnects longer than approximately 15 cm. This would be a rather long trace on a computer motherboard. However, at higher transmission rates, the crossover length is smaller, more in line with the average length of traces on a motherboard. There is the argument that copper interconnect technology will continue to improve with the improvement of dielectric materials on the motherboard and that optical components suffer from reliability issues. The debate remains, but it is suspected that eventually, improvements to copper interconnect technology will be too costly to implement and in terms of price and power, optical interconnects will be a better choice.

Regardless of when it happens, there are certain technologies that will be required to make it happen. One such requirement is the integration of a laser onto the silicon chip, or it may be possible to implement a system where the lasers reside off chip and the chip only modulates or amplifies the optical signal. The latter scenario is similar to the case of an electrical power supply, which sits off-chip for a microelectronics system. Transistors on-chip are used to modulate and amplify the signal. Such an optical system would most likely require on chip amplification of the optical signal as there is signal power loss in coupling light from a fiber onto an on-chip waveguide and vice versa. This required gain could come from an integrated semiconductor

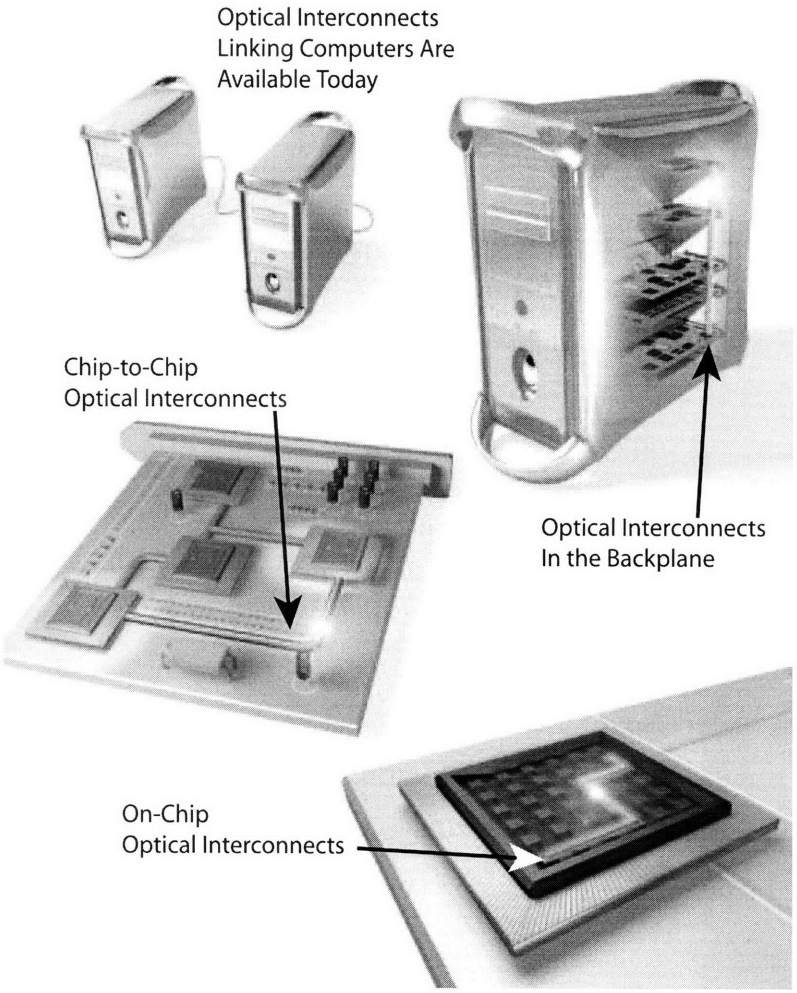

Figure 1-2: Optical interconnects already exist at length scales of 1 m and greater. The backplane and chip-to-chip interconnects are applications that could be enabled by the technology in this thesis.

optical amplifier (SOA) on the silicon chip which would restore signal levels to the level required for on chip distribution.

Some of the other necessary photonic devices can actually be made from the silicon material itself. For instance, it is possible that the photodetectors would be silicon or silicon-germanium. Many of the passive devices such as waveguides and couplers can be made from deposited dielectrics such as silicon dioxide and silicon oxynitride. However, as previously discussed, the efficient generation of light, or in the case of off-chip lasers, the efficient amplification and modulation[4] of light, necessitates the use of a material other than silicon. For these reasons, for optical interconnect systems at the chip-to-chip length scale, it is desireable to develop a method whereby III-V devices can be integrated onto a silicon substrate. As previously discussed, this work will focus on the integration of a III-V material, based on InP specifically, on a silicon substrate.

1.2 The Proposed Approach

The proposed approach for the integration of III-V devices on a silicon substrate requires four distinct capabilities:

1. Fabrication and accumulation of substrate-free III-V device pills.

2. Fabrication of a passive photonics platform with recesses on a silicon wafer.

3. Assembly of substrate-free III-V device pills in the recesses on the passive photonics platform wafer.

4. Mechanical bonding of pill, planarization, and formation of metal contacts.

[4]Silicon modulators do exist, but they are not as fast as their III-V counterparts. The operation of fast III-V modulators is based on the electro-optic effect, which is a very fast process whereby the refractive index of a crystal changes with the application of an electric field [12, 13]. The electro-optic effect is stronger in crystals lacking inversion symmetry such as GaAs and InP. The electro-optic response in silicon is weak[14]. Work is being done to overcome the problem of the weak electro-optic effect in silicon. The free carrier plasma dispersion effect, rather than the electro-optic effect, is being used to make silicon modulators [15, 16]

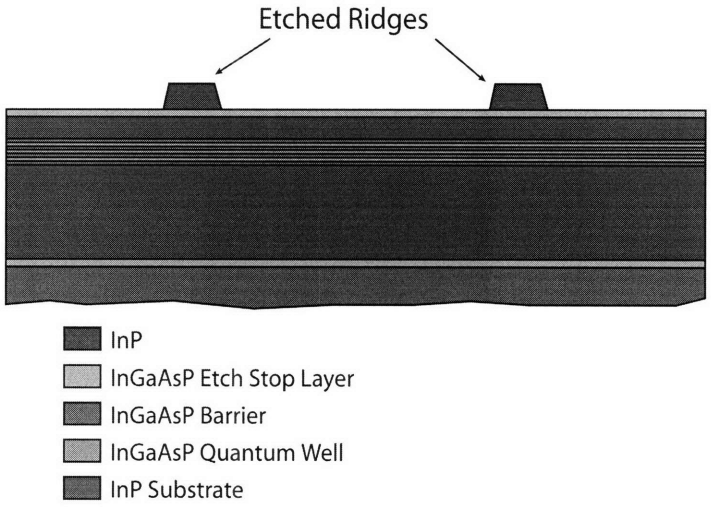

Figure 1-3: The 1^{st} step of the pill process. The waveguide ridges have been etched to the first etch stop layer.

Together, these four steps make up what is called, the RM^3, or Recessed Mounting with Monolithic Metallization technology. The work in this thesis is focused primarily on steps 2 and 3.

1.2.1 Pill Processing

The pill processing starts with InP/InGaAsP multi-quantum well epitaxial wafers. At the completion of the process, the 300 μm thick wafer has been etched and cleaved into several hundred 300 μm long, 145 μm wide, 5 μm thick InP/InGaAsP ridge waveguide pills with mirror-smooth end facets. These pills are then ready to be assembled on the silicon substrate. The significant steps in the pill fabrication process[5] are illustrated in Figures 1-3 through 1-6.

[5]The pill fabrication process described here is being developed by Joseph Rumpler as part of his Ph.D. work. Joseph is also credited with the fabrication of all of the pills that were used in this thesis.

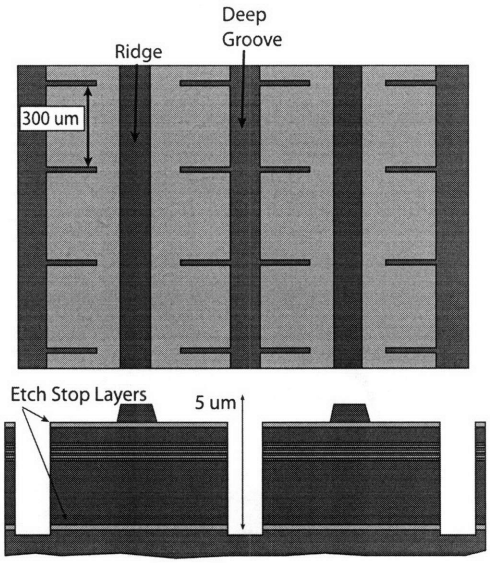

Figure 1-4: The 2^{nd} step of the pill process. The top image is looking from above the wafer surface (plan view). The lower image is looking at the vertical cross section (light going in/out of page in ridge waveguides). The deep grooves have been etched past the etch stop layer. The next step is the substrate removal.

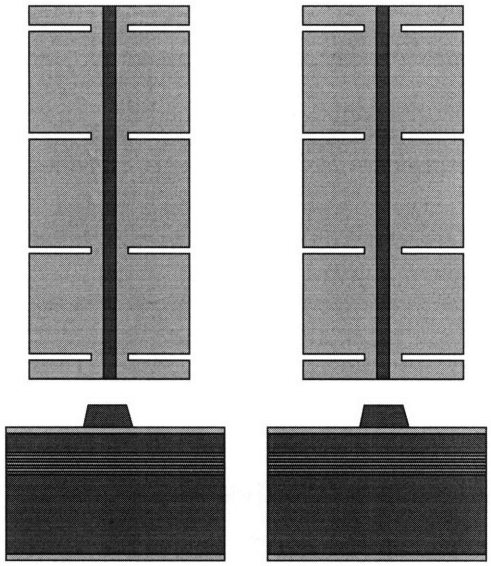

Figure 1-5: The 3^{rd} step of the pill process. The top image is looking from above the wafer surface (plan view). The lower image is looking at the vertical cross section (light going in/out of page in ridge waveguides). The InP substrate has been removed to form bars approximately 1 mm long, 145 μm wide, and 5 μm thick.

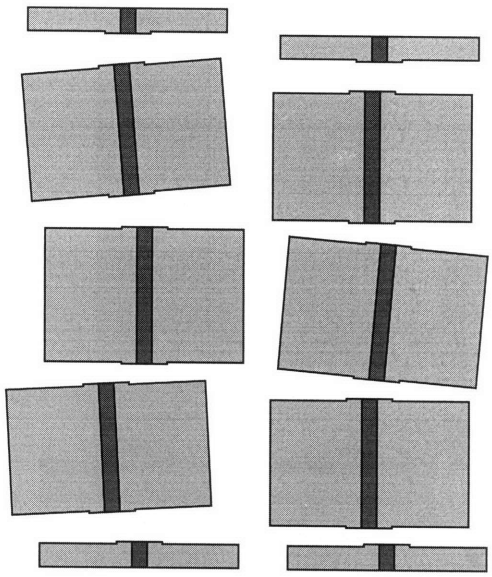

Figure 1-6: The 4^{th} and final step of the pill process. Ultrasonic agitation has cleaved the bars into 300 μm long InP/InGaAsP ridge waveguide pills.

1.2.2 Fabrication of Passive Photonics Platform

The passive photonics platform on silicon consists of waveguides designed to transport light over the surface of the chip and to couple light both to and from the InP/InGaAsP ridge waveguide pills. Wells etched into the waveguide stack house the integrated pills and facilitate end-fire coupling with the silicon oxynitride interconnect waveguides.

The interconnect waveguides are deposited as a lower cladding (3 μm of silicon dioxide), core (0.7 μm of silicon oxynitride), upper cladding (3 μm of silicon dioxide) waveguide stack on the silicon wafer. The total thickness of the stack is 6.7 μm. After the deposition of the silicon oxynitride core material, and before the deposition of the upper cladding, the silicon oxynitride is patterned and etched into the desired waveguide pattern as shown in Figure 1-7. The, following the deposition of the upper cladding, wells sized slightly larger than the ridge waveguide pills are etched into the waveguide stack all the way down to the silicon surface. A drawing of the silicon wafer with the full waveguide stack, with patterned waveguides and an etched well is shown in Figure 1-8.

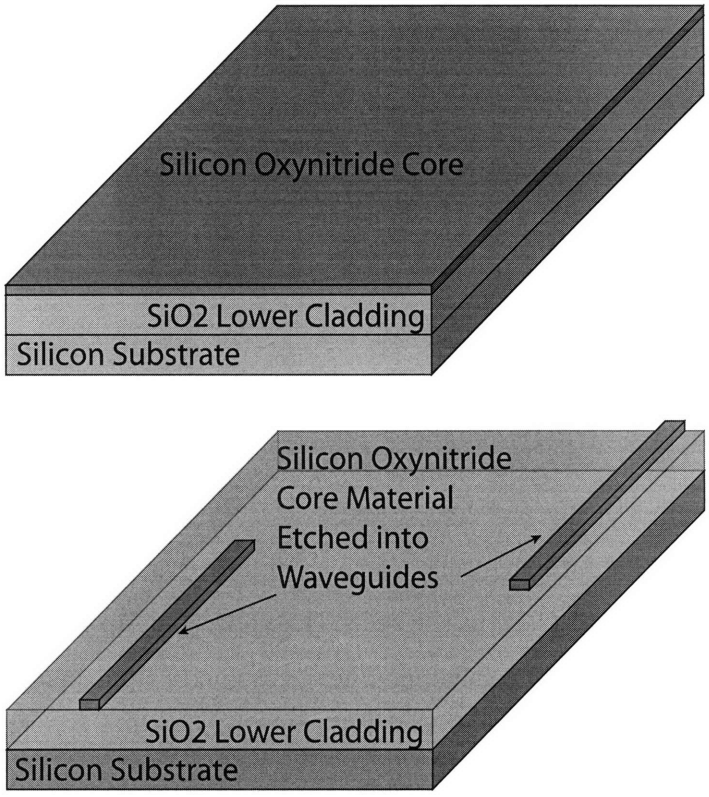

Figure 1-7: The 1^{st} and 2^{nd} steps in the waveguide fabrication sequence. In the top figure, the lower cladding and core layers have been deposited. In the lower figure, the core layer has been etched into the interconnect waveguide pattern.

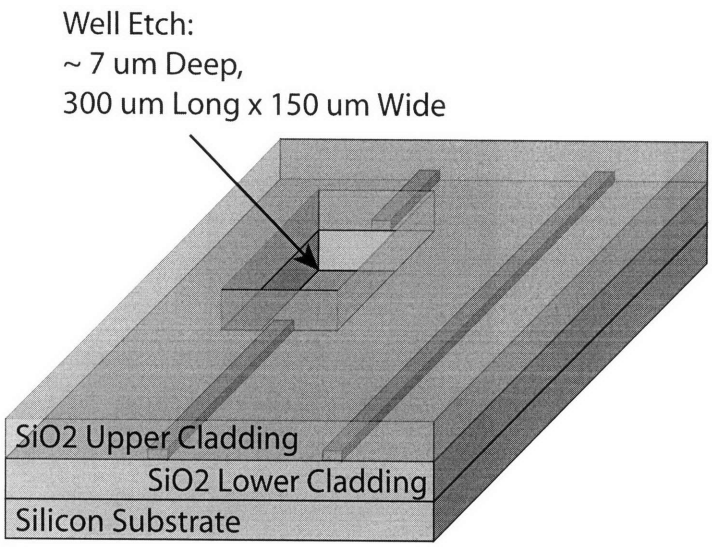

Figure 1-8: The 3^{rd} and 4^{th} steps in the waveguide fabrication sequence. The upper cladding layer (3 μm thick) has been deposited and a well has been etched through the entire waveguide stack all the way down to the silicon surface.

1.2.3 Pill Assembly

The next step after the deep etching of the wells is the assembly of the InP/InGaAsP ridge waveguide pills into the wells. A micropipette was used to pick up the pills and assemble them into place in the wells. The micropipette is able to pick up the pills with the application of a vacuum. The micropipette tip is bevelled (as shown in Figure 1-9) so that when in contact with the pill, the pill and the micropipette may be viewed from above with a microscope.

1.3 Alternative Approaches

In this section, a brief survey of current or recent alternative approaches to the integration technology used in this thesis will be given. Rather than attempting to systematically describe the entire integration space, specific examples taken from the literature will be discussed with the objective being to provide a general picture of the various methods and technologies that have been developed to integrate either multiple photonic devices on a single chip to integrate photonic functionality on sili-

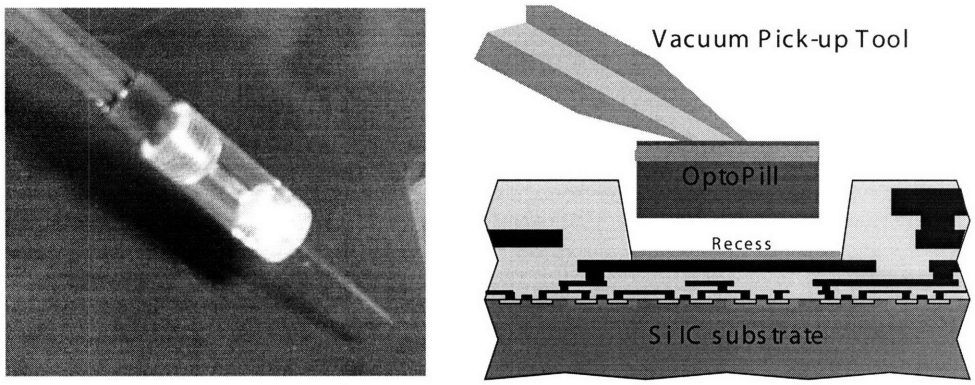

Figure 1-9: On the left, an image of the micropipette tool. On the right, a drawing showing the assembly of the pill into a well. While not actually done in this work, this drawing shows the case of integrating the pill into the inter metal layer dielectric stack of a fully processed silicon CMOS wafer.

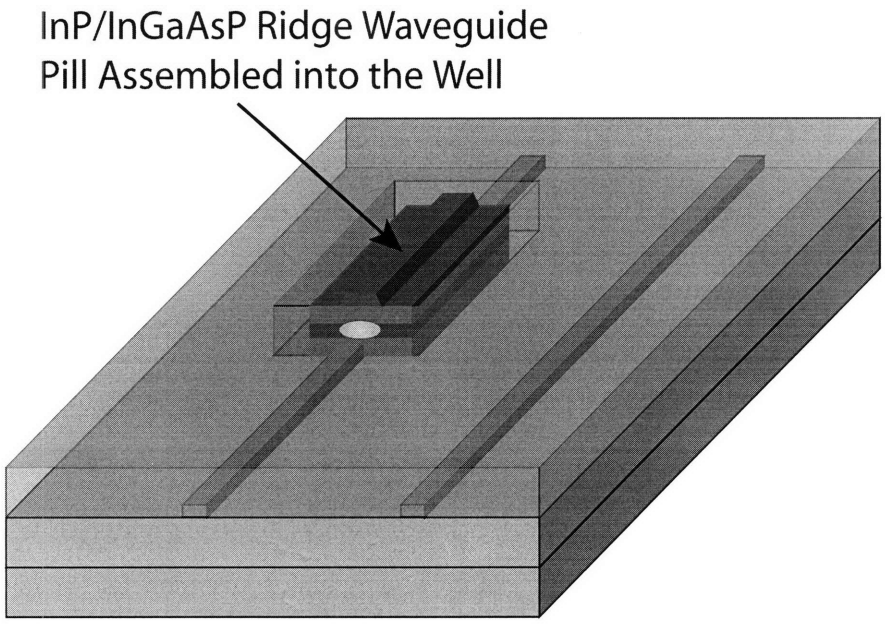

Figure 1-10: The pill assembled into the well. Light is shown exiting the pill at the level of the core material (shown as the darker region) in the pill.

con.

The technology proposed in this thesis allows for the integration of active and passive photonic devices based on any number of III-V material systems, together on a common silicon substrate which could contain silicon microelectronics. Consequently, it is the most complete of the integration types. Most of the alternative approaches that will be discussed in this section are for a less comprehensive level of integration, as the target application may be different, but they still provide a relevant comparison in that they provide a reference for the work in this thesis. For instance, the first technology that will be discussed does not involve the integration of electronics and is targeted for use in current optical fiber interconnects, but it does provide a target value for coupling efficiency (and the size of the coupling region required to achieve the given coupling efficiency) between integrated active and passive devices.

Integration Examples

Three examples taken from the literature will be examined:

1. Asymmetric Twin Waveguide: InP based active and passive photonic device integration

2. Fabless Photonics on Silicon: silicon waveguide and modulators seamlessly integrated with silicon microelectronics

3. Surface Mount Technology: similar to the work in this thesis, allows for the separate optimization of the photonic devices

Before continuing it is worthwhile to reiterate the basic shortcoming of wafer based microfabrication when it comes to the integration of multiple material or multiple structure devices. While photolithography and etching steps allow for the highly precise lateral (in the wafer plane) definition of devices and structures of nearly limitless complexity, the vertical cross-section, particularly of the active devices, is extremely simple by comparison. The integrated devices on the circuit can have very different lateral geometry, but they all share the same vertical structure. This all stems from

the fact that a given semiconductor material can only be grown on a select few other semiconductor materials. Solutions, therefore, either involve adding vertical complexity and developing a way to route optical and/or electrical signals in the vertical direction, or developing ways to alter the vertical structure in selective areas on the chip.

This need to alter the structure to perform various functions is not only a requirement of photonic/electronic integration but, it is also a requirement of photonic integration where more than one of the three photonic functions (generation, transmission, and detection of light) is integrated on a single chip. This is illustrated with the following scenario. Light is coupled onto waveguides at the edges of the chip. It is then coupled into an optical amplifier on the chip. At the exiting side of the amplifier, it is coupled back into an output waveguide which splits into several branches and terminates at a detector. Imagine that a single growth step over the entire surface of the wafer was used to create the core and cladding layers and that photolithography and etching were used to define the waveguides, etc. The problem is that the epitaxial structure that optimizes the gain is typically a strained quantum well structure with transition energies at the photon energy. The wave guiding sections require a structure with transitional energies that are greater than the photon wavelength, and the transition energies of the detector should be lower than the photon energy. Obviously, there is no single structure that meets these needs.

1.3.1 Asymmetric Twin Waveguide

In References [17] and [18], the development of a versatile technology based on an asymmetric twin waveguide structure is described. This technology is one of the approaches in which vertical complexity is added[6].

The asymmetric twin waveguide solution employs a structure with two core layers separated by a cladding layer. One of the core layers is designed to optimize the wave

[6]Solutions involving the alteration of the vertical structure in selective areas on the chip include material regrowth ([19], [20], [21], [22]), quantum well intermixing ([23], [24]), and selective area regrowth ([25], [26])

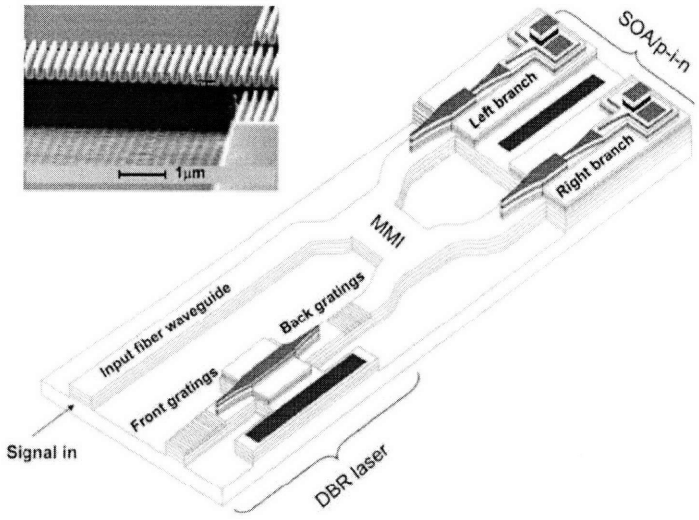

Figure 1-11: Taken from Reference [27], a three-dimensional schematic view of the integrated heterodyne receiver chip. Inset: Scanning electron micrograph of an LO laser grating fabricated on top of the fiber waveguide.

guiding function, the other is designed to optimize either the gain or detection function[7]. Transfer between the lower guiding waveguide and the upper gain waveguide is achieved with adiabatic tapers (see the dark tapered sections in Figure 1-11). At a taper length of 200 μm, 50% power transfer is achieved, and at a taper length of 400 μm and greater, 90% power transfer is achieved.

In Reference [27], the twin waveguide structure was used to fabricate a heterodyne receiver in the InP/InGaAsP material system. This involved the integration of a laser, waveguides, an optical amplifier, and a p-i-n photodetector. A schematic of the receiver is shown in Figure 1-11. Operation at 3 GHz was demonstrated. The advantage of this technique is that

As a final note, this technology has moved beyond the lab and has been commercialized by a company called Apogee Photonics. As reported in Reference [28], with this technology and others, Apogee is able to address all segments of the 10 Gb/s fiberoptic market, from very short-reach datacom links to high-performance, DWDM transport networks.

[7]Actually, in one of the papers (Reference [27]) employing this structure, three layers were included, so that each function was separately optimized

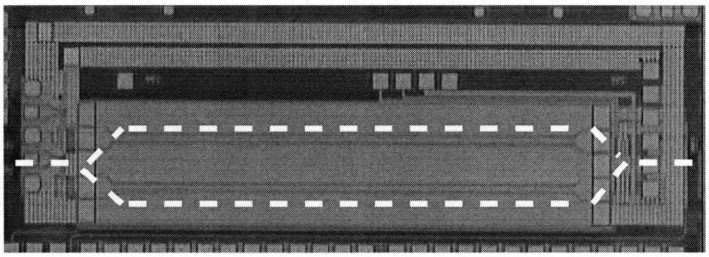

Figure 1-12: Taken from Reference [29], silicon optical Mach-Zehnder modulator. Dashed lines illustrate the path of the waveguides, which are hidden under the metal.

1.3.2 Fabless Photonics on Silicon

The goal of the work in Reference [29] is very similar to the goal of the work in this thesis. Passive (high index contrast silicon waveguides) and active (Mach-Zehnder modulators) photonic devices are integrated seamlessly with silicon microelectronics. This technology is particularly interesting because it uses only standard silicon microfabrication processes. Figure 1-12 shows the integrated Mach-Zehnder modulator which operates via the plasma dispersion effect in silicon[8]. As previously discussed, it is very difficult to make a laser from silicon. Rather than generating the optical signal on the silicon chip, the approach here is to couple light onto the chip from an off-chip laser. Figure 1-13 is an SEM image of the holographic lens used to transfer surface normal light from a fiber to in-wafer-plane light into the on-chip waveguides. Optical switching is then achieved by the modulator which is electrically driven by the readily available silicon microelectronics.

This technology is currently being commercialized by Luxtera [31]. Perhaps the main advantage of this technology is the fact that it makes use of standard silicon microfabrication processes. The disadvantage is that it relies on silicon-based modulators, which are not as efficient as their III-V counterparts.

[8]Faster modulators made from GaInAs discussed in Reference [30] make use of the Franz-Keldysh effect. Other modulators make use of the electro-optic effect. The electro-optic effect is a fast process whereby the refractive index of a crystal changes with the application of an electric field [12, 13]. Silicon, however, exhibits a weak electro-optic effect. The electro-optic effect is stronger in crystals lacking inversion symmetry such as GaAs and InP. The small electro-optic response of silicon was studied in [14]

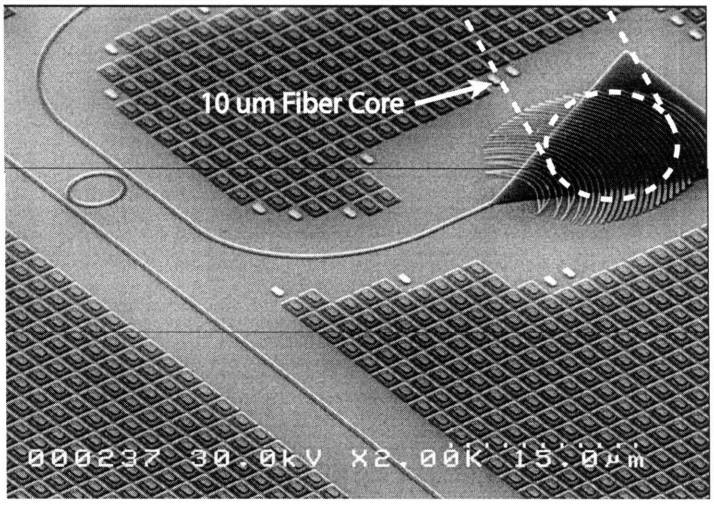

Figure 1-13: Taken from Reference [29], SEM photograph of a holographic lens (upper right corner) illuminated by an optical fiber (represented by dashed lines). Light is coupled into the submicron waveguides shown.

1.3.3 Surface-Mount Technology

A technology developed by a company called Xponent that combines the adiabatic tapers of the asymmetric twin waveguide with the III-V mounting technology similar to the III-V device mounting in this thesis is discussed in Reference [32] and [33]. This surface mount technology for optical components is inspired by the success of hybrid microelectronic packaging. Figure 1-14 is an overview of the surface mount technology process taken from [34]. The particular application for this work is the triplexer found in passive optical network transceivers (see Reference [35]). The success of passive optical networks depends on many factors, but a crucial aspect in particular is the price of the triplexer. This surface mount technology enables a reduction in the packaging costs of the triplexer through an order of magnitude increase in the laser diode and alignment tolerances. The technology allows for the separate optimization of the components for the three different wavelengths handled by the triplexer.

Another surface mount technology, designed to evanescently couple light from a surface mounted AlGaInAs laser operating at 1568 nm into a silicon waveguide on an SOI wafer, is discussed in References [36] and [37]. The technology has been developed

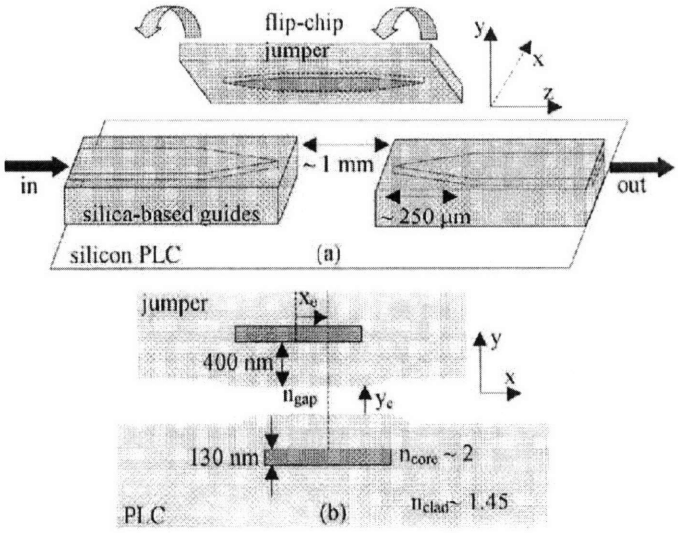

Figure 1-14: Taken from Reference [33], this drawing shows the use of an adiabatic jumper chip that is flip chip mounted to connect two separate waveguides. This jumper increases the alignment tolerances compared with the case of end-fire coupling between the two separate waveguides without the jumper.

for the pumping of the silicon Raman laser developed at intel as reported in Reference [4]. Figure 1-15 shows the cross section of the structure. These structures were optically pumped showing a pump power threshold of 200 mW at room temperature. In this case, alignment sensitivity is related to the alignment of the pump laser, not the mounted III-V structure. The III-V structure is invariant in the wafer plane.

1.3.4 Summary of Alternatives

Three different alternative technologies for photonic integrated circuits were shown. Each method has its advantages and disadvantages. In general, it is seen that the more flexible the technology, the more complex. The twin waveguide structure and the fabless photonics on silicon approach are elegant in design as they require no mounting and alignment of structures as with the surface mount techniques. However, they are limited in flexibility in that only one material, in the case of the fabless photonics on silicon, and one lattice matched material system, in the case of the twin waveguide,

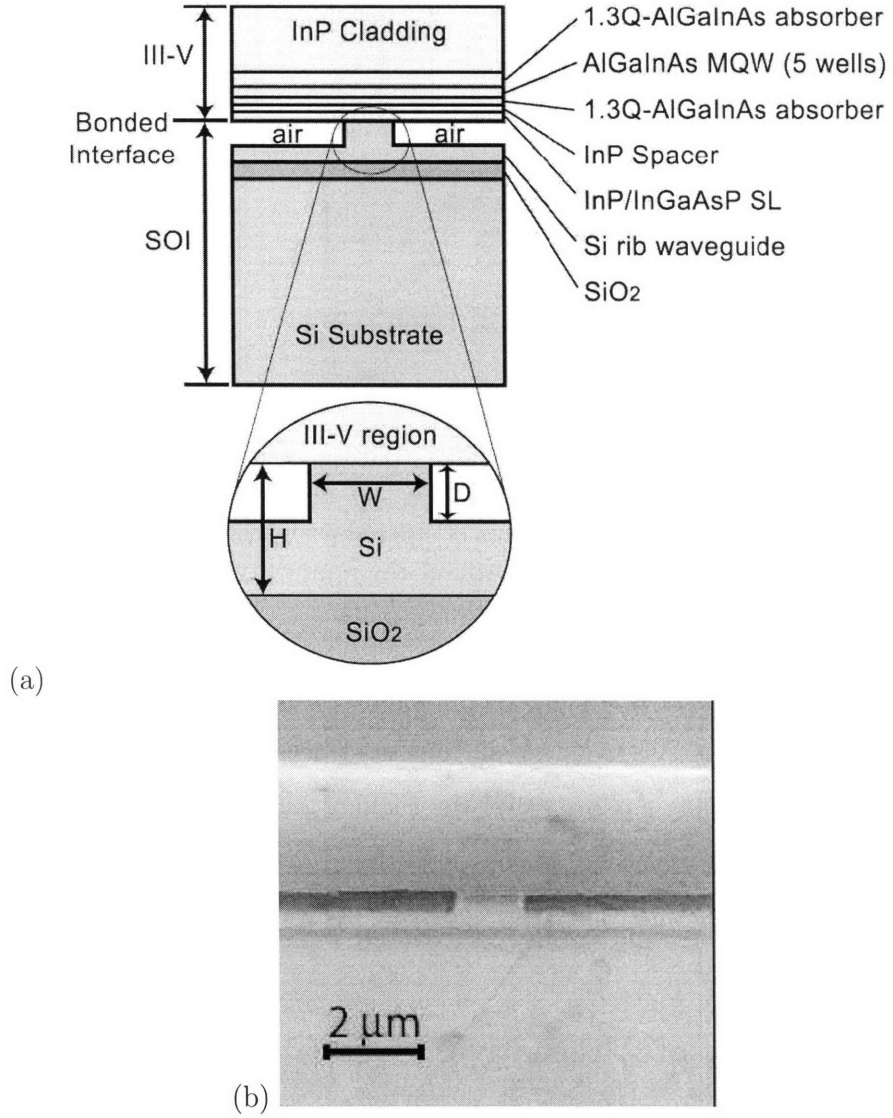

Figure 1-15: Taken from Reference [37], (a) drawing of the cross-section device structure of an SOI rib waveguide bonded to a III-V active region epitaxial structure. (b) SEM cross-section of the fabricated device showing the rib and the mounted III-V structure.

is available for use.

The technology proposed in this thesis is extremely flexible in that any III-V material can be integrated on silicon (or on some other III-V material for that matter), and it is correspondingly more difficult to implement than, for instance, the twin waveguide approach.

1.4 Overview of Thesis

This thesis is divided into six chapters, including this introductory chapter.

In the second chapter, the suitability of a fully processed (front-end and back-end) silicon CMOS wafer is examined for use as a substrate for low loss deposited dielectric waveguides. This would be desirable given the RM^3 technology applied to fully processed silicon wafers in which active optoelectronic devices are integrated into the back-end inter metal layer dielectric stack. In this case, the deposited waveguides would be required to carry light over the surface of the wafer between the various integrated devices. The concern, however, which is examined in the chapter, is that a fully processed wafer may be too rough to serve this purpose and the waveguides might be very lossy. It is shown in Chapter 2 that this is not the case.

The third chapter details the design of the silicon oxynitride waveguides. Finite Difference Time Domain (FDTD) simulation software is used to determine the interconnect waveguide (i.e. the silicon oxynitride waveguide) design that optimizes the optical coupling between the interconnect waveguides and the integrated InP/InGaAsP ridge waveguide pills. The effects of several non-idealities, such as pill misalignment, on the coupling efficiency are examined as well.

In chapter four, the waveguide and well fabrication is discussed. In addition, the preparation of waveguide samples for measurement and the assembly of InP/InGaAsP ridge waveguide pills is detailed.

The results and analysis of the optical testing and characterization of the waveguides and the InP/InGaAsP ridge waveguide pills are addressed in the fifth chapter. The analysis of measurements taken on integrated ridge waveguide pills are examined

in this chapter as well.

The final chapter provides a summary of the significant findings in this work and highlights some directions for future work.

Appendix A describes the optical measurement setup that was used for the majority of the experiments in this thesis. Appendix B gives the derivation for an approximate end-fire coupling equation given in Chapter 3. Appendix C contains detailed process recipes for all of the fabrication steps given in Chapter 4. Appendix D contains the Matlab code for several of the scripts written to aid in the analysis of the data. In particular, the code for calculating the multimode Transmission Matrix for an arbitrarily complex series of lossy dielectric materials.

Chapter 2

Waveguides on Processed Wafers

This chapter details the work (see Reference [38]) that served as the introduction to the main project of this thesis. In this chapter, the suitability of a fully processed (front-end and back-end) silicon CMOS wafer as a substrate for low loss deposited dielectric waveguides is examined. This would be desirable given a technology in which active optoelectronic devices could be integrated into the back-end inter metal layer dielectric stack, in which case the deposited waveguides would be required to carry light over the surface of the wafer between the various integrated devices. The concern, however, is that a fully processed wafer is too rough to serve this purpose and the waveguides would be very lossy.

In this chapter, the "roughness" of a processed wafer will be defined and a worst case roughness will be determined. It will then be shown that given a minimum waveguide index contrast, the added loss from the surface roughness is negligible.

2.1 Problem Background

Using processed silicon integrated circuit (IC) wafers as the foundation for forming optoelectronic integrated circuits (OEICs) has become an important approach to heterogeneous integration, and several different technologies ranging from flip-chip surface mounting [39] to recess mounting with monolithic metallization, [40] have now been demonstrated. With these techniques, III-V light emitters and detectors

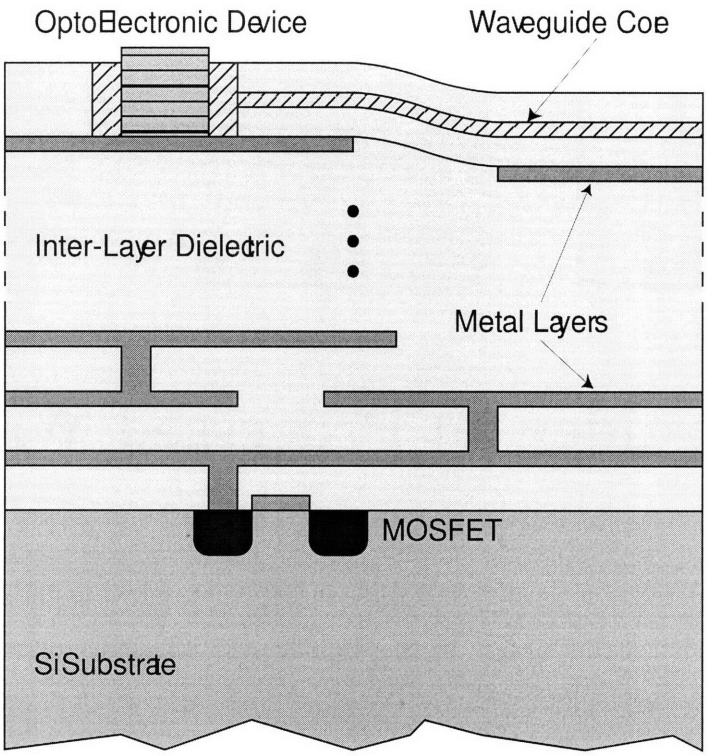

Figure 2-1: Schematic cross section of a Si CMOS IC integrated with optoelectronic devices and dielectric waveguides. Figure is not to scale.

can readily be integrated monolithically on high performance silicon ICs that have been fabricated on state-of-the-art commercial production lines. An example of an OEIC with a fully-processed Si substrate is shown in Figure 2-1. 2-1.

The reported applications of OEICs fabricated on Si foundations are almost exclusively directed at surface-normal input and output of the optical signals. While this is the desired geometry for many applications, there is another broad collection of applications for which it would be desirable to direct and guide the optical signals in the plane of the wafer. This is particularly true for on-chip optical interconnect applications; this geometry is also attractive for some fiber-coupled applications. This paper addresses the issue of adding monolithic dielectric waveguides to silicon IC wafers to provide thin film interconnect lines for optical signals similar to those which are formed for the electrical signals in the various metal layers.

The problem of forming dielectric waveguides on silicon wafers has been addressed

by numerous groups [41], but this work has almost exclusively been done on unprocessed wafers, rather than on wafers that have gone through a complete IC fabrication process. The published work has thus addressed the issues of choosing cladding and core materials, of reducing side-wall losses, and of forming bends, couplers, splitters, etc., but not the issue of forming these guides and structures on the surface of a fully processed integrated circuit wafer.

An important additional complication is introduced when waveguides are deposited on a processed integrated circuit wafer as part of the back-end process because the upper surface of the wafer is no longer perfectly smooth and planar. Chemical mechanical polishing (CMP) can be used to effectively restore the local planarity by reducing the topography caused by the metal traces, and CMP is able to significantly reduce the microroughness that is typical of the surfaces of low temperature deposited dielectric layers. These two properties of the CMP step are crucial to obtaining low loss waveguides. However, while the CMP process improves local planarity and minimizes microroughness, the CMP process itself introduces long range global non-planarity on the order of several millimeters. This is explained in Section II. Because of this global non-planarity, waveguide bending losses must be considered for bending in the direction perpendicular to the substrate in addition to the typical in-plane lateral bending losses. In this paper we examine these waveguide bending losses using the Marcuse waveguide bending loss equation [42] and the beam propagation method (BPM) [43] to develop a range of waveguide and process parameters for which these surface undulation losses may safely be ignored. It should be noted that the Marcuse equation models only radiation losses and was consequently used only as a means of validating the results from the BPM at short bending radii where radiation losses dominate.

2.2 Estimating Wafer Surface Non-planarity

Prior to the formation of the waveguide structure and most likely as part of each metal layer formation, a wafer surface will typically undergo a series of chemical-mechanical-

polishing (CMP) steps to remove local microroughness and local structure left behind by patterning of the metal layers and via formation. However, as previously stated, this CMP process can introduce long range or global non-planarity, loosely defined here as over a range of several mm, due to variations in underlying pattern density [44]. In order to determine the bending losses resulting from these long-range surface variations, it is necessary to know the details of the shape of the post-CMP wafer surface profile. The following model can be used to determine this profile and is discussed in detail in [44] . Consider the typical case in which the CMP technique is applied to an oxide layer deposited over an area with metal traces. According to the model proposed by Stine et al. [45], the relationship between ILD thickness and pattern density can be expressed as [44]:

$$z = \left\{ \begin{array}{ll} z_0 - \left[\frac{Kt}{\rho_0(x,y)}\right], & for\ t < \rho_0 z_1/K \\ z_0 - z_1 - Kt + \rho_0(x,y)\, z_1 & for\ t > \rho_0 z_1/K \end{array} \right\} \tag{2.1}$$

Here z is the ILD thickness referenced from the top of the metal regions, z_0 is the amount of dielectric deposited before CMP, $z1$ is the as-deposited metal step height, K is the removal rate for blanket or unpatterned wafers, t is time, and ρ is the pattern density. The pattern density for metal traces over some area is defined as the fraction of that area that is covered by the metal traces. Note that $t = \rho_0 z_1/K$ is the time required to remove the step height and is smaller for a lower pattern density, ρ_0. This is based on Preston's equation [46] in which the removal rate is proportional to the pressure, which is inversely proportional to the raised area or pattern density.

This model can now be extended to consider the differences in polishing for two separate areas. It is typical to have various areas of uniform pattern density on a chip. For instance, an area for SRAM memory has a fairly constant pattern density and may differ considerably from an area corresponding to an adder. Consider two such areas A and B on a wafer with the same z_1 and z_0 and different pattern densities ρ_A and ρ_B. For the purposes of this discussion, A and B represent areas that are

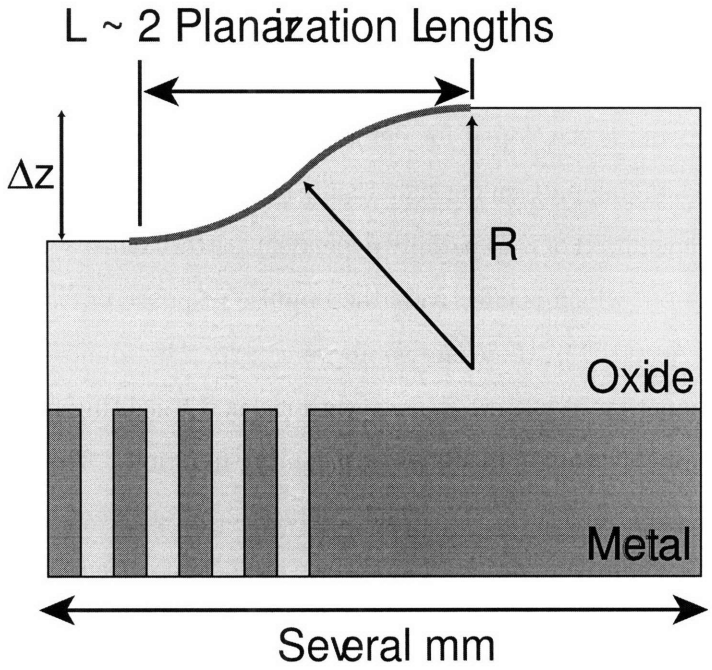

Figure 2-2: Schematic of a CMP oxide surface over a 0.5-1.0 pattern density variation over approximately two planarization lengths. R is the radius of each arc making up the approximated surface transition. Figure is not to scale.

approximately 10 μm x 10 μm. The following applies for $t > \rho_0 z_1/K$:

$$z_A = z_0 - z_1 - Kt + \rho_A z_1 z_B = Z_0 - z_1 - Kt + \rho_B z_1 \tag{2.2}$$

$$\Delta z = z_B - z_A = z_1 (\rho_B - \rho_A) \tag{2.3}$$

The as-deposited step height, z_1, is the maximum Δz for two areas, A and B, corresponding to the case in which $\rho_B = 1$, and $\rho_A = 0$.

An additional parameter called the planarization length or interaction distance, which is a function of the CMP pad, is effectively the minimum distance between areas A and B over which the full Δz height difference will be realized from the CMP step. This is illustrated in Figure 2-2. A more precise definition of the planarization length will follow. This length is typically on the order of a few mm. For two areas, separated by less than the planarization length, a fraction of the full Δz height will

be realized. The details of the surface profile transition over the Δz height variation requires an understanding of how the CMP pad flexes as it polishes.

In [44], a model is developed for determining the shape of the post-CMP wafer surface over a changing pattern density. Using a linear systems approach, the shape is found as the convolution of the spatially dependent pattern density with the CMP pad weighting function, which is effectively the impulse response of the pad. The profile between areas A and B in the example above can then be found as the convolution of a unit step function in pattern density with the pad weighting function. This case was simulated in [44] using four different weighting functions. The results were then compared with experimental results. The two most accurate weighting functions were a gaussian and an elliptic function. The surface profile data taken from the simulation using the gaussian weighting function matched the experimental data to within an RMS error of 56 $\mathring{A}$ over a surface profile which varied over 3000 $\mathring{A}$. For ease of use, the gaussian function was considered for the work presented in this paper. The error function is the result of the convolution of the gaussian function with a step function. When considering a gaussian weighting function, the planarization length is formally defined as twice the standard deviation:

$$L = 2\sigma \tag{2.4}$$

The planarization length is a function of the CMP pad type. In general a stiffer pad will have a longer planarization length while a more flexible pad will have a shorter planarization length. Typically, the planarization length falls in the range of 1 to 5 mm [44].

Because it is not possible using the BPM software to simulate waveguides shaped as an error function, it was necessary to fit the error function with two arcs to form an S-bend. The S-bend could then easily be simulated using the BPM software. In order to verify that an S-bend yields a close approximation to the error function, a Matlab simulation was run comparing the two curves for a one dimensional (1-D) problem. The simulation consisted of convolving the weighting function with the

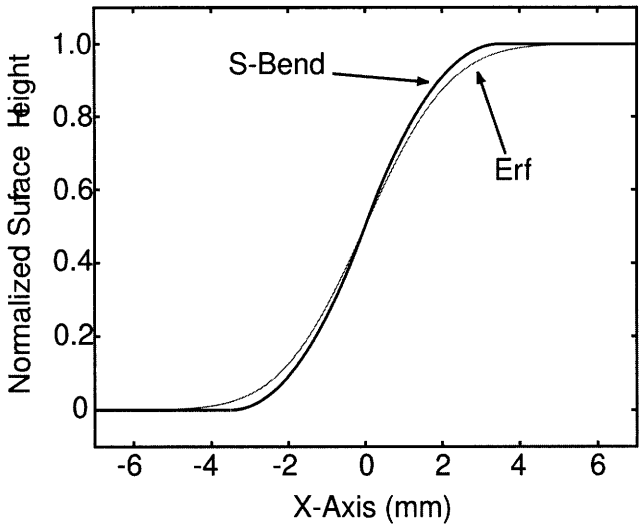

Figure 2-3: Error function curve corresponding to the surface profile based on the model in [44] compared with S-bend. L_{bend} is twice L, the planarization length.

pattern density function and then graphically comparing this result with an S-bend. A normalized Gaussian weighting function was used with a standard deviation, σ, of 1.75mm corresponding to a 3.5mm planarization length:

$$w(x) = \frac{1}{\sigma\sqrt{2\pi}} e^{-x^2/2\sigma^2} \tag{2.5}$$

This was then convolved with the pattern density function $\rho_0(x)$, which was a step function in this case. Referring to Figure 2-4, the height of the S-bend was fixed as Δz, and the length, L_{bend}, was adjusted to obtain a close match with the error function. Close matching was found with

$$L_{bend} = 2L \tag{2.6}$$

where L is the planarization length from Equation 2.4. The coefficient in Equation 2.6 controls the curvature of the S-bend. A higher coefficient yields a lower curvature.

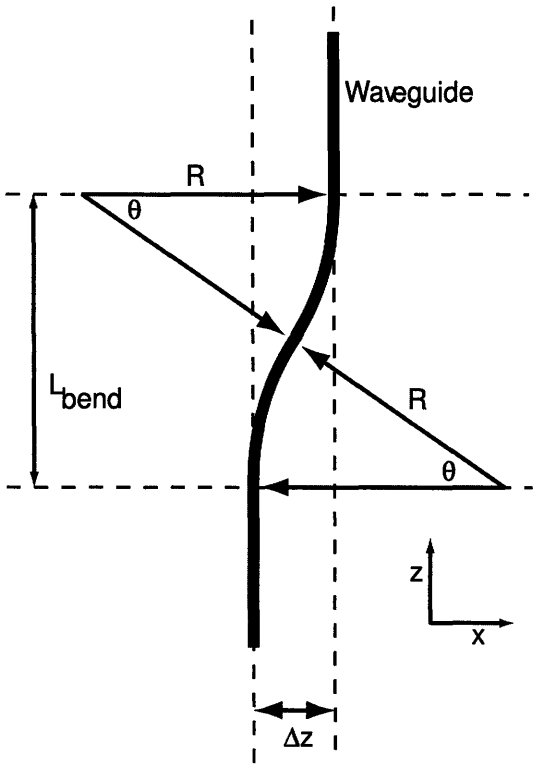

Figure 2-4: S-bend waveguide structure as entered into BeamProp. The x-axis is perpendicular to the wafer surface. A Δz of 5 μm was maintained for each simulation, L_{bend} was varied to vary the radius (R).

The radius, R, is then found from the following equation

$$R = \frac{L_{bend}^2 + \Delta z^2}{4\Delta z} \tag{2.7}$$

Using Equations 2.6 and 2.7, an S-bend was plotted along with the error function. The result is shown in Figure 2-3. Notice that the S-bend has greater curvature than the error function, meaning that to first order, losses from the simulated S-bend will be greater than losses from the actual error function. A coefficient of 2 in Equation 2.6 represents a conservative matching since the goal is to find the worst case bending loss. Based on Equations 2.3 through 2.7, a range of possible out-of-plane bending radii can be calculated for typical to worst-case back-end process scenarios. The worst case scenario corresponds to the case with the tightest bends and consequently the

largest bending losses. From Equation 2.7, clearly the minimum radius corresponds to the minimum L_{bend}, or minimum planarization length. The minimum planarization length for typical CMP pads is approximately 1 mm. Since L_{bend}^2 is much larger than Δz^2 (i.e. the typical height variations are on the order of microns while the interaction distances are on the order of millimeters), the minimum radius corresponds to the maximum Δz. Typical metal layers are at most approximately 0.5 μm thick. If there were 10 such metal layers all perfectly aligned so that the 0.5 m height variation added from one layer to the next, there would be at most a 5 m height variation on the final wafer surface. Inserting these values ($L_{bend} = 2L = 2$ mm, $\Delta z = 5\mu$m) into Equation 2.7 yields a worst case bending radius of approximately 20 cm.

2.3 Modelling Loss Due to Surface Curvature

2.3.1 Restriction To Single Mode

It has been observed that single mode guides see less total bending loss than multi-mode guides [47]. When the confined, guided modes of a straight waveguide encounter a bend, they couple into corresponding bending modes which radiate as they go around the bend. For a multi-mode guide, the fundamental mode of the straight portion couples into the fundamental bending mode as well as higher order bending modes which are non-existent for the single-mode case. These higher order bending modes radiate more power than the fundamental bending mode due to the fact that the field intensity of the higher order modes is larger at the waveguide boundaries than the fundamental mode [47]. No attempt was made to model this effect in either the BPM or Marcuse equation simulations, and thus the present study is restricted to single-mode guides.

2.3.2 Marcuse Formalism

The bending loss for a two-dimensional slab waveguide was approximated by Marcuse [42] as

$$\alpha = \frac{\gamma^2}{\beta\,(1+\gamma d)}\frac{\kappa^2}{(n_1^2-n_2^2)\,k_0^2}e^{2\left\{\gamma d - R\left[btanh^{-1}\left(\frac{\gamma}{\beta}\right)-\gamma\right]\right\}} \tag{2.8}$$

where α is one half the power loss coefficient, γ is the extinction coefficient which is the magnitude of the transverse portion of the k-vector in the cladding, κ is the magnitude of the transverse portion of the k-vector in the core, β is the propagation coefficient, d is one half the waveguide width, k_0 is the magnitude of the free-space k-vector, R is the bending radius, n_1 is the core index, and n_2 is the cladding index. Given d, n_1, n_2, and k_0, γ, β, and κ can be determined for a propagating mode from the dielectric slab two-dimensional waveguide eigenvalue equation

$$tan\,(\kappa d) = \frac{\sqrt{k_0^2\,(n_1^2-n_2^2)-\kappa^2}}{\kappa} \tag{2.9}$$

and the following relationships

$$k_0^2 n_2^2 = \beta^2 - \gamma^2 \tag{2.10}$$

$$k_0^2 n_1^2 = \beta^2 + \kappa^2 \tag{2.11}$$

2.3.3 Beam Propagation Method Simulation

The beam propagation method (BPM) was also used to estimate bending losses using a software package from Rsoft called BeamProp[1]. The package includes the option of using a Pade-based model to simulate bending greater than 15^o from the z-direction (the direction of propagation). In most of the simulations reported here, this was not the case and so the basic BPM model was used. BeamProp allows the user to inject the fundamental mode into a 3 dimensional guide and monitor the power of that mode along the guide by computing overlap integrals of the waveform with the

[1]BeamPROP is a product of Rsoft Design Group, Ossining, N.Y.

initial injected mode at certain points along the guide. In this way it was possible to determine the losses for various bending radii and various 3-D waveguide geometries. A basic parameterized waveguide structure was used for each simulation and the parameters were adjusted or automatically stepped for each simulation. The structure consisted of two straight sections connected by an S-bend structure composed of two arcs of equal radius and angle. The straight sections were offset laterally by 5 μm, corresponding to the worst case height variation across a planarization length. The structure is illustrated in Figure 2-4. As the radius was increased in steps, the length of the S-bend was increased to maintain the constant 5 μm lateral separation. 3-D waveguide structures were graphically entered as 2-D objects, where the details of the third dimension, depth, were defined numerically through various menus in the program. It is important to recognize the proper orientation of the axes in Figure 2-4, with respect to the surface. The x-axis in the figure is perpendicular to the plane of the wafer surface. The z-axis, or propagation axis is parallel to the wafer surface. The y-z-plane (the y-axis, not shown, is directed into the page) is parallel to the wafer surface.

2.4 Simulation Results

Using both the Marcuse equation and the BeamProp software, S-bend waveguide structures with square cross-sections were simulated. In all cases the cladding was taken to be silicon dioxide (n = 1.45) and the various indices of refraction assumed for the cores of the simulated waveguides were chosen based on representative waveguides found in the literature. Table I shows the core/cladding indices, the typical material system used to achieve the index contrast, the maximum waveguide dimensions for single-mode operation, typical propagation loss for a straight guide, and the targeted application. It should be noted that not all of these waveguide material systems are necessarily compatible with post back-end processing usually because of the requirement of high annealing temperatures, or because they are, by definition, a part of the front-end process. Nevertheless they represent typical waveguide designs and,

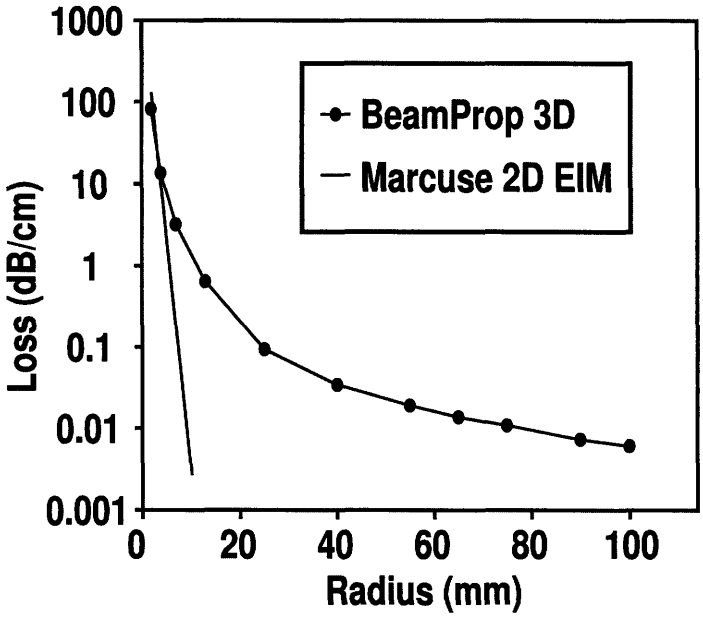

Figure 2-5: Waveguide loss at $\lambda = 1.55$ μm versus bending radius predicted by the Marcuse formula and by the BPM simulation in a guide with a 4.5 μm wide silicon oxynitride core ($n = 1.46$) and silicon dioxide cladding ($n = 1.45$).

therefore, provide some relevance to actual waveguides.

The results of a typical simulation showing predicted bending loss versus bending radius for the two models are shown in Figure 2-5. Notice the large discrepancy at large radii between the BPM and Marcuse equation results. As previously mentioned, this is due to the fact that the Marcuse equation is modeling only radiation losses in the bending structure and does not take into account modal coupling losses between the straight and curved sections or between the two opposing curves of the S-bend. For this reason, the results are similar only in the small bending radius regime where radiation loss dominates. The Marcuse results are included to stress the importance of including the coupling losses of the BPM model when considering bending losses at large radii.

The waveguide simulated in Fig. 5 has a width of 4.5 μm and the propagating radiation has a wavelength of 1.55 μm. The core index is 1.46, and the cladding index is 1.45. This results in a Δn of 0.01, which is the lowest index contrast that

TABLE I
TYPICAL WAVEGUIDE CHARACTERISTICS

Core Clad	Indices	Application	Dimension Wavelength	Loss dB/cm	Ref.
Si SiO_2	3.45 1.45	Dense integrated optics on SOI	.5 μm 1.55 μm	> 10	[13]
Si SiO_2	3.45 1.45	SOI ridge guides, Fiber Coupling	8 μm 1.55 μm	0.25	[14]
Si_3N_4 SiO_2	2.0 1.45	Sensors, Microphotonics	~1 μm 1.3-1.55, 0.85	~1	[16]
$SiO_{x1}N_{y1}$ $SiO_{x2}N_{y2}$	1.57 1.49	Passives	1.6 μm 850 nm	1.9	[12]
SiO_xN_y SiO_2	1.5 1.45	Sensors Optical Communications	3 μm 1.55 μm	0.2	[11]
SiO2 : Ge SiO2	1.465 1.445	Passives, Fiber Coupling	5.5 μm 1.3 – 1.55 μm	0.042- 0.23	[15]
SiO2 : Ge SiO2	1.455 1.445	Passives, Fiber Coupling	5.5 μm 1.3 – 1.55 μm	0.063	[15]

Typical waveguide materials, parameters, applications, dimensions, and experimentally measured transmission losses [10].

was simulated. Because a low index contrast translates into weaker confinement and, therefore, a larger bending loss, this waveguide simulation illustrates the worst case of the simulated guides (i.e. greatest loss for a given bending radius).

BPM simulations like those illustrated in Figure 2-5 were also performed for waveguides with silicon dioxide cladding (index = 1.45) and cores with indices yielding index steps of 0.05, 0.1, 0.55, and 2.0. The plots of loss as a function of bending radius look qualitatively similar to those in Figure 2-5, but, of course, show smaller losses. Rather than showing several plots, three points from each simulation for the various indices of refraction are included in Table II. The values given in the table are the radii in microns that yield a bending loss of 10, 1, or 0.1 dB/cm for a given index contrast.

Recall that a radius of 20 cm was determined to be the worst case (minimum) bending radius for a wafer surface profile. It is clear from Fig. 5 that for radii of 20 cm or greater, the bending losses may be ignored. Note that 20 cm, or 200 mm, falls well to the right of the x-axis values included in the figure. For an index contrast of 0.01, a 20 cm bending radius is nearly an order of magnitude greater than the 2.2 cm (see Table II) bending radius that gives a loss of 0.1 dB/cm. This is entirely consistent with the fact that rectangular dielectric waveguides are designed to maintain low losses in lateral bends in the wafer plane, and that in most cases bending radii considerably less than 20 cm are sought. Table II shows that the bending radii on the wafer would have to be much smaller than 20 cm to contribute any significant loss. The values in Table II are valuable in that they show the order of magnitude of the bending radii that produce a certain loss. Because the exact values were not verified experimentally, they represent an approximation.

One important observation to make regarding the BPM simulations is that they become increasingly sensitive to round-off errors in the computation as the bending radius is increased and the accuracy of the modeling must be questioned and in particular the leveling off of the loss at large radii, which was seen in all cases, may be in part an artifact of the modeling and in reality the loss may be smaller than indicated. The calculation can be viewed as yielding a conservative estimate of the

TABLE II
BENDING RADII

	0.01	0.05	0.1	0.55	2.0
10 dB/cm	4300	600	275	52	20
1dB/cm	11000	1550	610	140	50
0.1 dB/cm	22000	4000	1800	450	300

The values in the table are the bending radii (μm) which produce a given bending loss (row) for a given waveguide index contrast (column). These values are taken from the BeamProp simulations.

loss and in spite of this possible effect, still indicates that the loss is negligible.

2.5 Discussion and Conclusion

Using equations which govern the dependence of underlying pattern density on the removal rate of inter-layer dielectric oxide by CMP, a worst case wafer surface profile for a deposited waveguide has been calculated. This corresponds to the surface profile of a Si CMOS wafer after completion of the back-end processing including all metal layers. Given a minimum planarization length of 1 mm and a total step height of 5 μm, a deposited waveguide would see approximately a 20 cm out-of-plane bending radius. The identification of 20 cm with the worst-case bending radius associated with the surface undulations on processed IC wafers is clearly a key result of this study. This work translates the problem from one of understanding waveguide loss due to post CMP global non-planarity into the more common problem of waveguide loss given a certain bending radius. Simulations using the Marcuse bending loss equation and Rsoft's BeamProp BPM software package, both indicated that for even the worst case scenario, out-of-plane bending losses may be safely ignored as they typically fall well below the range of propagation loss for the corresponding material systems. This implies that modern, CMP-processed integrated circuit wafers can be used as low-loss substrates for the deposition of rectangular dielectric waveguides, and that addition of dielectric waveguide interconnect layers to the back-end process sequence is a viable approach to implementing intra-chip optical interconnects and optical clock distribution networks.

Chapter 3

Interconnect Waveguide Design for Optimum Coupling to Integrated III-V Devices

In an on-chip integrated photonic system, an interconnect waveguide provides the path for transmission of the optical signal from one device or on-chip location to another. An interconnect waveguide is the optical equivalent of a metal wire interconnect in an electronic circuit. Just like a metal wire interconnect, the waveguide should be compact and capable of providing low loss, low distortion signal transmission all in a manner that does not adversely affect the performance of the devices it connects. Figure 3-1 is an illustration of a silicon chip with integrated III-V devices (InP SOA and an InP laser) connected to the edge of the chip and to other devices by interconnect waveguides[1]. As discussed in the introductory chapter, in the context of the proposed III-V device integration technique, the interconnect waveguides must be designed for optimized coupling to the integrated III-V devices[2] (which also incorporate waveguides), taking into account the non-deterministic nature of the III-V

[1]The term, *interconnect waveguide* will be used repeatedly throughout this thesis. This is done to distinguish these waveguide from the ridge waveguides in the integrated III-V devices.

[2]The actual III-V devices used in this work were fabricated using InP/InGaAsP multiple quantum well material that was specifically designed for ridge waveguide lasers. While the design methods used in this chapter can be generalized to a different material and/or device structure, the quantitative results are based on the specific InP/InGaAsP material and structure that was used in this work.

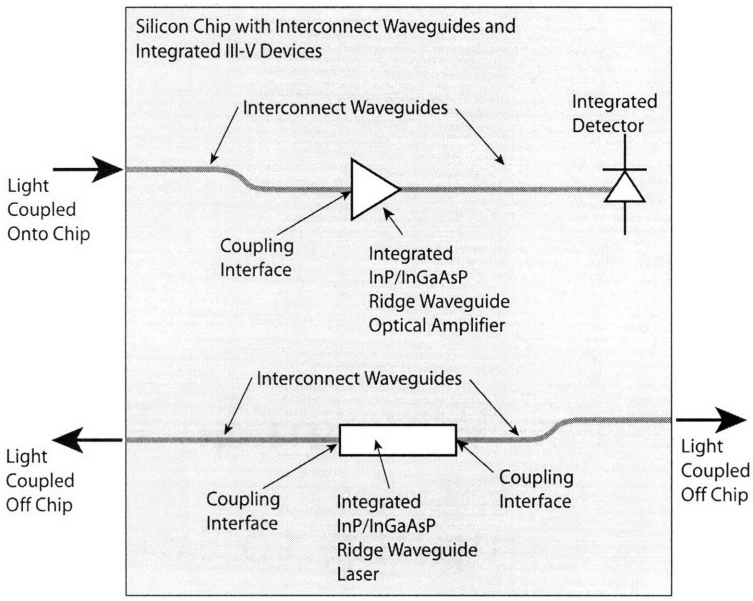

Figure 3-1: Illustration of integrated InP/InGaAsP devices connected to the edge of the chip and other devices via the interconnect waveguides. The interconnect waveguides are designed to maximize the efficiency of the coupling interface.

device placement. In addition, the waveguide design requires a consideration for the fabrication of the waveguide, and this must be compatible with the fabrication of the other components in the system.

This chapter details the design of the interconnect waveguides. It is divided into three sections, one for each of the three distinct interconnect waveguide design stages. In the first stage, the focus is primarily on rough design. That is, no waveguide parameters are finalized, but a suitable range is found based on the consideration of the available materials, the size of the III-V structure, the approximate desired maximum for the waveguide propagation loss, etc.

In the next section, the design is focused on maximizing the coupling between the interconnect waveguides and the III-V device waveguides for the most simple case, perfectly aligned end-fire coupling[3] with no gap between the waveguides.

In the final section of this chapter, Finite Difference Time Domain simulation soft-

[3]End-Fire coupling of two waveguides simply involves bringing the two ends of the waveguide together so that they share the same propagation axis. The end facets of the two waveguides butt up against each other

ware, which was used extensively for the design of the waveguides will be introduced and used to determine the effect of integrated device misalignment and various other real-world imperfections on the coupling efficiency. The basic goal is to determine the waveguide design that maximizes the interface coupling efficiency and minimizes the sensitivity of this coupling efficiency to random fabrication and integration process variations. The simulations in this section are also useful in that they provide expected values for the experimental coupling loss measurements.

3.1 Basic Waveguide Background and Design

This section focuses on the first waveguide design stage where basic waveguide parameters will be discussed. The goal is to give the reader some basic waveguide background in addition to explaining the rationale behind some of the basic design decisions involving waveguide materials, geometry, etc.

3.1.1 Waveguide Composition

A waveguide is a device composed of both a high refractive index and a low refractive index optically transparent material. The higher refractive index material, called the core, is surrounded by the lower refractive index material, called the cladding. The light propagates in the core through a series of lossless reflections at the core/cladding interface as illustrated schematically in Figure 3-2.

The following sections will discuss the significance of the waveguide geometry, index of refraction of the core and cladding materials, the propagation loss in a waveguide due to material absorption and other imperfections, and the operation of the most basic waveguide: the slab waveguide.

3.1.2 Waveguide Geometry

The cross-section of a waveguide typically takes one of the forms shown in Figure 3-3. On-chip waveguides are fabricated using planar processing techniques which result

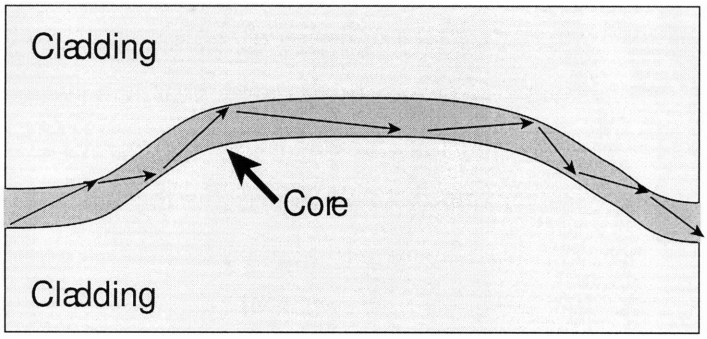

Figure 3-2: Light propagating in a waveguide through a series of reflections at the core/cladding interface.

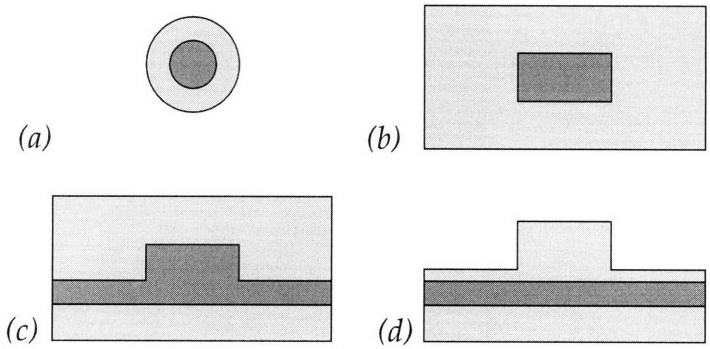

Figure 3-3: Common waveguide cross sectional geometries: (a) circular (b) buried rectangular channel (c) strip-loaded (d) ridge. The core material is shown as the darker material.

in waveguides of the planar variety (Figure 3-3 part (b), (c), or (d)). Based on the waveguide material system or the application, one shape may be more appropriate than another. For instance, the buried rectangular channel guide, while capable of supporting compact modes, is more sensitive to core sidewall roughness (rough core/cladding interface induced by etching of the core) than the ridge guide. The ridge and strip-loaded geometries are useful when the core material cannot be etched or when it is difficult to do so. The rectangular channel waveguide geometry is chosen for the waveguides in this thesis because it allows for more confinement and a correspondingly more compact design. The interconnect waveguides are buried rectangular channel guides while the InP/InGaAsP device waveguides are ridge waveguides.

3.1.3 Index Contrast

Waveguides are characterized by the degree of index contrast and are often referred to as being either high index contrast or low index contrast waveguides. The index contrast, Δ, is the difference between the refractive index of the core and the cladding.

$$\Delta = n_{co} - n_{clad} \tag{3.1}$$

The index contrast is also sometimes [48] defined as a percentage

$$\Delta = \frac{n_{co} - n_{clad}}{n_{co}} \tag{3.2}$$

While there is no standard crossover point between low and high index contrast waveguides, an index contrast larger than 0.1, using the definition of Equation 3.1, is typically considered high index. Typical low index contrast waveguides may have an index contrast as small as 0.005 or lower. High index contrast waveguides on silicon formed using silicon as the core material ($\eta_r(Si) = 3.5$) and silicon dioxide as the cladding material ($\eta_r(SiO_2) = 1.45$) have a very high index contrast ($\Delta = 2.05$). The interconnect waveguides in this work have a moderately high index waveguides with index contrasts on the order of 0.2. This permits a relatively compact design with small waveguides and small low loss bending radii on the order of 200 μm.

3.1.4 Single-Mode vs. Multi-Mode Waveguides

Depending on the geometry and composition of a waveguide, the propagating light in the waveguide can take on a variety of configurations or modes. The modal characteristics of the waveguide play an important role in the performance of the overall photonic system and must be taken into consideration during waveguide design. Waveguides are classified as being either single-mode or multi-mode. Single-mode waveguides are capable of supporting only one mode, whereas multi-mode waveguides can support two or more guided modes.

The question of employing single-mode or multi-mode waveguides is dependent

upon the target application. In general, higher performance (i.e. high speed, low power consumption) and longer interconnect lengths require single-mode waveguides, while multi-mode waveguides can be used for lower performance applications and shorter interconnect lengths. It is also possible to utilize a hybrid approach in which both single-mode and multi-mode guides are used. The majority of the work in the thesis was done with single-mode waveguides, however some consideration was made for the applicability of multi-mode waveguides. Because of the existence of only one mode, single-mode waveguides do not suffer from intermodal dispersion. A lower bound on the length at which intermodal dispersion (IMD) becomes a significant factor in a slab waveguide can be found as a function [49] of the waveguide core and cladding indices and the period of the optical signal:

$$L_{IMD} = \frac{cT}{n_{co}(\frac{n_{co}}{n_{cl}} - 1)} \tag{3.3}$$

where c is the speed of light in a vacuum, T is the period of the signal, n_{co} is the refractive index of the core, and n_{cl} is the refractive index of the cladding. Equation 3.3 gives an L_{IMD} of approximately 18cm for a 10GHz signal with $n_{co} = 1.6$ and $n_{cl} = 1.45$. This implies that any waveguide interconnect operating at 10GHz with the given refractive index characteristics will suffer from intermodal dispersion for lengths greater than 18cm. This falls within the typical length range of on-board interchip interconnects. So that the results of this work could be applied to any general high frequency, long-range optical interconnect, the waveguides presented here were designed for single mode operation.

Besides intermodal dispersion, there are other characteristics related to overall performance that vary depending on the choice of single-mode or multi-mode waveguides. Both coupling loss and propagation loss may increase or decrease depending on the modal characteristics of the waveguides.

Material	Refractive Index
SiO_2	1.45
SiO_xN_y	1.45 - 2.0
Si_3N_4	2.0
Silicon-Rich Nitride	2.0 - 3.5
Metal Oxides	1.6 - 2.2
Silicon/Polysilicon	3.5

Table 3.1: Refractive index of common waveguide materials.

3.1.5 Waveguide Material Selection

Selection of the proper waveguide materials requires a consideration of the wavelength of light that will be used in the system (1550 nm for this work as mentioned in the first chapter), the absolute refractive index that is most compatible with the active photonic devices, the order of the index contrast that will be required, and the compatibility of the waveguide materials, the substrate, and the active devices.

Due to advancements in thin film processing, there are a wide variety of materials that meet the low temperature, silicon processing compatibility requirements for the interconnect waveguides. These materials include silicon dioxide, silicon oxynitride, silicon nitride, silicon-rich nitride, metal oxides, polysilicon, doped versions of these materials, and many other materials as well.

Table 3.1 lists these materials and the corresponding refractive index ranges. There is often more than one way to deposit each of these materials. For instance, silicon dioxide films can be deposited by CVD, sputtering, flame hydrolysis deposition, sol-gel processing [50], or via spin-on techniques. It is necessary, therefore, to determine not only the waveguide material, but also the manner in which the material will be deposited.

Silicon Oxynitride

The problem of silicon compatible waveguides is not new, and much has been published in this area ([48], [51], [52], [53], [54]). Silicon oxynitride (SiO_xN_y) is becoming a standard material for low-loss waveguides that are compatible with silicon processing.

Silicon oxynitride can, in theory, be deposited with any nitrogen:oxygen stoichiometric ratio, with resulting films ranging from pure SiO_2 to pure Si_3N_4. Consequently, the refractive index of the film may be varied from 1.45 to 2.0 as indicated in Table 3.1. Waveguides with an index contrast as high as 0.55 can be formed when silicon nitride is used as the core material with SiO_2 as the cladding material. The ability to vary the index contrast over this range simply by varying the deposition conditions makes silicon oxynitride an attractive waveguide material, particularly in the context of this work where it is desirable to be able to make refractive index changes throughout the learning and design phase. In addition, silicon oxynitride is easily deposited using plasma enhanced chemical vapor deposition (PECVD) which is a common and readily available technique. For these reasons, silicon oxynitride was chosen as the material for the waveguide core and silicon dioxide was chosen for the cladding.

3.1.6 Propagation Loss

Much discussion will be made of the propagation loss of the waveguides in this thesis. There is always loss in any real waveguide. The optical loss per unit length of a waveguide, typically measured in dB/cm, is a result of material absorption, scattering due to waveguide sidewall roughness [55], scattering due to random discontinuities in the refractive index of the waveguide materials, and may also be due to evanescent coupling to nearby higher index materials such as the substrate. Each of these sources of loss must be taken into account in the design of a waveguide.

The material absorption is an issue with PECVD deposited dielectric materials like silicon oxynitride due to incorporated hydrogen during the deposition process as discussed in Reference [48]. In the vicinity of 1550 nm, the N-H bonds in the material contribute to an increased absorption due to optical coupling to the vibrational states of these bonds. As will be discussed in Chapter 4, this problem can be alleviated with a high temperature anneal.

The increase in absorption loss due to scattering from sidewalls of a given roughness sets a lower bound on the waveguide cross-sectional dimensions (Reference [56] and [57]). The single mode condition sets an upper bound on the cross-sectional di-

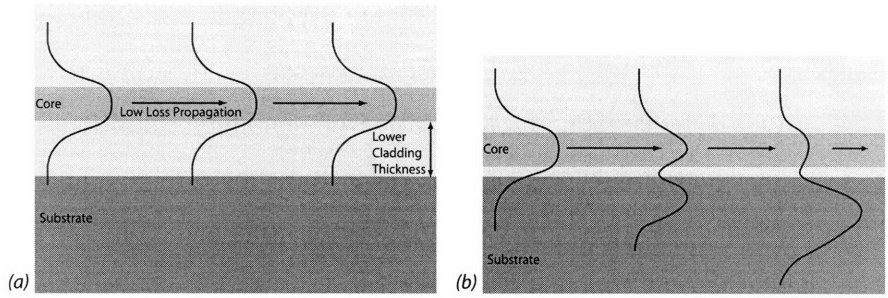

Figure 3-4: Schematic comparing (a) ideal lower cladding thickness resulting in minimal substrate coupling with (b) relatively high substrate coupling loss due to thin lower cladding.

mensions. The lower the index contrast of the waveguide, the larger the range between this lower and upper bound. However, the lower the index contrast, the less compact the design as waveguide bends must be larger in radius and cladding thicknesses must be larger to increase the shielding of the waveguide mode to surrounding high index materials. With regards to these tradeoffs, the selection of silicon oxynitride is a good compromise.

3.1.7 Minimum Cladding Thickness

As mentioned above, a reduction of the propagation loss includes reducing the evanescent coupling to nearby higher index materials. In an effort to maintain a compact, simple design, it is necessary to find the minimum cladding thickness for which the evanescent coupling losses are sufficiently low. The cladding of the interconnect waveguides is bounded by the silicon substrate which has an index of refraction of 3.45. The silicon dioxide cladding must be thick enough to "shield" the optical mode from the high index silicon substrate. If the cladding is too thin, the guided mode will couple into the silicon substrate (see Figure 3-4) inducing substrate coupling loss. However, if the cladding is too thick, it will be difficult to deposit the required silicon dioxide to form the cladding during fabrication. Thick layers are also undesirable because they create large stress that can lead to wafer bowing which makes processing difficult at best.

Therefore, it is desirable to know the substrate coupling loss as a function of lower cladding thickness. This thickness dependent loss can be determined analytically [58, 59, 60]. In Reference [59], the application of boundary conditions is used to develop a set of equations whose solution yields the substrate coupling loss for a given lower cladding thickness[4]. In the next section, this equation will be used to determine the evanescent coupling losses for slab waveguides with a silicon dioxide cladding (refractive index is 1.45) and a silicon oxynitride core where the index is varied from 1.5 to 1.65 in increments of 0.05.

Substrate Coupling Loss: Analytical Solution

As discussed, the equations mentioned above were used to determine the evanescent coupling loss as a function of lower cladding thickness. The goal is to find the lower cladding thickness that yields a relatively low substrate coupling loss. Here, a loss is relatively low if it is much smaller than the expected propagation loss due to scattering and material absorption. Based on the literature (References [48] and [61]), the waveguides are expected to have a total propagation loss on the order of 5dB/cm. For the purpose of this exercise, any substrate coupling loss less than 1dB/cm is considered to be relatively low.

The results of the calculations for the 4 different core refractive indices: 1.5, 1.55, 1.6, and 1.65, with a silicon dioxide cladding and a silicon substrate are shown in Figure 3-5.

Based on this calculation, a lower cladding thickness of 3.3um yields a substrate coupling loss below 1dB/cm for each of the four waveguides for both polarizations. Fortunately, this is a thickness that can easily be deposited using standard deposition techniques so any of the given core index values may be used. As shown in the plot, the higher the index of the core, the lower the substrate coupling loss.

[4]While only numerical solutions exist for these equations, it was shown in Reference [58, 60] that a perturbation technique valid for guided modes far from cutoff resulted in a purely analytical solution.

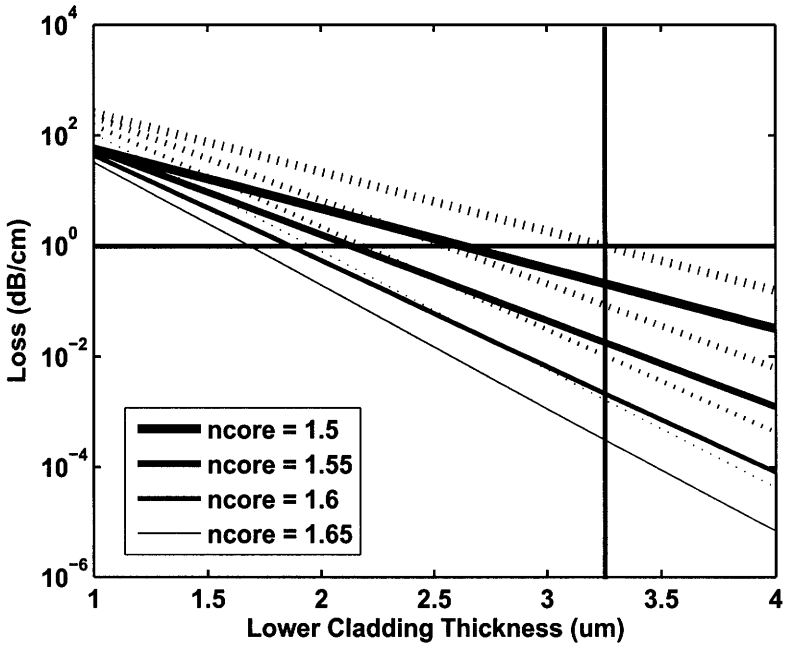

Figure 3-5: Calculated (using equation in [58]) substrate coupling loss in units of dB/cm for slab waveguides as a function of lower cladding thickness and core refractive index. For all cases, the refractive index of the cladding is 1.45 and the substrate is silicon with a refractive index of 3.5. The solid and dashed lines are for TE and TM polarization respectively. The horizontal line shows the target threshold of 1dB/cm. This threshold condition is met for each case for lower cladding thicknesses to the right of the vertical line (corresponding to 3.3um).

Summary

The choices of interconnect waveguide type (buried channel waveguide) and material (silicon oxynitride for the core and silicon dioxide for the cladding) have been chosen and justified. It has been shown that for a range of core refractive index values consistent with waveguides in the literature, the lower cladding thickness should be at least 3.3 μm to ensure minimal substrate coupling loss.

The focus is now shifted to the task of designing the interconnect waveguides for optimum coupling to the III-V devices that will be integrated on the silicon wafer.

3.2 Interconnect to III-V Waveguide Coupling

The successful integration of the III-V devices in this work rests largely on the ability to couple light between the silicon oxynitride interconnect waveguides and these devices. If the III-V device is a semiconductor optical amplifier (SOA), light from an input silicon oxynitride (interconnect) waveguide must be coupled to the gain region of an integrated ridge waveguide SOA and then back again to an output interconnect waveguide. In the case of an integrated laser, light must be coupled from the laser to the interconnect waveguide. These two scenarios are illustrated in Figure 3-6.

In this section, the details of the III-V structure used for the work in this thesis will be given. Two types of coupling, evanescent and end-fire, will be compared and it will be shown that the choice of end-fire coupling makes the most sense for this work. Given the end-fire coupling arrangement, an equation that highlights the two factors that affect the coupling efficiency will be developed and used to find an approximation for the interconnect waveguide parameters for optimum coupling to the III-V device in the absence of a gap.

3.2.1 InP/InGaAsP Ridge Waveguides

Much of the remainder of this chapter deals with the design of interconnect waveguides for optimum coupling to the integrated III-V devices. One specific III-V structure

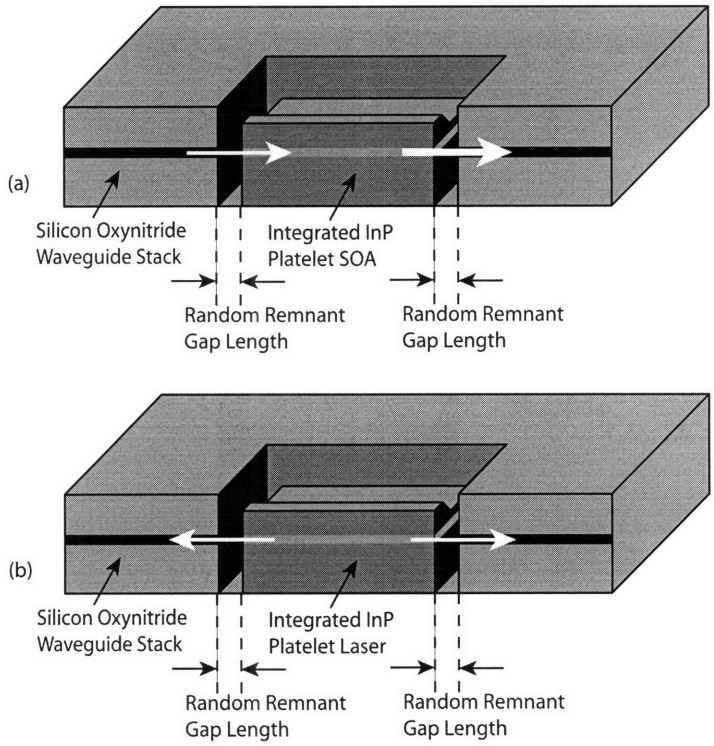

Figure 3-6: (a) For an integrated SOA, light must be efficiently coupled from the interconnect waveguide to the gain region of the SOA. At the end of the SOA, the light must be efficiently coupled back into the core of the interconnect waveguide. (b) For an integrated laser, light must be efficiently coupled from the laser gain region to the core of the interconnect waveguide.

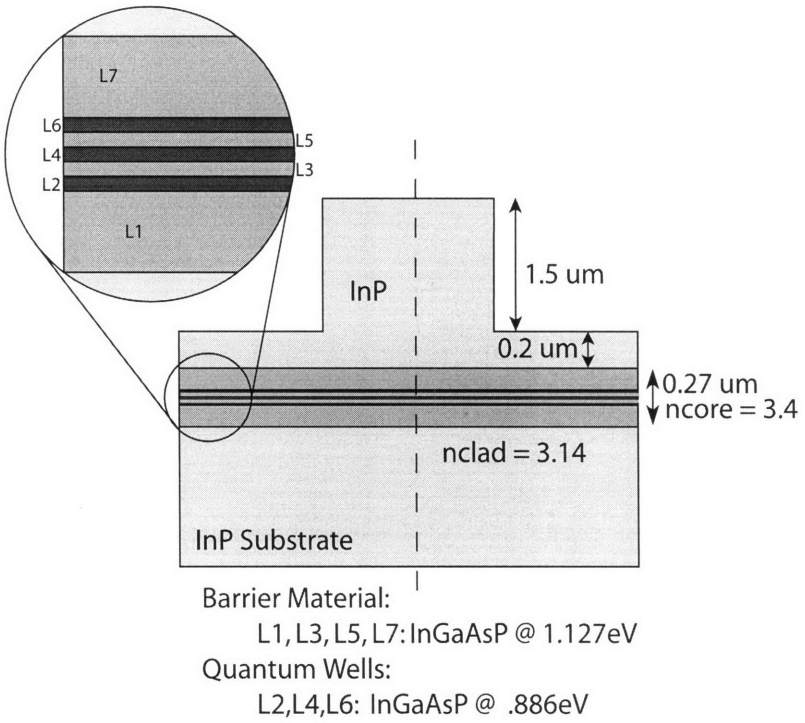

Figure 3-7: Cross-section of the InP/InGaAsP ridge waveguide material from Landmark Optoelectronics. The plane formed by extending the dashed line into and out of the page is the plane for which the majority of the calculations and simulations are considered.

was used for all of this work so it is necessary to examine the details of this structure.

The device structure is a multi-quantum well ridge waveguide structure based on the InP/InGaAsP material system. The cross-section of the structure is shown in Figure 3-7. Throughout this thesis, these waveguides will often be referred to as the InP/InGaAsP ridge waveguides to distinguish them from the silicon oxynitride buried channel waveguides.

The width of the ridge is not given in the figure because no single width was used. The earlier measurements taken in this work were with 8 μm wide ridges. Later in the work after improvements were made to the fabrication process, micro-cleaved pill structures were fabricated with 6 μm wide ridges. Either way, the waveguides are multimode. Given this structure and these values for the index of refraction, the waveguide is multimode for a ridge width greater than approximately 2 μm. In the

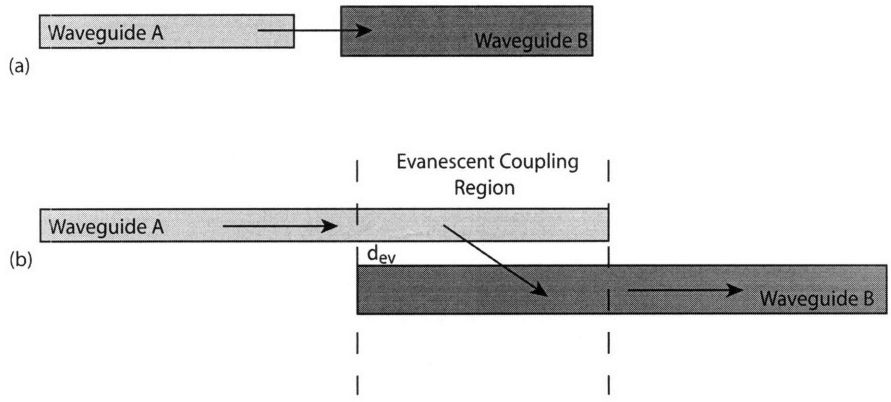

Figure 3-8: (a) End-fire coupling arrangement. (b) Evanescent coupling.

event that these devices are "activated" as either optical amplifiers or lasers, the wide ridge is not ideal. It does, however, reduce the sensitivity of the coupling efficiency to the width of the interconnect waveguides. Consequently, in the work that follows, coupling will be studied primarily for the vertical cross section plane (shown in Figure 3-7 as the dotted line, running in and out of the page).

A parameter that will be useful throughout the following sections is the effective index (see Reference [49] for a discussion of the effective index method) of the various modes of the ridge waveguide structure. The effective index of the fundamental TE mode is 3.192. The effective index of the highest order mode (TM03) is 3.159. These are both for the 6 μm wide ridge, but the values change by less than 1% for the 8 μm wide ridge.

3.2.2 End-Fire vs. Evanescent Coupling

The task of coupling light between two separate waveguides is accomplished by either end-fire coupling, which was used for this work, or evanescent coupling. This section compares the two types and gives reasons for the choice of using end-fire coupling.

End-fire coupling, as the name implies, is accomplished by positioning the two waveguides coaxially and bringing the two ends close together (see Figure 3-8a). The light is emitted from the end of the first waveguide, and some component of this light is coupled into the guided mode(s) of the second waveguide. Invariably, a gap

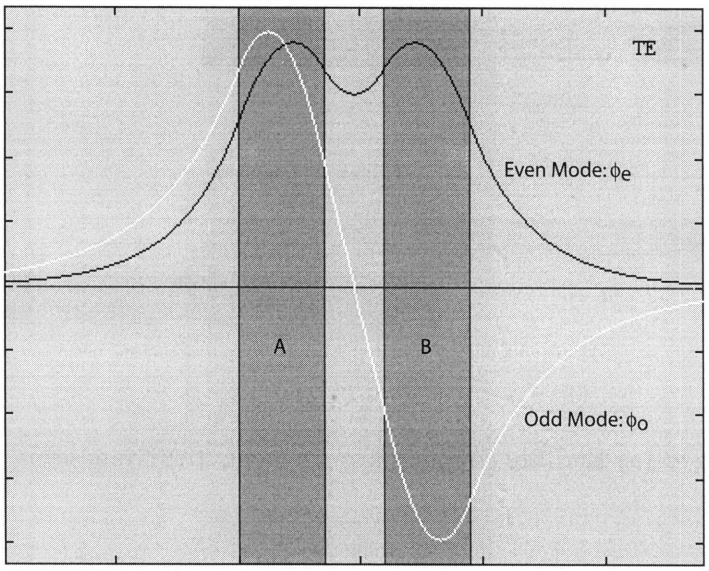

Figure 3-9: Even and odd TE modes for two evanescently coupled waveguides.

of some length exists between the two ends, and this affects the coupling efficiency. Depending on the details of the modes in the two waveguides, the gap length that maximizes the coupling may or may not be the shortest achievable length. When possible, an index matching material may be placed between the two ends to enhance the coupling.

Evanescent coupling involves positioning the two waveguides, A and B, parallel to one another with a certain separation distance, d_{ev}, between them as shown in Figure 3-8b. One way to understand the coupling between the two waveguides is to consider the modal properties of two identical single mode waveguides brought close together. Notice in Figure 3-9, that the two adjacent waveguide system has two modes: an even mode , ψ_e, with an effective index n_e and an odd mode, ψ_{odd} with an effective index n_o. When light is incident on this two waveguide system, some component, c_e, of this light couples into ψ_e at some phase ϕ_e, and some component, c_o, couples into ψ_o with some phase ϕ_o.

Consider the case in which the even and odd modes are excited such that the phase of each mode is zero and that $c_e = c_o$. At z = 0, the modes add together in such a way that constructive interference occurs in waveguide A, with destructive interference in

waveguide B. This would be the case if the even and odd modes as shown in Figure 3-9 were added together. At some later distance, z_{crit}, the phase difference between the two modes is π and constructive interference occurs in waveguide B with destructive interference in waveguide A. The distance, z_{crit} is then the distance required for the light to couple from one waveguide to the other. Given zero phase difference at $z = 0$, the distance, z_{crit}, is found as follows:

$$\phi_e - \phi_o \tag{3.4}$$

where

$$\phi_e = k_e z_{crit} \tag{3.5}$$

$$\phi_o = k_o z_{crit} \tag{3.6}$$

and where

$$k_e = \frac{2\pi n_e}{\lambda} \tag{3.7}$$

$$k_o = \frac{2\pi n_o}{\lambda} \tag{3.8}$$

Solving for z_{crit} yields

$$z_{crit} = \frac{\lambda}{2\left(n_e - n_o\right)} \tag{3.9}$$

In the case of two different single mode waveguides A and B, with two different effective indices $n_a > n_b$, it can be shown (paperref or bookref) that n_e for the evanescently coupled A and B waveguides is greater than n_a and that n_o is less than n_b. This means that the difference, $n_e - n_o$ is larger than the difference $n_a - n_b$. As a result, $n_a - n_b$ (a known value from simple analysis of the isolated waveguides A and B) can be used in place of $n_e - n_o$ in Equation 3.9 to get an upper bound on z_{crit}. Solving for z_{crit} using the typical effective indices for the interconnect waveguide and the InP/InGaAsP ridge waveguide gives a critical distance of less than 0.5 μm. This would mean that the evanescent coupling region would have to fabricated with a margin of error on the length that is less than a fraction of 0.5μm. The statistics for the mean length of micro-cleaved devices is shown i! n the plot in Figure figref.

Notice that a margin of error of 2 μm is typical with the current process. It would be extremely difficult to design the evanescently coupled waveguide region to guarantee good coupling from the interconnect waveguides to the III-V waveguides and then back again[5].

It was shown in Reference [17] that even in the case of waveguides, A and B, with more similar effective indices, it can still be difficult to control the coupling as the tolerances on the effective indices can be difficult to meet. There are also sources of coupling loss that must be addressed for the evanescent coupling case. They showed that many of these issues can be alleviated with the use of an absorbing layer and tapered waveguides. The tapers, however, must be made quite long which means that the design is less compact.

In summary, while evanescent coupling is a viable option, the large index contrast between the interconnect and III-V waveguides makes the coupling difficult to control, and solutions compromise the desired compact design. Consequently, end-fire coupling was chosen as the method for coupling between the interconnect and III-V waveguides.

3.2.3 End-Fire Coupling without a Gap

Recall that the planned approach for end-fire coupling involves integrating III-V devices in wells etched into the silicon oxynitride/silicon dioxide waveguide stack. The result is that a gap exists between the edge of the wells and the III-V device facet. While it is important to understand the impact of this gap on the coupling, it is useful to start by looking at the case of coupling without the gap. As mentioned in the introduction to this chapter, the more complex problem of coupling across a gap (as well as other real-world complications such as misalignment).

[5]Notice that the critical length could be made much larger if the two waveguides had more similar effective indices. This would require a much higher index interconnect waveguide material system than the silicon oxynitride used in this work. While much work has been done paperref with silicon/silicon dioxide core/cladding waveguides which would meet this higher index requirement, these waveguides must be made very small to maintain single mode operation. This makes the waveguide fabrication much more challenging, and it would place even stricter tolerances on the allowable misalignment for the gap coupling regions.

This section addresses a basic design question, and in so doing, provides some general end-fire waveguide coupling intuition. This is important because the majority of the actual analysis that comes later in this chapter is the result of FDTD simulations only, where little insight is required to simply run the simulations and compile the results. The design question:

Given the InP/InGaAsP ridge waveguide structure, and considering only the 2D cross section shown in Figure 3-7, and given that silicon dioxide is used as the cladding material for the interconnect waveguide and that the core of the interconnect waveguide is the same thickness as the core of the InP/InGaAsP ridge waveguide, what value for the index of refraction of the core gives the best coupling between the interconnect and InP/InGaAsP waveguides?

Figure 3-10 is a cross section of the interface between the two waveguides, A on the left and B on the right, showing the given parameters. The incident wave from the left is the fundamental mode of waveguide A. Upon incidence, a transmitted wave travels to the right and a reflected wave travels back to the left. A component, R_{mode}, of the incident wave power couples back into the fundamental mode of waveguide A, and a component, T_{mode}, of the incident wave power couples into the fundamental mode of waveguide B and is guided to the right. Typically, $R_{mode} + T_{mode} \neq 1$ because there are unguided modes in both waveguides that are excited as a result of the reflection. The value T_{mode} is the value that must be maximized to achieve maximum coupled power from waveguide A to waveguide B. To calculate this value, one must solve for the electric and magnetic fields at the interface between the two waveguides. This can be done numerically, as in Reference [62], by discretizing the reflected and transmitted modes by placing perfect electric conductors at some large distance away from the waveguide core. The interface field is found as the weighted sum of the discrete reflected and transmitted modes that meets the interface boundary conditions[6]. The weights of the modes are found as the least squared error solution to the equations set by the boundary conditions. The accuracy of this equation can

[6]The boundary conditions require continuity of the tangential component of the electric and magnetic fields at the interface.

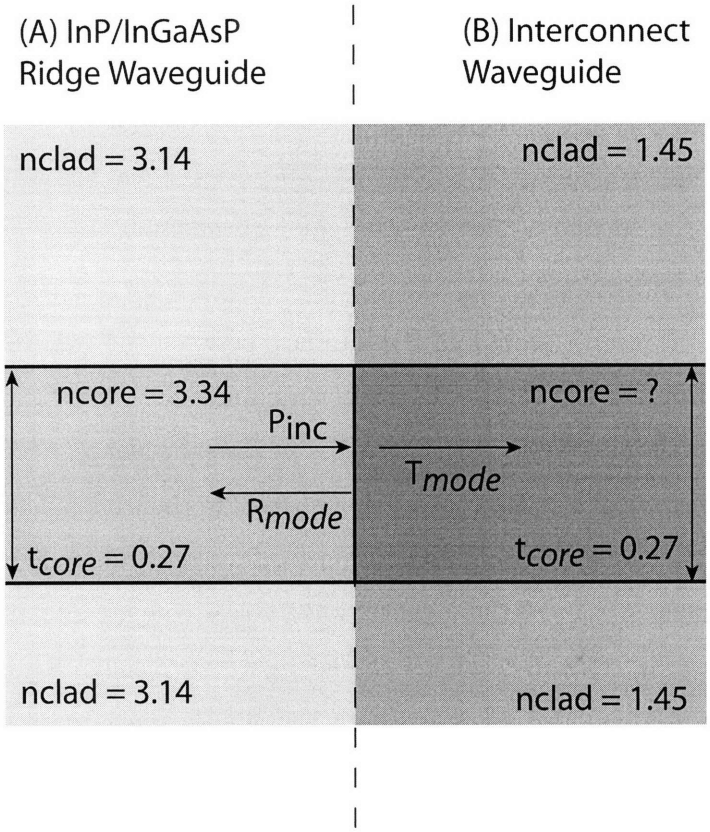

Figure 3-10: Drawing of the end-fire coupled InP/InGaAsP ridge waveguide and interconnect waveguide. The refractive index of the core of the interconnect waveguide is the desired parameter.

be made arbitrarily high by increasing the number of included modes by increasing the distance between the perfect electric conductors (i.e. moving them away from the waveguide core). However, this numerical solution gives little intuition into what is actually affecting the coupling efficiency. On the other hand, an approximation can be made that permits an analytical solution.

A perturbation approach will be used in which it is first assumed that the lateral mode matching between waveguide A and B is perfect, which allows for a simplifying assumption to be made. The perfect mode matching can then be relaxed and its effect on the coupling examined.

The simplifying assumption is this. Instead of finding the electric field profile at the interface, it will be assumed that the field profile is just the fundamental mode profile of waveguide A, which is the incident mode profile. This can be justified as follows. Assuming that the waveguides are designed such that the fundamental mode profiles of waveguide A and waveguide B are identical (perfect lateral mode matching), it would be required that the electric field profile of waveguide A is identical to the electric field profile of waveguide B. For the case of a TE wave[7], this implies that the magnetic field profile of waveguide A is identical to the magnetic field profile of waveguide B. Therefore, the fundamental mode profile of waveguide A must be a solution to the boundary condition. If this is the case then the following equation, which finds the coupled power for two electromagnetic waves, m and n, in the same space can be applied.

$$P_{m,n} = \frac{1}{4}\int\int (E_m \times H_n^* + E_n^* \times H_m)\, dxdy \tag{3.10}$$

The application of this equation for the TE case where the fundamental mode field profiles for the two waveguides E_A and E_B are allowed to differ (given in Appendix A) yields the following equation for T_{mode} where T_{mode} is the power transmitted into

[7]For a TM wave, it is not the case that two slab waveguides with identical magnetic field profiles will have identical electric field profiles because the solution for the profiles is dependent on the ratio of the permittivity of the core material to the cladding material which will be different for the two waveguides. However, for a TE wave, the solution of the profiles is dependent on the ratio of the permeability of the core and cladding materials, which at optical frequencies, is essentially unity for these materials.

the fundamental mode of waveguide B.

$$T_{mode} \simeq T_{Fresnel}\Omega_{AB} \tag{3.11}$$

where

$$T_{Fresnel} = 1 - R_{Fresnel} = 1 - \left(\frac{n_{eff,A} - n_{eff,B}}{n_{eff,A} + n_{eff,B}}\right)^2 \tag{3.12}$$

where $n_{eff,A}$ and $n_{eff,B}$ are the effective indices of the fundamental modes of waveguide A and B respectively, and where

$$\Omega_{AB} = \frac{\int E_A(x)E_B(x)dx}{\sqrt{\int E_A^2(x)dx \int E_B^2(x)dx}} \tag{3.13}$$

The closer Ω_{AB} is to unity, the better this approximation becomes. In the case that Ω_{AB} is unity, Equation 3.11 is exact (as this was the original assumption upon which this analysis was based). In order to maximize the coupled power, the product $T_{Fresnel}\Omega_{AB}$ must be maximized. While the two terms in this product are not independent, it is useful to examine the way to maximize each separately before examining how to maximize the product as a whole.

Maximization of Ω_{AB}

At this point, the design question from above is still being answered. An equation for T_{mode}, the portion of the incident power that is transmitted into the fundamental mode of waveguide B has been developed based on the assumption of perfect mode matching or identical mode profiles for the two waveguides. Allowing for the mode profiles to vary in the derivation results in Equation 3.13.

This section now examines how the waveguide parameters should be chosen to maximize Ω_{AB}. To maximize Ω_{AB}, the mode shape for the two slab waveguides must be identical. An analytical solution exists to the problem of choosing the core and cladding indices of waveguide B given the core and cladding indices of waveguide A to match the mode shape of waveguide B to the mode shape of waveguide A. That is, there is an analytical solution to the problem of forcing Ω_{AB} to equal unity given

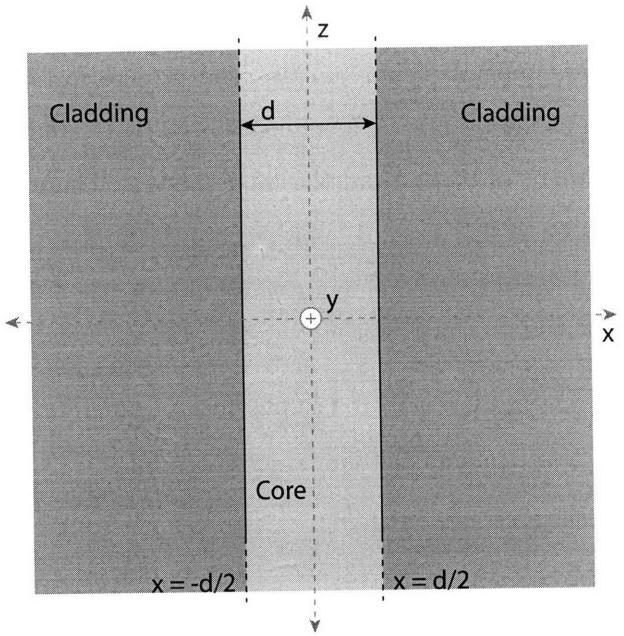

Figure 3-11: Slab waveguide.

the parameters for waveguide A. The electric and magnetic field equations for a TE slab (see Figure 3-11) mode taken from Reference [63] are

$$E_y(x,z) = \left\{ \begin{array}{cc} Ce^{\gamma x}e^{i\beta z} & for\ x < d/2 \\ Dcos(k_x x)e^{i\beta z} & for\ |x| \leq d/2 \\ Ce^{-\gamma x}e^{i\beta z} & for\ x > d/2 \end{array} \right\} \tag{3.14}$$

And from Faraday's Law, the magnetic field in the z-direction:

$$H_z(x,z) = \left\{ \begin{array}{cc} \gamma Ce^{\gamma x}e^{i\beta z} & for\ x < d/2 \\ -k_x Dsin(k_x x)e^{i\beta z} & for\ |x| \leq d/2 \\ -\gamma Ce^{-\gamma x}e^{i\beta z} & for\ x > d/2 \end{array} \right\} \tag{3.15}$$

where $E_y(x,z)$ is the electric field in the y-dimension, $H_z(x,y)$ is the magnetic field oriented in the z -dimension, β is the propagation vector, k_x is the wave vector in the x-dimension inside the core, γ is the wave vector in the x-dimension in the cladding, and C and D are constants, the solution of which follows from the application of the

boundary conditions.

Notice that Ω_{AB} is dependent only on the field profiles in the x-dimension. The x-dimension portion of the profiles is dependent on k_x, γ, C, and D. The coefficients C, and D are dependent on k_x, γ, and the mode power. Therefore, if waveguide B is designed with the same thickness, d, as waveguide A, and k_x and γ for waveguide B are designed to be equal to k_x and γ for waveguide A, then Ω_{AB} will be equal to unity.

The expressions relating k_x and γ to the physical parameters, n_{core} and n_{clad} come from the dispersion relations and the boundary conditions.

The dispersion relations are

$$k_x^2 + \beta^2 = n_{core}^2 k_0^2 = n_{core}^2 \left(\frac{2\pi}{\lambda}\right)^2 \tag{3.16}$$

for the core and

$$-\gamma^2 + \beta^2 = n_{clad}^2 k_0^2 = n_{clad}^2 \left(\frac{2\pi}{\lambda}\right)^2 \tag{3.17}$$

for the cladding. where λ is the wavelength.

Subtracting Equation 3.17 from Equation 3.16 yields

$$k_x^2 + \gamma^2 = \left(n_{core}^2 - n_{clad}^2\right) \left(\frac{2\pi}{\lambda}\right)^2 \tag{3.18}$$

Applying the tangential E-field continuity requirement at the $x = -d/2$ interface and at $z = 0$ yields

$$Ce^{-\gamma\frac{d}{2}} = Dcos(-k_x\frac{d}{2}) \tag{3.19}$$

Applying the tangential H-field continuity requirement at the $x = -d/2$ interface and at $z = 0$ yields

$$\gamma Ce^{-\gamma\frac{d}{2}} = -k_x Dsin(-k_x\frac{d}{2}) \tag{3.20}$$

Dividing Equation 3.20 by Equation 3.19 yields

$$\gamma = k_x tan(k_x\frac{d}{2}) \tag{3.21}$$

Equations 3.18 and 3.21 are two equations for the two desired values, k_x and γ. The goal now is to develop an equation that gives n_{core} and n_{clad} for waveguide B given n_{core} and n_{clad} for waveguide A so that k_x and γ for waveguides A and B are identical. This will guarantee that the mode shapes are the same for both waveguides which means that $\Omega_{AB} = 1$.

At this point, the subscripts A and B will be used to denote waveguide A or waveguide B. Rewriting equations 3.18 and 3.21 for waveguides A and B:

$$k_{x,A}^2 + \gamma_A^2 = \left(n_{core,A}^2 - n_{clad,A}^2\right)\left(\frac{2\pi}{\lambda}\right)^2 = G_A \tag{3.22}$$

$$\gamma_A = k_{x,A} tan(k_{x,A}\frac{d,A}{2}) \tag{3.23}$$

$$k_{x,B}^2 + \gamma_B^2 = \left(n_{core,B}^2 - n_{clad,B}^2\right)\left(\frac{2\pi}{\lambda}\right)^2 = G_B \tag{3.24}$$

$$\gamma_B = k_{x,B} tan(k_{x,B}\frac{d,B}{2}) \tag{3.25}$$

Notice that the term, G_A or G_B is a constant, dependent only on the core/cladding indices and the wavelength, λ. By studying these equations, it is clear that if $d_B = d_A$ and if $n_{core,B}$ and $n_{clad,B}$ are chosen such that $G_B = G_A$, then $k_{x,B}$ must be equal to $k_{x,A}$ and γ_B must be equal to γ_A[8]. This means that $n_{core,B}^2 - n_{clad,B}^2$ should be set equal to $n_{core,A}^2 - n_{clad,A}^2$:

$$\Omega_{AB} = 1 \tag{3.26}$$

if $d_B = d_A$ and

$$n_{core,B}^2 - n_{clad,B}^2 = n_{core,A}^2 - n_{clad,A}^2 \tag{3.27}$$

Solution and Discussion

The original design question can now be answered. Refer back to Figure 3-10. Remember that the goal was to find the index of refraction of the core of waveguide B to optimize the coupling given all of the other parameters. Applying Equation 3.27,

[8]This is only true for single mode waveguides. If the waveguides are multimode, then this condition will guarantee that for each mode, $k_{x,B}$ will be equal to $k_{x,A}$ and γ_B will be equal to γ_A.

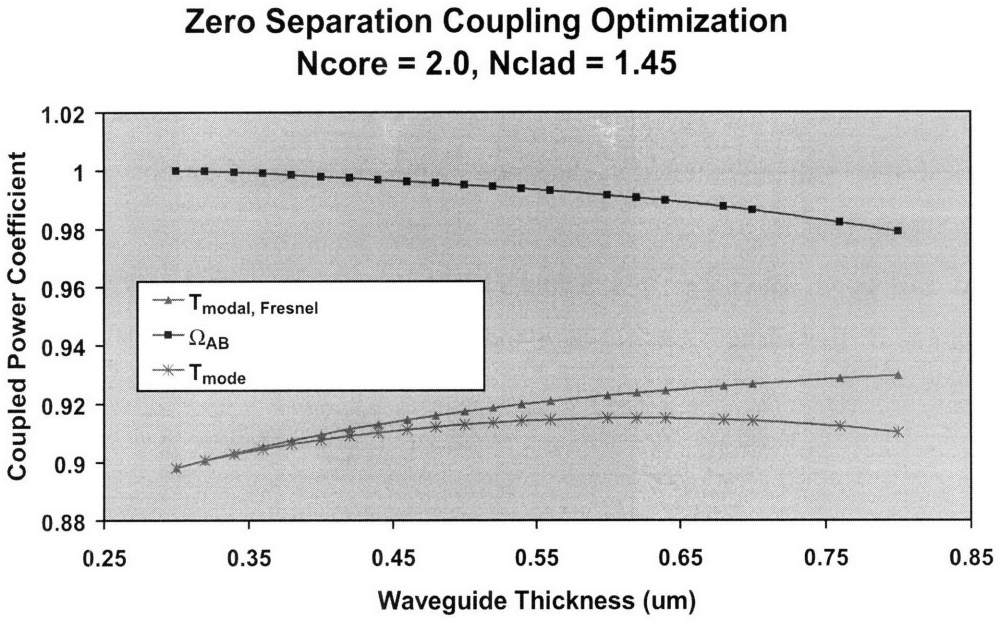

Figure 3-12: Optimization of Equation 3.11 given a core index of 2.0 for waveguide B in Figure3-10 by varying the thickness of waveguide B.

the matching core index is found to be 2.0. To find T_{mode}, one must simply solve for the Fresnel transmissivity using the effective index of the two modes. The effective index is found as $\beta\lambda/2\pi$, which gives 3.193 and 1.654 for the InP/InGaAsP ridge waveguide and the interconnect waveguide respectively. Applying Equation 3.12, a value of 0.899 is found for T_{mode}.

However, this isn't really the maximum T_{mode}. It is the maximum T_{mode} when Ω_{AB} is unity. It is possible that $T_{modal,Fresnel}$ could be made larger without significantly reducing Ω_{AB}. The Fresnel modal reflectivity and transmissivity equations are repeated here:

$$R_{modal,Fresnel} = \left(\frac{n_{eff,1} - n_{eff,2}}{n_{eff,1} + n_{eff,2}}\right)^2 \tag{3.28}$$

$$T_{modal,Fresnel} = 1 - R_{modal,Fresnel} \tag{3.29}$$

Clearly, maximum $T_{modal,Fresnel}$ occurs when $n_{eff,1} = n_{eff,2}$. This would require the use of very high index materials for the interconnect waveguides as the effective index

for the InP/InGaAsP ridge waveguide is on the order of 3.2.

Recall that at the design question was for identical core thicknesses for waveguides A and B. Given, that a core index of 2.0 maximizes Ω_{AB}, it would be interesting to see if T_{mode} can be increased by increasing the thickness of waveguide B, keeping the core index constant. The results for this sets of calculations is shown in Figure 3-12. As the thickness is increased, the effective index of the mode in waveguide B is increasing so $T_{modal,Fresnel}$ is increasing. Of course, as the thickness is changed, the mode profiles no longer perfectly overlap so Ω_{AB} decreases. At a thickness of approximately 0.63 μm, T_{mode} is at a maximum for a core index of 2.0.

This analysis has proven useful in showing that the problem of end-fire transmission optimization is a problem of lateral field profile matching and effective index matching. It is also interesting that even for the rather large difference in effective indices for waveguide A and B above, the Fresnel transmissivity was as high as 0.9, or less than 0.5 dB. In the next section, it will become more clear that the matching of the lateral mode profiles will have the greatest effect on the coupling efficiency.

A recap of the steps that have been taken to find the optimum conditions for slab waveguide coupling is given here.

- *Starting with the actual core thickness and core and cladding indices of the InP/InGaAsP device waveguide and given the cladding index of the interconnect waveguide as 1.45 (that of silicon dioxide), the core index of the interconnect waveguide that maximizes the mode overlap, Ω_{AB}, was found to be 2.0. This is for equal waveguide thicknesses.*

- *It was then found that given the core/cladding index values of the interconnect waveguide of 2.0/1.45, the coupling could be maximized by increasing the interconnect waveguide core thickness to 0.63 μm. This was a result of an increase in the effective index of the interconnect waveguide mode and the resulting increase in $T_{modal,Fresnel}$.*

Although this analysis is useful for the purpose of understanding the coupling, the calculated interconnect waveguide thickness and core refractive index are not, in

practice, the best values to use. The materials with a refractive index of 2.0 (like silicon nitride) are more difficult to process and have a higher propagation loss as compared with lower refractive index materials (silicon oxynitride). Also, as previously discussed, the dimensions for single mode operation with a high index contrast make the task of fabricating a low loss waveguide very difficult. In addition to these material issues, there is, in practice, a remnant gap between the interconnect waveguides and the III-V device due to imperfect device alignment. Because there is no guiding in this gap, the wave spreads in the gap region with the result that the optimum interconnect waveguide parameters for coupling across a gap are different from those calculated thus far for the case of no gap. For these reasons, the waveguide parameters that have been determined up to this point (i.e. core refractive index of 2.0 and thickness 0.63) will serve only as an approximate starting point.

3.3 End-Fire Coupling Across a Gap

Up until this point, solutions given for the problem of coupling between the interconnect waveguides and the InP/InGaAsP ridge waveguides have been for the ideal case of perfect alignment and the absence of a gap. They have also been based on approximations to provide some intuition. Now, the affect of device misalignment will be considered and the FDTD method will be used instead of approximations. In Figure 3-13, an InP ridge waveguide platelet device is shown integrated in the interconnect waveguide stack. There is invariably some random gap between the edges of the well and the III-V device facets where no wave guiding occurs. In addition, the device could be sitting higher or lower in the well. Situations such as these will be examined in this chapter.

Given that there is a gap, it is possible to fill the gap with some material to potentially improve the coupling. So the coupling will be studied as a function of the refractive index of the material used to fill the gap in addition to the misalignment.

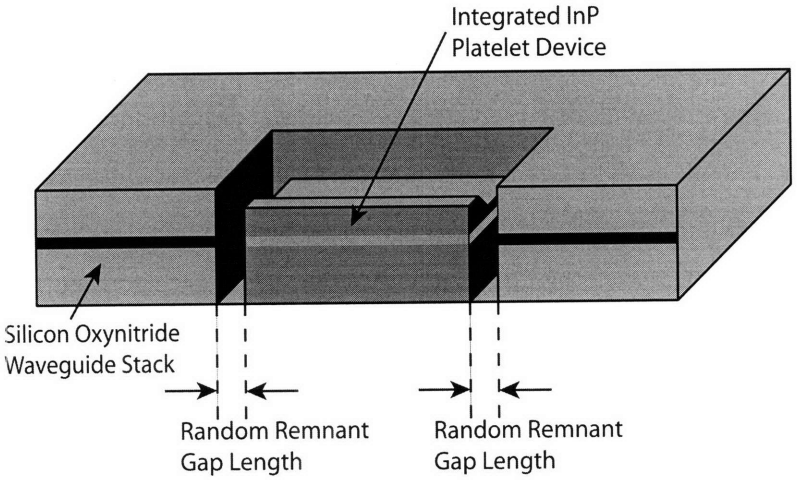

Figure 3-13: An integrated device and the unguided gap between the well edge and the InP platelet device facet.

The FDTD Method: Accurate Maximization of T_{mode}

To obtain a more accurate value for T_{mode} than that given by the approximate method of the previous section, and to study the effect of misalignment which makes it even more difficult to find analytical solutions, the 2D Finite Difference Time Domain (FDTD) method[9] will now be used (see References [64] or [65] for more on the FDTD method). The 2D FDTD method is the most accurate method for simulating a 2D simulation window consisting of dielectric objects and a given source. It is based on the discrete solution of Maxwell's Equations. The input to the FDTD simulation software is a text file with a description of the geometry of the waveguides and the refractive index of the waveguide core and cladding. The input text file also instructs the simulator to use a Gaussian (in time) input source with a given time duration and center wavelength (1550nm for all of the simulations in this work) which is matched in shape to the fundamental mode of the input slab waveguide. This input source starts at a specific point in the input waveguide and travels towards the interface and output waveguide. The simulation is run long enough for the input wave to travel the length of the simulation window. There are three important simulation outputs

[9]The particular software that was used for this thesis was developed by Christina Manolatau and Milos Popovic

that were used repeatedly throughout this work. The first is T_{mode}, the fraction of the input wave at the center wavelength that couples into the fundamental mode of the output waveguide. The second is R_{mode}, the fraction of the input wave at the center wavelength that upon reflection at the interface, couples back into the fundamental mode of the input waveguide. The third is a set of field[10] magnitude snapshots which is useful for visualizing where and how the wave is propagating. Figure 3-14 is a set of snapshots taken from a simulation for coupling from the interconnect waveguide on the left, to the InP/InGaAsP ridge waveguide on the right. The 2D cross-section plane is that shown by the dashed line in Figure 3-10. Notice the progression of the wave from the left waveguide to the right. Also, notice the shorter wavelength in the higher index InP/InGaAsP ridge waveguide on the right as compared with the wavelength on the left.

3.3.1 Mode Spreading

In the last section, the coupling efficiency was optimized for the ideal case of no gap. The results of that analysis were an interconnect waveguide core thickness of 0.63 μm and a core refractive index of 2.0 (recall Figure 3-12). The structure shown in Figure 3-17 will now be simulated using the parameters shown for the InP/InGaAsP ridge waveguide on the right and an interconnect waveguide core thickness of 0.63 μm and a core refractive index of 2.0 on the left. The gap is varied from 0 to 5 μm in 0.5 μm increments[11] and the gap is simply air-filled at this point ($n_{gap} = 1$). The results are shown in Figure 3-15 for the case of TE polarization. The y-axis in the plot is the loss measured in dB (i.e. $-10log(T_{mode})$). So a large value implies a low T_{mode} or a high loss. A value of zero implies perfect coupling. Notice the very low loss (approximately 0.45 dB) at zero gap length. However, at a separation of 5 μm, there

[10]The field magnitudes given in the snapshots is the electric field for TE simulations and the magnetic field for TM simulations.

[11]A maximum value of 5 μm was chosen for the gap length in this and most other simulations. This value was chosen without knowing what the gap length would typically be. As shown by the results in the chapters on fabrication and testing, this was a good value to use. The maximum gap length experimentally observed for the integrated pills was 7.9 μm and the average gap length was on the order of 3 μm.

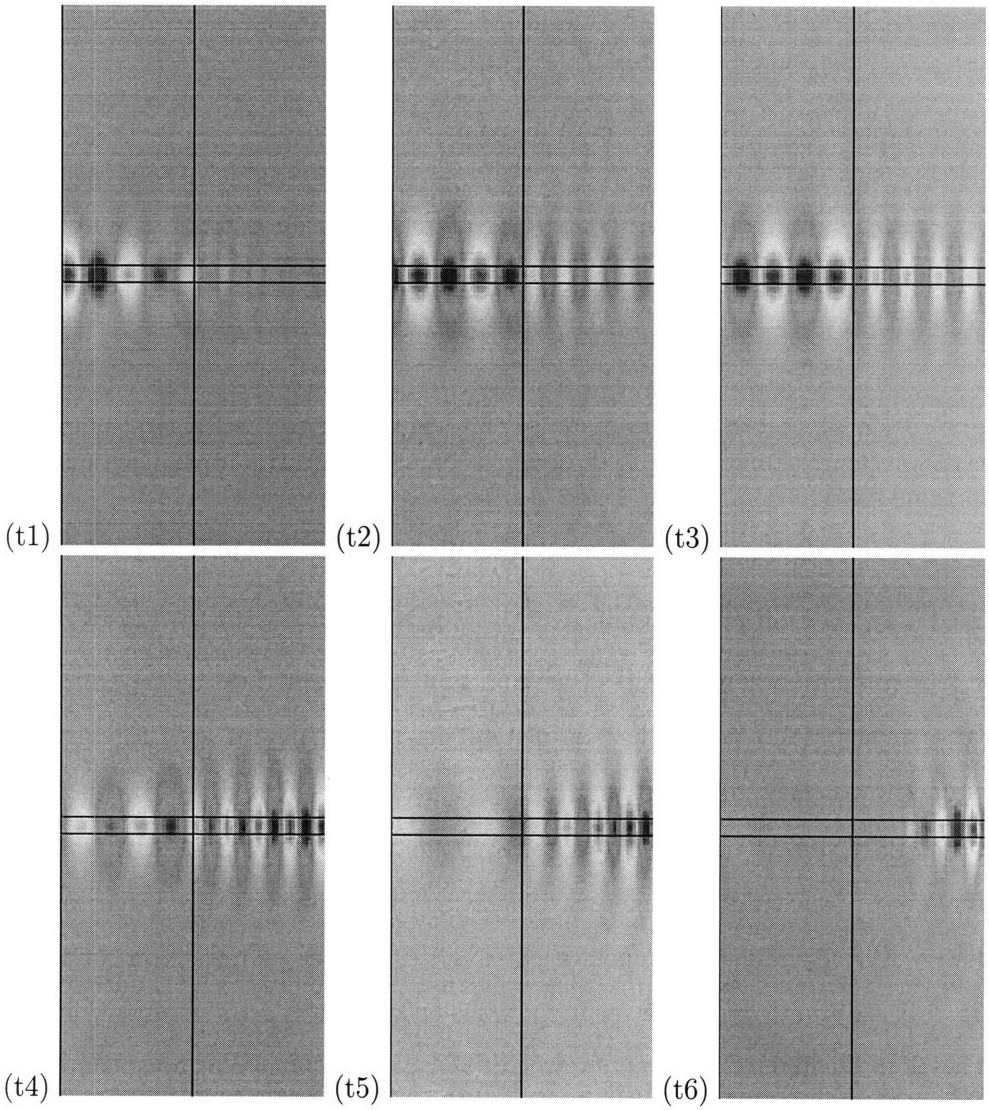

Figure 3-14: Six field snapshots equally spaced in time taken from a FDTD simulation.

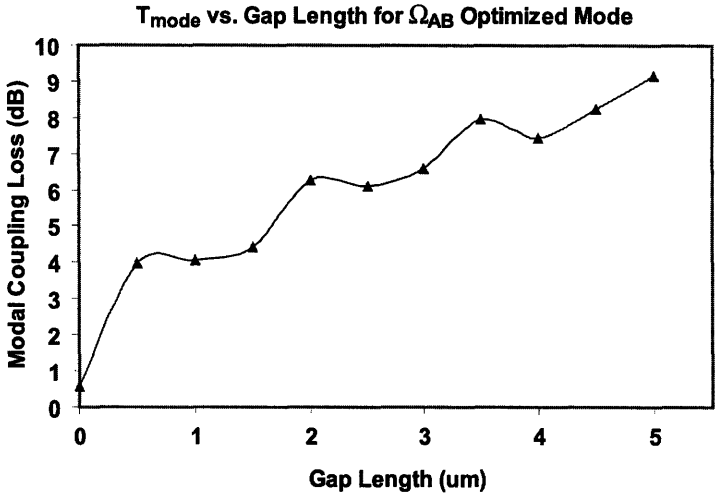

Figure 3-15: T_{mode} loss as a function of gap length and core refractive index for the interconnect waveguide optimized for zero separation (the Ω_{AB} optimized mode. The gap is air-filled.

is nearly an order of magnitude loss. The periodicity seen is due to gap resonance.

This simulation demonstrates the importance of considering the gap in the design of the waveguides. While the parameters were optimum for zero separation, the coupling worsened significantly as the gap length was increased.

The next step is to see if the gap dependence can be reduced with some other interconnect waveguide parameters. The same simulation that produced the results above was run again, this time with four lower indices of refraction for the core, 1.55, 1.6, 1.65, and 1.7. The results are shown in Figure 3-16. Notice that at zero separation, the highest index core waveguide ($n_{core} = 1.7$) has the lowest coupling loss. However at a gap length of 5.0 μm, the lowest index core waveguide ($n_{core} = 1.55$) has the lowest coupling loss. The transition occurs at a gap length of approximately 1.5 μm. Given that the gap length is expected to be larger than 1.5 μm in practice, it would appear that a core index of 1.55 would give the best results.

In Figure 3-18, the results from the Ω_{AB} optimized mode (Figure 3-15) are shown along with the results from the 1.55 core index mode (best coupling at large gap

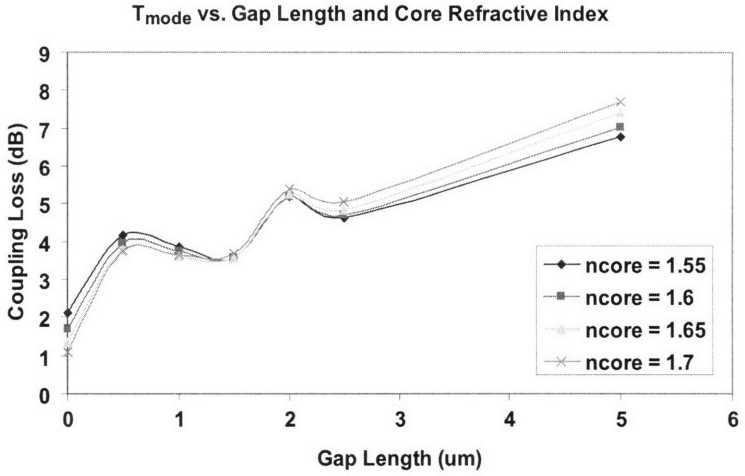

(a)

Figure 3-16: T_{mode} loss as a function of gap length and core refractive index. For each core index, the waveguide was sized to the maximum size at which single-mode operation is maintained. This ensures ease of fabrication and a lower sidewall scattering loss. The gap is air-filled.

lengths in Figure 3-16). Notice the improvement of a little more than 2 dB in the loss at a 5 μm gap length. The penalty for the lower gap loss at the long gap length is a higher gap loss at a zero separation. However, the crossover point for these two modes is at a gap length of less than 0.5 μm and it is certainly expected that the gap will be at least that long experimentally.

To examine what is causing this difference in average slope of the loss versus gap length for the two different modes, the mode profiles must be examined. Figure 3-19 shows the mode profile for the two modes. Notice that the gap optimized mode (which is the mode for a core index of 1.55) is wider than the Ω_{AB} optimized mode with a core index of 2.0. The reason for this is that a higher index contrast waveguide confines the light more than a lower index contrast waveguide.

To see what how this affects the coupling across a gap, the field profiles are plotted in Figure 3-20 for the case of a 5 μm gap (refer to Figure 3-17 to see what the structures are). Notice that the originally narrower mode from Figure 3-19 is wider in front of the InP/InGaAsP ridge waveguide facet than the originally wider mode from Figure

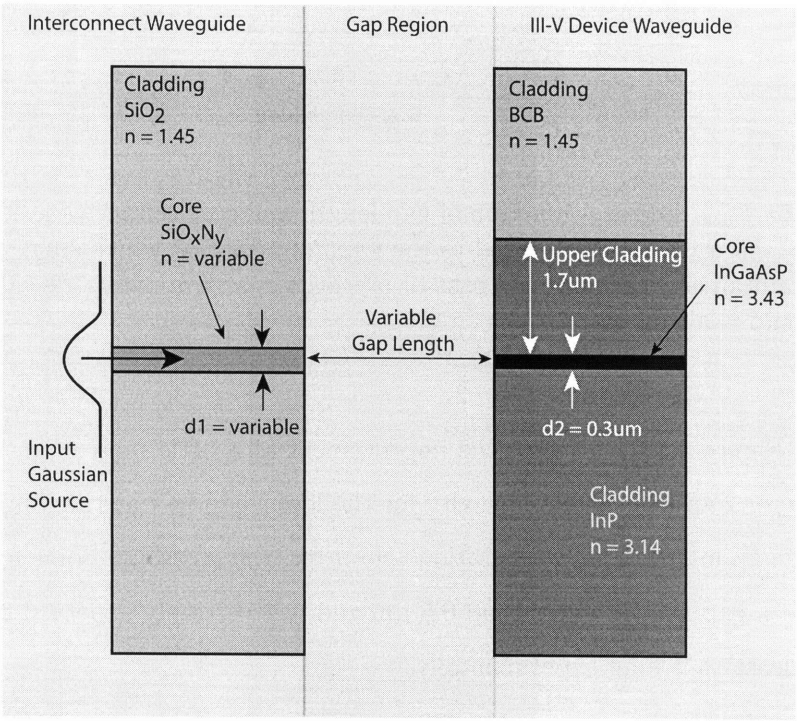

Figure 3-17: Structure for FDTD simulations of coupling across a gap.

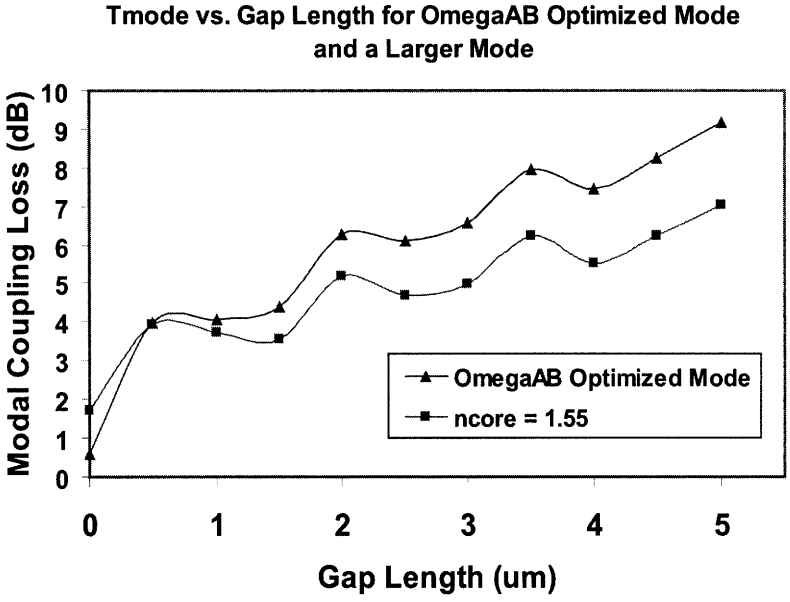

Figure 3-18: Comparison of the coupling results for the Ω_{AB} optimized mode and the mode for a core index of 1.55.

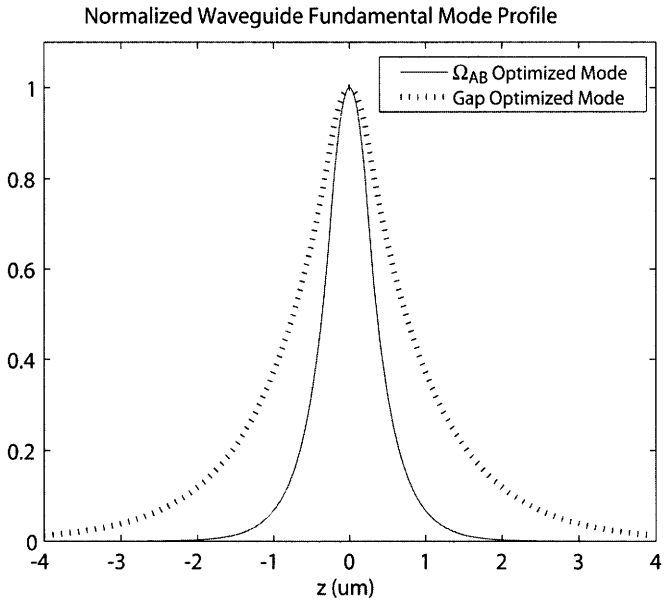

Figure 3-19: Normalized mode profiles for the two waveguides used in the FDTD simulations shown in Figure 3-18. The gap optimized mode is for the waveguide with a core refractive index of 1.55.

3-19. So it can be seen now that the difference in the average slope of the two curves in Figure 3-18 is due to the different angle of wave spreading in the gap for the two modes. The power density is lowered and less power couples into the InP/InGaAsP ridge waveguide at the end of the gap for the mode with the larger gap spread angle. To understand why a narrower mode spreads faster than a larger mode, the reflection and transmission at the waveguide/air interface must be examined more closely. A basic understanding can be gained by thinking of the mode width at the end facet as the slit width in the classic slit diffraction experiment. The width of the resulting diffraction pattern is larger for a narrower slit, just as the spreading of a narrow mode exiting a waveguide is greater than the spreading of a larger exiting mode.

In this section, it was observed that modes that couple well at zero gap length coupled with much higher loss at a large gap length than modes that did not match as well at zero separation. By examining the mode profiles and looking at the electric field plots from the FDTD simulations, mode spreading was identified as the cause of this effect.

3.3.2 Coupling Efficiency vs. Gap Fill Index

The previous simulations show the effect of the mode shape on mode spreading in the gap. Another parameter that affects the mode spreading is the refractive index of the gap. In all of the previous simulations, the refractive index of the gap was 1.0, implying an air-filled gap. In practice, it will be necessary to fill the gap with some material with a refractive index other than that of air, so it is essential to look at this effect in more detail. Figure 3-21 compares the coupling loss vs. gap length for the same waveguide parameters but for three different gap materials with varying index of refraction. Notice that the best coupling is for a gap index of 2.2. The air-filled gap (which is the exact same data plotted in Figure 3-18 labelled $n_{core} = 1.55$) yields the highest loss. At certain points, the highest index gap fill ($n_{gap} = 5.0$) yields the best results. But because of the high index, the reflectivity at the facets is higher for this mode so the resonances are sharper. This is a moot point , however, because there is no material that has a refractive index of 5.0 at the relevant optical frequencies. There

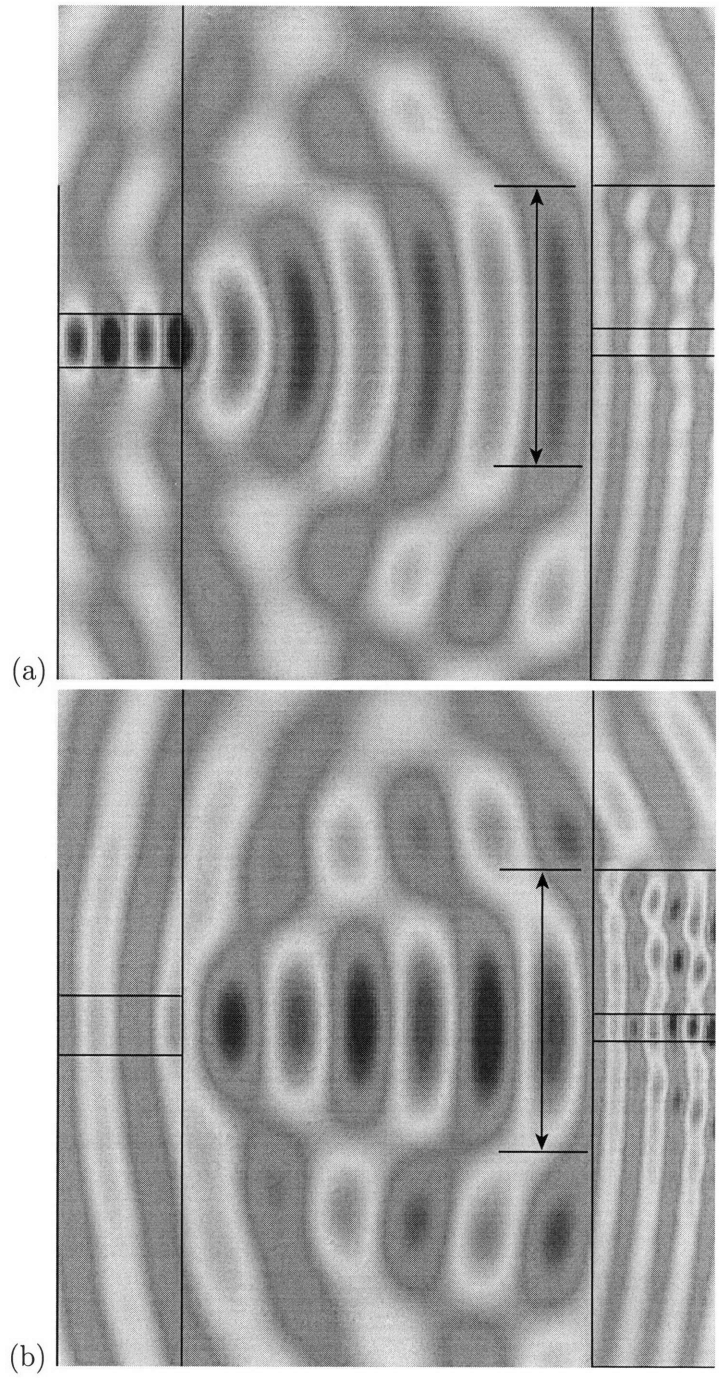

Figure 3-20: Electric field magnitude contour plots (the wave is travelling from the interconnect waveguide on the left to the InP/InGaAsP ridge waveguide on the right) for the same time in the simulation that resulted in the 5 μm loss value in Figure 3-18 for (a) Ω_{AB} optimized mode and (b) Gap optimized mode (core index of 1.55). The line segment in the two figures is the same length which allows for the comparison of the width of the modes for the two cases right at the InP/InGaAsP ridge waveguide facet. The wave in (a) has spread more than the wave in (b).

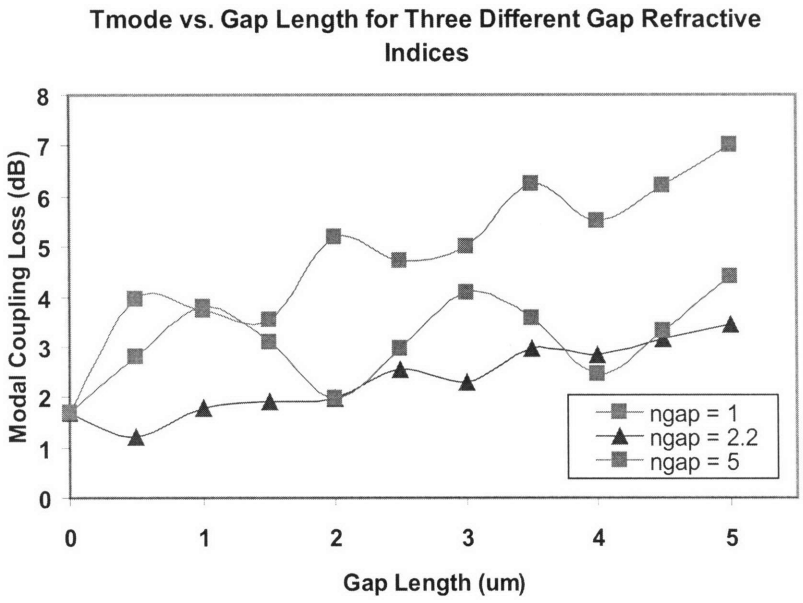

Figure 3-21: FDTD simulation results: T_{mode} loss versus gap length for three different gap indices. For each case, the interconnect waveguide parameters are the same that generated the lower loss in Figure 3-18, the 1.55 core index.

is, however, a material with a refractive index of 2.2 (which is why it was specifically shown). Silicon rich nitride can be deposited with this index of refraction using the same tool that was used to deposit the silicon oxynitride interconnect waveguide materials.

The reason for the improvement for the higher index gap fill is that the wave spreads less in the lateral direction when propagating in a higher index material. A basic explanation comes from thinking about ray refraction at a dielectric interface in which the ray is transmitted into a higher index material. The ray bends towards the interface normal (i.e. in the direction of propagation, left and right in Figure 3-20), and the higher the index of refraction, the closer the ray bends towards the normal. The radiating wave transmitted into the unguided region at the waveguide facet can be thought of as being composed of many rays all bending towards the normal. The higher the gap refractive index, the more these constituent rays bend towards the normal, the less spreading of the overall wave. In the limit that the gap index of refraction is very large, however, most of the incident mode reflects back into the interconnect waveguide from the waveguide/gap interface.

It was demonstrated in this section that filling the gap with a material with an index of refraction of 2.2 can reduce the coupling loss by approximately 4 dB as compared with an air-filled gap.

3.3.3 Misalignment and Other Imperfections

The gap that was analyzed in the previous two sections is just one of the practical device alignment issues that affects the coupling efficiency. Given that the integrated device is resting flat against the bottom of the well and assuming that the bottom of the well is flat and parallel to the the propagation plane of the interconnect waveguides, there are four degrees of freedom for the device: the three degrees of freedom for the device position (x, y, and z) and one degree of freedom for the orientation: yaw. Given the length of the integrated devices in this work (approximately 300 μm) and a typical space between the integrated device and the well edge of a few microns, the device yaw is rather small so its effect on coupling will not be explored. This

leaves the translational misalignment in the x, y, and z directions to be examined (where for the purposes of this section, z is the wave propagation direction, x is into the page in Figure 3-17, and y is directed out of the wafer, or up, in Figure 3-17. Misalignment in z has been handled by the above gap analysis. In the following sections, the impact of vertical misalignment (y) and the lateral misalignment (x) on the coupling efficiency will be examined.

Vertical Device Misalignment

The vertical alignment of the integrated devices should, in theory, be well controlled. The individual layers that make up the InP/InGaAsP device waveguide are deposited via MOCVD, and, as such, have well controlled thicknesses. The interconnect waveguide core and cladding layers are deposited with thicknesses controlled to better than 0.05 μm so the layer thickness variation should not be a significant problem. There is, however, thickness variability in the final thermo-compression bond layers used to bond the III-V device in place. The bonding was not carried out for this work so the details of this variability are not known, but given that the metal layers involved in the bonding have a thickness on the order of hundreds of nanometers, it is expected that the vertical misalignment would be on this order.

To determine the sensitivity of the coupling power to vertical misalignment, FDTD simulations were preformed on the structure shown in Figure 3-17 where the vertical position of the III-V device was varied. The refractive index of the gap was 1.0. The results are shown in Figure 3-22. To remove the effect of resonance on the data, $T_{mode}/(1-R_{mode}$ is plotted rather than T_{mode}. This permits a comparison based solely on vertical shifting and mode spreading.

The data shows that at a large gap length, 5 μm for instance, vertical shifting by 750 nm incurs less than 1 dB of additional loss. However, at zero separation, the loss increases by 4.5 dB. Looking at the nominal range of a 2 to 3 μm gap, a 0.5 μm vertical shift incurs a loss only 0.5 dB greater than for no shift. Also, notice that the change in loss from in shifting vertically from 0 to 0.3 μm, is less than the change in loss in shifting vertically from 0.3 to 0.6 μm. This can be understood by looking at

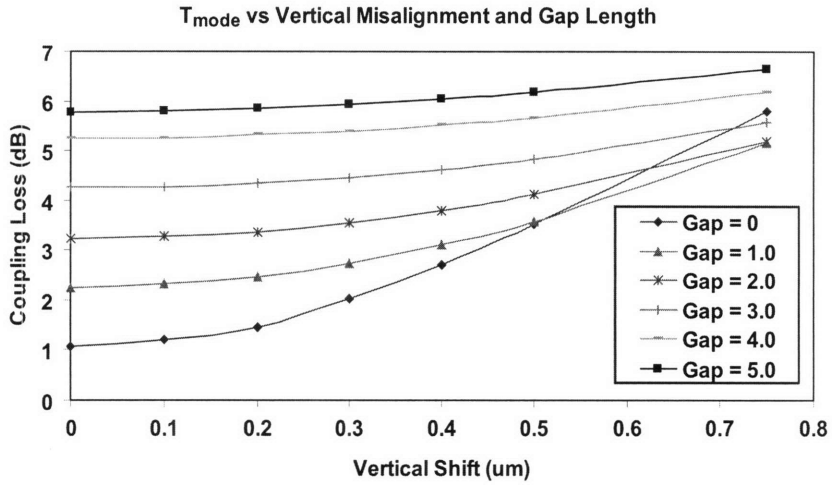

Figure 3-22: FDTD simulation results: normalized T_{mode} versus vertical displacement for six different gap lengths.

the mode shape in Figure 3-19 and the electric field plots in Figure 3-20. They are approximately gaussian in shape. As one is shifted relative to the other, the overlap of the two decreases and the rate of decrease is increasing.

This implies that the pill can be vertically shifted by some amount on the order of 300 nm without a significant impact, but the coupling efficiency falls off faster for a larger shift. In terms of practical sources of vertical misalignment, if the total bonding metal thickness is on the order of 300 nm, it would not be possible to have a vertical shift greater than 300 nm. This might be a good target value for the thickness of the metal bonding layers when that is studied experimentally.

Lateral Device Misalignment

In addition to misalignment resulting in the gap and vertical shifting, the integrated device does not perfectly line up with the interconnect waveguide in the lateral direction. In actual integration misalignment tests discussed in Chapter 5, the maximum lateral shifting was on the order of 4 μm and the average was approximately 2 μm. To determine the effect of this misalignment on coupling, FDTD simulations were

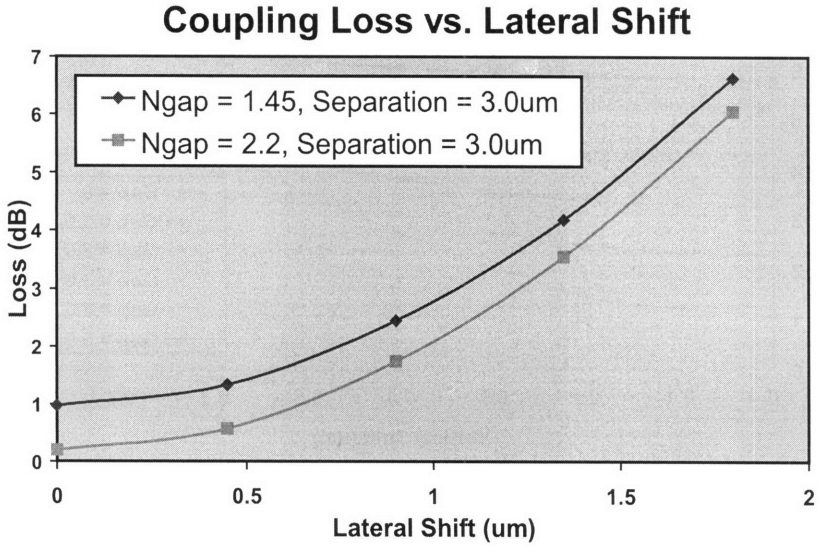

Figure 3-23: FDTD simulation results: T_{mode} loss for coupling from the interconnect guides to a laterally shifted InP/InGaAsP ridge waveguide. The width of the interconnect waveguide is 1.7 μm. The width of the InP/InGaAsP ridge waveguide is 2 μm.

performed. The 2D simulation window for these simulations is, of course, a different cross-section than for the vertical shifting. These simulations are conducted with a simulation window of the wafer plan view. The results of the simulation are shown in Figure 3-23. The results compare the case of a cladding index matching material in the gap ($n_{gap} = 1.45$) with the silicon rich nitride gap fill ($n_{gap} = 2.2$). The two curves are at a gap length of 3 μm. A width of 1.7 μm was used for the interconnect waveguide (based on maximum size for single mode operation) and a width of 2 μm was used for the InP/InGaAsP ridge waveguide. Note that while 2 μm is the required width for single mode operation of the InP/InGaAsP ridge waveguides, the actual width used in the experimental coupling section of this thesis was 6 μm. It is expected that the change in coupling loss for lateral shifting for 6 μm wide InP/InGaAsP ridge waveguides is smaller than implied by the results shown in Figure 3-23.

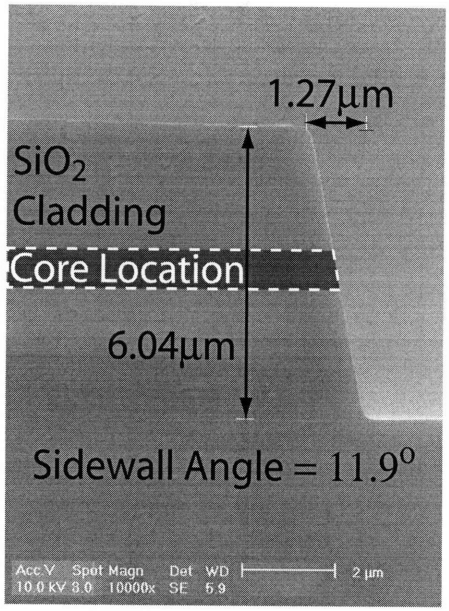

Figure 3-24: SEM image of the deep etched sidewall of the wells. The location of the core is shown with an overlain shape as it cannot be seen in the SEM.

Sidewall Angle

In addition to the misalignment, another imperfection that affects the coupling efficiency is the sidewall angle of the deep waveguide stack etch. A scanning electron microscope image of the deep etched sidewall is shown in Figure 3-24.The sidewall angle is approximately 12^o and this can have an adverse effect on the coupling. In Figure 3-25, the FDTD simulation window is shown for the angled facets on the interconnect waveguides. The image has been overlain with the electric field magnitude contour plot from one of the simulations. The results for a particular set of simulations is shown in Figure 3-26. These results are for the standard 1.55 core index for the interconnect waveguide and all of the values are for a separation of 3 μm. What is plotted is the difference between the loss with the angle and for the same parameters but with no angle. Vertical shift is varied along the x-axis. The reason the vertical shift was examined, is because it was suspected that the additional loss of approximately 0.55 dB at no shift was due to the fact that the wave exiting the waveguide bends up as seen in Figure 3-25 because of the angled etched facet. It

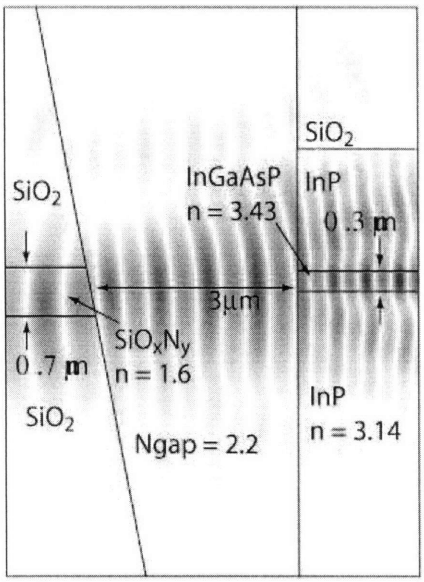

Figure 3-25: FDTD simulation window for the angled facet simulations.

was suspected that this could be corrected for by shifting the InP/InGaAsP ridge waveguide vertically. This was the case to some extent as the additional loss was reduced to 0.45 dB, but further shifting did not improve the loss as can be seen by the curve flattening out. The conclusion is that for a nominal gap length of 3 μm, the angled facet adds 0.5 dB to the coupling loss.

3.4 Summary

In this chapter, the choices of interconnect waveguide type (buried channel waveguide) and material (silicon oxynitride for the core and silicon dioxide for the cladding) were chosen and justified. Through the development of an approximate coupling equation, the problem of end-fire transmission optimization was shown to be a problem of lateral field profile matching and effective index matching.

The problem of finding the ideal waveguide parameters for coupling across a gap was examined with FDTD simulation software. It was found that the optimum index of refraction for the core is 1.55 and the thickness corresponds with the maximum

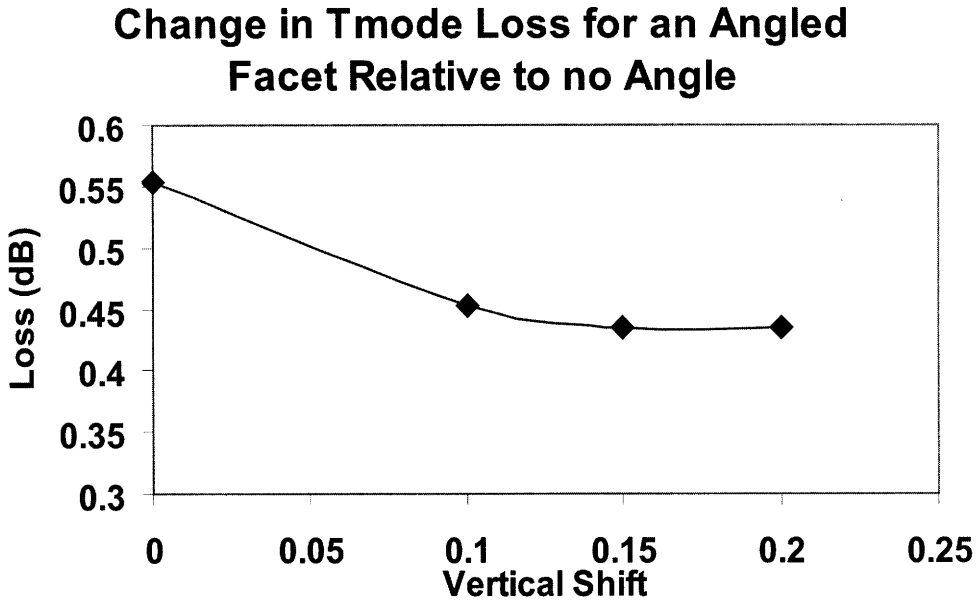

Figure 3-26: FDTD simulation window for the angled facet simulations.

thickness for single mode operation (0.7 μm). By allowing for variations in the refractive index of the gap, it was shown that the coupling efficiency could be maximized with a refractive index of 2.2 in the gap (silicon rich nitride).

Various imperfections were studied. Specifically, it was shown that a vertical misalignment of 300 nm contributed only an additional 0.5 dB of loss. The lateral misalignment sensitivity was shown to be quite large, but this was for the case of a narrow single mode InP/InGaAsP ridge waveguide. It is expected that for the wide 6 μm ridge guides in the experimental section of this work, that the additional loss would be much smaller. Finally, the effect of an angled facet due to an etch angle of 12^o was shown to be an additional loss of 0.5 dB.

Assuming the worst case of 7 dB loss for a 5 μm air-filled gap with 0.5 dB for vertical misalignment, 0.5 dB for angled facets, and 4 dB for lateral shifting, the total worst case loss would be 17 dB. The nominal case, however, with silicon rich nitride gap fill and nominal shifting would be on the order of 5 to 6 dB per facet.

Chapter 4

Waveguide and Well Fabrication

Of all the work in this thesis, the fabrication and preparation of the waveguide chips and the integration of the InP devices is the most crucial. While the design and testing phases of this project are important, it is the device fabrication and integration that typically set the limitation to how well the system performs. The waveguides can be designed, in theory, to ensure optimized coupling, but if they cannot be fabricated to the necessary specifications, the quality of the design is irrelevant.

In addition to being so important, the fabrication stage is also the most challenging. There are approximately 30 steps in the fabrication sequence, and each step was carefully tailored to deliver a certain result. Interestingly enough, while the fabrication stage is difficult and crucial, rare is the case when the success or failure of a given step can be attributed to some known measurable quantity that can be fully controlled and engineered to deliver the desired effect. Rather, much of the progress comes from a series of systematic trials and errors with a foundation in basic theoretical considerations. So while the development of the working fabrication sequence is extremely important, it is less the result of the application of theory and more the result of developing over time an understanding of what does and does not deliver the desired results. This is, of course, not meant to imply that the final working process came out of blind trial and error. There are specific examples in which changes made to the process based on the literature and some theoretical considerations led to improved results.

The goal of this chapter is to detail the complete process, discuss the cases in which success was born out of a greater understanding of a particular failure, and discuss the parts of the process to which the system performance is the most sensitive as these are the parts that require the most control.

There are four major parts to the fabrication sequence for a fully integrated[1] InP pill device on silicon. The four parts are:

1. *Waveguide Deposition and Etch*
2. *Well Etch*
3. *Die-Saw Assisted Cleave*
4. *Pick-and-Place Pill Integration*

These four parts will be described in detail in the following sections.

4.1 Waveguide Deposition and Etch

The waveguide fabrication consists of depositing the cladding and core materials, annealing, patterning and etching the core, deposition of the upper cladding, and finally a second anneal of the entire waveguide stack[2]. The specifications needed from the results of the design phase are the thicknesses of the lower cladding, the core, the upper cladding, and the refractive index of the core and the cladding. While some of these values were varied for certain tests[3], the standard parameters used are shown in Table 4.1 [4].

[1] "Fully integrate" refers to the full integration for this work, which is actually not the completed integrated chip. What is left out of the "fully integrated" process is the postprocessing required to replanarize and electrically contact the integrated III-V device.

[2] The waveguide stack refers to the combination of the lower cladding, waveguide core, and upper cladding layers.

[3] The lower cladding thickness, the core thickness, and the upper cladding thickness were varied in certain instances to obtain information about the waveguide loss as a function of these parameters. The standard process, however, was based on the numbers given above.

[4] In the previous chapter, the value for the refractive index of the core was given as 1.55. However, that was for 2D slab waveguide simulations. The value of 1.55 is actually the effective index of the TM mode for a 1.7 μm wide waveguide. So the actual material index of 1.6 is consistent with the effective index of 1.55 used in the previous chapter.

Waveguide Stack Parameters	
Lower Cladding Thickness	3 μm
Core Thickness	0.7 μm
Upper Cladding Thickness	3 μm
Cladding Material & Index of Refraction	SiO_2: 1.45
Core Material & Index of Refraction	SiO_xN_y: 1.6

Table 4.1: Table listing the standard parameters used for the waveguide stack fabrication. The selection of these parameters was based on the design phase and the consideration of available materials.

4.1.1 DCVD Dielectric Layer Deposition

The dielectric waveguide materials used for the waveguide stack were deposited using a Dense Chemical Vapor Deposition (DCVD) system. The system consists of a deposition chamber with an RF power source and gas inlets. At low chamber pressures, the RF source accelerates electrons in the gas which bombard and excite neutral gas species creating more charged particles. At the proper pressure and RF power, a plasma is induced containing reactive gaseous species (called free radicals) which accumulate on the surface, reacting with each other to form a thin layer of material (Reference [66]). Given the proper gases and deposition time, the desired material with the desired thickness is deposited on the surface of the wafer. The primary gases used for the deposition of silicon dioxide are silane (SiH_4), and oxygen (O_2). The addition of nitrous oxide (N_2O) to the silane is necessary for the deposition of silicon oxynitride. By varying the relative gas flows, the refractive index of the silicon oxynitride can be varied from silicon dioxide (no nitrous oxide) to silicon nitride (no oxygen). As shown in Table 4.1, the desired silicon oxynitride index of refraction is 1.6. The detailed recipe which has been tailored to deposit material with this desired index of refraction is provided in Appendix C (along with all of the recipes and details for the fabrication sequences in this work).

Once the desired recipe has been developed, the waveguide stack deposition is a relatively straightforward part of the process. There are, however, two issues that make the rest of the process slightly more complex. Compressive stress, and the presence of unwanted hydrogen in the deposited material must be dealt with through

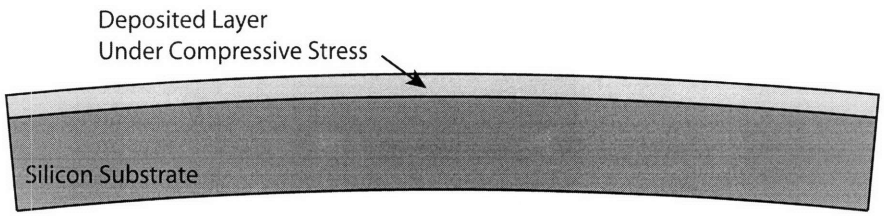

Figure 4-1: A compressively strained layer deposited on the surface of a silicon wafer causes the wafer to bow. A thicker deposited layer causes a greater wafer bow.

the addition of more processing steps.

Stress in Deposited Dielectric Layers

There are two primary sources of stress in CVD deposited materials: intrinsic and thermal. The intrinsic stress is generated during the deposition of the material and is strongly related to the process conditions (see Reference [67] and [68]). It is caused by ion bombardment of the surface ([69]). The thermal stress is a result of the deposition of the silicon dioxide and silicon oxynitride materials at a temperature of 400^{o}C. When the deposition is complete and the wafer is brought back to room temperature, both the deposited layer and the silicon wafer slightly contract, but not by the same amount. This difference is due to the difference in coefficient of thermal expansion (c_{TE}) of the silicon wafer and the deposited layer. Depending on the film composition, $c_{TE,silicon}$ - $c_{TE,layer}$ may be positive or negative. In this work, the difference was positive meaning that the silicon contracts more when cooling from 400^{o}C to room temperature. As a result of both compressive internal stress and compressive thermal stress, the wafer bows out (as shown in Figure 4-1). The exact geometry of the bow is a function of the amount of stress in the deposited layer, the thickness in the layer, and the silicon wafer thickness (and silicon bulk modulus). The thicker the deposited layer, the greater the stress and the greater the bow in the wafer. While there are some important adverse effects of the material stress on the optical properties of the waveguides[5] the problem at this point is mechanical in nature. If

[5]Stress in the waveguide core material can produce birefringence. The result is a difference in the effective index for a TE versus a TM polarized wave. This can lead to pulse spreading for a

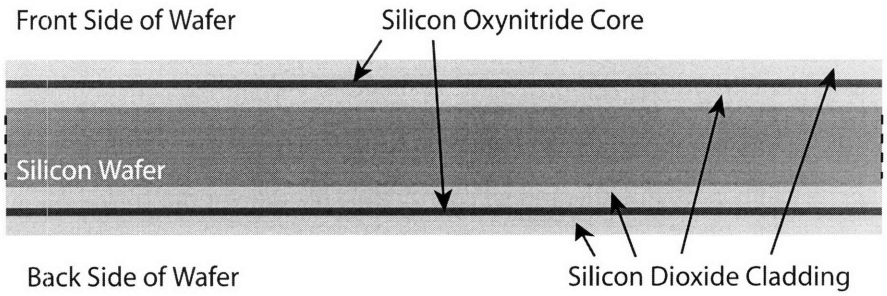

Figure 4-2: The waveguide stack is deposited on both the front and back sides of the wafer to balance the stress and virtually eliminate any wafer bow.

the wafer bow is large enough, the wafer handlers in the process tools are unable to get sufficient vacuum to hold the wafers, or they are unable to sense the wafers. These issues are in addition to the reduction in correct focus across the surface of a bowed wafer during photolithography. The easiest solution to this problem is simply to deposit the waveguide stack on both the front and back of the wafer (see Figure 4-2). The stress in the layers on the backside of the wafer balance the stresses on the front of the wafer.

Deposition on both sides of the wafer requires that the wafer be flipped upside down during the DCVD layer deposition. In order to protect the front side of the wafer during this deposition, a sacrificial oxide layer is deposited on the front of the wafer prior to the deposition on the backside of the wafer, and is approximately 0.5μm thick. Any scratches from the DCVD wafer handler on the front of the wafer that occur during backside deposition are located in this sacrificial layer and are removed with the complete removal of the sacrificial layer via a buffered oxide etch[6]. In order to protect the backside of the wafer during this etch (the etch attacks both sides of the wafer because it is a wet etch), a 0.5μm thick sacrificial oxide layer is deposited as the final layer on the backside of the wafer.

---

wave composed of both polarizations. While this is important, it is beyond the scope of this project. Measures can be taken to reduce this birefringence ([70])

[6]Buffered Oxide Etch (BOE) is a mixture of hydrofluoric acid (HF) and deionized (DI) water.

Effect of Incorporated Hydrogen on Waveguide Loss

As discussed in Chapter 3, the propagation loss of a waveguide is dependent, in part, on absorption in the waveguide core and cladding materials. Absorption in insulating materials like silicon oxynitride and silicon dioxide occurs via photon-phonon interactions. Unfortunately, the first harmonic of the vibrational modes of N-H bonds is well matched to light at wavelength of 1550nm (citeRefWorks:13). The result is enhanced absorption at a wavelength of 1550nm for these dielectric layers. The hydrogen, which appears in the first place as an unwanted adsorbent during the dielectric layer deposition[7] can be removed from these layers by annealing at high temperatures. This is an unacceptable solution for waveguides deposited on fully processed silicon CMOS wafers, as such wafers cannot tolerate temperatures greater much greater than 500°C. There are ways of depositing the waveguides without using hydrogen containing precursors. Sputtering from a silicon nitride target is one suggested solution (Reference [71]). While the eventual goal of this work is the fabrication of waveguides and integrated III-V components on fully processed silicon wafers, at this phase of the project, the starting material is just a bare silicon wafer. Future generations of this project must deal with this issue, but because solutions do exist (mentioned in [72]), the focus at this point is to get a working process on bare silicon.

In Reference [73] and [52], it was demonstrated that an anneal at 1150°C for several hours resulted in a significant reduction in absorption loss. However, due to processing restrictions, the waveguides in this work are annealed at a temperature of 1050°C for 4 hours. While the longer anneal at higher temperatures has been proven to be more effective, annealing at this temperature still results in an absorption loss reduction.

4.1.2 Waveguide Etch

Once the lower cladding and core layers have been deposited, the waveguide core must be etched in the desired waveguide pattern. This etch is carried out in a reactive ion

[7]The CVD reaction with hydrogenated precursors such as silane results in an amorphous layer with a high concentration of hydrogen.

etch (RIE) chamber. An RIE chamber is similar to a CVD chamber, but the gas chemistry and flow rates are such that material is not deposited on, but removed from the surface. For this step, there are two primary issues. The etch selectivity[8] must be high enough to remove the 0.7μm of silicon oxynitride core material before the photoresist is removed, and the sidewalls of the waveguides must be nearly vertical. These, however, are divergent requirements. High selectivity is achieved with gases that promote polymer deposition that decreases the etch rate of the photoresist more than it decreases the etch rate of the silicon oxynitride. However, this polymer also builds up on the sides of the wall that forms during the etch (see Reference [74]), effectively increasing the width of the mask resulting in a sloped sidewall.

Silicon Dielectric Etching Chemistry

A brief discussion of silicon dioxide (and similar films, i.e. silicon oxynitride) etching chemistry is necessary at this point. Silicon dioxide can be etched with a variety of fluorine (F) containing gases, and for this work, the primary fluorine containing gas that was used is carbon tetrachloride (CF_4). When used alone, CF_4 offers a very low selectivity. When used with CHF_3, the presence of the hydrogen improves the selectivity. During the silicon dioxide etch with CF_4, a C_xF_y passivation layer grows. At some passivation layer equilibrium thickness, the layer stops growing. The thicker the passivation layer, the slower the etch, but the higher the etch selectivity. This passivation layer is etched by F atoms. The more available F atoms, the thinner the passivation layer and, therefore, the faster the etch and the lower the selectivity. Adding a hydrogen containing gas such as CHF_3 lowers the concentration of F atoms due to F scavenging by the hydrogen atoms (see Reference [75]).

As mentioned above, this passivation layer causes the etch sidewalls to be sloped. As this is not desired for the waveguides, a lower selectivity, vertical etch with a 1:1 ratio of CHF_3:CF_4. The lower selectivity was not a major problem because the

[8]Etch selectivity is the ratio between the etch rate of the material that is purposely being etched and the material that is masking the etch (usually, but not always, the latter material is photoresist). A high selectivity means that little of the masking material is removed relative to the amount of the etched material.

waveguides were only 700 nm thick. For the etch of the deep wells, the ratio CHF_3:CF_4 was increased to 3:1. This was required to get a high enough selectivity to etch the 6 μm thick waveguide stack.

Figure 4-3 contains SEMs of the cross-section of the vertical and non-vertical waveguide etch. The implications of this have admittedly not been fully explored. The propagation loss may be larger for the case of vertical sidewalls if a rougher sidewall accompanies the vertical profile. However, the mode matching may be better for vertical sidewalls. As will be seen later in this chapter, the more dominant issue for coupling is device alignment, and at the stage of the project, slight differences (angular variation from 80^o to 90^o) in the waveguide sidewall profile are not a first order concern.

4.1.3 Upper Cladding Deposition

The upper cladding serves two main purposes. The upper cladding matches the upper vertical confinement of the guided mode to the lower confinement of the lower cladding. The result is a vertically symmetric mode. It also protects the core from contamination due to the accumulation of particulates which could increase the scattering from the top side of the core. Finally, it matches the height of the waveguide stack to the integrated pill device. This helps to hold the pill in place and to maintain planarity once the pill device is in place. In the event that any subsequent metal layers are deposited above the upper cladding (this is the case for a fully metal connected pill as shown in Figure 4-4), the upper cladding shields the guided mode from this metal layer. Without the upper cladding, the mode would terminate at the surface of the metal, and depending on the conductivity of the metal, suffer absorption loss in the metal layer.

The upper cladding deposition varies from the lower cladding deposition only in that the front side layer is deposited first, followed by the backside layer. Any scratches in the upper cladding on the front side should not significantly effect the mode propagation in the waveguide[9]. Again, the purpose for the front and back

[9]It is true that scratches in the silicon layer prior to the lower cladding and core layer deposition

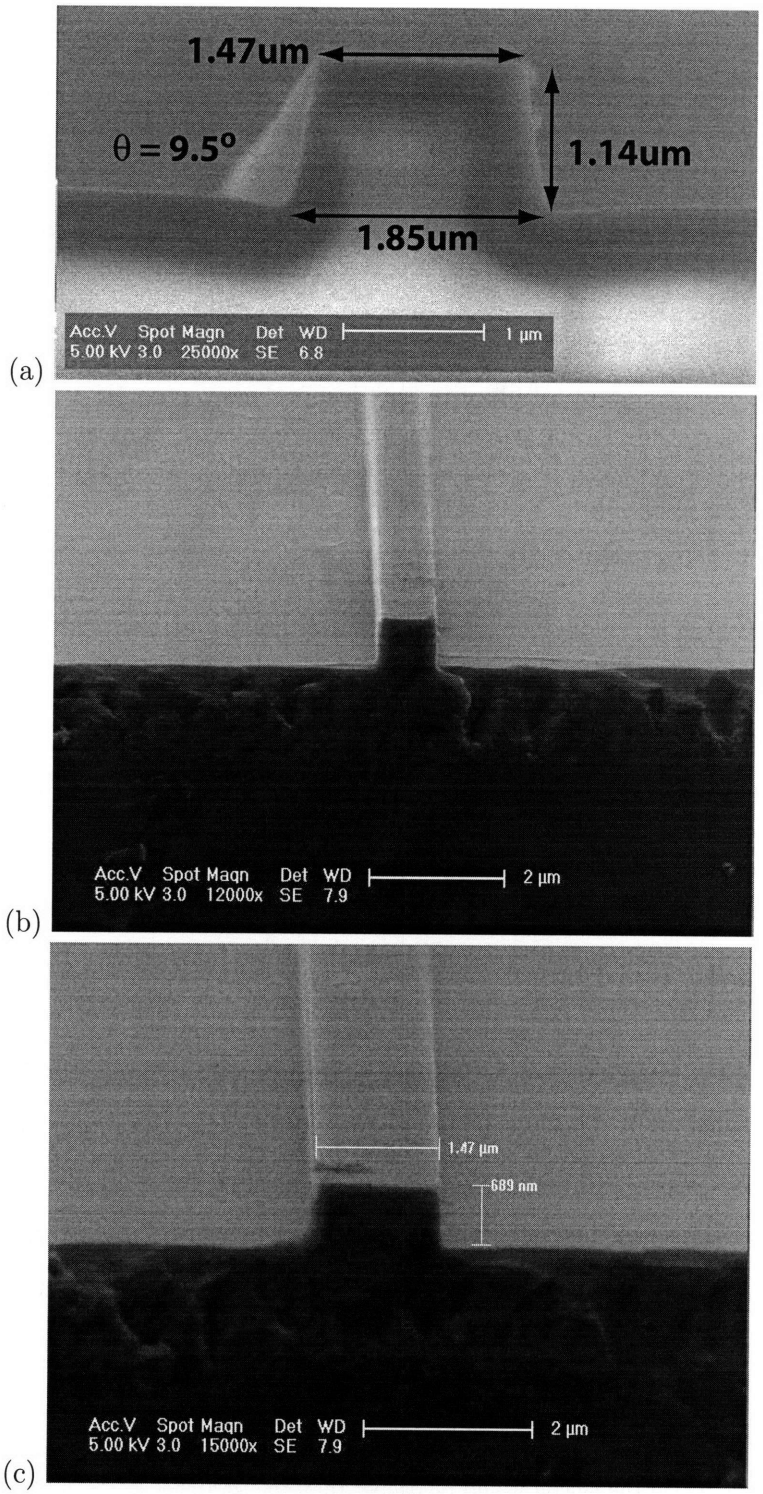

Figure 4-3: (a) SEM of a waveguide etched with the 3:1 CHF_3:CF_4 chemistry. (b) SEM of a waveguide etched with the 1:1 CHF_3:CF_4 chemistry. This was the narrowest waveguide fabricated with a width less than 1μm. (c) SEM of a 1.5μm wide waveguide etched with the 1:1 CHF_3:CF_4 chemistry.

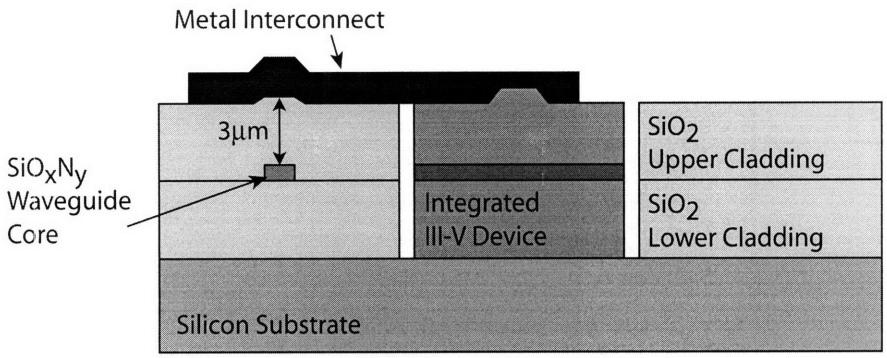

Figure 4-4: Illustration of a fully integrated, metal contacted III-V device. The light is propagating normal to the page for both the III-V device and the nearby, unrelated silicon oxynitride waveguide. The thick upper cladding ($\geq 3\mu$m) shields the silicon oxynitride waveguide mode from the metal.

side deposition is to balance the stresses on the front and back side of the wafers to minimize wafer bowing.

The thickness of the upper cladding was set at 3μm to properly shield the mode from any metal layers above and to match the approximate height of an integrated pill device.

4.2 Well Etch

Once the entire waveguide stack has been deposited and defined, the next step is the deep well device etch. These wells are the receptacles for the integrated pill devices. The wells are etched completely through the waveguide stack all the way down to the silicon layer. The well needs to be etched to a depth of 6.7μm ($3\ \mu$m for the lower cladding, $0.7\ \mu$m for the core, and $3\ \mu$m for the upper cladding). In some tests, the lower cladding thickness was increased by as much as 1.2μm, making the well depth as large as 7.9μm. The challenge with etching to this depth is finding an etch mask

are just as close to the core as scratches in the top of the upper cladding layer. However, it is likely that scratches in the silicon would be deeper than the scratches in the deposited oxide. Also, scratches in the silicon surface would propagate up to the core layer with some smoothing whereas scratches in the upper cladding layer would not affect the topography of the core layer. Due to this difference between upper cladding to surface scratches and starting silicon scratches, no sacrificial scratch removal layer was included for the upper cladding.

material and an etch chemistry that yields a high enough etch selectivity to etch the nearly 8μm of dielectric. The need to etch oxide depths on the order of several microns does not occur in standard silicon CMOS processing, but it is rather common in the area of MEMS (Micro-Electro Mechanical Systems), particularly optical MEMS. The masking material typically used by the MEMS community for this etch is either polysilicon or aluminum. Due to process restrictions regarding metals in the etching tools, polysilicon was used for this work.

4.2.1 Polysilicon Hardmask

In order to achieve the high etch selectivity required for the deep well etch, a polysilicon hardmask[10] was employed. The process of defining a hardmask requires an extra etch step, but the advantage is an increased selectivity. First the hardmask is etched, then the hardmask is used as an etch mask for the deep waveguide stack etch. To determine the sufficient thickness of the polysilicon to withstand this deep etch, etch selectivity tests were carried out with chemistries similar to the two discussed in the waveguide etch section. The highest selectivity achieved was approximately 6:1[11]. As with the waveguide etches, the higher selectivity well etch yields sloped sidewalls at an angle of 80^o. The impact of the sloped sidewalls on coupling loss was discussed in Chapter 3.

Initial Polysilicon Hardmask Thickness

The polysilicon hardmask must be thick enough to withstand the deep oxide etch, but it must be thin enough so that the photoresist can stand up to the polysilicon

[10]The term hardmask refers to a material that is deposited above the layer to be etched before the application of photoresist. The photoresist is then patterned using the standard resist exposure and develop. The hardmask is then etched followed by the material which was originally to be etched.

[11]The actual selectivity obtained is a function of the specifics of the local etch pattern and varies for low versus high aspect ratio etches. This value of 6:1 was for the low aspect ratio portions of the pattern. Because the dimensions of the wells (150x300μm) are very large relative to the waveguide stack thickness, the etch of the wells is a low aspect ratio etch. There are, however, narrow 1μm wide test structures on the well etch mask which are used to characterize the quality of the etched facets. The selectivity in these high aspect ratio areas is lower than 6:1, but this is not a problem because these areas only need to be etched through the upper cladding and the core, not the whole way through the lower cladding.

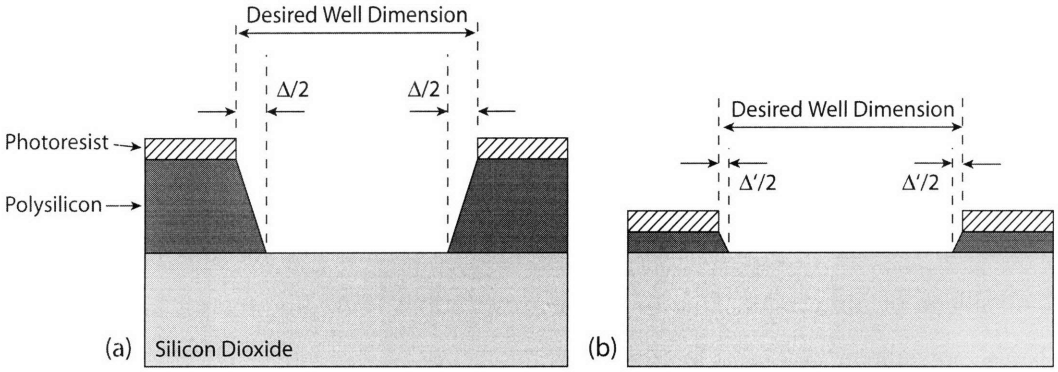

Figure 4-5: (a) For a sidewall other than vertical, a thicker hardmask results in more total error (Δ) in the desired well dimension. (b) For a thinner hardmask, the error (Δ') is smaller.

etch. In addition, if the hardmask is too thick, it becomes difficult to control the lateral dimension of the etch because there will invariably be an angle to the polysilicon sidewall as a result of the polysilicon etch (see Figure 4-5). Therefore, it is important to determine the minimum polysilicon thickness that can withstand the deep waveguide stack etch. The etch selectivity value of 6:1 was determined for trials in which 1μm of polysilicon was chosen as the hardmask thickness. This initial polysilicon thickness of 1μm was chosen because of the known 3:2 selectivity of the polysilicon etch. With this selectivity, exactly 1.5μm of polysilicon could be etched with the standard 1μm photoresist thickness[12]. To be on the safe side, 1μm of polysilicon was used. As mentioned, the etch selectivity was determined to be 6:1. With a 1μm thick polysilicon layer, 6μm of waveguide stack was removed. This is enough to remove the lower and upper cladding oxide which together are 6μm thick. However, this is not enough to remove the 6.7μm or even worse, 7.9μm, total waveguide stack thickness which exists above the waveguide core in the center of the well.

[12]In theory, the photoresist thickness could be increased beyond 1μm to withstand a thicker polysilicon layer. However, this requires a recalibration of the exposure and develop steps. A better solution will be discussed in the next section

4.2.2 Oxide and Polysilicon Hardmask

Once the actual etch selectivity was known, the exact polysilicon thickness required to etch the nearly 8μm of waveguide stack could be determined. With a selectivity of 6:1, approximately 1.35μm of polysilicon is required to etch 8μm of waveguide stack. To allow for process variations, 1.5μm of polysilicon was used. The polysilicon was deposited using Low Pressure Chemical Vapor Deposition (LPCVD) at a rate of approximately 90Å/minute. With 1.5μm of polysilicon, 1μm of photoresist is only just enough to stand up to the polysilicon etch (recall the 3:2 selectivity of this etch). Initial trials with this thickness of polysilicon resulted in wells with tall lines running down their center. This is seen in the SEMs shown in Figure 4-6. The issue can be better understood by looking at a cross section of the waveguide stack where the waveguide is coming out of the page as shown in Figure 4-7(a) with a zoomed-out perspective drawing shown in Figure 4-7(b). Notice the bump due to the conformal deposition of the upper cladding. In order to guarantee that the end of the waveguides meet exactly with the edge of the wells, the waveguide pattern was drawn in a continuous line through the wells. So the cross section shown in Figure 4-7 is the pre-etch cross section for the entire length of the well. The polysilicon deposition is conformal, and as a result, the polysilicon thickness is greater at the edges of the bump than on the surrounding flat surfaces (see Figure 4-8). The actual amount of polysilicon deposited is determined by measuring the thickness on a monitor wafer with no topography. Therefore, the measured thickness on the monitor was always less than the thickest part of the polysilicon on the bump edges. Because the polysilicon etch was tailored to the monitor thickness, some polysilicon remained along the edges of the bump resulting in the lines seen in Figure 4-6. However, this was not the only issue. Increasing the polysilicon etch time was not an option because the polysilicon:photoresist etch selectivity was low enough that the photoresist was nearly completely etched after etching the 1.0μm. Another method was required to allow for the complete etching of 1.5μm of oxide plus the extra amount on the edges of the waveguide bump.

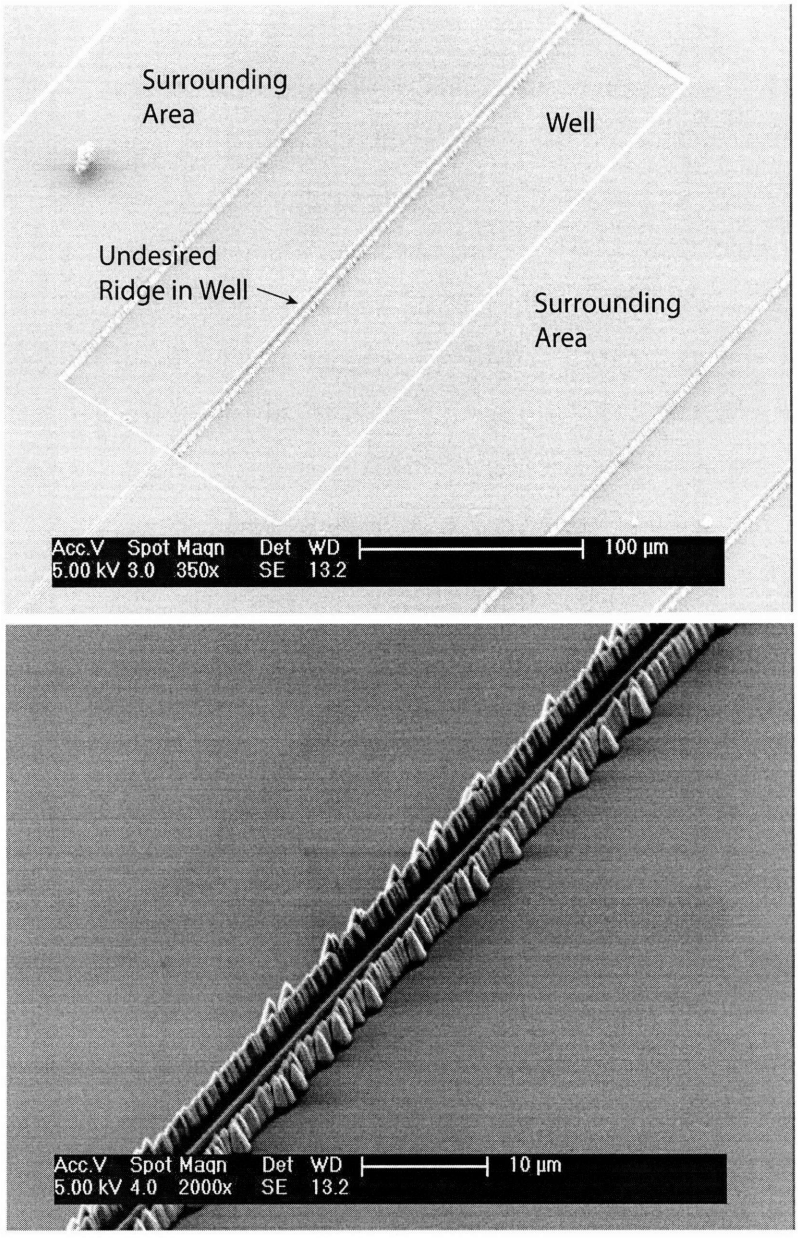

Figure 4-6: (a) SEM of a well etch with an undesired ridge in the center of the well. (b) SEM Close-up of the undesired ridge.

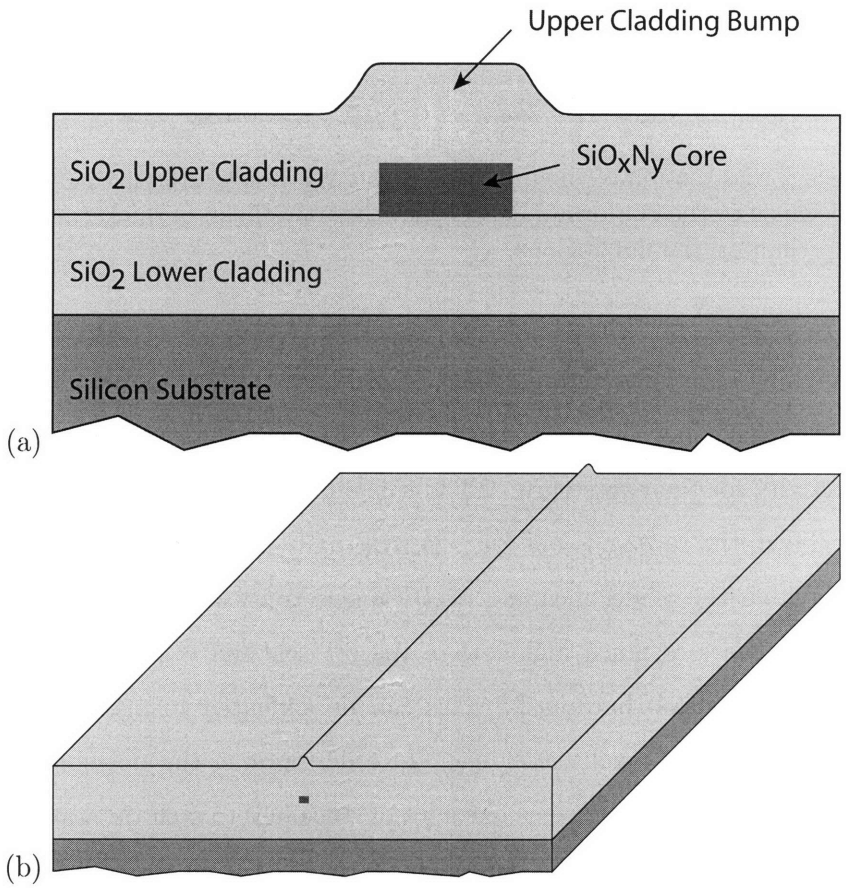

Figure 4-7: (a) Cross section of the dielectric waveguide stack showing the bump in the upper cladding. (b) Perspective drawing showing the bump running in a line parallel to the waveguide core at the surface of the waveguide stack.

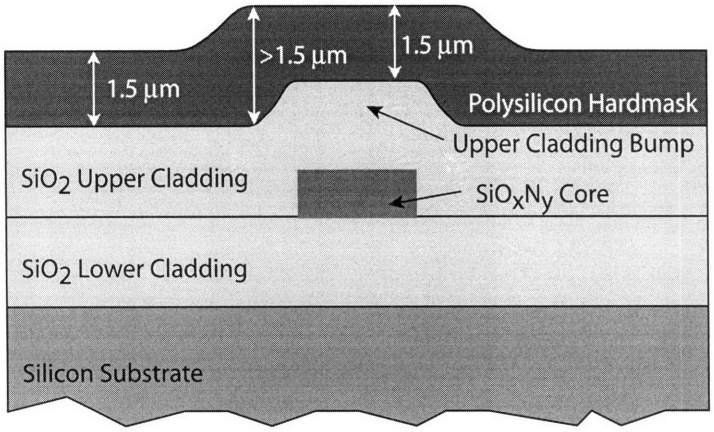

Figure 4-8: Cross-section of the dielectric waveguide stack after the polysilicon deposition. Because of the conformal deposition, the polysilicon is thicker at the edges of the bump than on the flat regions.

The etching of oxide with a polysilicon hardmask is much more difficult than the etching of polysilicon with an oxide hardmask. The reason for this is the difference in etch selectivity for the two etches. While it is difficult to etch oxide without etching the polysilicon, the reverse is not true. It is actually much easier to etch polysilicon without etching the oxide, meaning that the selectivity for a polysilicon etch with an oxide hardmask is much higher than the 6:1 selectivity achieved for the oxide etch with a polysilicon hardmask. This can be exploited to make the polysilicon hardmask etch step a much easier one. In order to etch the polysilicon, an oxide hardmask was employed. It seems like a lot of steps just to etch the waveguide stack, but it guarantees that all of the polysilicon is removed from the well area when the polysilicon is etched, so that all of the waveguide stack in the well area can be etched during the waveguide stack etch.

Figure 4-9 is an SEM of the well etch with the additional oxide hardmask step. Notice that there is still a line in the center of the well but it is much smaller than the ridges in Figure 4-6. Figure 4-10 is an SEM of one of the gaps that was used to systematically measure the gap coupling losses (this will be discussed in greater detail in the following two chapters).

The following argument explains why this bump is still present even for full re-

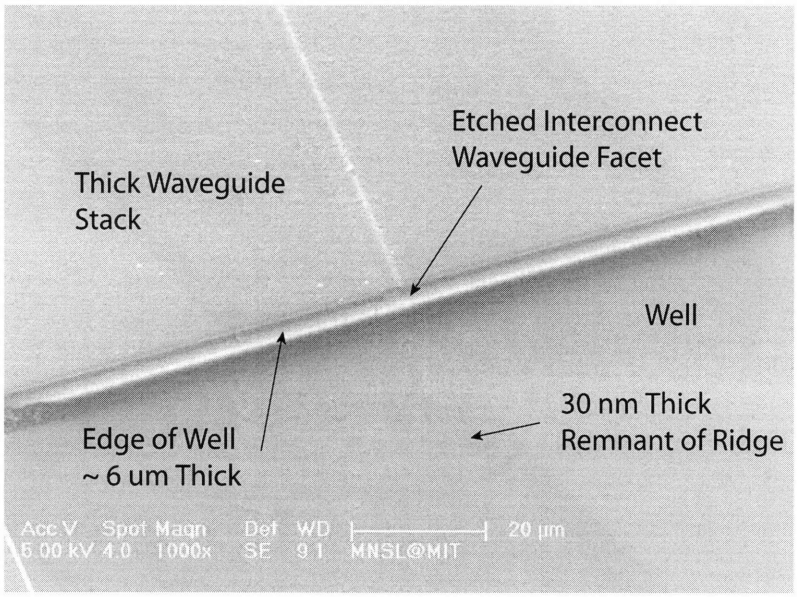

Figure 4-9: SEM looking down into a well at an angle. This well was etched using the additional oxide hardmask step. A slight remnant of the original bump can be seen running down the middle of the well, but it is only about 30 nm thick.

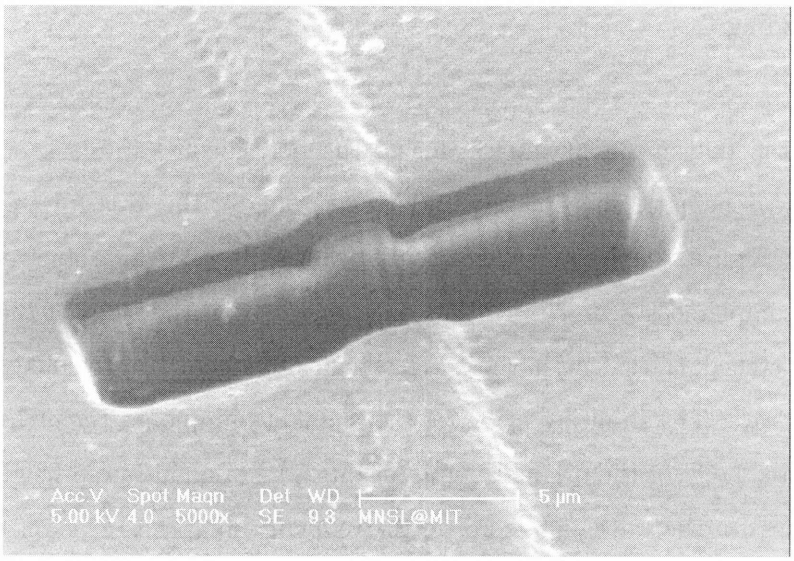

Figure 4-10: SEM looking down into an etched gap at an angle. This gap was etched using the additional oxide hardmask step.

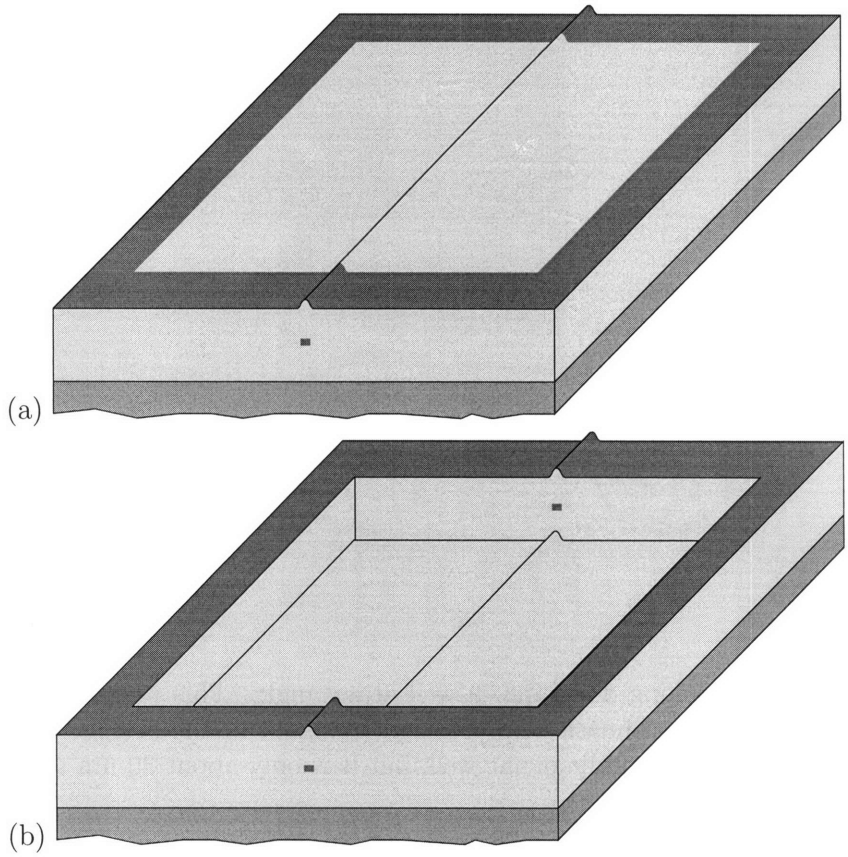

Figure 4-11: Cross section of the dielectric waveguide stack showing the bump in the upper cladding.

moval of the polysilicon hardmask during the polysilicon hardmask etch. Figure 4-11(a) is a schematic showing the initial patterning of the area for the waveguide stack etch. Figure 4-11(b) is a schematic that shows the waveguide stack etch at some partially completed stage. Notice that once the area on the sides of the bump has been fully etched, the silicon in those areas begins to etch at a rate equal to $1/6^{th}$ the oxide etch rate. The resulting height of the remnant bump once the etch is complete is, therefore, $1/6^{th}$ of the original bump height. The original bump height is 0.7μm, the thickness of the waveguide core, so the remnant bump height is on the order of 0.1μm[13].

[13]In practice, the bump etches slightly faster than the surrounding area, so the remnant bump was smaller even than this theoretical value. Furthermore, the selectivity of 6:1 is for the entire waveguide stack, including the silicon oxynitride core. This material actually etches slower than the

4.3 Die-Saw Assisted Cleave

Once the waveguides and the deep well etch have been completed, the wafer must be die-sawed into individual die. In the case of preparation for optical measurements, the edges of the die perpendicular to the waveguides must be as smooth as possible to allow for good coupling both into and out of the waveguides. This is accomplished with a die-saw assisted cleave[14]. It is very difficult to cleave samples smaller than $1cm^2$ from a 6" silicon wafer because it is quite thick (approximately 0.65mm). Any roughness in the silicon cleave edge shows up as an even rougher edge in the overlying dielectric waveguide stack because it is an amorphous, rather than crystalline, material. The die-saw assisted cleave alleviates the problem of the thick silicon wafer.

4.3.1 Basic Process

As mentioned, the die-saw assisted cleave can be used to improve the quality of the waveguide facets that form during the wafer cleave step. In short, the wafer is sawed from the back side, but instead of slicing entirely through the wafer, approximately $100\mu m$ of silicon is left. A slight torque is applied to the wafer and it cleaves readily along the sawed line (see Figure 4-12). The silicon cleavage plane is the $\langle 111 \rangle$ plane which is at an angle of 54.74^o to the wafer surface as shown in Reference [76].

In order to protect the front side of the wafer during the die-sawing, a few microns of photoresist are applied to the front of the wafer prior to die-sawing. With a standard die-saw step, a thick tape it applied to the back-side of the wafer and cuts are made from the front. With the die-saw assisted cleave, the tape is applied to the front of the wafer and cuts are made to the back side of the wafer. The thick photoresist protects the front wafer surface from the tape.

The die-saw cuts are then made with the cuts parallel to the waveguides (between the die) made through the wafer and the cleave cuts perpendicular to the waveguide

silicon dioxide cladding, so the selectivity to silicon dioxide is slightly higher than the stated 6:1 value for the entire stack. Considering these two points, the actual remnant bump height varied in practice between 0.02 and $0.08\mu m$.

[14]This technique was developed by Tymon Barwicz, a post-doc at MIT. This author is unaware of any publications that discuss the die-saw assisted cleave technique.

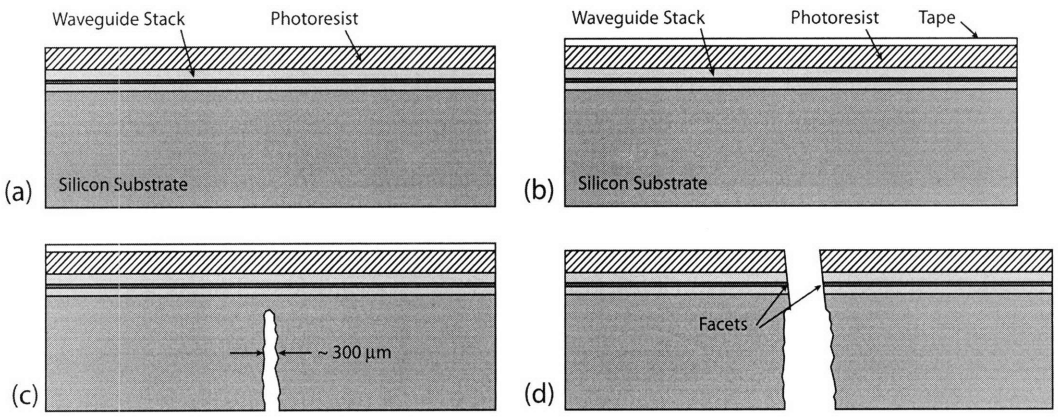

Figure 4-12: The four steps of the die-saw assisted cleave technique (a) Starting point, wafer coated with a thick protective layer of photoresist. (b) Die-saw tape applied to front side of wafer. (c) Die-saw cut made from back side most of the way through the wafer (typically leaving 100μm of silicon). (d) The piece is cleaved and the tape is removed (or vice versa in some cases).

made as discussed above. Once the cuts have been made to the backside of the wafer, the tape is carefully removed leaving long pieces of wafer one die in width and 4 or 5 die in length (see Figure 4-13). With the front side of the wafer facing down, the individual die are cleaved, one facet at a time, until all of the die have been separated by cleaves. The individual pieces are then inspected and placed in acetone to strip away the protective photoresist. The pieces are cleaned using a standard solvent degrease clean (acetone, methanol, isopropanol) and then mounted on special aluminum mounts.

4.3.2 Optimum Die-Saw Parameters

For even the best recipe, the yield for this technique is approximately 20%. It seems that the facet quality is a function of how carefully the tape is removed, the length of the sample being cleaved, and the depth of the backside die-saw cut.

Ideally, the wafer does not cleave while the tape is being removed. If it does, the cleave is typically very poor. However if the sample survives the tape removal without cleaving and is then cleaved properly later, a much better facet typically results.

The length of the piece being cleaved also affects the quality. For many of the

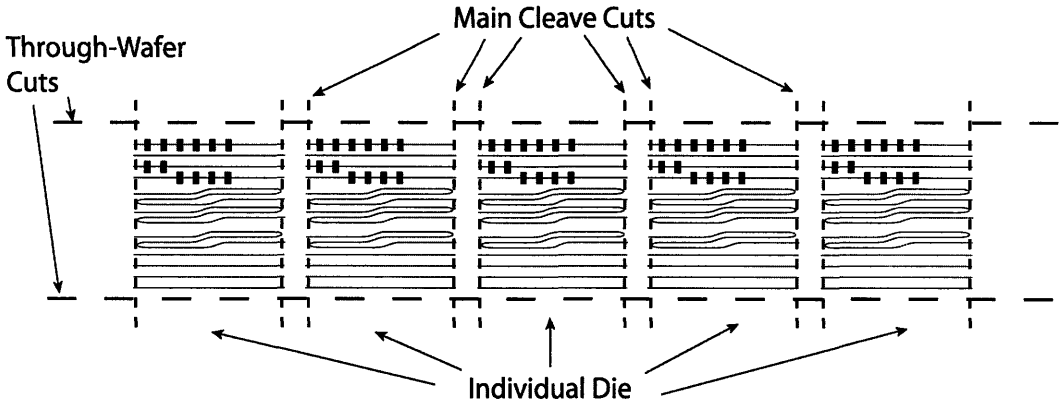

Figure 4-13: In the case of cleaving a die at the ends of the long waveguides that extend across the entire die, a strip with several die is cut with two long through-wafer cuts. The individual die are each removed with two cleaves.

Fabry-Perot measurements, a good waveguide length is about 4mm. The best way to cleave a length this short is to make four cuts, two main cuts which are at the required location, 4mm apart, and two other cuts, each positioned at least 1cm away from the main cuts. The distant cuts are cleaved first, followed by the main cuts (see Figure 4-14). This seems to improve the quality of the cleave by spreading the force evenly over the length of the cut.

The depth of the backside die-saw cut determines how much silicon remains to be cleaved. It seems that the less remaining, the better the cleave. However, if too little remains, the sample typically cleaves either while removing it from the die-saw chuck or while removing it from the tape. To complicate matters, the amount remaining is a relative term affected by the length of the sample. It is the torque on the cut that determines when the cut cleaves, so for a given cut depth, a longer sample will cleave with less force than a short sample. So it is better that the backside cut be deeper for short samples and shallower for longer samples.

4.3.3 Cleave Setup and Sample Mounting

A very simple setup was used to cleave the samples (see Figure 4-15). The sample was placed between two aluminum blocks, each covered with a fabwipe. The sample

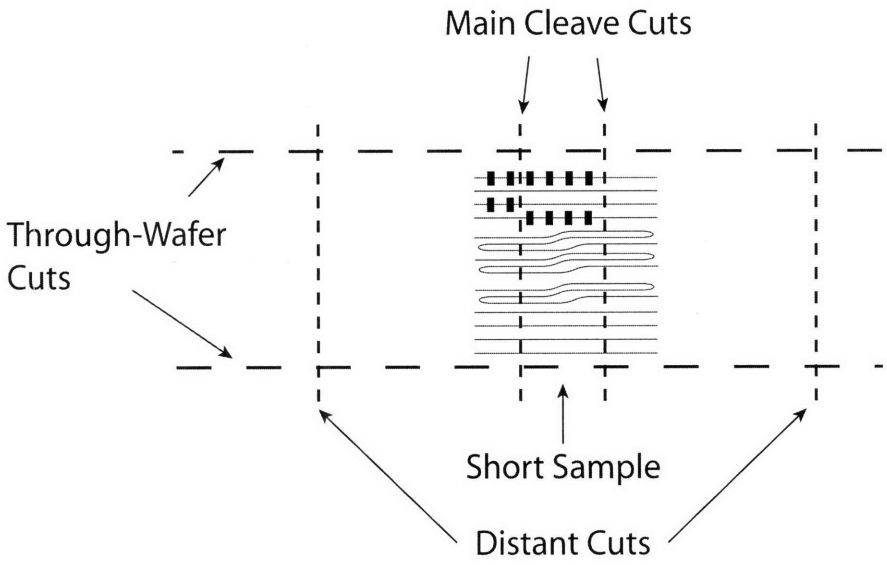

Figure 4-14: In the case of cleaving a short length piece, two main cleave cuts and two distant cleave cuts are made. The distant cuts are cleaved first followed by cleavage along the main cuts.

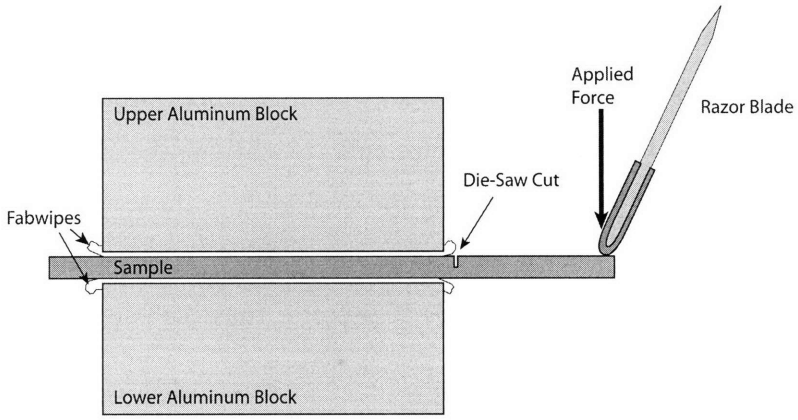

Figure 4-15: Schematic of the setup used to cleave samples for waveguide facet formation.

was mounted backside up with the cut sitting just past the edge of the two blocks. The dull edge of a razor blade was used to apply an even force along the length of the sample.

Occasionally, very good facets resulted from cleaving the samples while they were still attached to the tape. The samples were then just peeled away from the tape. The difficulty is that this often worked for just one sample on the wafer. The act of cleaving and peeling would usually cause other samples on the wafer to cleave prematurely. The cleaved faces would then grind against each other while the wafer was being handled causing the edges to become very rough. As previously mentioned, coating the wafers with photoresist helped to alleviate this problem somewhat.

Once the samples were cleaved, the photoresist was stripped and the samples were cleaned using a solvent degrease as described above. The samples were then mounted to thin aluminum mounts using crystal bond. The mount was designed for a chuck that was specifically designed for the experimental setup. At this point, the samples are ready for measurements or III-V device mounting, whatever the case may be.

4.4 III-V Device Pick-and-Place

The final fabrication step involves the integration of the III-V device on the prepared silicon photonic substrate. At this stage, the III-V devices with an approximate dimension of 300 x 150μm have been prepared with a ridge waveguide and micro-cleaved facets, and they are sitting on a bare silicon wafer ready for pick-and-place (see Figure 4-16). While many of the pills have cleaved and are ready for pick and place, the most notable pills are those that haven't cleaved and remain in a bar of three attached pills. There is clearly some stress in the pills although no significant bowing was seen for the single pills. The preparation of the III-V devices is the work of another student, Joseph Rumpler and is discussed in a paper pending publication.

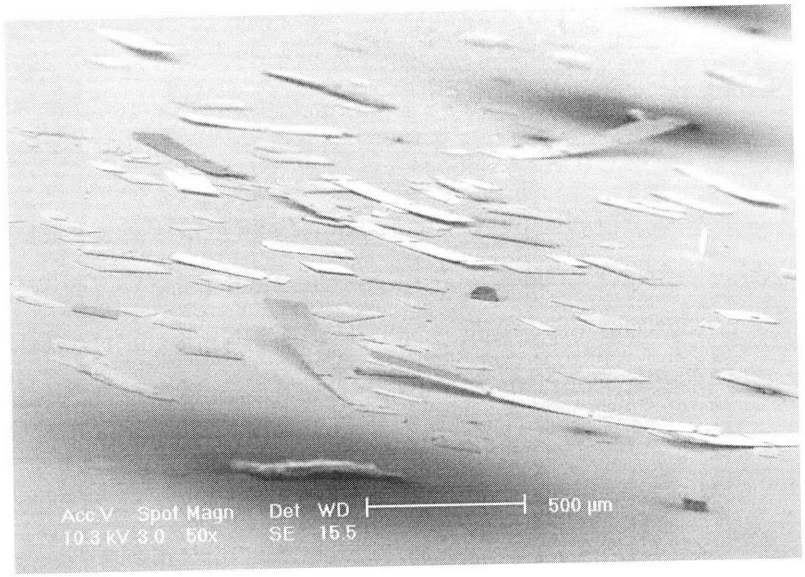

Figure 4-16: SEM of many pills sitting on a substrate.

4.4.1 Pick-and-Place Setup

The setup for the pick-and-place method consists of a microscope and a micropipette attached to a 3-axis micro-positioning stage. The micro-pipette (see Figure 4-17) is placed at an angle so that neither the positioning controls nor the micro-pipette itself interfere with the microscope view of the device and the substrate. The micro-pipette tip is bevelled at the end so that its surface is flush with the III-V device surface. The outer diameter of the micro-pipette tip is approximately 50 μm and the diameter

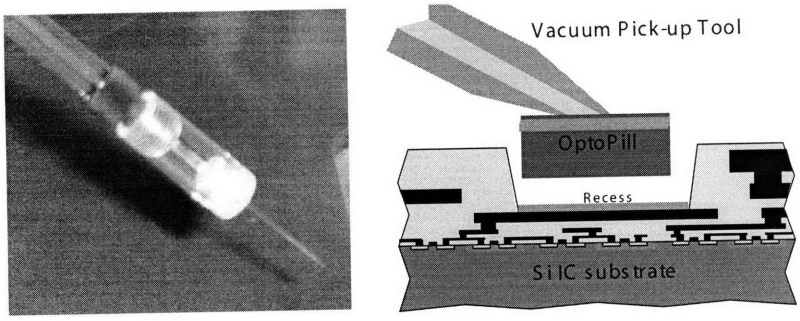

Figure 4-17: On the left, an image of the micro-pipette used for pick and place. On the right, a schematic showing the bevelled edge and the pill attached to the micropipette tip as it is lowered into place.

of the cavity is 20 μm. At this size, the micro-pipette tip is smaller than half the width of the III-V device so it can be placed on either side of the ridge for device pick-up. The end of the micro-pipette opposite the tip is fitted with a hose and a valve to which a vacuum is applied. The valve can be turned on to pick up a device and turned off once the device is in place.

While the method requires some patience and practice, it is fairly straightforward. The micro-pipette vacuum is turned on it is lowered so that the tip is pressing down against the top of a device. The micro-pipette is moved laterally until a good seal forms. The micro-pipette and attached device are moved up and positioned over the device well on the silicon substrate using the micro-positioning knobs. The device is then lowered into place in the well and the vacuum is turned off. Usually the micro-pipette tip must be moved laterally at this point to completely break free from the device[15]

For the purpose of this work, the device was placed in the device well and received no further processing. It was determined that the devices stayed in place for careful moving and handling so no method was developed to permanently secure them. In the case that further processing (metal interconnects, etc.) is required, such a securing method must be developed.

4.4.2 Pick-and-Place Results

Three main sets of device pick-and-place were performed during this work. In total, over 30 devices were integrated, with an average pick-and-place time of about 30 minutes. The purpose of the three sets is listed below:

1. *Initial Trials and Tests*

2. Multiple Device Placement for Transmission Measurements 1

3. Isolated Device Mounting (not in a well)

[15]It is this final lateral movement that sets the limit to the positioning accuracy of this technique. In order to improve the placement accuracy, a technique must be developed to hold the device in place while the tip is being removed. Another possibility is to use a well with angled sides so that the device has a stable resting place to which it returns via gravity after it is slightly disturbed.

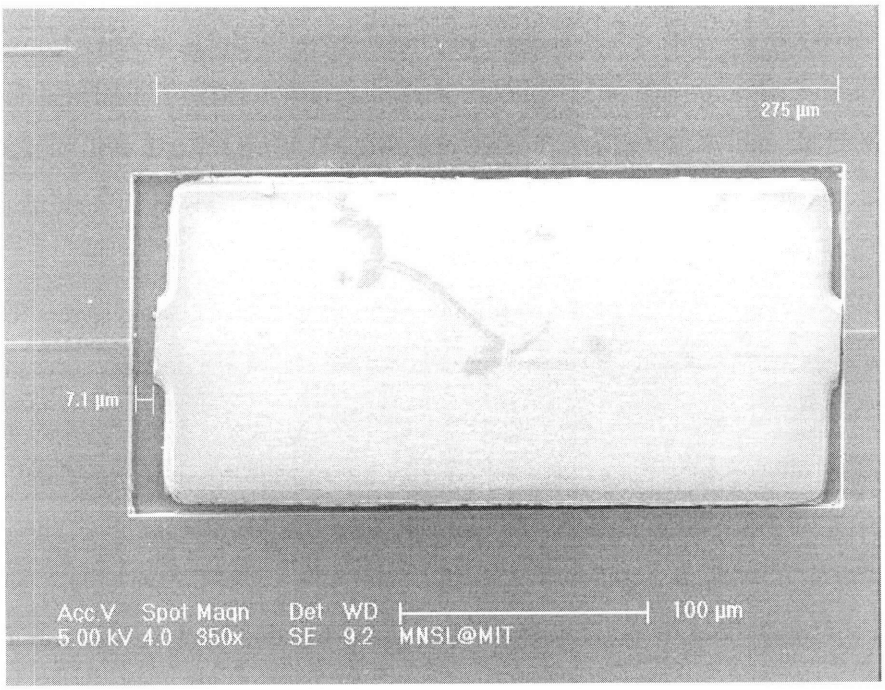

Figure 4-18: SEM of the first integrated device.

4.4.3 Initial Trials and Tests

The *Initial Trials and Tests* phase was the practice phase in which incomplete[16] III-V devices were integrated to verify the feasibility of the pick-and-place technique. The size of the wells into which the III-V devices fit was determined, and an understanding was developed as to what, in practice, affects device placement and yields the best results. Finally, the test phase was useful for obtaining some statistics on the device placement, such as the typical gap lengths and the lateral misalignment.

The first step was to determine the feasibility of the pick-and-place technique. This basic capability was verified with the first successful integrated device shown in Figure 4-18. To improve upon this first integration, devices were placed in wells with a tighter fit. The fit was improved systematically by attempting to place the devices in smaller and smaller wells to find the best fit. A grid of wells on the silicon substrate was used for this purpose. The well width increases by 5μm from 135μm

[16]Some of the devices had no ridge or lacked the quantum wells.

to 150μm from the leftmost to rightmost column, and the well length increases by 1μm from 293μm to 312μm from the uppermost row to the lowest row. The devices typically fit into the 150μm wide wells with lengths ranging from 307 to 312μm.

In practice, the lateral device alignment (see Figure 4-19 for visualization of the different alignment terms) is a function of how much time is spent aligning the device. At this point, the placement is not a very exact process. With patience, the device can be placed with a lateral misalignment of less than about 2μm. The translational alignment of the device is better controlled than the lateral alignment. The III-V device is always placed in the well such that one of the III-V device facets is closer to the well edge than the other facet. The reason for this is that when the device is in place, the micro-pipette tip is removed by sliding it sideways off the device. When this happens, the devices moves slightly in the direction that the micro-pipette tip is slid. To maintain the lateral alignment, the tip is slid in the direction of the well edge, which pushes the device towards one well edge. This is illustrated in Figure 4-21. Figure 4-20 is an image of an integrated device showing an extreme example of this gap length disparity. Based on the trials, the short gap length is on the order of a few hundred nanometers, and the long gap length is typically in the range of 3 to 5μm.

Given perfect lateral and vertical alignment, the cross-gap coupling efficiency is exponentially related to the gap length (see Chapter 3). However, in practice, the lateral alignment (vertical and sideways) is not perfect and this reduces the sensitivity of the coupling on the gap length. This effect was also discussed in Chapter 3.

4.4.4 Multiple Device Placement

Once the initial trials were complete, an investigation into the optical coupling through a passive integrated device was conducted. This step was the culmination of all of the design, fabrication, and testing efforts. This required the integration and measurement of pills with ridges (see Figure 4-22 for an SEM of the first integrated ridge pill). The goal was to determine whether any light could be sent through the silicon oxynitride waveguides, coupled across the gap into the III-V device, and then

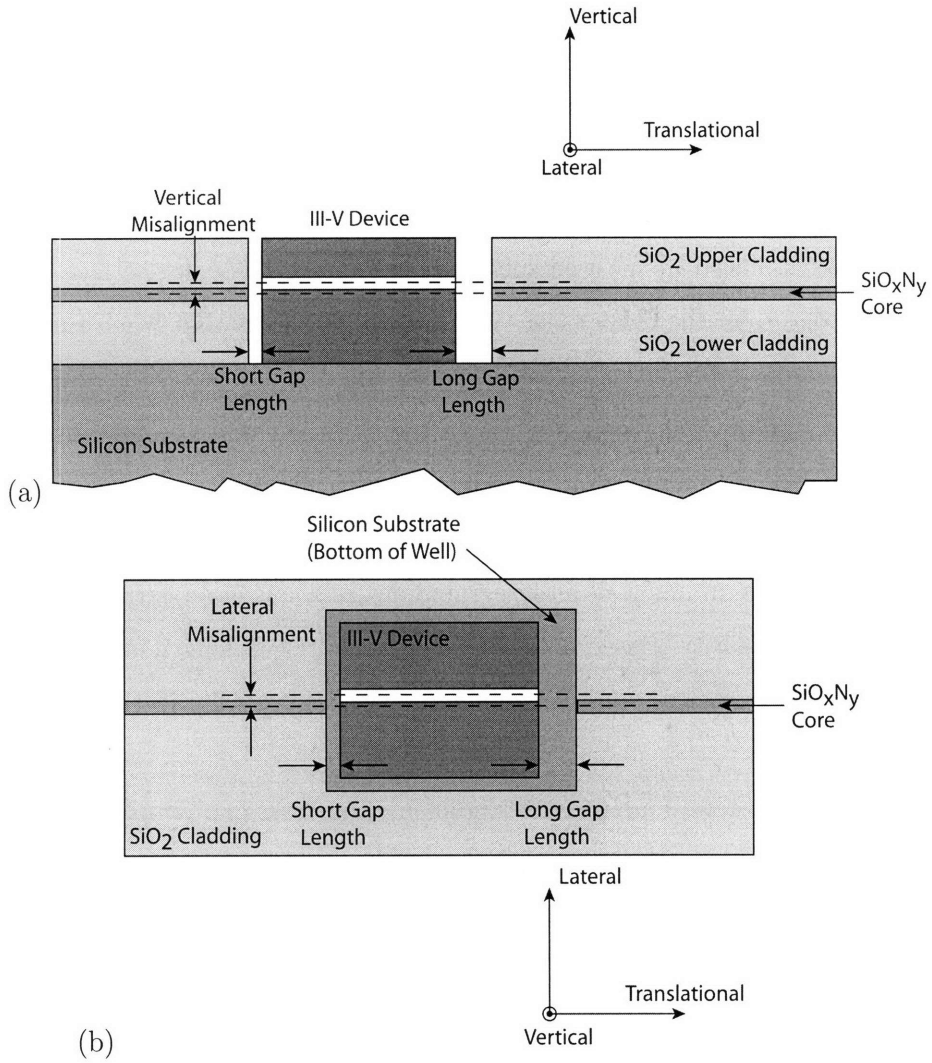

Figure 4-19: Schematics of the device misalignment in the well and the terms used for each direction. (a) Cross-section plane containing the wafer surface normal and the waveguide propagation direction. (b) Wafer plan view.

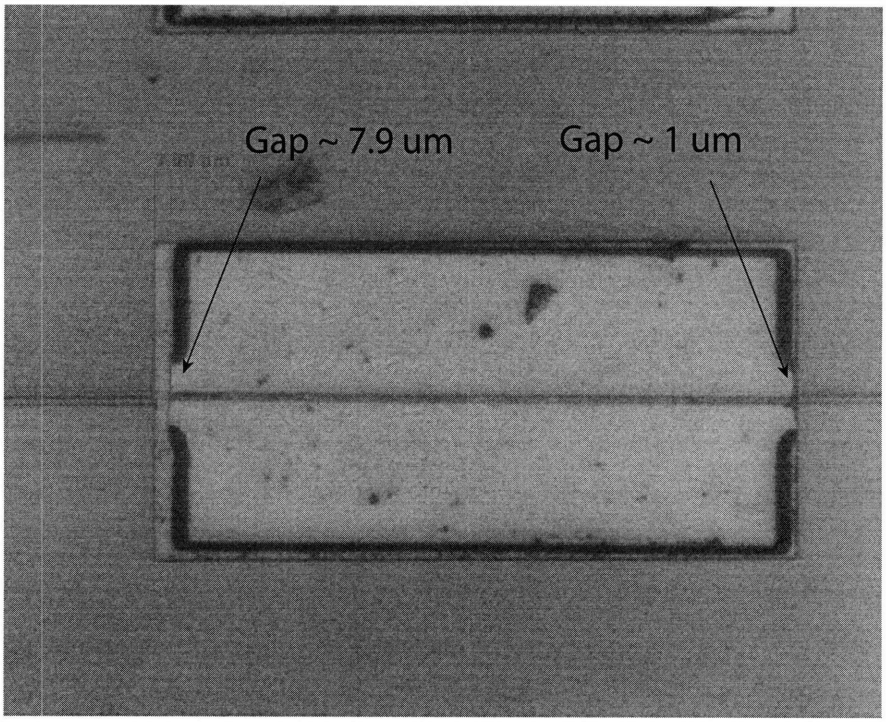

Figure 4-20: Microphotograph of a pill with two very different gap lengths. This is a result of pushing the pill to the right during removal of the micropipette tip.

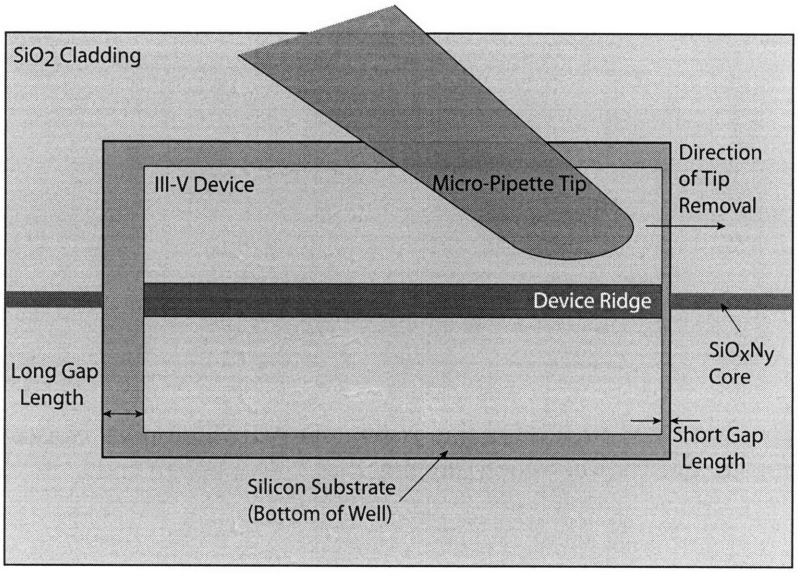

Figure 4-21: Plan view schematic of the removal of the micro-pipette tip and the resulting short and long gap length.

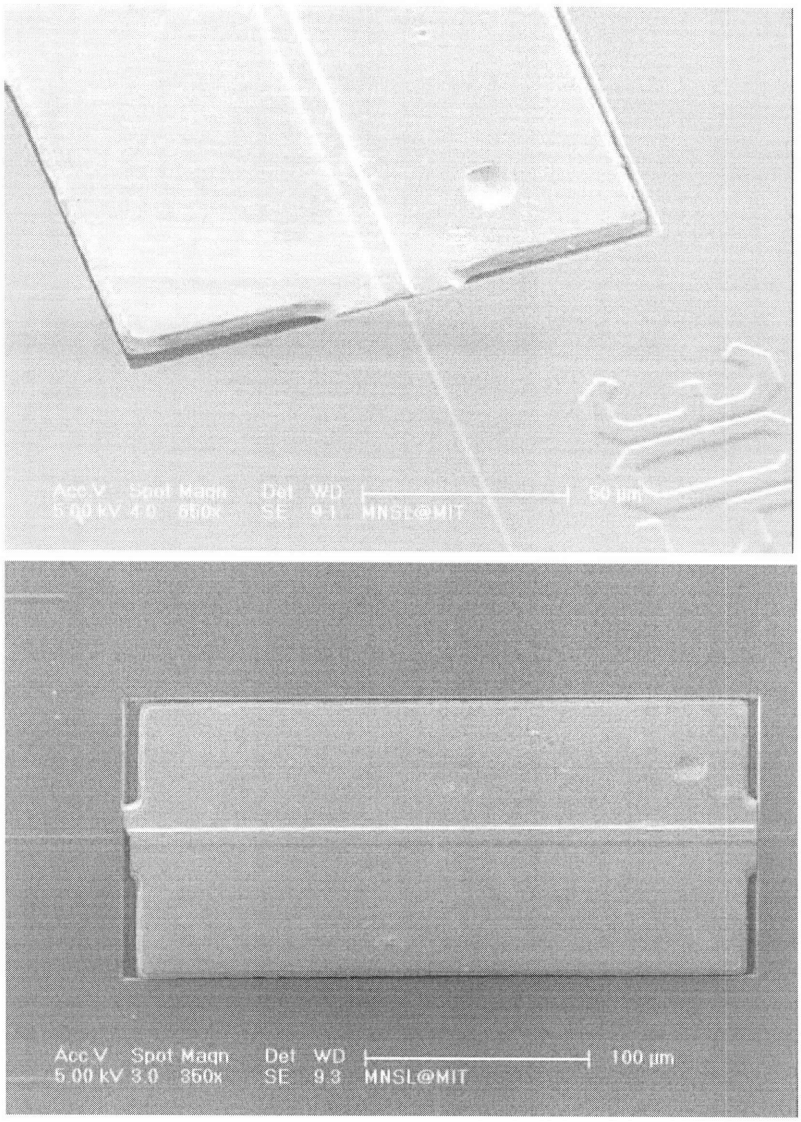

Figure 4-22: Two SEM images of the first integrated ridge pill. Notice the broken facet at one end and the very good alignment at the opposite end.

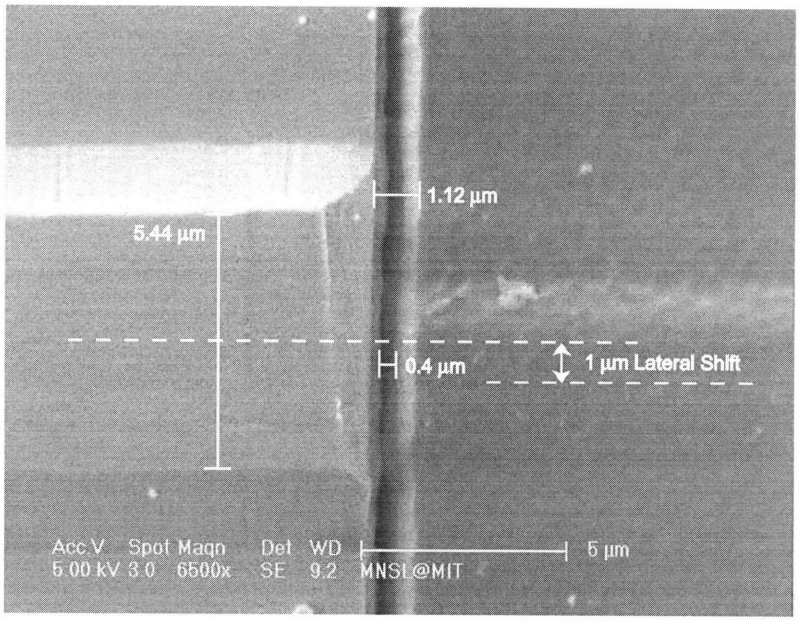

Figure 4-23: Close up SEM image of the ridge waveguide pill shown in Figure 4-22.

coupled across the second gap into the silicon oxynitride waveguide. In addition, a quantitative determination of this total coupling loss, and the dependence of this loss on device placement was desired.

Six InP/InGaAsP ridge waveguide pill devices were integrated onto a single silicon chip with processed waveguides and etched wells. The pill lengths were distributed about a mean length of 300 μm with a standard deviation of 2 μm. The six pills were placed in the six longest wells ranging in length from 308 to 312μm (see the microphotograph in Figure 4-24). Transmission measurements spanning the full wavelength range of the tuneable laser were taken for each integrated device. High magnification microphotographs of both gaps were taken for each device (see Figure 4-25) to determine the lateral and translational misalignment[17] As mentioned, the goal was to relate the data extracted from the transmission measurements to the alignment data to determine a typical, and perhaps, best case, value for the coupling loss. This is discussed in Chapter 6 with the other measurement results.

[17]It is, of course, not possible to measure the vertical misalignment from a standard microscope. Attempts were made to measure the vertical misalignment using a profilometer, but the probe tip moved the device during the profiling.

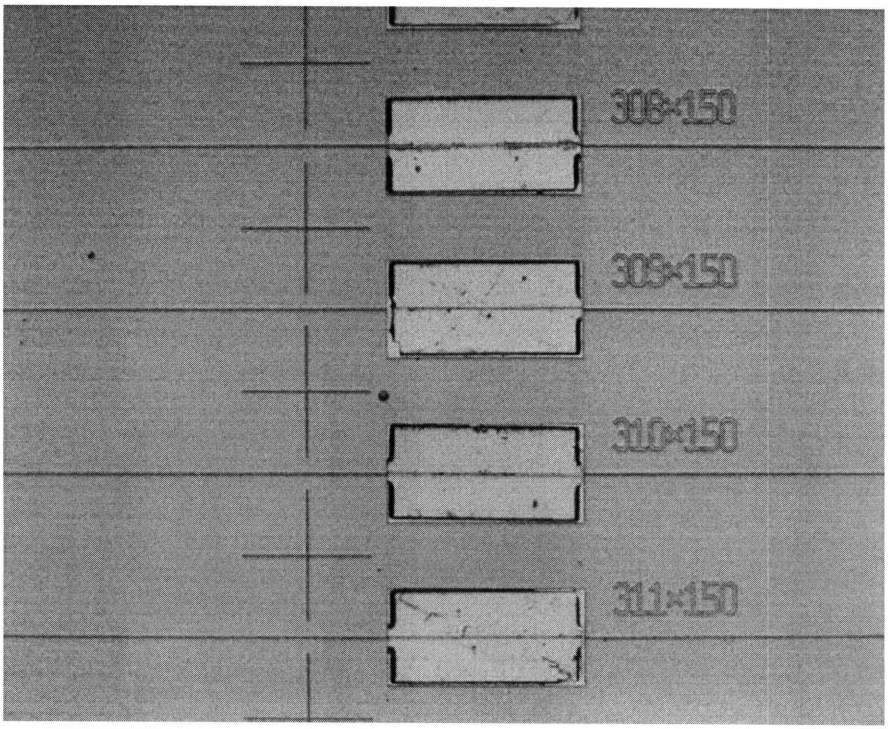

Figure 4-24: Microphotograph of 5 pills (the pill in the 307 μm long well can just be seen at the top of the image). There is another integrated pill just out of view in the 312 μm long well.

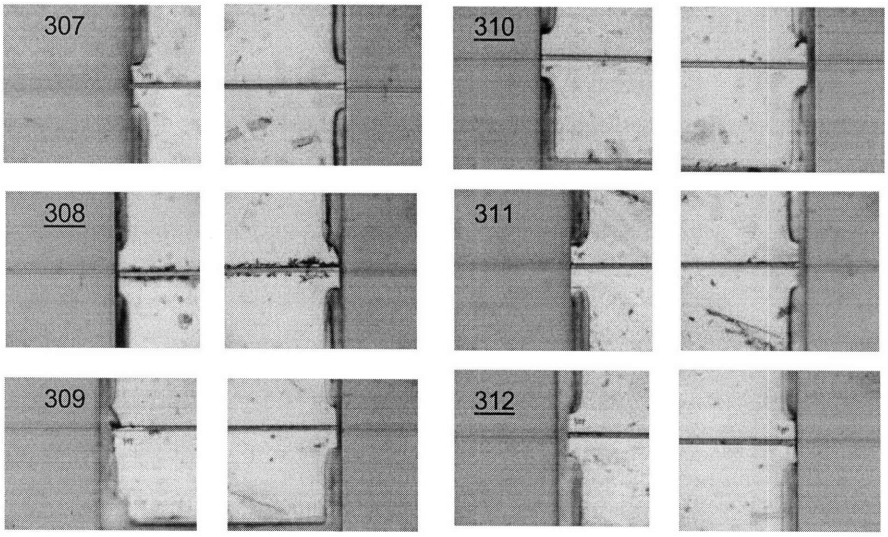

Figure 4-25: Microphotograph of the left and right facet of each of the six integrated pills.

4.4.5 Isolated Device Mounting

During the analysis of the data from the Multiple Device Placement I transmission measurements, it became clear that a better understanding of the transmission measurements for a single isolated device was needed. Transmission measurements had been taken for a long (several millimeters) III-V ridge waveguide fabricated in the full wafer material[18], but not for the fully micro-cleave processed device (i.e. the devices that were being integrated in the wells). A single micro-cleaved device is only 300μm long and about 6μm thick. The modal properties for a ridge waveguide made from such a thin device can be quite different from that for the much longer, full wafer thickness InP/InGaAsP waveguide.

The difficulty comes in trying to measure the transmission spectrum for a single isolated micro-cleaved device. More so than the short length being a problem, the very small thickness makes it impossible to measure the spectrum with the standard setup. If such a device were mounted on the standard mounts, which are 5 mm long, the input and output fibers in the transmission measurement setup would be too thick to align the vertical center of the fibers (125μm above the surface of the mount) with the vertical center of the micro-cleaved devices (3μm above the surface of the mount). What was needed was a way to mount a single device on a mount that was narrower than the 300μm device length. A razor blade is about 250μm at its thickest. When placed sideways, it is the perfect mount for the 300μm long device. The device was mounted to the razor blade edge using the standard pick and place method. To hold the device in place, the razor blade edge was covered with a thin layer of nearly cured epoxy just prior to mounting the micro-cleaved device.

Because not all of the devices cleave during the ultrasonic agitation stage of the micro-cleave technique, there are readily available 930μm long devices (this is the length of the bars prior to the micro-cleave ultrasonic agitation step, or the length after the step in the case that the bar fails to cleave). A device of this length was also

[18]The InP/InGaAsP quantum well material comes from a 2 inch diameter epitaxial wafer. The "full wafer material" designation is used to contrast the waveguide made from this material from the much thinner micro-cleaved device.

mounted on the edge of the razor blade in order to compare the transmission spectra for the two different lengths.

4.5 Summary

In this chapter, the various fabrication and assembly steps were discussed. Waveguides were fabricated with a silicon oxynitride core with a refractive index of 1.6, a core thickness of 0.7 μm, and an upper and lower cladding thickness of 3 μm based on the identification in Chapter 3 of these parameters as the optimum parameters for coupling to the InP/InGaAsP ridge waveguides.

The significant difficulty associated with the selectivity of the approximately 7 μm thick dielectric stack well etch was resolved with the use of a double hard mask approach (silicon dioxide was used to mask the polysilicon, which was used to mask the deep well etch) and a high selectivity etch was achieved with the addition of CHF_3 to the standard CF_4 etch chemistry.

InP/InGaAsP ridge waveguide pills were fabricated with a length of 300 μm. They were integrated in wells ranging in length from 307 to 312 μm. The maximum gap length was 7.9 μm. The minimum gap length was on the order of 400 nm.

Chapter 5

Waveguide Loss and Coupling Efficiency Results

This chapter details the results of the measurements that were taken to determine the interconnect and InP/InGaAsP waveguide propagation loss and the coupling between the interconnect waveguides and integrated III-V devices. The bulk of this information is obtained from transmission spectra (see Appendix A). Interpretations of these spectra and comparisons with the FDTD simulations of Chapter 3 are made. Analysis of this data yields the propagation loss for the interconnect waveguides and the InP/InGaAsP ridge waveguides. The data confirms the theorized conclusion that coupling across a gap is improved when the gap is filled with a high index material. This chapter concludes with the experimental demonstration of optical coupling between the interconnect waveguides and an integrated passive InP/InGaAsP pill, which is the ultimate result of this work.

At several points throughout this chapter, the analysis of the measured data is enhanced by the comparison of this data with the results of a Matlab program. The program was written to generate transmission spectra based on a model that makes use of the T-matrix discussed in Appendix A. Because the model is a physical model with inputs based on actual waveguide geometries and material properties, it plays a vital role in interpreting the measured data.

This chapter is organized into four sections. The first section details the results

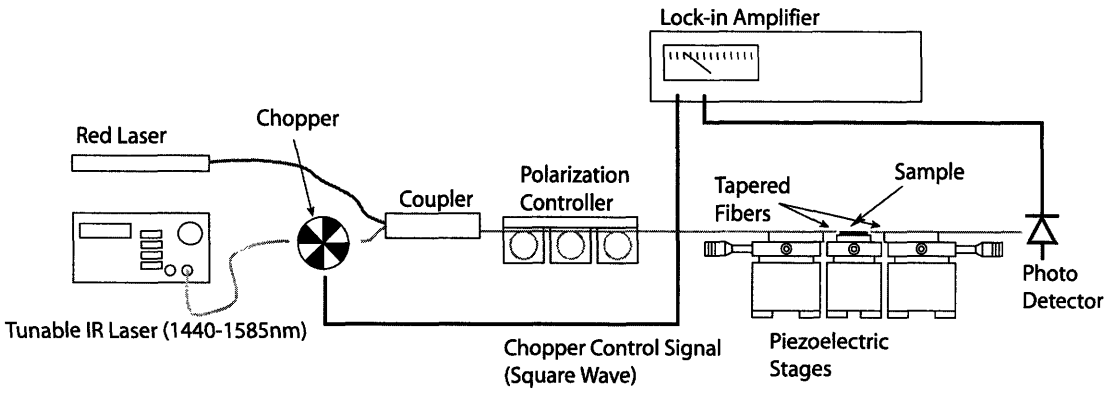

Figure 5-1: On-chip waveguide transmission measurement setup.

of the waveguide Fabry-Perot measurements to determine the propagation loss of the interconnect silicon oxynitride waveguides. The second section examines the properties of the InP/InGaAsP ridge waveguides for the case of conventionally cleaved facets with InP substrate intact and the micro-cleaved ridge waveguide pills. The third section deals with the analysis of the transmission measurements of interconnect waveguides with etched gaps. The final section concerns the aforementioned integrated pill measurements.

5.1 Silicon Oxynitride Interconnect Waveguide Loss Measurements

As discussed in the previous chapter, transmission spectra were used repeatedly to obtain information about the waveguides in this work. In this section, the propagation loss of the interconnect waveguides is measured as a function of waveguide width. The minimum measured loss is then compared with values for the propagation loss taken from the literature.

The setup shown in Figure 5-1 was used to measure the transmission spectrum for silicon oxynitride waveguides to determine the waveguide propagation loss. The measured spectrum for a single mode waveguide with a 1.7 μm wide core and a core thickness of 0.7 μm is shown in Figure 5-2.

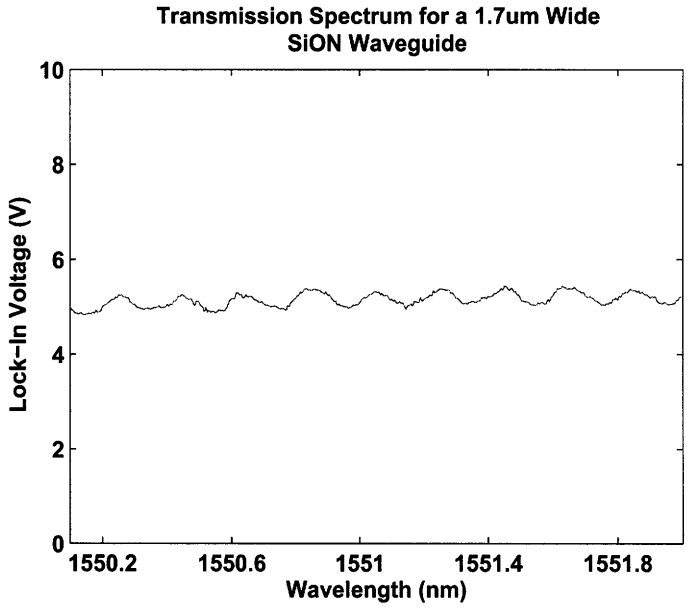

(a)

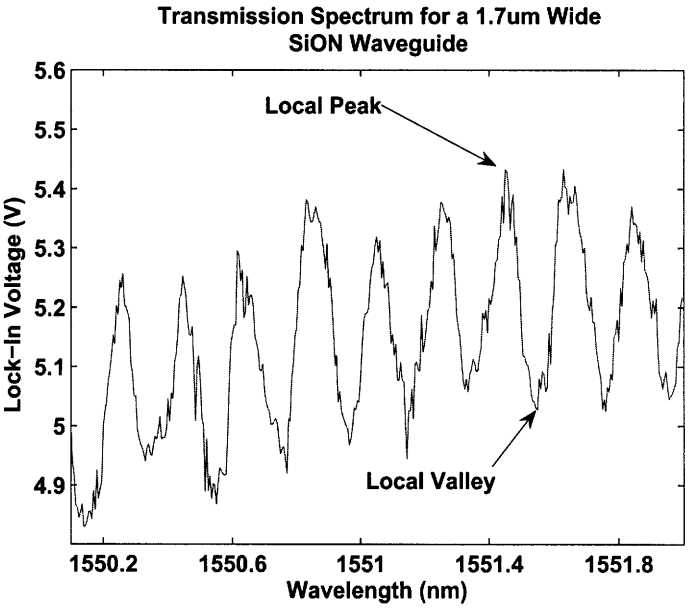

(b)

Figure 5-2: Transmission spectrum for a standard 4mm long silicon oxynitride interconnect waveguide with width 1.7 μm and thickness 0.7 μm: (a) Zoomed out. (b) Zoomed in.

5.1.1 Transmission Spectrum Period

Notice that there are approximately 10 periods of oscillation in the 2nm spectral range from 1550nm to 1552nm. A single period, then, is on the order of 2nm/10, or 0.2 nm. The following analysis shows that a period of approximately 0.2nm makes sense given the known length of the sample (4mm) and the expected effective index of the mode, 1.49 (calculated using a 2D modesolver).

A maximum in the spectrum occurs when the phase of the propagating mode is increased by an even multiple of 2π over one round trip (lengthwise) in the waveguide. The phase is found by multiplying the propagation vector, β by the propagation length, twice the length of the waveguide in this case. Equating this with an integer multiple of 2π,

$$\beta 2L = m2\pi \tag{5.1}$$

Expressing β in terms of the effective index:

$$\beta = \frac{2\pi n_{eff}}{\lambda} \tag{5.2}$$

Substituting β from Equation 5.2 in Equation 5.1 yields:

$$\frac{2Ln_{eff}}{\lambda} = m \tag{5.3}$$

and for the nearest shorter wavelength at which the phase is increased by $(m+1)2\pi$, the following holds

$$\frac{2Ln_{eff}}{\lambda'} = m + 1 \tag{5.4}$$

Solving for the difference between λ and λ',

$$\Delta\lambda = \lambda - \lambda' \tag{5.5}$$

$$\Delta\lambda = \frac{2Ln_{eff}}{m} - \frac{2Ln_{eff}}{m+1} \tag{5.6}$$

Substituting m from Equation 5.3 into Equation 5.6 and simplifying yields

$$\Delta\lambda = \lambda - \frac{2Ln_{eff}}{\frac{2Ln_{eff}}{\lambda} + 1} \tag{5.7}$$

Putting the length (4mm), effective index(1.49), and wavelength (1550) into this equation gives a $\Delta\lambda$ of 0.202, which is in agreement with the data in Figure 5-2.

Equation 5.7 is very useful when analyzing the transmission spectra for various structures because it can be used to extract an unknown parameter, the contributing cavity length or the effective index for instance, given the measured value for $\Delta\lambda$ at a given wavelength.

5.1.2 Estimation of Waveguide Propagation Loss

Given the measured peak/valley ratio (as in Figure 5-2) of the waveguide transmission spectrum, the calculated facet reflectivity, and the waveguide length, the propagation loss can be calculated using Equation A.11. In practice, as Figure 5-2b shows, the peak/valley ratio is difficult to determine exactly from the data as there is some noise. This noise can be attributed to the edge roughness of the waveguide core (see Reference [55]) in addition to mechanical vibrations and drift present in the measurement setup. An averaged result can be obtained by calculating the loss using the peak/adjacent valley ratio for each local peak and valley and then averaging these loss values to get an average loss. This was done for the spectrum shown in Figure 5-2 and for 10 other waveguides ranging in width from 0.7 to 1.6 μm. For each waveguide width, two waveguides were measured using this averaged loss technique and those two loss values were averaged to arrive at the data plotted in Figure 5-3. The data demonstrates the expected trend of reduced loss for wider waveguides. Again, this is expected because for wider waveguides, the field is lower at the rough core-cladding interface so less of the guided mode is scattered (Reference [55]).

The final conclusion from this data is that the lowest propagation loss can be achieved with 1.7 μm wide waveguides. In theory, a lower loss would be achieved at an even greater width as implied by the downward trend of the data. However, at a

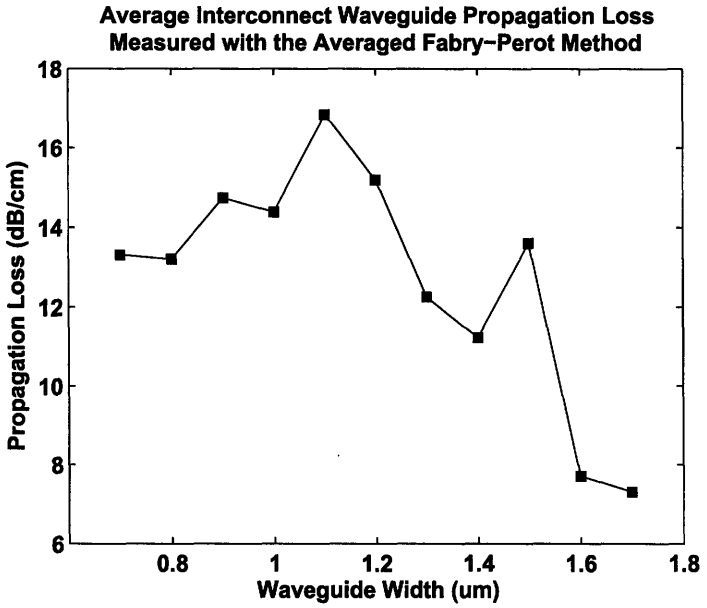

Figure 5-3: Propagation loss for interconnect waveguides measured using the averaged Fabry-Perot method. The data is the average of the loss for two waveguides at each width.

width of 1.7 μm, these waveguides are close to the cutoff of the second mode. Making the waveguides any wider would result in propagation of this second mode which is undesirable.

As shown in Figure 5-3, the averaged measured loss at the width of 1.7 μm is 7.3 dB/cm. This is quite high compared with record low propagation loss values on the order of 0.01 dB/cm taken from the literature (Reference [48]) for silicon oxynitride waveguides. However, it is consistent with the propagation loss values in the range of 0.1 dB/cm (Reference [48]) to 5 dB/cm (Reference [61]) for silicon oxynitride waveguides in which the primary goal of the work was not ultra low-loss propagation. In these papers, the processing techniques that were used were very similar to the techniques used for this work. In addition, the propagation loss values quoted above are for waveguides that are twice the size of the waveguides in this thesis. No reports were found for waveguides with comparable dimensions. The larger waveguide size can reduce the loss significantly as shown in Reference [55]. Finally, due to processing restrictions, the annealing temperature, which has a significant

effect on the propagation loss, was lower than the temperature used in the literature (Reference [77]) where it is shown that higher annealing temperatures result in lower waveguide propagation loss. For these reasons, a propagation loss of 7.3 dB/cm is reasonable and consistent with the literature.

5.2 InP/InGaAsP MQW Ridge Waveguide Transmission Spectra

The presentation and analysis of the transmission spectra for InP/InGaAsP multi-quantum well (MQW) ridge waveguides is given in this section. The stated ultimate goal of this thesis is the coupling of light through InP/InGaAsP ridge waveguide pills which have been integrated in wells etched into the interconnect waveguide stack. Before proceeding to that point, it is useful to characterize these ridge waveguides in isolation.

Two different structures are examined in this section. Both structures use the same epitaxial InP/InGaAsP MQW structure from Landmark Optoelectronics that was used throughout this thesis. The first structure is a simple ridge waveguide fabricated with a wet etch and cleaved with a conventional cleave technique to a length of 8 mm. Nothing else was done to these structures. They were not etched into pill devices. The InP substrate was left intact. These waveguides will heretofore be referred to as the conventionally cleaved ridge waveguides. The second structure is the individual isolated micro-cleaved waveguides with lengths of approximately 300 and 900 μ [1]. An estimation of the ridge waveguide fundamental mode propagation loss is given in this section. Through the analysis of the transmission spectra for the isolated pills, a better understanding of how light travels in the pills will be gained.

[1]The 900 μ long devices were actually three connected pills for which the outer facets cleaved, but the two inner facets did not cleave.

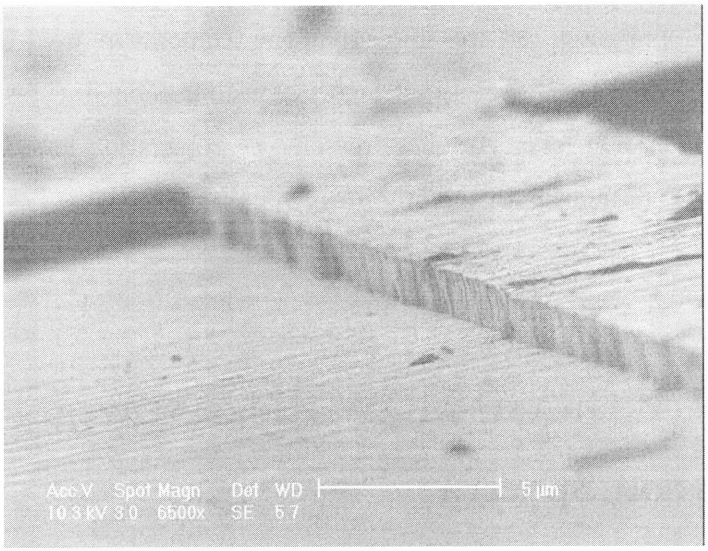

Figure 5-4: Wet etched InP/InGaAsP waveguide ridge. The width of this waveguide is 8 μm.

5.2.1 Analysis of the Conventionally Cleaved Ridge Waveguide Transmission Spectra

The analysis of the conventionally cleaved ridge waveguides is complicated by the absorbing quantum well layers and by the fact that the waveguides that were analyzed were multimode waveguides. Figure 5-4 is an SEM of the etched waveguide ridge showing that it is 8 μm wide, which is certainly wider than the 2 μm width necessary for single mode operation. The result of the absorption is a variation in the propagation loss over the measured spectrum, and the result of the multiple propagating modes is mode beating or mode interference. Both of these effects can be seen in the measured transmission spectrum in Figure 5-5.

Absorption in the Quantum Well Structure

The integrated InP/InGaAsP ridge waveguide structure is shown in Figure 5-6. The quantum wells, which provide gain when activated via a current, are instead absorbing when in a passive state as is the case for this work. Figure 5-5b is a close-up of the transmission spectrum for this ridge waveguide in the wavelength range from 1500-

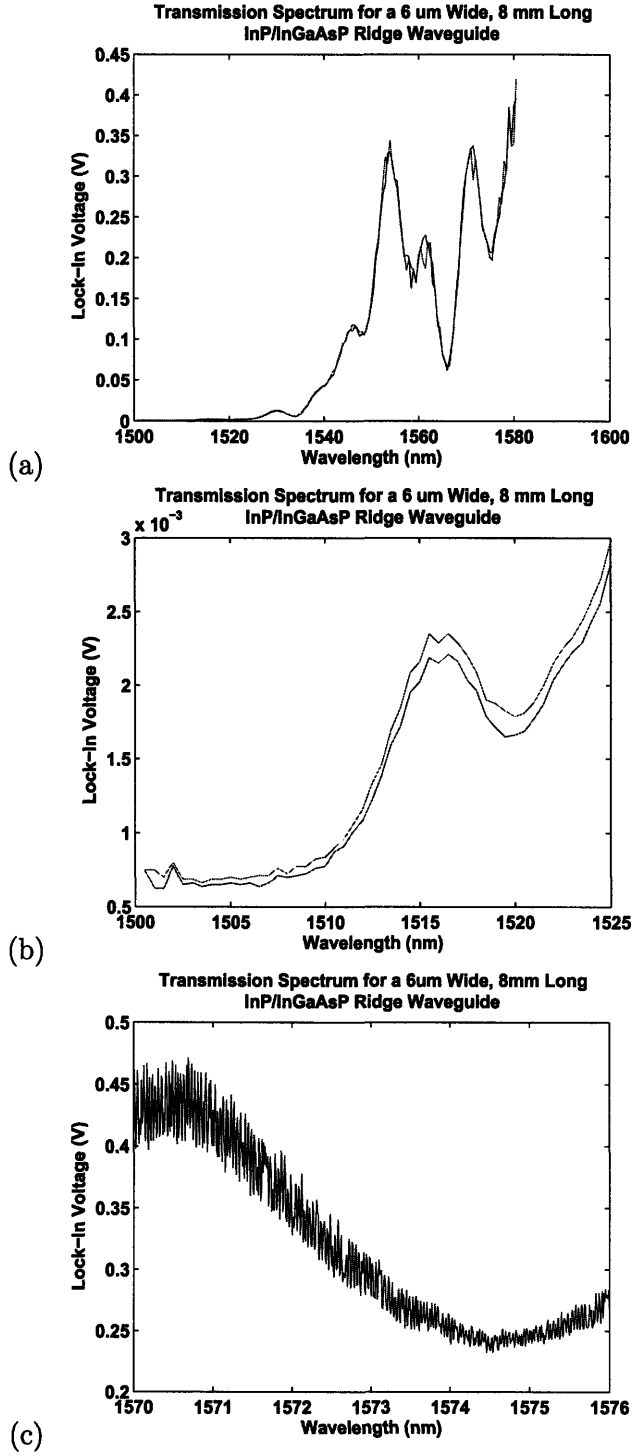

Figure 5-5: Conventionally cleaved InP/InGaAsP ridge waveguide transmission spectrum: (a) Full measured spectrum. (b) Zoomed in to examine the shorter wavelength part of the spectrum. (c) Higher resolution measurement of the longer wavelength part of the spectrum.

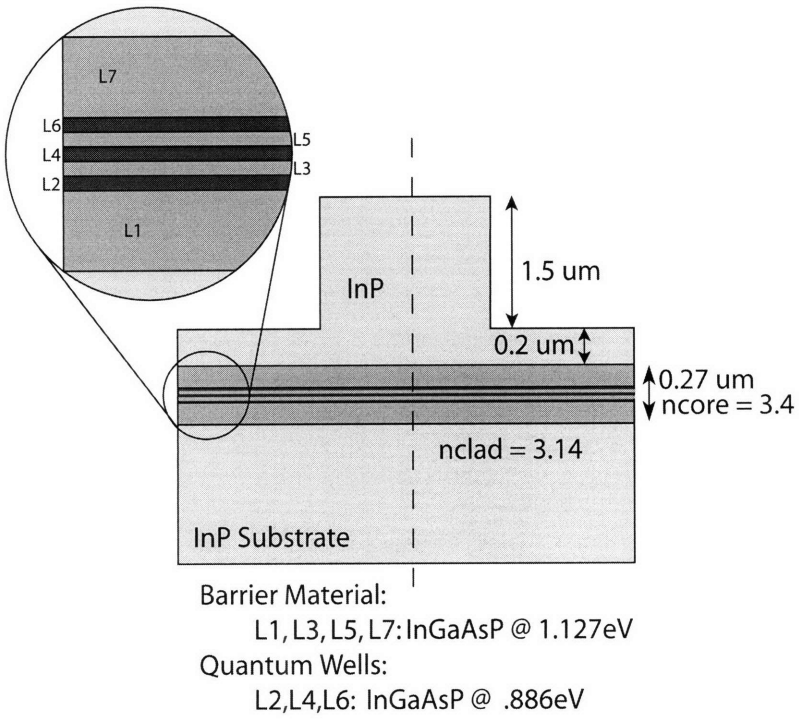

Figure 5-6: Cross-section of the InP/InGaAsP ridge waveguide material from Landmark Optoelectronics.

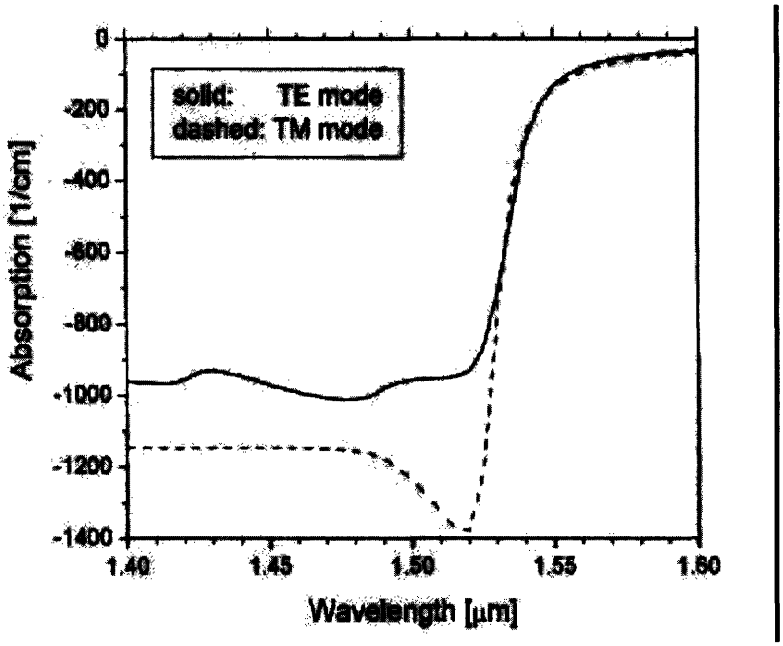

Figure 5-7: Measured absorption spectrum for TE and TM modes of an InP/InGaAsP MQW structure used as an electro-absorption modulator (taken from Reference [78]).

1525 nm. Notice that the measured lock-in voltage is nearly 3 orders of magnitude smaller in the vicinity of 1500 nm relative to values near 1580 nm. This increased propagation loss at shorter wavelengths is due to absorption by the quantum well structure. The peak in the gain for this structure is designed to be at 1550 nm, so it is expected that the absorption edge is in the vicinity of 1550nm. A calculated absorption spectrum for a similar InP/InGaAsP MQW structure taken from Reference [78] is shown in Figure 5-7. Notice the sharp transition at 1520 to 1530 nm[2].

A clear, sharp transition in the vicinity of 1550 nm is not seen in the measured transmission spectrum of Figure 5-5 because the transition is obscured by the interference of the multiple guided modes. In Section 5.5, the transmission through integrated InP/InGaAsP ridge waveguide pills will be examined, and the presence of

[2]It is tempting to use this absorption spectrum to calculate the difference in absorption loss at short and long wavelengths for an 8 mm long waveguide to see if the 3 orders of magnitude difference measured for the waveguides in this work is consistent with this spectrum. However, the absorption in Figure 5-7 is the material absorption and does not take into account the overlap of the mode with the quantum well regions (often referred to as Γ_{QW} in the literature). This would make the magnitude of the modal absorption lower than the values in the figure.

this wavelength dependent absorption will be used as an indicator that light is indeed propagating in the quantum well structure.

5.2.2 Multimode Behavior

Beyond the vicinity of the absorption edge, at wavelengths greater than 1550 nm, the transmission spectrum in Figure 5-5 has peaks separated by approximately 8nm. These peaks are not due to the waveguide cavity as seen in a typical Fabry-Perot transmission spectrum. If that were the case, they would be spaced at approximately 0.045 nm (for an 8 mm long waveguide cavity with an effective index of 3.3, calculated using Equation 5.7). It is hypothesized that they are due, instead, to interference of the various modes of the InP/InGaAsP ridge waveguide structure.

In order to see if this 8 nm period is consistent with the effective indices of the ridge waveguide modes, a 2D modesolver[3] was used to determine the modal properties of the ridge waveguide structure. The input to the modesolver is the cross-sectional geometry and refractive index information for the ridge waveguide structure as well as the desired number of computed modes. The output is the effective index for each mode, the loss for each mode[4], and a plot window containing four separate plots (Figure 5-8). The upper left hand plot is the cross-section of the ridge waveguide (where areas with different refractive indices have different shading), the upper right hand plot and the lower left hand plot are respectively the real part of the x-oriented and y-oriented electric field. The lower right hand plot is useful in determining where power is flowing in the lateral direction (i.e. towards the edges of the simulation window). If it is present inside the waveguide, then there is no loss, as this is just the wave propagating in the waveguide at a slight angle to the z direction. If it is present outside of the waveguide, as in Figure 5-8b, then there is loss.

The modesolver simulation shows that the zero-order TE mode has an effective

[3]This 2D modesolver is a Matlab program written by Milos Popovic

[4]If perfectly matched layers (see Reference [64] for more on perfectly matched layers or PMLs) are used at the boundaries of the cross-section simulation window, the modesolver will find modes with complex propagation vectors. The imaginary part of the vector determines the loss. The presence of loss for a computed mode means that the mode is a lossy mode (see Reference [49] for a formal discussion of lossy modes) or unguided mode.

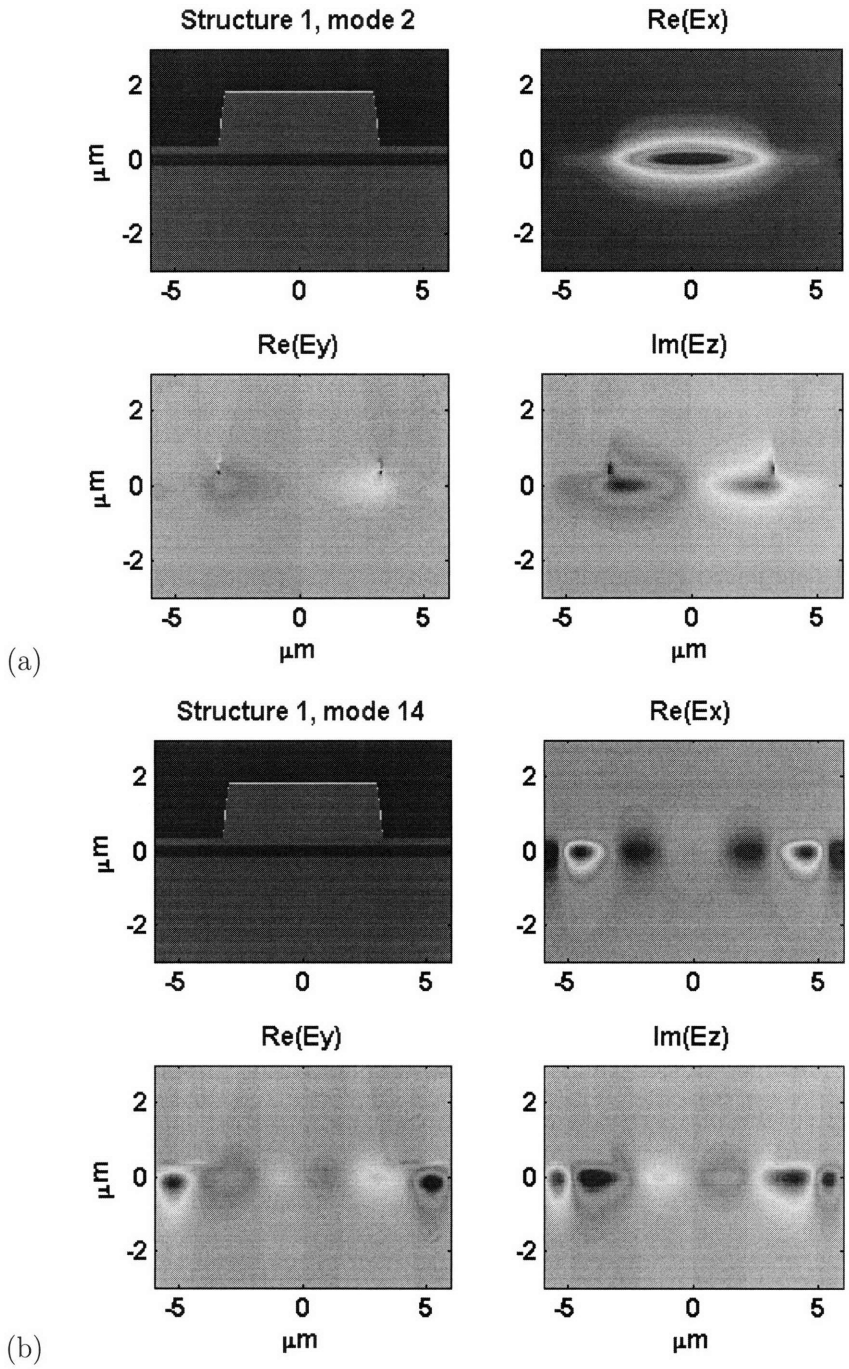

Figure 5-8: 2D modesolver output plot window showing the properties of the (a) fundamental quasi-TE mode for the InP/InGaAsP ridge waveguide structure and (b) a higher order lossy mode. In each set of four plots, the upper left hand plot is the cross-section of the ridge waveguide, where areas with different refractive indices have different shading. The core of the ridge waveguide structure can be seen as the thin, wide dark stripe centered vertically at 0 μm. The upper right hand plot and the lower left hand plot are respectively the real part of the x-oriented and y-oriented electric field. The field max/min appear as the dark regions. The lower right hand plot is useful in determining where power is flowing in the lateral direction (i.e. towards the edges of the simulation window). If it is present inside the waveguide, as in set (a), then there is no loss, as this is just the wave propagating in the waveguide at a slight angle to the z direction. If it is present outside of the waveguide, as in set (b), then there is loss.

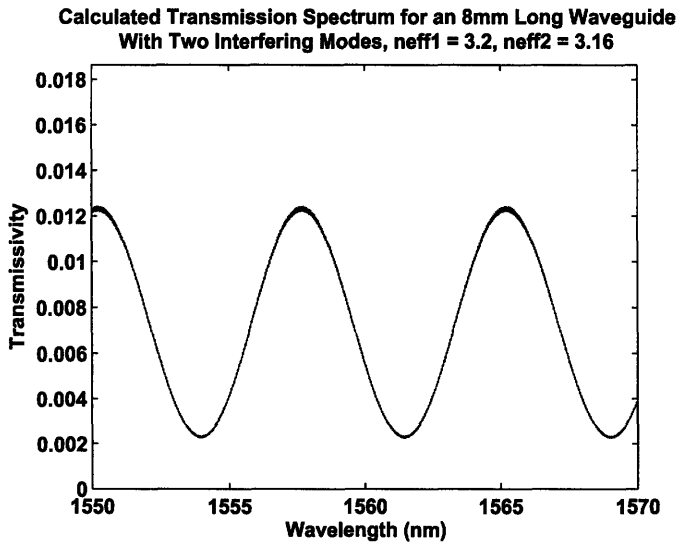

Figure 5-9: Calculated transmission spectrum for a waveguide cavity with two interfering modes.

index of 3.2, and that the highest order guided mode has an effective index of 3.16. There are 7 guided modes all together. This makes the transmission spectrum more complicated than the simple single mode Fabry-Perot transmission spectrum. In Appendix A the electric field transmission coefficient is found as a function of wavelength (i.e. the transmission spectrum) for this simple single mode case. To model the effects of two or more modes, the field transmission coefficient must be found for each mode. The total transmission spectrum taking into account all of the modes is then found by summing the individual transmission coefficients and squaring the magnitude of the total. That is,

$$T_{total}(\lambda) = \left| \sum_{m=1}^{M} S_{21,m} \right|^2 \tag{5.8}$$

where M is the number of modes, and $S_{21,m}$ is the electric field transmission coefficient for the m^{th} mode. S_{21} is the S-parameter which is the ratio of the transmitted field strength to the incident field strength. This is used instead of T because T is used to represent the modal Fresnel transmissivity.

Figure 5-9 shows the result of the calculation in Equation 5.8 for the two modes with effective indices of 3.2 and 3.16. Notice that the peaks are separated by 8nm, the

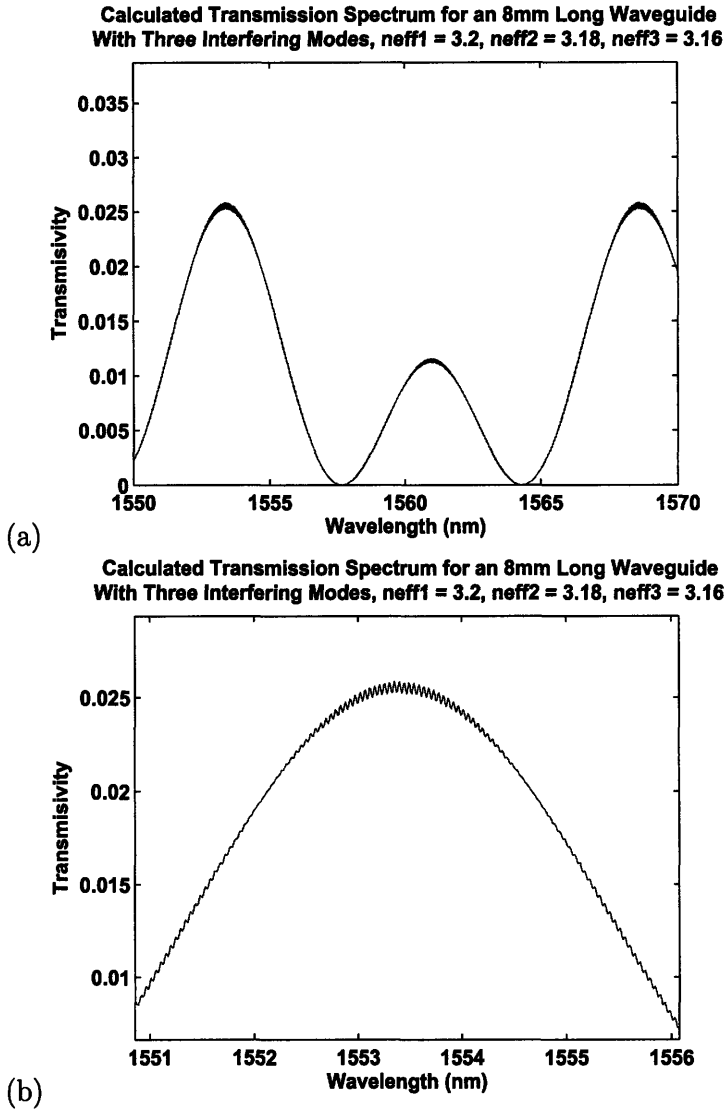

Figure 5-10: (a) Calculated transmission spectrum for a waveguide cavity with three interfering modes. (b) Close-up of part of the spectrum showing the "fast" oscillations which is a cavity resonance effect seen in the standard Fabry-Perot transmission spectrum. The period of these oscillations is much shorter than the period of the multi-mode interference oscillations.

same as the separation of the peaks in the measured transmission spectrum in Figure 5-5. The spacing of the peaks is a function of the length of the cavity and the difference between the effective indices of the interfering modes. The shorter the cavity and the smaller the difference in effective index, the greater the spacing between the peaks. This means that the shortest observable period is due to interference between the modes with the greatest difference in effective index, 3.2 and 3.16. So when looking at an 8nm range of the spectrum, the observable periodic behavior is due to the interference of these two modes only, permitting the use of a model that considers only 2 modes.

Of course, the measured spectrum in Figure 5-5 has more structure than the simple calculated spectrum of Figure 5-9. This is because there are more than just two interfering modes in the actual transmission spectrum. Figure 5-10a shows the results of Equation 5.8 in which three interfering modes contribute to the overall transmission spectrum. From this calculated spectrum, it is easier to see how the measured transmission spectrum could be composed of several interfering modes. Based on the modesolver results, the InP/InGaAsP ridge waveguide has 7 guided modes. It is a combination of these modes that makes up the total transmission spectrum as seen in Figure 5-5.

Approximating Propagation Loss in Multimode Waveguides

Figure 5-10b is a close-up of the calculated spectrum of Figure 5-10a revealing the short period oscillations in the simulated InP/InGaAsP ridge waveguide spectrum. These are the typical Fabry-Perot resonances that are the result of the reflecting end facets of the waveguide, the period of which is determined by Equation 5.7. In the case of a single mode guide with no higher order interfering modes, the peak/valley ratio of these shorter period oscillations can be used to determine the loss of the mode. This is done using the Fabry-Perot loss equation, Equation A.11, as was discussed in Section A.2. However, because of multimode interference which adds long period oscillations to the spectrum, it is difficult to extract a peak/valley ratio. And if one takes the local peak to valley ration, the ratio varies leading to varying results. This is,

of course, because the loss equation was derived from the Fabry-Perot transmissivity for a single mode. Therefore, it is necessary to consider the transmissivity for two modes, to see if it is possible to determine an approximate value for the propagation loss of the two interfering modes.

The Fabry-Perot transmission coefficient which was derived in Section A.2 using T-matrices is repeated here.

$$S_{21} = \frac{t^2 e^{i\underline{\beta}L}}{1 - r^2 e^{2i\underline{\beta}L}} \tag{5.9}$$

where S_{21} is the standard field transmission S-parameter for the m^{th} mode, $\underline{\beta}$ is the complex propagation vector defined in Equation A.9, L is the cavity length, and r and t are the fresnel reflection and transmission coefficients found from the effective index of the m^{th} mode. The right side of Equation 5.9 can be rewritten in terms of a real and imaginary part, F and G respectively.

$$t_m = F_m + iG_m \tag{5.10}$$

where

$$F_m = \frac{A_m cos\left(\beta_m L\right)}{\left[A_m cos\left(\beta_m L\right)\right]^2 + \left[B_m sin\left(\beta_m L\right)\right]^2} \tag{5.11}$$

and

$$G_m = \frac{-B_m sin\left(\beta_m L\right)}{\left[A_m cos\left(\beta_m L\right)\right]^2 + \left[B_m sin\left(\beta_m L\right)\right]^2} \tag{5.12}$$

where

$$\beta_m = \frac{2\pi n_{eff,m}}{\lambda} \tag{5.13}$$

and

$$A_m = \frac{1 - R_m e^{-2\alpha_m L}}{T_m e^{-\alpha L}} \tag{5.14}$$

$$B_m = \frac{-1 + R_m e^{-2\alpha_m L}}{T_m e^{-\alpha L}} \tag{5.15}$$

When the transmission spectrum is measured experimentally, it is the power, or transmissivity, that is actually measured. For a single mode, the transmissivity is

just the square of the magnitude of S_{21}.

$$|S_{21}|^2 = F^2 + G^2 \tag{5.16}$$

The transmissivity for two interfering modes can be written out using Equation 5.8.

$$|S_{21}|^2_{1,2} = |(F_1 + iG_1) + (F_2 + iG_2)|^2 \tag{5.17}$$

$$|S_{21}|^2_{1,2} = |(F_1 + F_2) + i\,(G_1 + G_2)|^2 \tag{5.18}$$

$$|S_{21}|^2_{1,2} = (F_1 + F_2)^2 + (G_1 + G_2)^2 \tag{5.19}$$

$$|S_{21}|^2_{1,2} = F_1^2 + 2F_1F_2 + F_2^2 + G_1^2 + 2G_1G_2 + G_2^2 \tag{5.20}$$

$$|S_{21}|^2_{1,2} = |S_{21}|^2_1 + |S_{21}|^2_2 + 2\,(F_1F_2 + G_1G_2) \tag{5.21}$$

where $|S_{21}|^2_{1,2}$ is the total transmissivity for the two modes and $|S_{21}|^2_1$ and $|S_{21}|^2_2$ are the transmissivity for Mode 1 and Mode 2 respectively. The actual measured spectrum is the sum of the spectra for the two individual modes and the cross-product term.

At this point, it is useful to summarize what has been done so far in this section. It was noted that the Fabry-Perot loss equation yields varying results when applied to the Fabry-Perot transmission spectrum of a multimode waveguide. In an effort to understand how the spectrum changes with the addition of a second mode, the transmissivity was derived for the case of two modes by squaring the sum of the two individual field (as opposed to power) transmission coefficients. The result of this derivation is Equation 5.21. This equation was then applied to a waveguide with parameters similar to those of the ridge waveguide sample used to generate Figure 5-5. The goal was to obtain a calculated spectrum using this equation that has a similar shape to the part of the spectrum shown in Figure 5-5c. Through trial and error parameter selection, this goal was achieved and the calculated spectrum is shown in Figure 5-11b. Notice the close agreement between the measured and simulated data. This exercise shows that the measured transmission spectrum corresponds, at least qualitatively, with the calculated spectrum for two interfering modes with

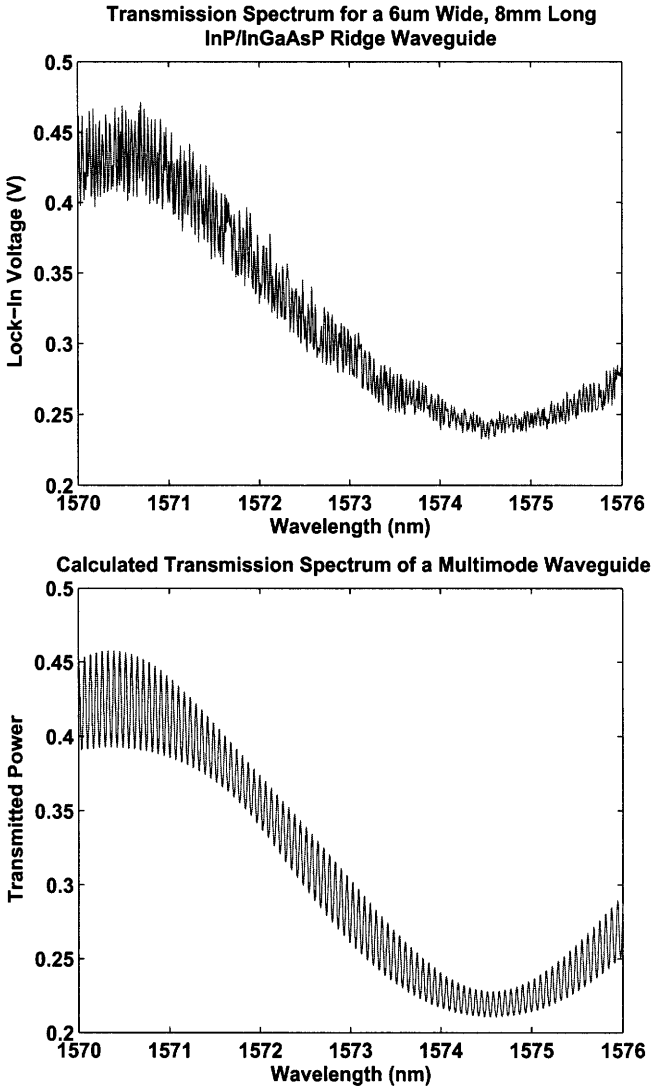

Figure 5-11: (a) Measured InP/InGaAsP ridge waveguide transmission spectrum in which both the Fabry-Perot (short period) and multimode oscillations (~8 nm period) can be seen. (b) Calculated (with Equation 5.21) transmission spectrum for the same part of the spectrum as in (a) with a similar shape. This calculated spectrum was obtained with the following parameters: $n_{eff,1} = 3.2$, $n_{eff,2} = 3.17$, $loss_1 = 15$ dB/cm, $loss_2 = 20$dB/cm, and a ratio of input fiber power coupled into mode1 to input fiber power coupled into mode2 of 5:1.

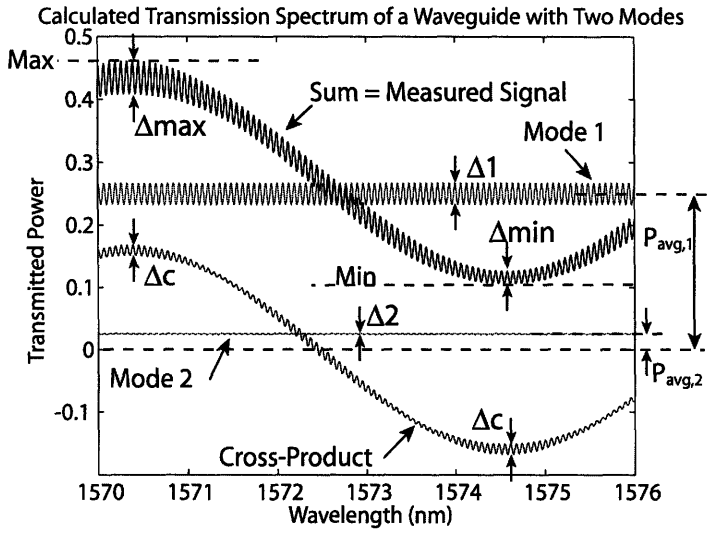

Figure 5-12: Calculated transmission spectrum (labelled *Sum*) for a waveguide with two modes shown with the three constituent parts of this spectrum. These three parts are taken from the right hand side of Equation 5.21 and are the transmissivity for mode 1, the transmissivity for mode 2, and the cross-product term. This spectrum is the same as the spectrum plotted in Figure 5-11b.

$n_{eff,1} = 3.2$, $n_{eff,2} = 3.17$, $loss_1 = 15$ dB/cm, $loss_2 = 20$dB/cm. It makes sense that the higher order, lower effective index mode, would have a slightly higher loss than the fundamental mode. Also, the coupling from the input fiber to the fundamental mode should be higher than the coupling into the higher order more diffuse mode. However, Figure 5-11 is not meant to imply that these parameters are the exact parameters that existed in the measured waveguide.

The next step is to see if there is a way to extract the known fundamental mode propagation loss of 15 dB/cm from the simulated spectrum of Figure 5-11. The idea is that if this can be done, the same method could be applied to the measured data to extract the propagation loss of the fundamental mode for the actual measured waveguide. The calculated spectrum of Figure 5-11b is plotted in Figure 5-12 along with the three terms on the right hand side of Equation 5.21, which summed together, make up the spectrum of Figure 5-11b.

To determine the mode loss using the single-mode Fabry-Perot loss equation (Equation A.11), one must extract the $Mode_1$ and $Mode_2$ signals from, *Sum*, the

signal that is actually measured. The actual parameters that must be extracted are Δ_1, Δ_2, $P_{avg,1}$, and $P_{avg,2}$. These parameters can then be used to calculate the peak-to-valley ratio for each mode as

$$K = \frac{P_{avg,m} + \Delta_m}{P_{avg,m} - \Delta_m} \tag{5.22}$$

This peak-to-valley ratio parameter, K, is the parameter that is required in Equation A.11.

At the maximum of the cross-product term, the individual mode transmissivity spectra are in phase with each other and the cross-product term and all three components add constructively. At the minimum of the cross-product term, the individual mode transmissivity spectra are in phase with each other, but are 180^o out of phase with the cross-product term. Based on this observation, the following equations can be written[5].

$$\Delta_1 + \Delta_2 + \Delta_c = \Delta_{max} \tag{5.23}$$

$$\Delta_1 + \Delta_2 - \Delta_c = \Delta_{min} \tag{5.24}$$

Summing these two equations and dividing by two yields

$$\Delta_1 + \Delta_2 = \frac{\Delta_{max} + \Delta_{min}}{2} \tag{5.25}$$

The sum of the average transmitted power for the two modes is equal to the "DC" offset of the measured signal. This offset is the average of the background long period oscillation in the measured signal.

$$P_{avg,1} + P_{avg,2} = \frac{\left(Max_{meas} - \frac{\Delta_{max}}{2}\right) + \left(Min_{meas} - \frac{\Delta_{max}}{2}\right)}{4} \tag{5.26}$$

[5]The proof of these equations follows from the simplification of Equation 5.21, where F_m and G_m are defined in Equations 5.11 and 5.12.

Applying Equations 5.25 and 5.26 to the spectrum of Figure 5-11b yields the following,

$$\Delta_1 + \Delta_2 = 0.0364 \tag{5.27}$$

$$P_{avg,1} + P_{avg,2} = 0.2756 \tag{5.28}$$

The sum of the required parameters for the two modes has been extracted. Another two equations are required to extract the individual parameters for each mode. At this point, however, an approximation can be made for the case in which there is a large disparity in the power of the two modes, which can be caused by a disparity in the propagation loss and/or the input power coupled into the particular mode. This is assumed to be the case for the two modes contributing to the interference in the measured spectrum of Figure 5-11. Assuming that both Δ_2 and $P_{avg,2}$ are small relative to Δ_1 and $P_{avg,1}$ respectively, they can be ignored in Equations 5.27 and 5.28 above. An approximate calculation of the loss using the standard single-mode Fabry-Perot loss equation (Equation A.11) with $\Delta_1 = 0.364$ and $P_{avg,1} = 0.2756$ results in a fundamental mode loss of 15.34 dB/cm. Recall from the caption of Figure 5-11 that the actual loss for this mode was 15 dB/cm, so this is good approximation. Of course, in order to use this approximation in the first place, one must be able to assume that there is a disparity between power of the two modes. This is the case for the two modes in the measured spectrum.

Waveguide Loss Conclusions

The important final step is to use the above method to find the approximate propagation loss of the fundamental mode of the InP/InGaAsP ridge waveguide based on the data in Figure 5-11a. The result of this calculation is 9.6 dB/cm. Recall that this is the loss found at a wavelength of approximately 1570 nm (the wavelength range of the data was 1570 to 1576 nm). At this wavelength, it is expected that the multi-quantum well absorption is relatively low and that this propagation loss is due to a combination of absorption and scattering from the rough wet etched ridge sidewalls.

Earlier in this section, it was determined experimentally that the lowest average

propagation loss for the silicon oxynitride interconnect waveguides was approximately 7.3 dB/cm. This was for a waveguide width of 1.7 μm.

5.3 Gap Measurement Results

Throughout this thesis, there has been much discussion of the effect of the gap between the etched well edge and the integrated III-V device (shown again in Figure 5-13a). Figure 5-13b shows the etched gaps in a previously continuous interconnect waveguide. The measurement of the etched gaps is important as it provides a means to measure the best case scenario for coupling, as there can be no lateral or vertical misalignment on either side of the gap given a continuous interconnect waveguide prior to the gap etch. The etched gaps also allow for control of the gap length so that the effect of gap length can be measured. Finally, by comparing the results of the measurements of these gaps with the FDTD simulations, the effect of scattering due to the roughness of the etched facet can be examined, as this was not modelled by the FDTD simulations. In other words, it is expected that the measured gap losses will be greater than the FDTD modelled gap losses by an amount that can be contributed to the rough etched sidewall. If the measured and simulated values are similar, it can be assumed that the rough etch does not significantly contribute to the coupling loss.

Figure 5-14 shows the arrangement of the etched gaps. Five different gap lengths (1-5 μm) were measured, and for each gap length, waveguides with 1, 2, 3, and 4 gaps were fabricated. That is, in total, 20 different waveguides were fabricated with etched gaps and measured to determine the gap loss for each length.

In addition to these air-filled gaps, gaps filled with silicon rich nitride with an index of refraction of 2.2 and gaps filled with index matching gel with an index of refraction of 1.52, were measured. Finally, air-filled gaps in which the waveguide on one end of the gap is shifted sideways in the wafer plane by 0.45 μm and 0.9 μm were also measured. The results are shown and discussed in this section.

This section is segmented into three subsections. The first subsection demonstrates the impact of the presence and location of the gap on the measured trans-

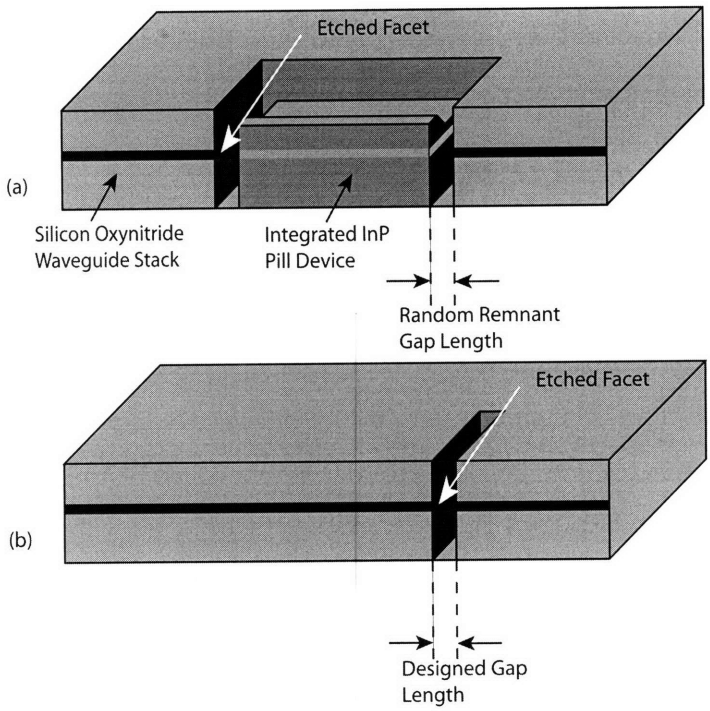

Figure 5-13: (a) Cross-section of an integrated pill where the gap exists because the well is slightly longer than the integrated InP pill device. The etched facet is created as a result of the deep well etch. (b) In order to determine the effects of the etched facet and the gap, the etched gap feature was replicated via a narrow etch (essentially a very short well). This is the gap to which this section refers.

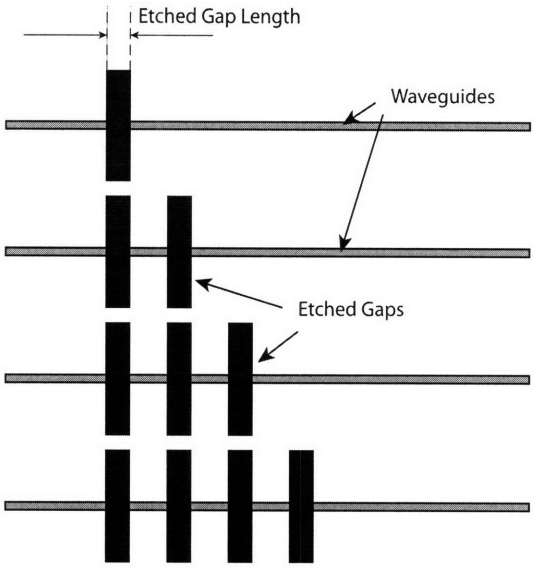

Figure 5-14: Illustration of the gap layout. The transmission through each waveguide was measured in succession and the measurements were compared to extract the gap loss. The details of the gap layout are important because the location of the gap relative to other gaps and the end facets affects the measured transmission spectrum.

mission spectrum by showing results obtained from a Matlab script that was written to model the transmission of multiple cavities (see Appendix A for an explanation of the model that was used and Appendix D for the Matlab code itself).

The second subsection discusses the effect of multi-mode interference on the transmission spectra. This subsection is essentially a reiteration of Section 5.2.2. It is included to stress that the transmission spectra in this section are affected by both the multiple gaps and multiple interfering modes.

5.3.1 Multiple Fabry-Perot Cavities

When one or more gaps are etched into a waveguide segment, the entire structure containing the separate waveguide segments and the gaps contributes to the overall shape of the transmission spectrum. Take for instance, a 4 mm long waveguide segment into which a 1 μm gap is etched at the center of the waveguide. This creates two separate waveguide segments 2 mm in length, separated by the 1 μm gap. Where

there was one 4 mm Fabry-Perot cavity, there are now two 2 mm long cavities and one 1 μm long cavity. The goal of these gap measurements is to determine the coupling loss across the gap by comparing the measured transmitted power at a certain wavelength for 1, 2, 3, and 4 gaps of a given length and then to extract the loss from this data. The problem is that the multiple Fabry-Perot cavities of varying arrangement for a waveguide with one gap versus a waveguide with four gaps (see Figure 5-14) can have very different transmission spectra, and it is misleading to compare measured transmission values at a single wavelength for waveguides with different numbers of gaps. Rather, an entire transmission spectrum must be taken so that values can be taken from comparable parts of the transmission spectrum, rather than at just a single wavelength.

In addition to the presence of multiple cavities, it is possible to have interfering modes. While the interconnect waveguides are designed to be single mode, there are some lossy modes that may result in the presence of mode beating in the measured spectrum.

In order to model the effects of multiple cavities on the transmission spectrum, a Matlab script was written to calculate the transmission matrix for a structure of arbitrary complexity. The input to the script is the number of segments and a set of parameters for each segment: the index of refraction of the material (or in the case of waveguides, the effective index of the waveguide mode), the length of the material segment, and the propagation loss (or gain) of the segment. To model the effects of m number of modes modes, the input index of refraction of the material and the input loss are arrays of length m containing the effective index and propagation loss of the contributing modes. Consequently, the script can handle multiple modes interfering in an arbitrarily complex structure. The results of this script were discussed in Section 5.2.2. It was used to find the multimode interference patterns in Figure 5-9 and Figure 5-10.

As a first pass in demonstrating the utility of this script, a comparison of the calculated transmission spectrum for a single mode waveguide with one, two, and three 5 μm long gaps is shown in Figures 5-15 through Figure 5-17. For each case, the

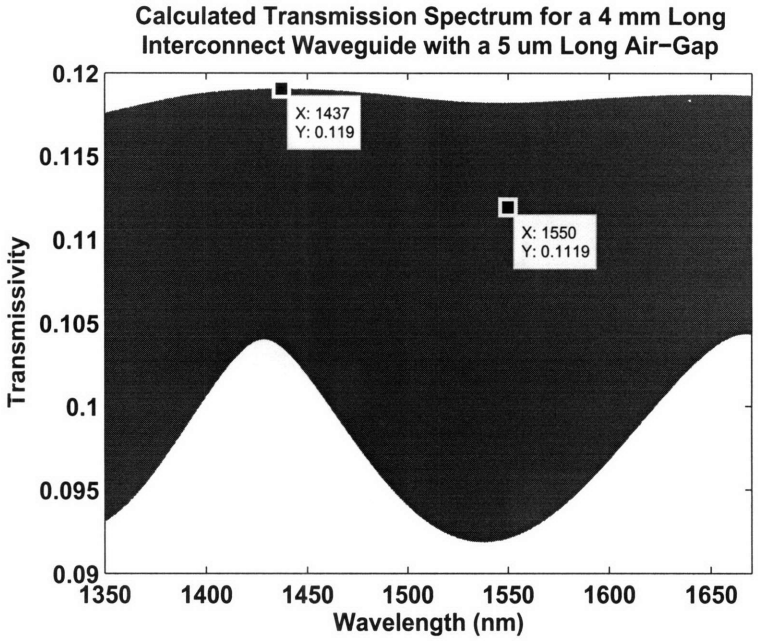

Figure 5-15: Calculated transmission spectrum for an interconnect waveguide cavity with one 5 μm gap. The spectrum is purposely shown at a scale at which the individual oscillations cannot be seen so that the variations over a much larger wavelength range can be seen. The long range oscillation with a period of approximately 280 nm is a result of the 5 μm gap. The two labels show the maximum transmissivity and the transmissivity at 1550 nm.

total structure length is 4 mm, the effective index of the mode is 1.49, the propagation loss in the interconnect waveguide is taken to be 10dB/cm, and the propagation loss[6] in the unguided gap segment is taken to be 1dB/μm.

[6]What really happens in the gap is that there is coupling loss in going from the fundamental mode of the guide on one end of the gap to the fundamental mode of the guide on the other end of the gap. The amount of coupling loss depends on the mode spreading in the gap and the overlap of this spread mode with the interconnect waveguide on the far end of the gap. It is not the case that this process of mode spreading and then coupling varies exactly exponentially with distance (gap length). It is not exact, therefore, to model the gap as a medium with the standard exponentially decaying signal (i.e. a constant loss in dB/cm). However, looking back at the FDTD simulation results for coupling across a gap, the log of the coupled power is nearly linear, so it is safe to use this model of exponential decay as an approximation. The given value of 1 dB/μm for the propagation loss in the gaps is consistent with these FDTD simulations. The goal of this model, after all, is to quickly gain some insight into the expected shape and magnitude of the transmission spectrum for these long structures with a varying number of gaps . It would be very time consuming (and most likely impossible on a standard PC) to model these waveguides and gaps using the FDTD algorithm.

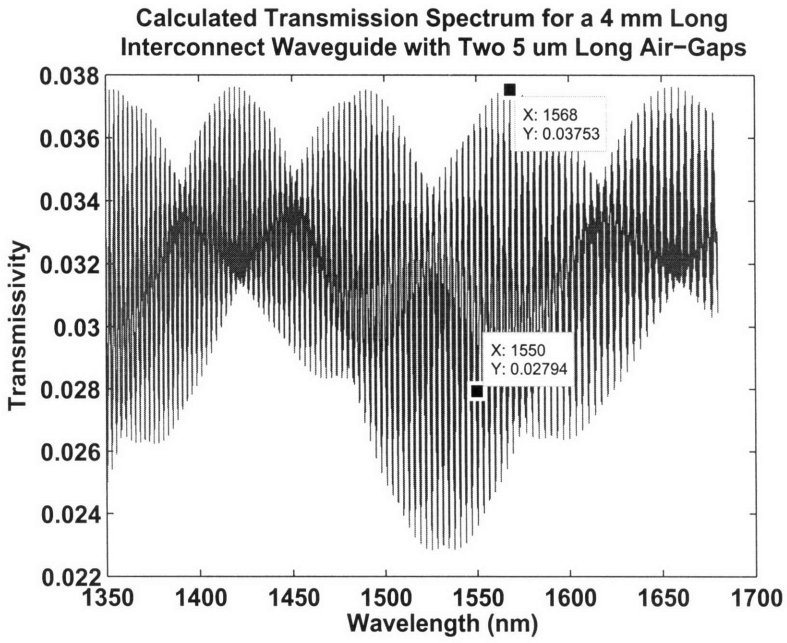

Figure 5-16: Calculated transmission spectrum for an interconnect waveguide cavity with two 5 μm gaps.

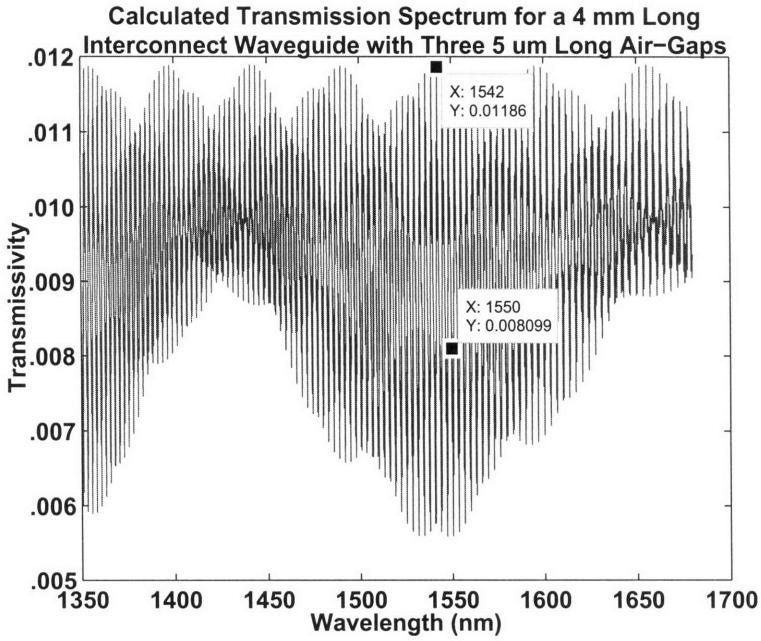

Figure 5-17: Calculated transmission spectrum for an interconnect waveguide cavity with three 5 μm gaps.

Extracting the Gap Loss

In theory, it should be possible to extract the gap loss from the transmission spectra for the waveguides with one, two, and three 5 μm gaps shown in Figures 5-15, 5-16, and 5-17. Because of the resonances, however, one could arrive at the wrong value if only a small part of the spectrum is examined, or even worse, only a single wavelength is used. Each of these figures has two labels, one showing the maximum transmissivity near 1550 nm, and another showing the transmissivity at exactly 1550 nm. The loss per gap in dB can be extracted using the following equation:

$$GapLoss = \frac{10log\left(\frac{T_{max,n}}{T_{max,m}}\right)}{n-m} \tag{5.29}$$

where $n > m$ and $T_{max,n}$ is the maximum measured transmissivity for a waveguide with n gaps, and $T_{max,m}$ is the same for a waveguide with m gaps. Using the data at the maximum of the single gap and double gap, the loss is calculated as 5.013 dB per gap. Using the data from the maximum of the double gap and the triple gap, the loss is calculated as 5.002 dB. This checks with the input data which was 1 dB/μm for 5 μm gaps, or 5 dB per gap. If only the values taken at exactly 1550 nm were used, the extracted losses would have been 6.03 and 5.38 dB/gap. This is not an overly significant difference, but a difference nonetheless. It is necessary, therefore, to take full transmission spectra when measuring the gaps, rather than just the transmission at a single wavelength. Again, comparisons of the spectra for the purpose of calculating the gap loss should be made between similar parts of the spectrum (i.e. compare peaks in one spectrum with peaks in the other spectrum). The validity of this approach will be examined in Section 5.3.3.

5.3.2 Multi-Mode Interference

After examining, in the previous section, the calculated transmission spectra for waveguides with gaps, it is clear that the presence of the multiple Fabry-Perot cavities requires that a wide transmission spectrum be measured, rather than just transmis-

sion at a single wavelength. In this section, an additional complication is examined. While the interconnect waveguides are single mode guides, it appears from the measurements that some of the higher order lossy modes or cladding modes are interfering with the fundamental mode. Even if a waveguide is a single mode guide, it is possible that for short lengths, depending on the source that excited the fundamental mode (the tapered fiber in this case) lossy modes could interfere with the fundamental mode and contribute to the shape of the transmission spectrum.

At this point, it is useful to understand, qualitatively, what effects the shape of the spectrum when two modes interfere. It has already been mentioned that the space between the peaks in the spectrum is greater for a shorter waveguide and for a smaller difference between the effective index of the interfering modes. In Figures 5-18 and 5-19, the effect of relative loss is examined. It is expected that the higher order modes that are interfering with the fundamental mode are lossy, so it makes sense to consider two interfering modes where one has a higher loss than the other. Notice that the interference is weaker for the higher order mode with a higher loss, but even with a loss of 150 dB/cm, there is a noticeable effect on the transmission spectrum. This is because the length of the cavity is quite short at 2 mm. The reason that 2 mm is being considered is that this is the length of the longer segment created when the gaps are etched in the center of the 4 mm long waveguides.

In the limit that the second interfering mode has an infinitely high loss, the transmission spectrum reduces to that of the case of just one mode[7] as shown in Figure 5-20.

Looking at Figure 5-19, it seems incorrect that a mode with such a high loss (150 dB/cm) could alter the transmission spectrum so significantly, especially if the transmission spectrum for only the lossy mode is considered (Figure 5-21). However,

[7]Actually, the transmission spectrum for a single mode with the given specifications would have twice the transmissivity of that shown in this Figure. This is a result of the way this spectrum was normalized. It was normalized so that the maximum transmissivity for the two modes together would be 1. This means that the power in each mode has been normalized to 0.5. Typically, the transmissivity is examined for a single mode and all of the power is put into this single mode. Because it is divided between the two modes in this case and one of the modes has a very high loss, the maximum transmissivity for the two interfering modes can only be 0.5 (which would be the extreme case of zero loss in the lower loss mode).

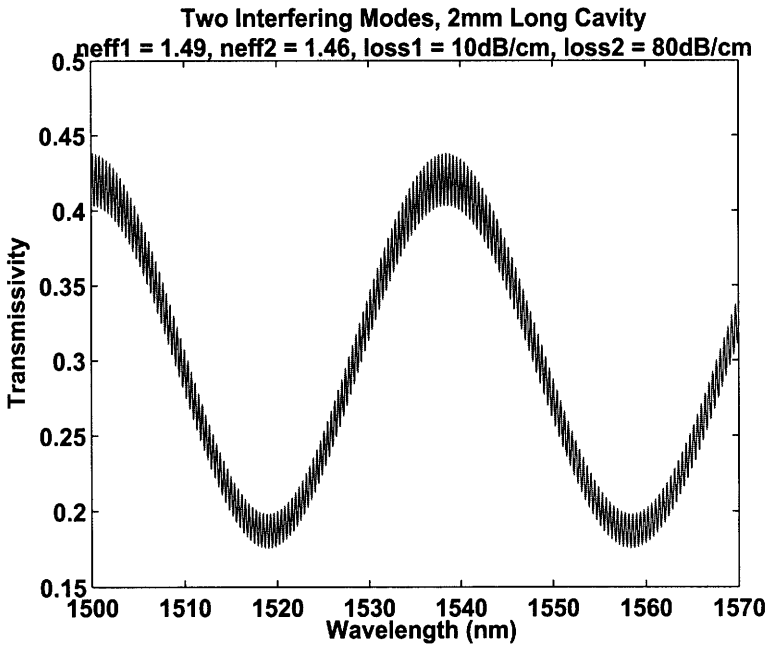

Figure 5-18: Calculated transmission spectrum for an interconnect waveguide cavity with two interfering modes.

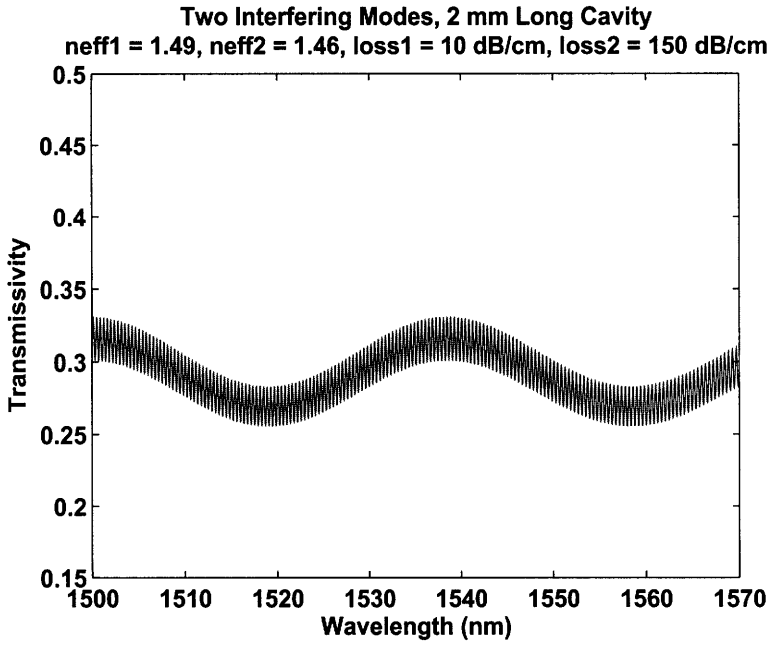

Figure 5-19: Calculated transmission spectrum for an interconnect waveguide cavity with two interfering modes.

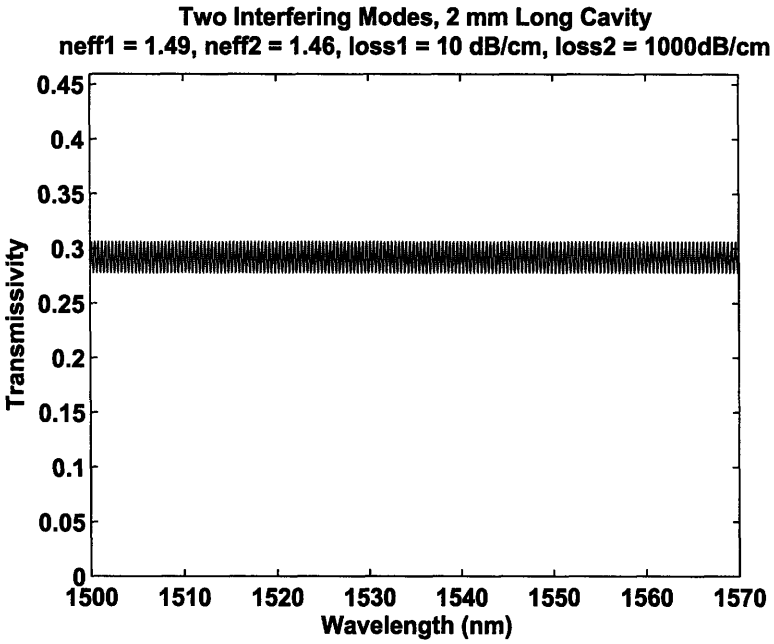

Figure 5-20: Calculated transmission spectrum for an interconnect waveguide cavity with two interfering modes. The loss of the higher order mode (lower effective index) is so high that this spectrum is just the same as the spectrum for a single mode.

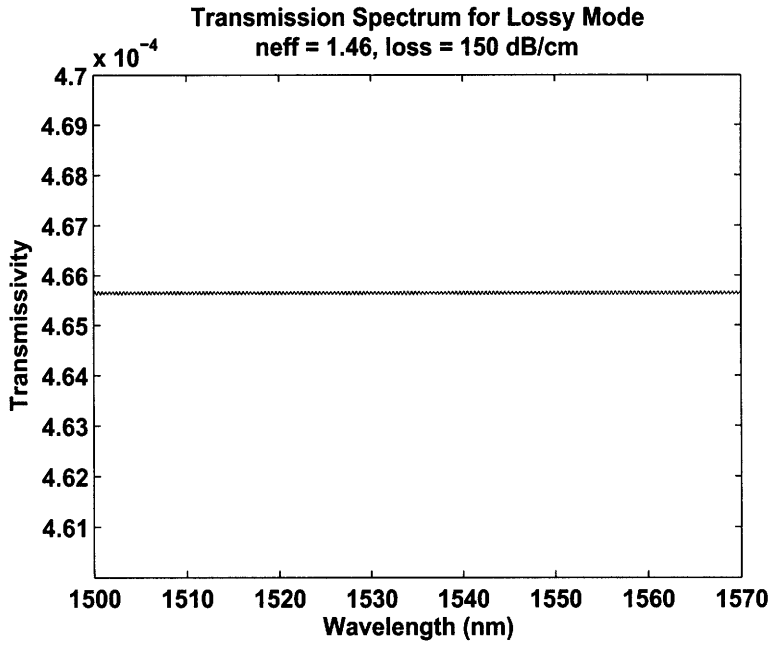

Figure 5-21: Calculated transmission spectrum for an interconnect waveguide cavity with two interfering modes. The loss of the higher order mode (lower effective index) is so high that this spectrum is just the same as the spectrum for a single mode.

the plotted transmission spectra are of the transmissivity (i.e. power) whereas it is the field magnitudes that interfere.

By comparing Figures 5-19 and 5-20, it can be seen that in order to extract an approximate transmissivity for the fundamental mode from a spectrum like that of Figure 5-19, one can simply take the average value from the spectrum. That is, if the slowly varying part of Figure 5-19 is removed, the resulting spectrum is very close to that of Figure 5-20, which is essentially just the spectrum for the fundamental mode only. This is exactly what was done in Section 5.2 to approximate the propagation loss of the fundamental mode in the InP/InGaAsP waveguides.

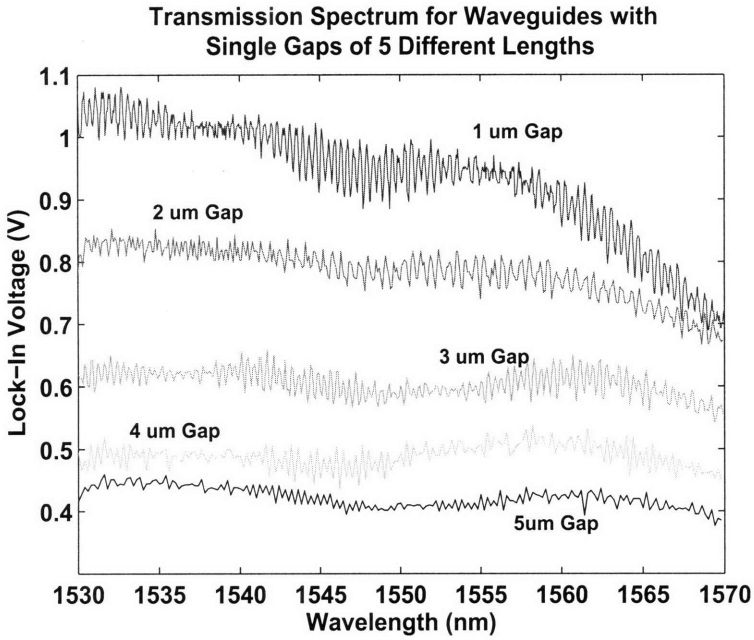

Figure 5-22: Measured transmission spectrum for waveguides with a single air-filled etched gap. The gap is positioned in the center of a 4mm long, 1.3 μm wide interconnect waveguide.

5.3.3 Measured Gap Transmission Spectra and Loss Extraction

After discussing at length what to expect from the gap measurements, the actual measurements will now be shown and an average gap loss will be calculated in this section.

Gap Data

In Figure 5-22, the transmission spectra for waveguides with a single gap of varying length (1 - 5 μm) are plotted. Figure 5-23 is a plot of the data for two gaps of varying length, and Figure 5-24 is a plot of the data for three gaps of varying length.

Within each of these three plots just mentioned, the effect of the gap length can be seen as the spectrum for each gap length is plotted. Another way of showing the data is to plot for a given gap length, the transmission spectra for each number of

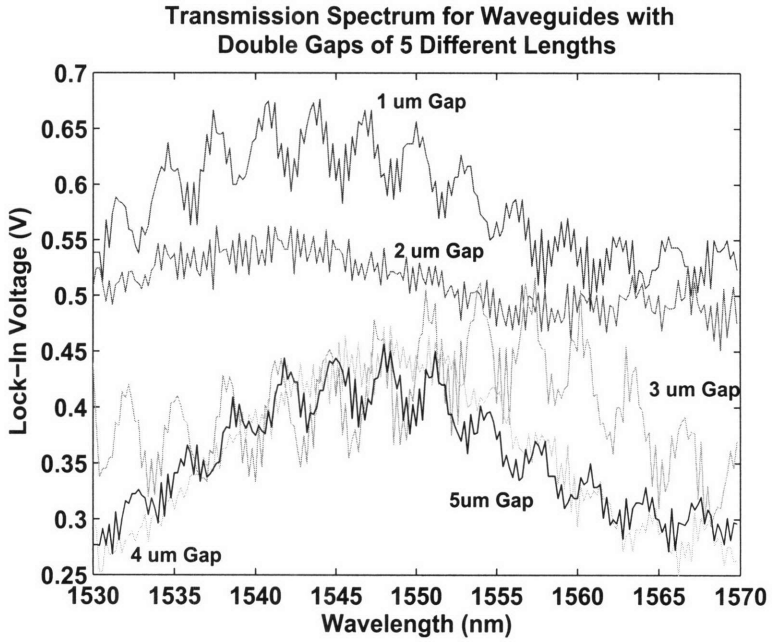

Figure 5-23: Measured transmission spectrum for waveguides with two air-filled etched gaps separated by 250 μm. The first gap is positioned in the center of a 4mm long, 1.3 μm wide interconnect waveguide. The second gap is located 250 μm from the first gap. This is important because the lengths of the segments of interconnect waveguide between the gaps (250 μm) and between the gaps and the end facet (2 mm and 1.75 mm) are, in addition to the multimode interference, what gives the measured transmission spectra its signature appearance.

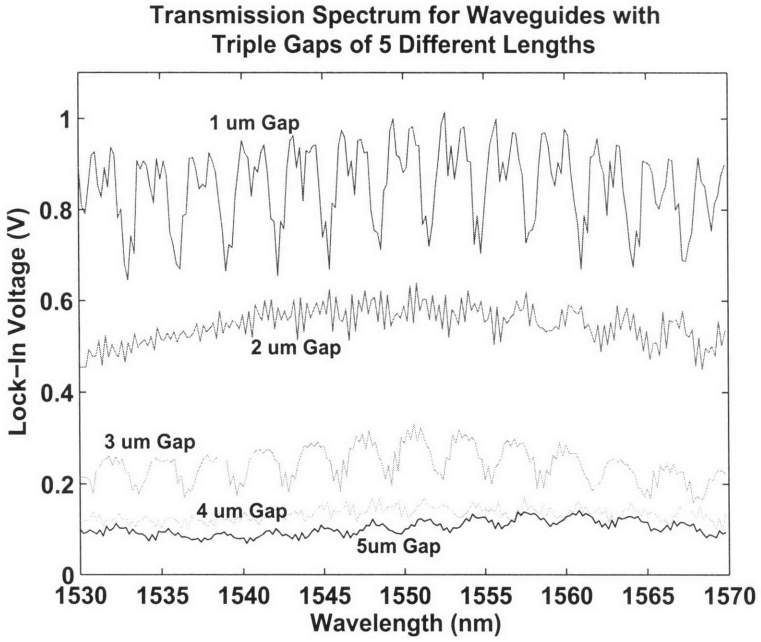

Figure 5-24: Measured transmission spectrum for waveguides with three air-filled etched gaps separated by 250 μm. The first gap is positioned in the center of a 4mm long, 1.3 μm wide interconnect waveguide. The second gap is positioned 250 μm from the first gap, and the third gap is position 250 μm from the second gap.

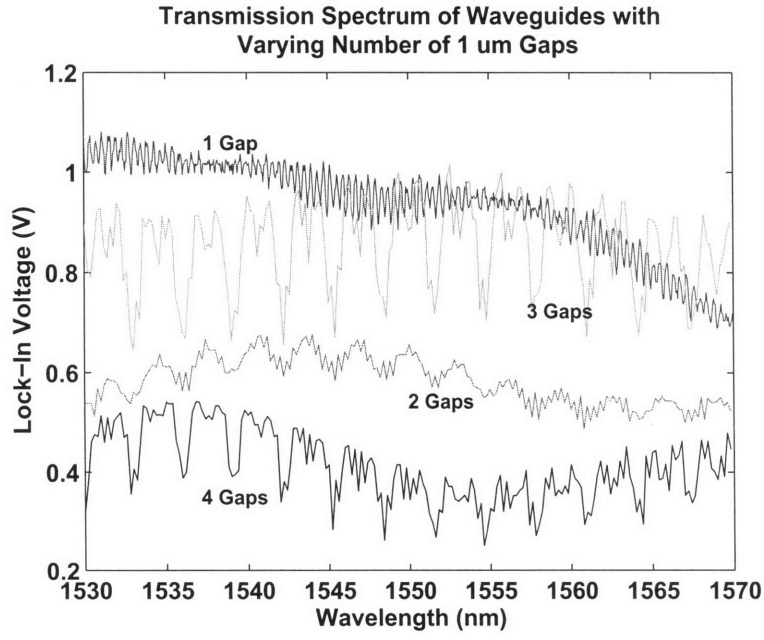

Figure 5-25: Measured transmission spectrum for waveguides with 1-4 1 μm Gaps.

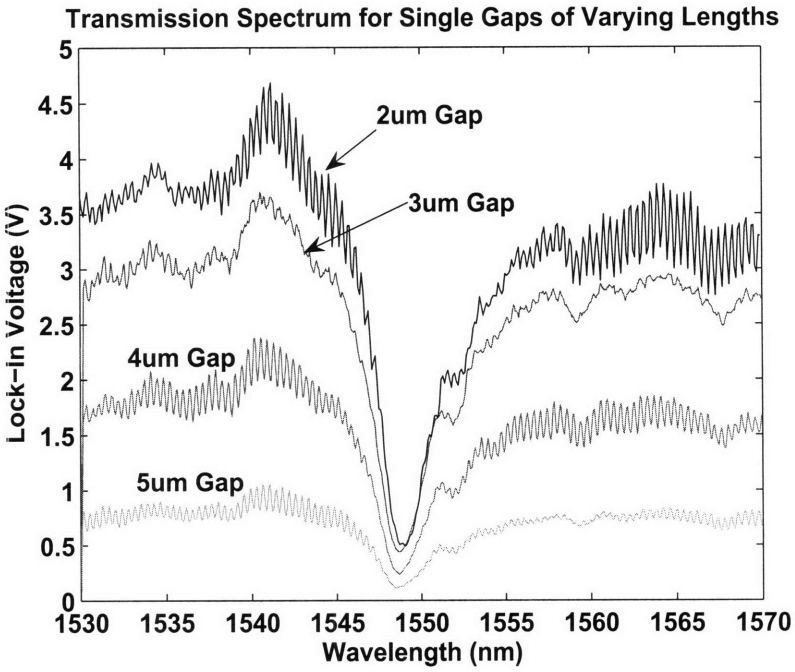

Figure 5-26: Comparison of the transmission spectrum for a single silicon-rich nitride filled gap of varying lengths. For each gap, the gap is positioned in the center of a 4mm long, 1.5 μm wide interconnect waveguide. The dip in the transmission spectra in the vicinity of 1550 nm is due to enhanced material absorption at this wavelength due to coupling due to incorporated hydrogen in the silicon-rich nitride.

gaps (i.e. 1, 2, 3, and 4 gaps). This is done in Figure 5-25 for the case of a 1 μm long gap. Each of these four plots just mentioned is for the air-filled gaps with no lateral shifting. There is nothing qualitatively different for the case of air-filled gaps with shifting so they are not shown. The results of the calculations will, however, be included with the gap measurement results in Section 5.3.3.

A change in the index of the gap filling material, does, however, qualitatively alter the transmission spectra. In figure 5-26, the measured transmission spectra for the five different gap lengths for a single gap are shown. The sharp dip in the spectrum in the vicinity of 1550 nm is not a resonant effect. It is also not affected by the number of gaps. It is most likely due to enhanced absorption by the silicon-rich nitride material in the gap at 1550 nm. This silicon-rich nitride material was not annealed after deposition. This absorption at 1550 nm is typical for PECVD deposited films such as the silicon-rich nitride used here [48]. When calculating the gap loss for the silicon-rich nitride gaps, only the 1560-1570 nm part of the spectrum was used in the calculation to avoid the influence of the dip in the spectrum

Modeling

The features of the data for the double gap measurements and a model that captures these features will now be discussed. The prominent features of the double gap data (Figure 5-23) are the result of the arrangement of the gaps along the waveguide as shown in Figure 5-27. The periodicity on the order of 3-4 nm comes from the 250 μm section between the gaps. The finer periodicity (which is difficult to see at this scale) comes from the two longer sections. The period on the order of 40 nm arises from the interference of two modes. Recall that Figure 5-16 was a plot of the transmission spectrum based on the T-matrix Matlab script for the waveguide and gaps. The scale was quite different for that plot and only one mode was included in the simulation. Shown here in Figure 5-28 with two interfering modes and at a scale that shows the similarity between the modelled spectrum and the data is the calculated results for two 5 μm gaps shown alongside the measured data for the same gap arrangement. The simulation results were multiplied by a fitting factor for ease of comparison with

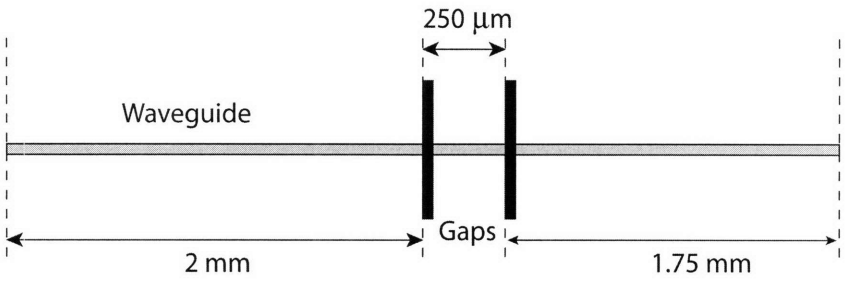

Figure 5-27: Illustration showing the arrangement of the two gaps for the simulated and measured data shown in Figure 5-28.

the measured data. This factor just normalizes the input power of the modelled data to that of the measured data and doesn't alter the shape of the modelled spectrum.

The qualitative and approximate quantitative similarity between the model and the data implies that the model is capturing the fundamental elements that are contributing to the shape of the measured spectrum, namely that there is a higher order lossy mode that is indeed interfering with the fundamental mode. The effective indices listed in the caption for Figure 5-28 are very well matched to the actual effective indices present in the measured waveguides because these values are based on the separation between the interference peaks (this gives the difference between the two effective indices) and the "faster" Fabry-Perot oscillation period (which gives the absolute effective index for the fundamental mode). The given propagation loss for the fundamental mode of 10 dB/cm is approximate, but is based on the data from Section 5.1.2. The given propagation loss for the higher order mode could be different than the actual value as a lower propagation loss and a lower power relative to the fundamental mode would result in a simulated plot similar to that shown in Figure 5-28.

Gap Loss Calculation

Figures 5-23 and 5-24 show the data for all of the gap lengths for double and triple gap arrangements respectively. For the double, triple, and quadruple (not shown) gap data, there are four different characteristic oscillations. The shortest period oscilla-

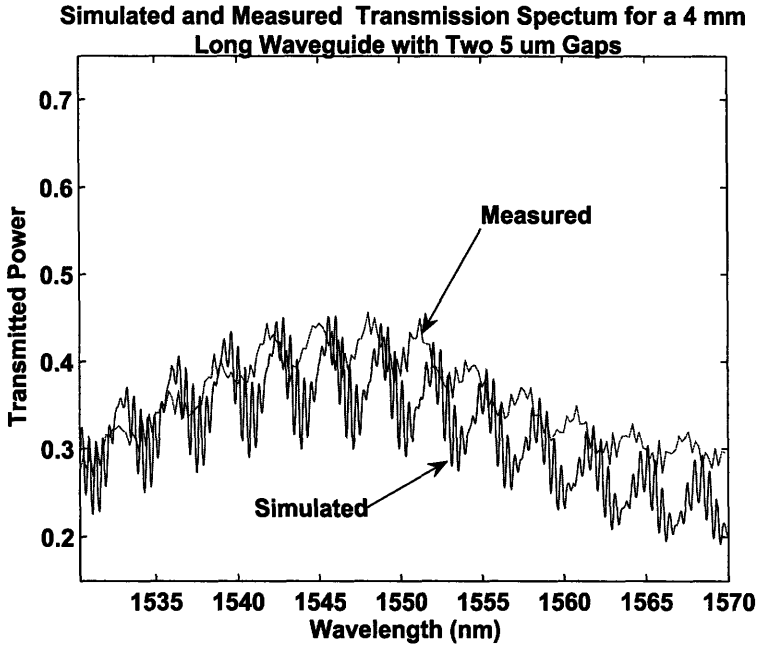

Figure 5-28: Comparison of the simulated and measured transmission spectrum for a waveguide with two 5 μm long air-filled gaps. This simulated results are from the T-matrix Matlab model for a waveguide with two gaps with two interfering modes. The parameters for the modes are $n_{eff,1} = 1.49$, $n_{eff,2} = 1.478$, $\alpha_1 = 10dB/cm$, $\alpha_2 = 55dB/cm$. The initial excited power ratio for the two modes is 1:1.

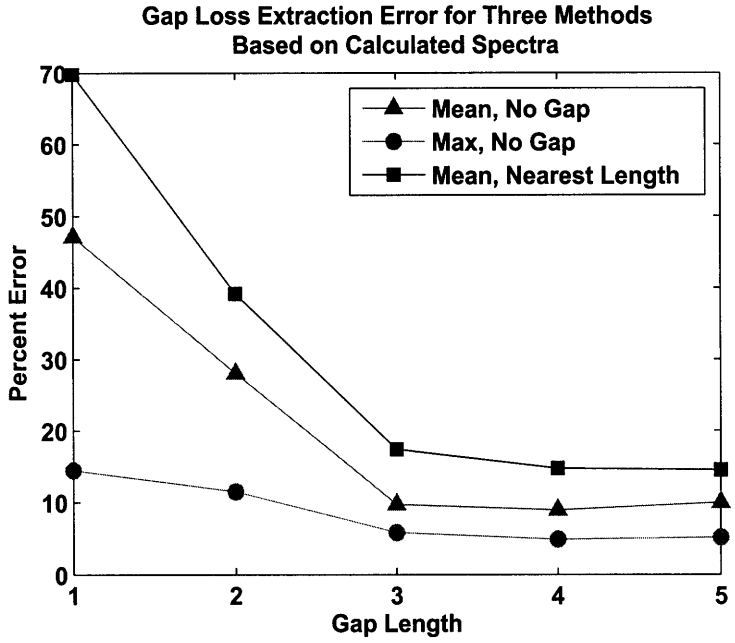

Figure 5-29: Extracted gap loss error for three different methods.

tions are due to the 2 mm long waveguide sections. The more prominent oscillations with a period on the order of 3-4 nm are due to the 250 μm long sections between the gaps, while the 35-40 nm period is due to mode interference. Finally, the gaps themselves contribute oscillations with a period of over 250 nm. With all of this structure, it is important to determine what points in the various spectra to use as the comparison points. To do this, one could extract the gap loss from the from the equations used in the model for the transmission spectrum for multiple Fabry-Perot cavities with two mode interference. This would be difficult at best. Instead of doing this, three different methods were employed to extract the known gap loss from the calculated spectra. The extracted gap loss was then compared with the known input gap loss and the error was recorded. The results of this exercise are shown in Figure 5-29. For each method, there are three parts to extracting the gap loss. First, for a given gap length, the five transmission spectra corresponding to 0, 1, 2, 3, and 4 gaps were calculated for two interfering modes using the Matlab script with the same parameters that were used in Figure 5-28. The propagation loss in the gap was assumed

to be 1 dB/μm which was based on the FDTD simulation results. The wavelength range for these spectra was the range of exactly one period of multimode interference (40 nm). The next step was to find the mean and the maximum transmissivity for each of the five spectra. Finally, for each gap length, the mean transmissivity was compared with the mean transmissivity for the next shortest gap length (*Mean, Nearest Length* in the figure). Also, the mean and maximum transmissivity were compared with the same value for the spectrum with no gaps (labelled *Mean, No Gap* and *Max, No Gap* respectively). As the data shows, *Max, No Gap* yielded the closest values. However, this method was not used to extract the gap loss from the actual measurements. This is because it is based on a single value, the maximum in the signal. Due to noise in the measured signal, it was possible that this method would actually lead to a greater error than shown here. Consequently, the *Mean, No Gap* method was used. This is based on an average value for the entire spectrum. It should be mentioned that the extracted loss for this method was always greater than the actual loss, so it can be considered a maximum value for the gap loss.

Gap Loss Calculation Results

At the beginning of this subsection, Section 5.3.3, the measured gap data was shown for air-filled gaps and for silicon-rich nitride filled gaps. It was mentioned that measurements were also taken for air-filled gaps with a lateral shift of 0.45 μm and 0.9 μm, but that there was no qualitative difference between this data and the unshifted air-filled gaps so that data was not shown. The results for all four types of gaps is shown in Figure 5-30 based on the application of the *Mean, No Gap* method.

Notice that the high-index gap fill results in the lowest coupling loss as theorized. Recall that this was theorized to be the result of a reduction in mode spreading for unguided propagation in a high index material. This effect is confirmed in the plot not only by virtue of the fact that the loss is lower for each gap length for the high index gap fill relative to the air-filled no shift gap, but that the amount by which it is lower is, on average, increasing for an increasing gap length. This confirms that the lower loss is indeed a gap length dependent effect, as would be expected for a

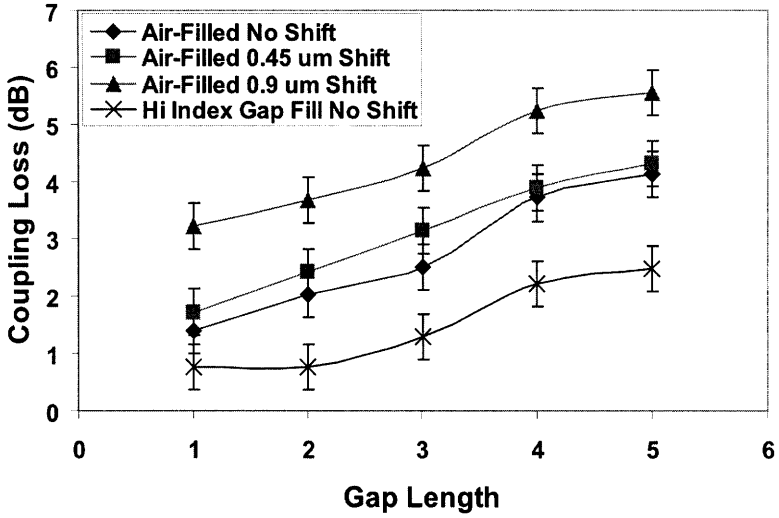

Figure 5-30: Gap loss in dB extracted from the gap measurement results. The gap loss for four different types of measured gaps was calculated.

decrease in mode spreading over the length of the gap.

Owing to the nonlinear distribution (approximately gaussian) of the power in the cross-section of the radiated mode in the gaps, a lateral shift of 0.9 μm results in a deviation of the loss from perfect alignment by more than twice the deviation of the loss from perfect alignment for a lateral shift of 0.45 μm.

The shifted data demonstrates another effect. The greater the gap length, the less the deviation of the loss from the case of no shift. That is the difference between the no shift and the 0.9 μm shift or the no shift and the 0.45 μm shift is smaller at a gap length of 5 μm than at a gap length of 1 μm. This can be explained as follows. The explanation for the greater gap loss at a greater gap length is that the propagating wave is unguided in the gap and, consequently, spreads, distributing the power over a greater area. This results in a weaker overlap with the waveguide facet after propagating through the gap. Therefore, at a gap length of 5 μm, the propagating mode is wider than it was at a gap length of 1 μm. For the purpose of this illustration, it will be assumed that after propagating 1 μm through the gap, the unguided wave perfectly overlaps with the fundamental mode of the waveguide

at the end of the gap. After propagating 5 μm, the mode has spread more and no longer perfectly overlaps with the fundamental mode of the waveguide at the end of the gap. These two cases are illustrated in Figures 5-31a and 5-31b respectively.

Now imagine that the waveguide at the front side of the gap has been shifted laterally 0.9 μm relative to the waveguide at the end of the gap. The same set of plots in the unshifted case in Figure 5-31 is shown in Figure 5-32 for this shifted case.

Notice that the 0.9 μm lateral shift has affected the overlap of the wave having propagated 1 μm in the gap (heretofore called the narrow field) more than the wave having propagated 5 μm in the gap (heretofore called the wide field). The shift changed the narrow mode overlap from 1.0 to 0.82, and the wide mode overlap from 0.77 to 0.74. A more complete way to show the affect of shifting on the overlap is to plot the convolution of the narrow field with the fundamental waveguide mode and the convolution of the wide field with the fundamental waveguide mode. The overlap integral for two field profiles $A(x)$ and $B(x)$ is

$$P_{A,B} = \frac{\int A(x)\, B(x)\, dx}{\sqrt{\int A^2(x)\, dx \int B^2(x)\, dx}} \tag{5.30}$$

The convolution integral normalized by the power of the two fields is

$$C_{A,B}(x) = \frac{\int A(u)\, B(x-u)\, du}{\sqrt{\int A^2(x)\, dx \int B^2(x)\, dx}} \tag{5.31}$$

Notice that the value of this normalized convolution integral for some x, is nothing other than the overlap integral in which B has been shifted by an amount x. Consequently, plotting the convolution integral as a function of the displacement, x, gives the overlap integral as a function of the shifting, x, of one mode relative to the other. Figure 5-33a is a plot of the convolution of the fundamental waveguide mode with the narrow field and the convolution of the fundamental waveguide mode with the wide field.

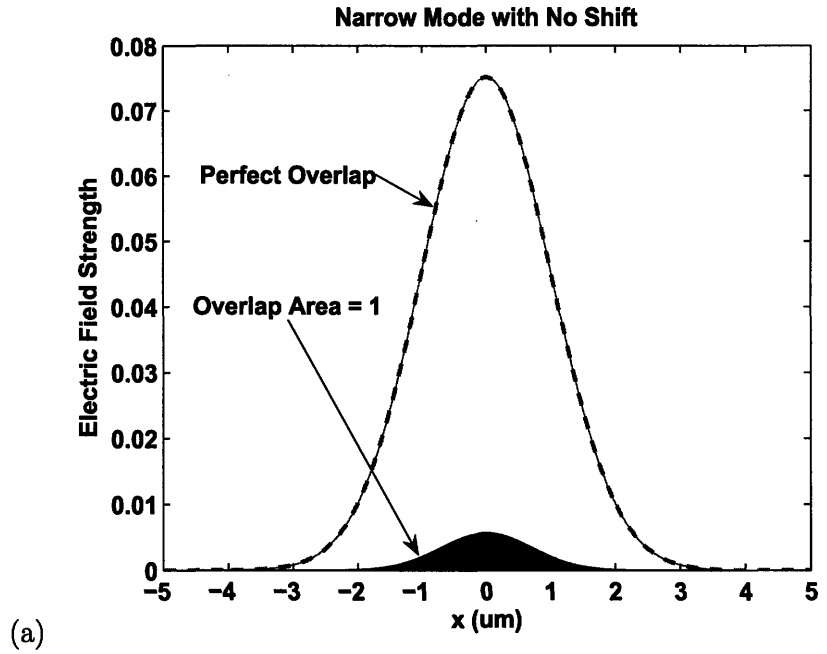

(a)

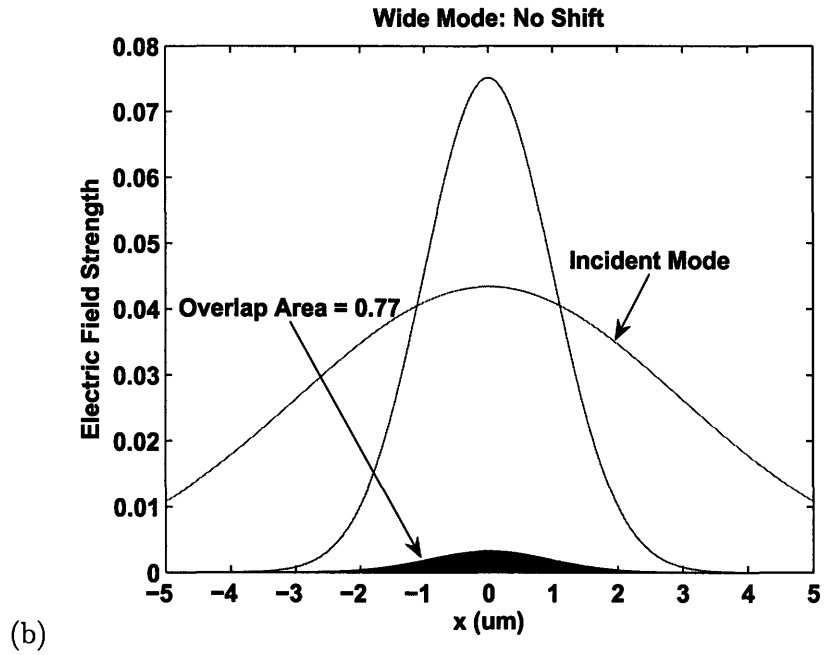

(b)

Figure 5-31: (a) Electric field profile of the unguided wave after 1 μm of propagation in the gap, the fundamental waveguide mode (these two profiles are sitting directly on top of one another) and the product of the two profiles. The profiles have been normalized for unity power. The area under the overlap (i.e. integral of the product of the two profiles) is unity for perfect overlap. (b) Electric field profile of the unguided wave after 5 μm of propagation in the gap, the fundamental waveguide mode and the product of the two profiles.

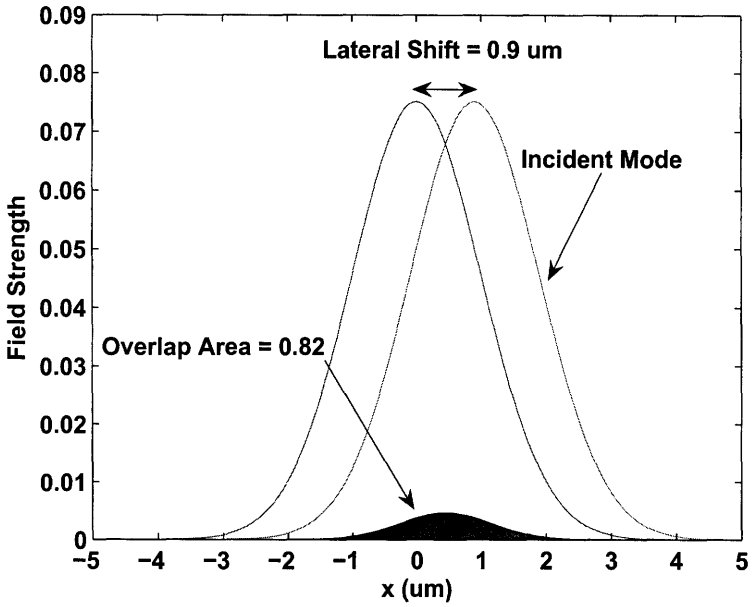

(a)

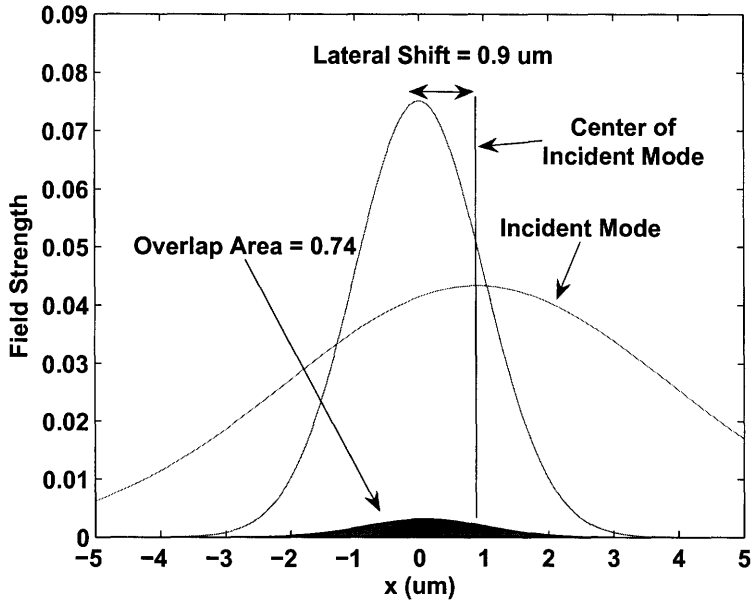

(b)

Figure 5-32: (a) Electric field profile of the 0.9 μm laterally shifted unguided wave after 1 μm of propagation in the gap, the fundamental waveguide mode and the product of the two profiles. (b) Electric field profile of the 0.9 μm laterally shifted unguided wave after 5 μm of propagation in the gap, the fundamental waveguide mode and the product of the two profiles.

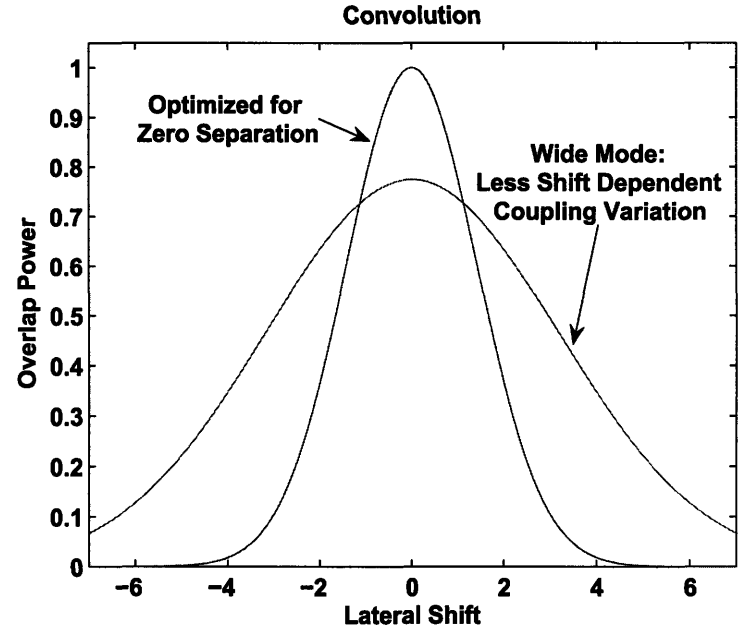

(a)

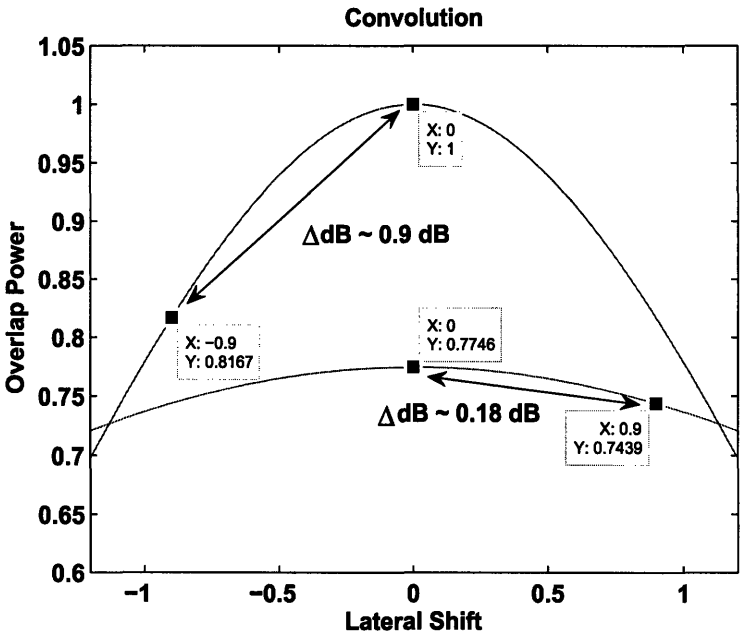

(b)

Figure 5-33: Convolution of the fundamental waveguide mode with the narrow field and the fundamental waveguide mode with the wide field. (a) Zoomed out. (b) Close-up showing that the values of the convolution integral at 0 μm shift and at 0.9 μm shift are indeed the values calculated using the overlap integral, Equation 5.30, as shown in Figures 5-31 and 5-32. Notice that the 0.9 μm shift affects the narrow field more so than the wide field.

Notice in Figure 5-33b, that at a shift of approximately 1.2 μm[8], the value of the wide field overlap is larger than that of the narrow field overlap. This analysis demonstrates the trade-off between efficient coupling and sensitivity to misalignment. Maximizing the coupling efficiency for perfect alignment would not yield the best results on average if the average misalignment were greater than 1.2 μm.

Extracting the Facet Scattering Loss

The measured results can now be compared with the results from the Finite Difference Time Domain (FDTD) simulations to extract the loss due to scattering at the rough facets. The simulation results are shown in Figure 5-34. Looking back at Figure 5-30, there is on average, a difference between the measured and simulated loss on the order of 1 dB, which is a factor of about 0.8. It is likely that this difference in loss is a result of scattering at the rough etched interface. Notice too that there is qualitative agreement between the measured and simulated data. The lowest losses are seen with the high index gap fill.

Gap Loss Section Summary

In this section, a model for the transmission spectra for a varying number of gaps of varying length was developed taking into account the effect of the multiple gaps and multi-mode interference. The measured gap transmission spectra were shown for air-filled gaps and silicon rich nitride filled gaps. The model for the gap transmission spectra was compared with the measured transmission spectrum for the case of a waveguide with two air-filled gaps with good qualitative agreement. Three methods for extracting the gap loss from the measured transmission spectra were developed and were tested using calculated data. This involved calculating the transmission spectrum for a given gap loss using the model. The three methods were then used to extract the gap loss from the calculated spectrum and this number was compared with the known gap loss. The second best method in terms of calculation error was

[8]The exact numbers presented here were chosen to exaggerate the effect of shifting on the coupling for the purpose of the illustration. This is not meant to imply that a shift of 1.2 μm for these waveguides would have resulted in a lower gap loss for a 5 μm gap than a 1 μm gap.

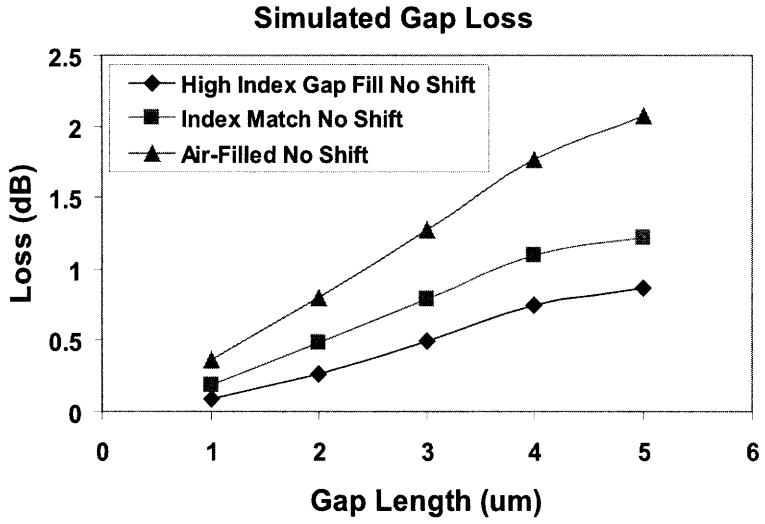

Figure 5-34: Gap loss in dB extracted from the gap measurement results. The gap loss for four different types of measured gaps was calculated.

chosen because it was based on an average over the entire measured spectrum rather than the transmissivity at a single wavelength.

The method was then used to calculate the gap loss from the measured spectra. The lowest gap loss was achieved for the silicon-rich nitride filled gaps. At 5 μm, the gap loss was less than 2.5 dB. While shifting the waveguides relative to one another increased the gap loss, it was seen that at the longer gap lengths, the effect of shifting was reduced. This was shown to be a result of mode spreading. This effect showed that there exists a tradeoff between maximum coupling efficiency and reduced sensitivity to lateral shifting.

Finally, the measured gap loss was compared with the FDTD data. There was good qualitative agreement. The quantitative difference between the measured gap loss and the FDTD simulated gap loss was attributed to scattering loss at the rough etched facet. Based on this assumption, the two facets combine on average for an additional 1 dB of loss.

5.4 Isolated InP/InGaAsP Pill Device Measurements

In order to characterize integrated InP/InGaAsP pill devices,it was useful to first examine the devices in isolation, outside of the wells in which they were to be integrated. Not only does this remove the influence of the surrounding gap and interconnect waveguides on the transmission spectrum, but it allows for the devices to be examined with optimum input and output (fiber) alignment. Going a step further, one can examine the effects of shifting the input (fiber) vertically or laterally relative to the optimum alignment position.

5.4.1 Isolated Pill Mounting and Initial Measurements

To accomplish this isolated measurement, devices were mounted on the back edge of a razor blade with adhesion provided by an epoxy. The razor blade was chosen because it is both rigid and narrow. The back part of a razor blade is only 250 μm thick. This was the perfect thickness because the devices are 300 μm in length. This extra 25 μm overhang per end facet guarantees that the input and output fibers can be brought right up to the device facet.

In addition to the standard length 300 μm device, a 900 μm long device was measured. Being able to compare the spectra for two devices allows for the removal of length dependent features. The longer device also has a greater length over which to "filter out" cladding modes that might interfere with the measured spectrum.

The measured transmission spectrum for an isolated 300 μm long pill waveguide is shown in Figure 5-35. Compare this with the measured spectrum for a 930 μm long pill waveguide shown in Figure 5-36. Notice that the peak value for both spectra is nearly the same. This is most likely the result of a better facet or better input fiber alignment for the 930 μm device measurement. Given identical coupling into the device, the longer device would have a lower output coupled power than the shorter device. So it is likely that more power was coupled into the longer device (or at

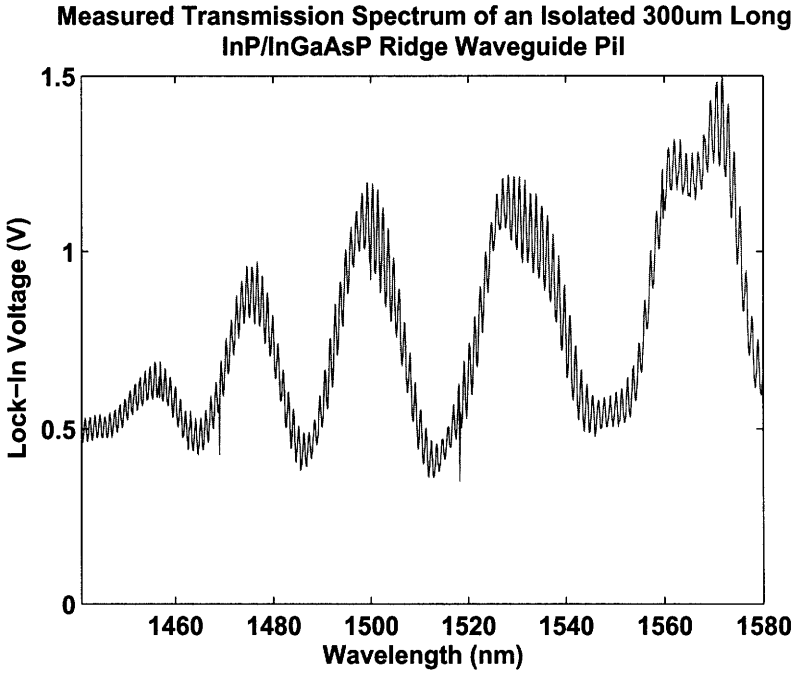

Figure 5-35: Measured transmission spectrum for an isolated 300 μm long InP/InGaAsP ridge waveguide pill.

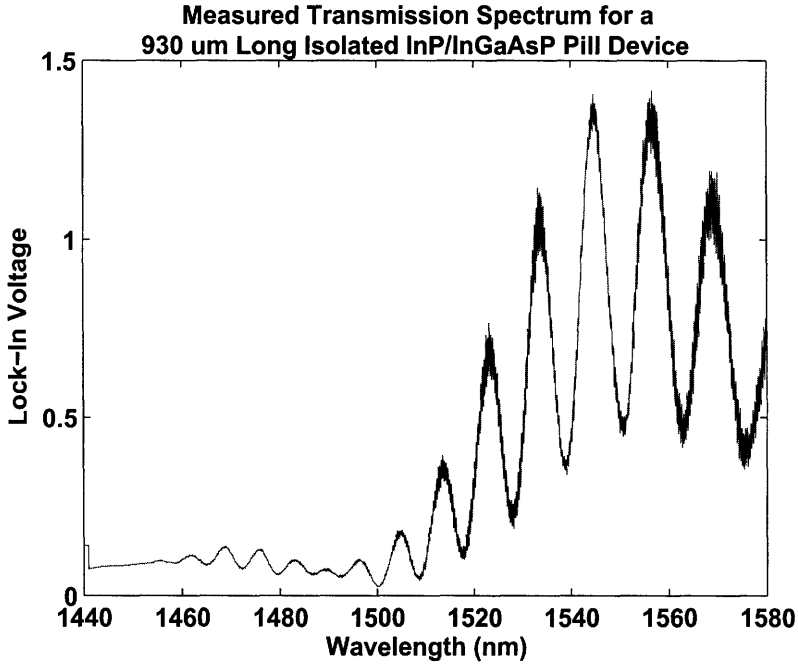

Figure 5-36: Measured transmission spectrum for an isolated 930 μm long InP/InGaAsP ridge waveguide pill.

least more of the power was coupled into the fundamental mode of the longer device than for the shorter device) . Another obvious feature is the difference between the transmitted power in the shorter wavelength range with respect to the longer wavelength range. This was seen in the transmission spectra for the long "bulk" ridge waveguides measured in Section 5.2. This is due to higher absorption in the multi-quantum well region at shorter wavelengths, with a pronounced transition from higher to lower absorption when increasing beyond wavelengths of approximately 1520 nm. Notice that this transition is more pronounced in the longer pill where there is a greater length over which to absorb the lower wavelength light. For this same reason, this transition is pronounced even more still when looking back at the transmission spectrum of the long "bulk" ridge waveguide in Figure 5-5.

The fact that the lower wavelength transmission is so high for the shorter pill is likely also related to the poorer input coupling to the fundamental mode as suspected above. If the light is coupled less efficiently into the fundamental mode of the shorter device (for whatever reason, be it a poor facet, operator error, etc.) manifesting itself in a lower output signal relative to the longer pill at the longer wavelengths where the MQW absorption is lower, this would further contribute to the relatively high output power measured at shorter wavelengths. This is because poor coupling to the fundamental mode implies that more of the light is coupled into cladding modes. These cladding modes are distributed throughout the thickness of the pill so they don't have as high of a MQW absorption loss as the fundamental mode which is concentrated in the quantum well region.

Figures 5-37 and 5-38 show the profile for a TE cladding mode of the InP/InGaAsP pill ridge waveguide structure. Notice that the peaks of this mode fall outside of the MQW core. As it is difficult to excite only the fundamental mode of the structure with a tapered input fiber, the presence of modes such as this TE20 mode must be considered in the analysis of the isolated and integrated measured pill spectra.

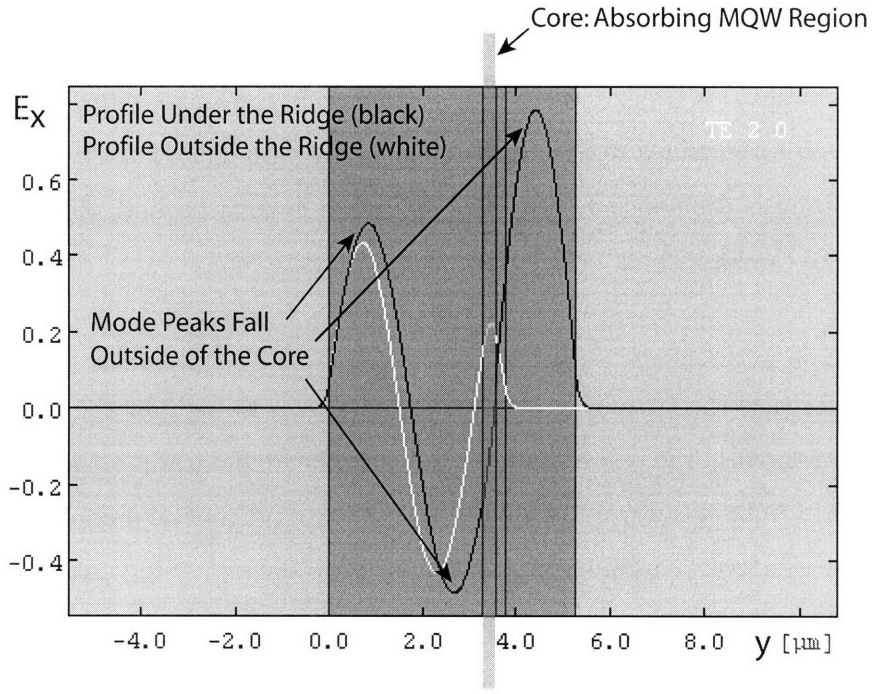

Figure 5-37: Side view (substrate is to the left, the top of the device is to the right) of the vertical cross-section of TE20 mode profile for the InP/InGaAsP pill ridge waveguide. The black mode is the vertical cross-section of the mode taken in the center of the ridge, while the white mode is taken outside of the ridge. Notice that the peaks of the mode under the ridge (the black mode) fall outside of the absorbing MQW core. If excited, this mode would propagate with less MQW absorption loss than the fundamental mode.

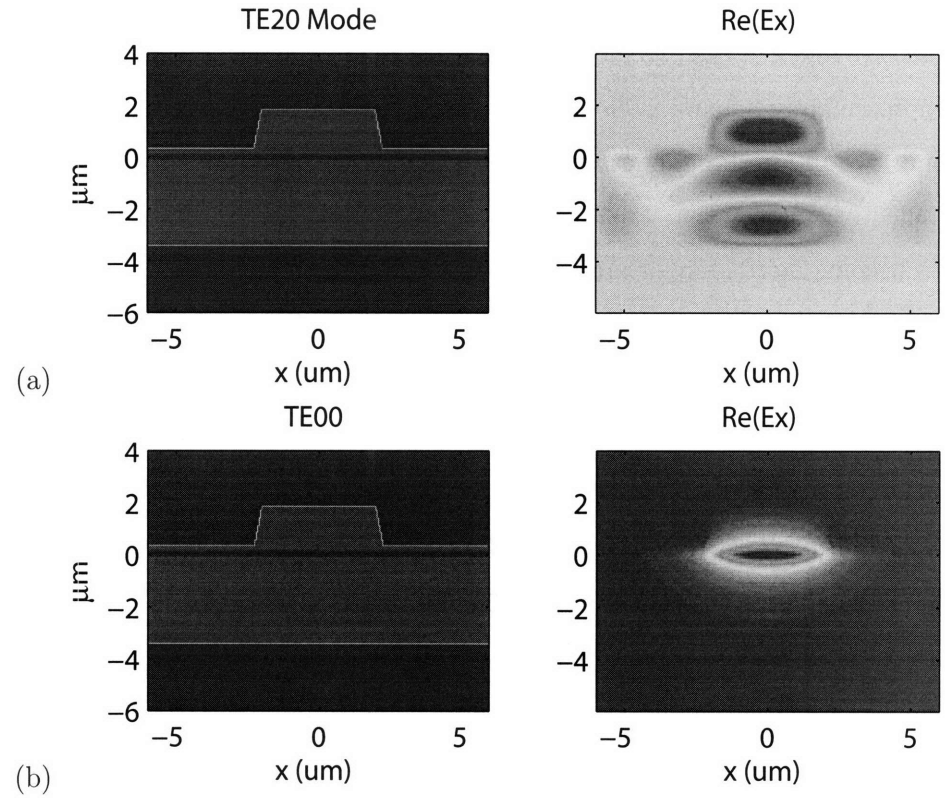

Figure 5-38: Cross-section of the (a) TE20 mode for the InP/InGaAsP pill ridge waveguide. While it is more difficult to see than in Figure 5-37, the mode peaks fall outside of the core. This is compared with the cross-section of the (b) TE00 mode, the peak of which is aligned with the core.

Multimode Interference

Another obvious feature of Figures 5-35 and 5-36 is the long period oscillations on the order of 30 nm and 10 nm for the 300 μm long pill and the 930 μm long pill respectively. Taking into account the period of the "fast" oscillations (Fabry-Perot resonance), which give the absolute effective index, and modelling the long period oscillations as the interference of two modes, which is a function of the difference of the effective index of the two modes, the effective indices of the two interfering modes are approximately 3.2 and 2.95. As said before, this is not meant to imply that there are only two interfering modes. Rather, this is an effective range. There are modes with effective indices that are lower than 2.95, but this is the point at which the modes become more lossy or are weakly excited by the input fiber.

Referring again to Figure 5-37, the InP cladding which makes up the bulk of the InP/InGaAsP ridge waveguide material, can be thought of as the core of a multimode waveguide where the cladding is the surrounding air. The effective indices of the higher order modes of this waveguide are very close to 1.0, the refractive index of the air-cladding. The overlap of these modes with the input fiber would be low but nonzero. As mentioned in the previous section, these higher order modes have a small overlap with the quantum wells in the core, and would, therefore, see little wavelength dependent loss. The existence of these modes explains the nonzero transmissivity for the shorter wavelength spectral range in the 300 μm long isolated pill transmission spectrum of Figure 5-35.

5.4.2 Vertical Shift Misalignment Measurements

One of the benefits of examining an isolated pill is the ability to shift the input fiber vertically away from perfectly centered alignment with the waveguide to examine the effect that vertical misalignment has on the pill transmission spectrum properties. If there are any notable differences between the spectrum for perfect alignment and the shifted spectra, this would provide a misalignment indicator that would be useful in characterizing the integrated pill transmission spectra.

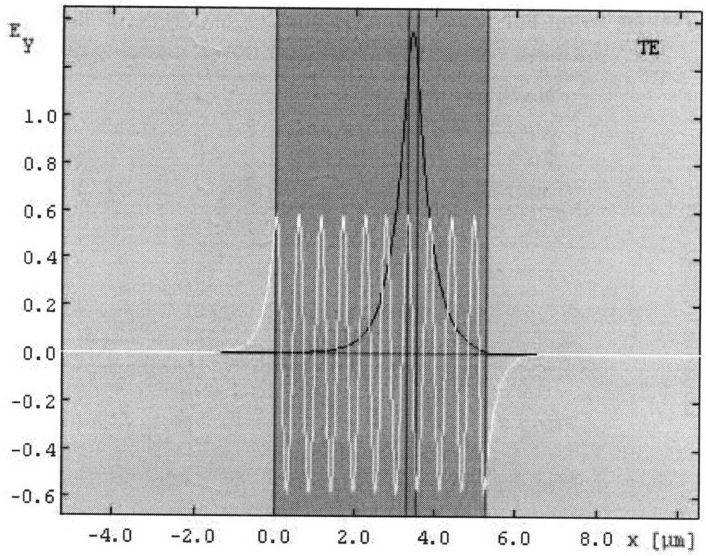

Figure 5-39: Vertical cross-section of the TE00 mode and the TE19-0 mode for the isolated InP/InGaAsP pill ridge waveguide taken at the center of the ridge waveguide. The overlap of this and other higher order modes with the tapered fiber input is small relative to the overlap with the TE00 mode.

Shown in Figure 5-40 are the transmission spectra for the isolated 300 μm long pill with the input fiber perfectly aligned, and shifted vertically towards the lower cladding of the pill waveguide in increments of 1 μm. The data shows the expected decrease in measured transmitted power as the input fiber is lowered.

In Figure 5-41, the maxima of the spectra in Figure 5-40 in the range of 1500 nm are plotted versus the fiber shift. The data from the measurements for the negative vertical shift was repeated for a positive vertical shift. This data was then fit with a spline curve. An ellipse was drawn with a width equal to the width of the curve at e^{-1} of the maximum point. This width, $\sim 3.5\mu$m is very close to the reported 2.5 $\pm$ 0.5 μm spot size of the tapered fiber used as the input for these measurements. The reason that the data was presented this way is to show that the variations in the spectra of Figure 5-40 for the different input fiber offsets are the result of a reduction in the overlap of the input fiber with the ridge waveguide.

It does appear, however, that shifting the input fiber does not simply scale the spectra. Looking at Figure 5-40, comparing the shape of the *no shift* spectrum with

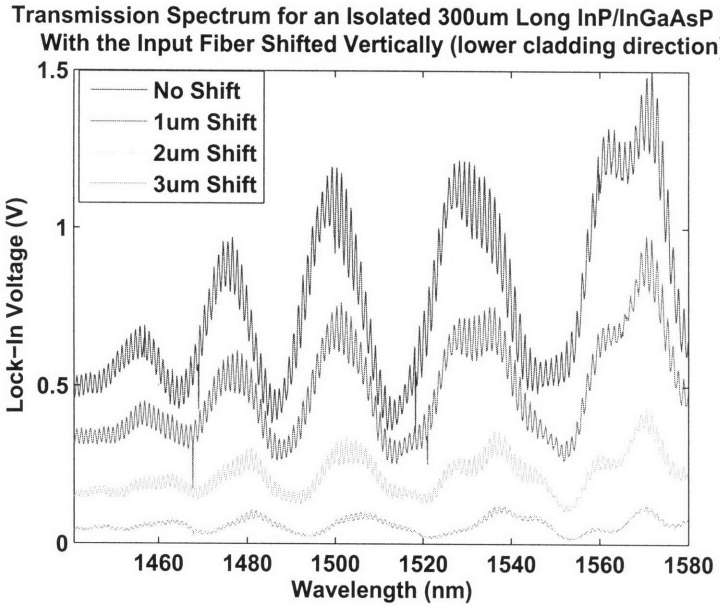

Figure 5-40: Measured transmission spectra for a 300 μm long isolated InP/InGaAsP ridge waveguide pill. The input fiber has been shifted vertically towards the lower cladding of the pill in 1 μm increments.

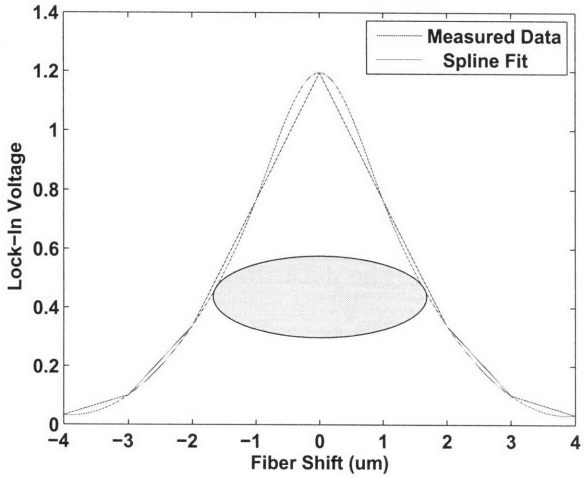

Figure 5-41: The measured data in this plot are the maxima taking in the vicinity of 1500 nm from the data in Figure 5-40 for a input fiber vertical shift of 0, -1, -2, -3, and -4 μm (not shown in Figure 5-40). The data shown for 1, 2, 3, and 4 μm are just a repeat of the data for a shift of 1 μm through 4 μm. The data was fit with a spline curve. The width of the ellipse is the width of the curve at e^{-1} of the maximum point.

the *2 μm shift* spectrum in the vicinity of 1540 nm, there is clearly a difference. This difference is the result of a different excitation of the various modes of the ridge waveguide pill.

Also notice the shift of the local max and min points in the spectrum by about 10 nm from the *no shift* spectrum to the *3 μm shift* spectrum for the shorter wavelengths. The absolute max, however, did not shift from a wavelength of about 1570 nm for each spectrum. A possible explanation, although admittedly speculative, is that the shifting is the result of a slight change in the effective indices of the modes (or the weights of the modes) that are contributing to the multimode interference. At the longer wavelengths, interference involving the core modes dominates regardless of the position of the input fiber.

Finally, the ratio of the absolute max (at 1570 nm) to the first local max (near 1460 nm) is 2.2 for the *no shift* spectrum and 1.2 for the *3 μm shift* spectrum. This implies that more of the power is distributed in modes that have less of an overlap with the quantum wells for the *3 μm shift* spectrum compared with the *no shift* spectrum. That is, as expected, more cladding modes are excited as the input fiber is shifted down towards the lower cladding.

Summary: Isolated Pill Measurements

The transmission measurements for the isolated pill are useful in that they permit an inspection of the transmission spectra without the confounding effects of the interconnect waveguides, the gaps, and the misalignment, all of which are present in the transmission measurements for integrated pills. The measurements showed that for these short 300 μm pills, the spectrum looks quite different than it did for the nearly 1 cm long "bulk" samples discussed in Section 5.2. The absorption edge is not as pronounced because there is less length over which to absorb the core guided modes. This is important information for the analysis of the integrated pill measurements in the subsequent section. It means that a lack of a sharp absorption edge does not necessarily imply that the pill is not well aligned.

5.5 Integrated InP/InGaAsP Ridge Waveguide Pill Measurements

The ultimate goal of this work is to demonstrate and measure coupling between interconnect waveguides and integrated InP/InGaAsP ridge waveguide pills. This section details the results of the measurements on integrated pills and compares these measured results with the expected results based on FDTD simulations. Throughout this work, approximately 30 InP/InGaAsP ridge waveguide pills were integrated in wells using the micropipette pick-and-place integration tool described in Chapter 4. This gives an indication as to the complexity or difficulty of the pill integration task. It was not something that could easily be done hundreds of times by a single person, but it was not so involved that it could only be done a few times. The majority of these approximately 30 integrated pills were used to characterize the pick-and-place process. This section deals with 6 integrated pills, in particular, that were integrated specifically for taking transmission measurements to determine the coupling efficiency.

5.5.1 Details of the Experiment

These pills were integrated in wells located in the center of a 4 mm long silicon oxynitride interconnect waveguide. The dimensions of the waveguide were 0.7 μm thick by 1.7 μm wide. The index of refraction of the core was 1.6 and the cladding was silicon dioxide with an index of 1.45. These were the parameters which yielded the highest coupling efficiency based on the FDTD simulations of Chapter 3. The approximate dimensions of the pills were 145 μm wide by 300 μm long. Each of the six wells into which these pills were integrated was 150 μm wide and the length varied from 307 to 312 μm. Figure 5-42 shows one of the pills integrated in the 312 μm long well. As discussed in Chapter 4, while future generations of integrated pills will be held in place in the well by the lower contact bond, these pills were simply held in place by gravity and possibly weak electrostatic forces. Once the six pills were placed in the wells, transmission measurements were taken for each of the six pills over the

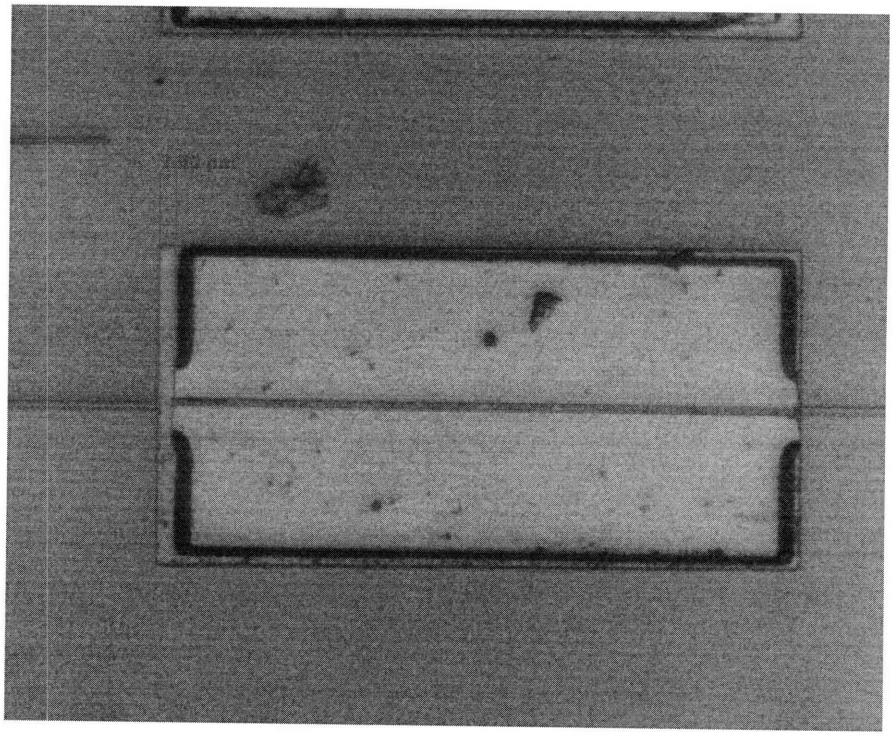

Figure 5-42: Photomicrograph of an InP/InGaAsP ridge waveguide pill integrated in a well etched into the interconnect waveguide stack.

full wavelength range of the input tuneable laser, 1440 to 1580nm.

5.5.2 Results

Three of the six measured transmission spectra are shown in Figure 5-43. These three spectra are a good representation of the six measured spectra. Of the six integrated pills, the pill integrated in the 312 μm long well had the highest transmitted power as seen in Figure 5-43a. The transmission spectrum shown in Figure 5-43b was for the 310 μm long well, but is very similar to what was seen for the 308 μm long well. The coupling loss at long wavelengths is about 3 dB higher than for the pill integrated in the 312 μm long well. In the shorter wavelength range, the transmitted power is higher than for the pill in the 312 μm long well. Very little transmission was seen for the other three integrated pills. Figure 5-43c is the spectrum for the 311 μm long well, and it is very similar to what was seen for the pills in the 307 and 309 μm long wells. Notice that the maximum on the y-axis for this plot is 10 times that of the other plots.

Pill Alignment in the Wells

Microphotographs of both interfaces for each of the six integrated pills were taken to see if there was any visibly noticeable difference between the alignment of the pills with measurable transmission as versus those with immeasurable transmission. These images were quite informative. The images for the pill integrated in the 312 μm long well are shown in Figure 5-44. The left gap length seen in Figure 5-44b was measured at 7.9 μm long. The right gap (seen in Figure 5-44c) length was measured at less than 1 μm. The lateral alignment looks very good for the right facet. The left facet is shifted by about 1.5 μm relative to the interconnect waveguide.

Compare these images with the images of the left and right facet for the pill integrated in the 310 μm long well. This was another case in which transmission was measurable. The peak measured transmission power was about 3 dB lower than for the pill in the 312 μm long well. Notice that the gap lengths are similar to the case

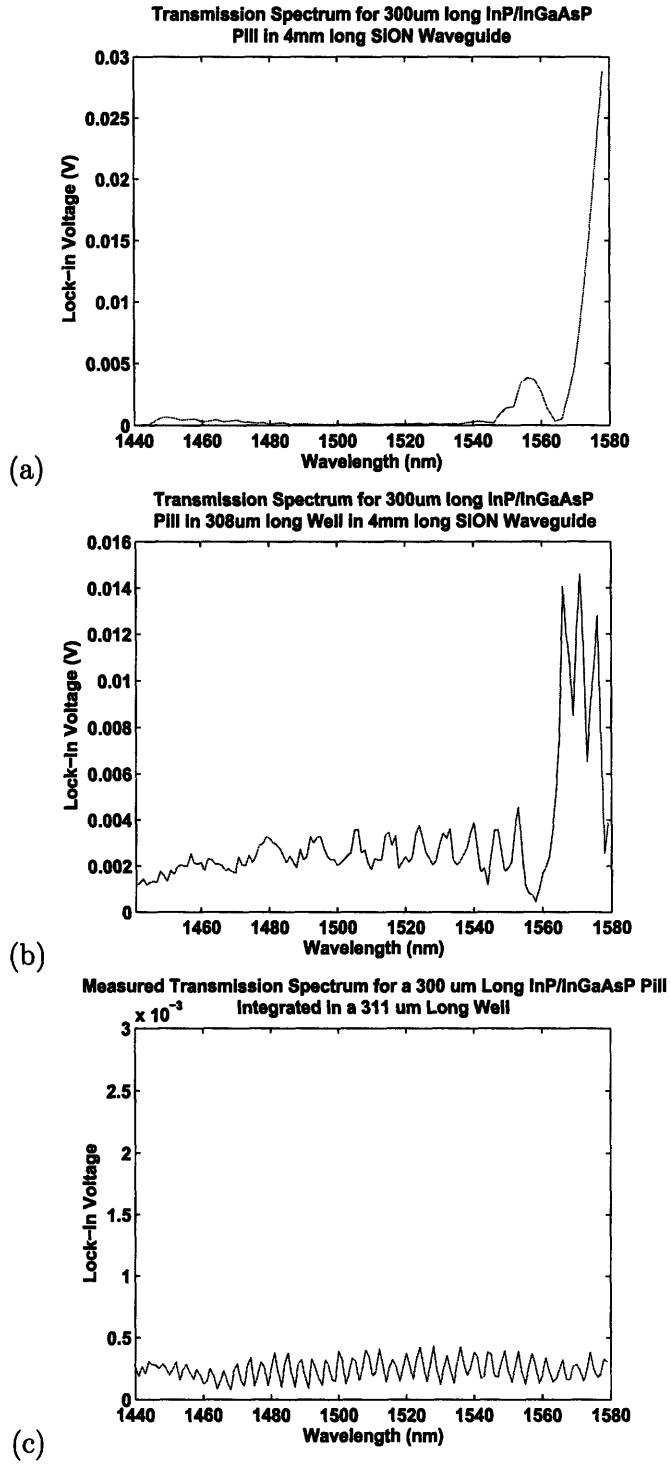

Figure 5-43: A comparison of the transmission spectra for three of the six integrated pills. These three spectra are a good representation of what was seen. (a) The transmission spectrum for the integrated pill with maximum transmission. This was for the pill in the 312 μm long well. (b) Transmission spectrum for the integrated pill in the 308 μm long well. (c) Transmission spectrum for the pill in the 311 μm long well.

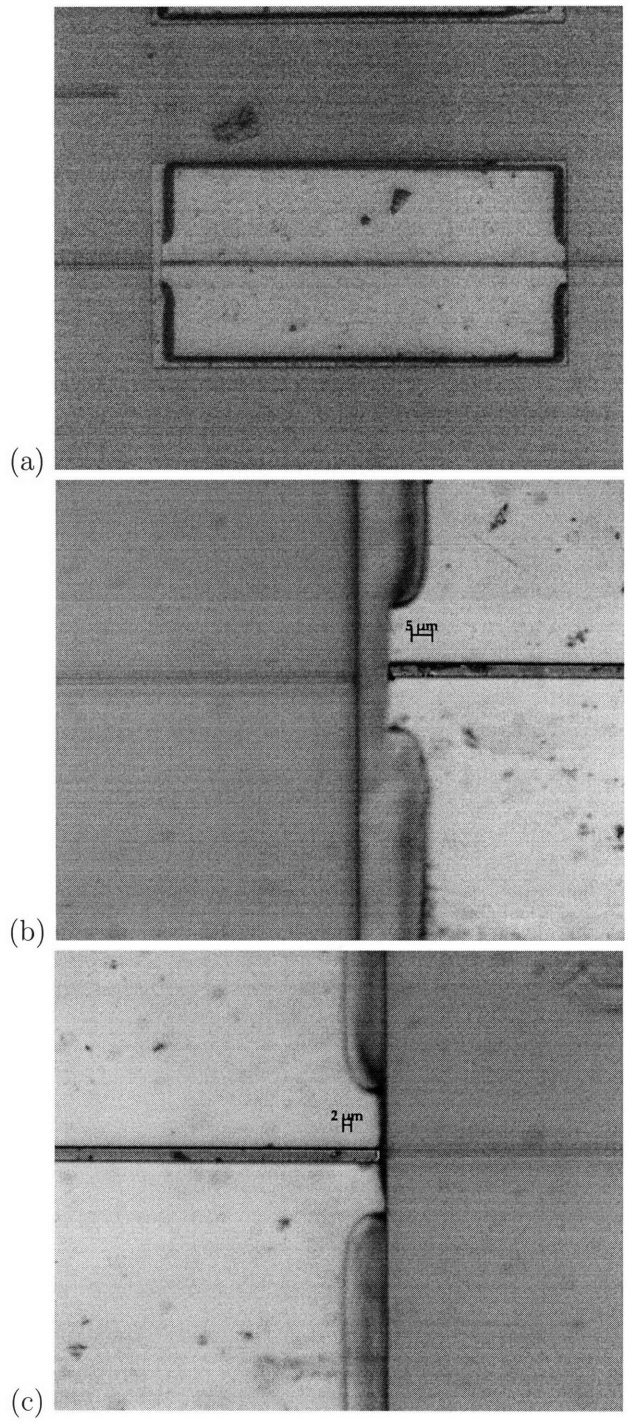

Figure 5-44: Photomicrographs of the integrated pill with the highest transmission. (a) Entire pill, (b) Left facet, (c) Right facet. The left gap is approximately 7.9 μm and the left facet is shifted approximately 2 μm laterally. The right gap is approximately 1.5 μm and the right facet is shifted approximately 0.5 μm.

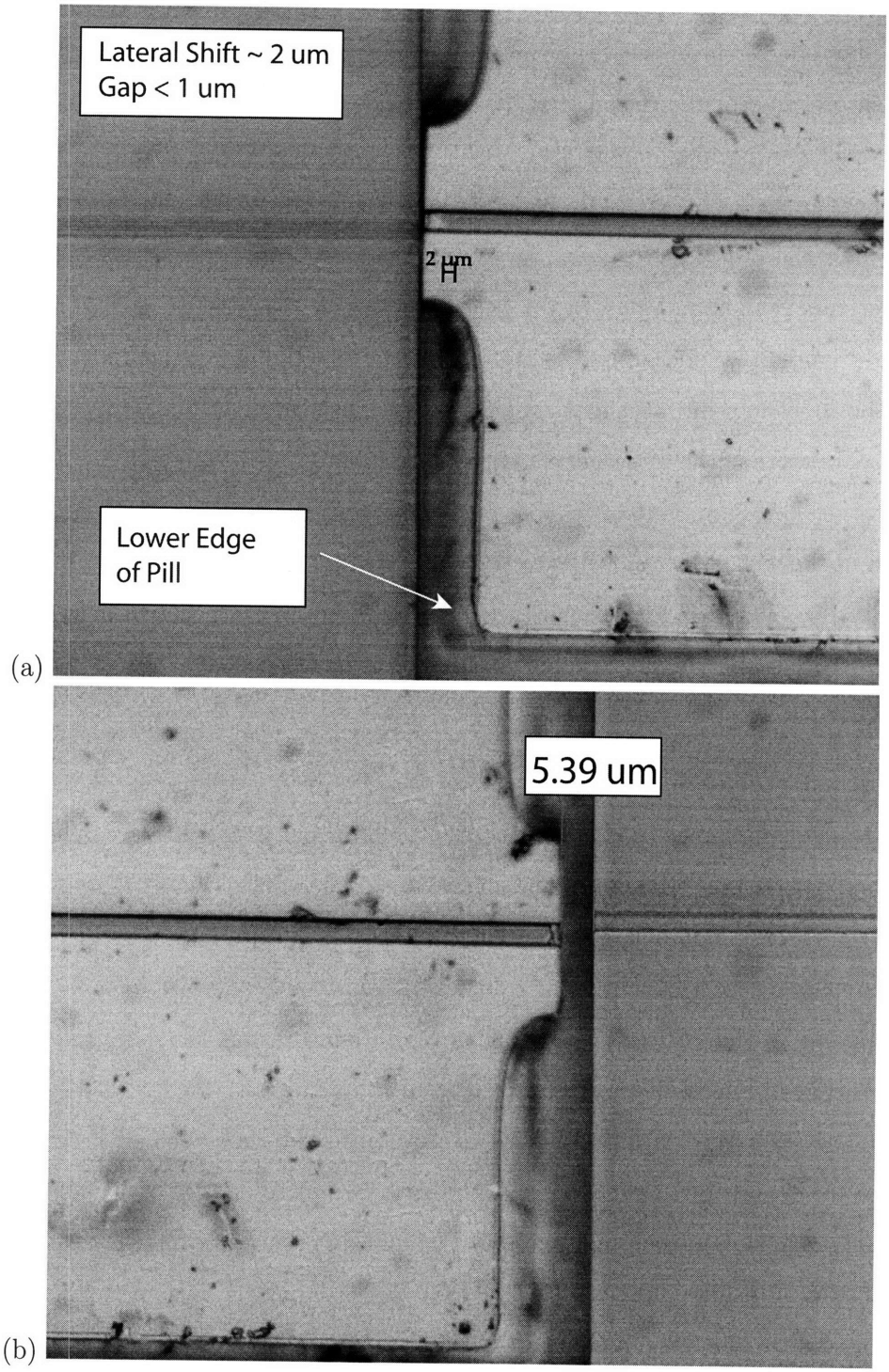

Figure 5-45: (a) Left and (b) Right facets of the integrated InP/InGaAsP ridge waveguide pill in the 310 μm long well.

for the 312 μm long well, with the longer gap about 2.5 μm shorter. However, in this case, the shorter facet with the shorter gap was not aligned as well as the facet for the shorter gap of the pill in the 312 μm long well (Figure 5-44c). Recall from the analysis resulting in the plots shown in Figure 5-33 that a lateral shift across a very narrow gap incurs more additional loss than the same lateral shift across a longer gap. For the pill in the 312 μm long well, the shifted facet was the facet with the longer gap. The lateral shift of the facet with the very short gap was immeasurable.

In Figure 5-46, photomicrographs of the facets for the pill in the 311 μm long well are shown. The right facet looks good, but the left facet looks almost too good to be true. Notice that the interconnect waveguide stack is out of focus, more so than for the images in Figure 5-44 or 5-45. It is believed that this pill was not actually sitting down in the well, which is why the transmission was immeasurable.

Finally, the facets for the pill in the 309 μm long well are shown in Figure 5-47. The reason for the immeasurable transmission is quite clear.

5.5.3 Transmission Spectrum Analysis

The transmission spectra for pills in the 308, 310 and 312 μm long wells have the characteristic shape of higher transmissivity at longer wavelengths, implying that the transmitted light has propagated through the multi-quantum well core. The periodicity in the spectrum is most likely the result of mode interference as seen in the spectra for the isolated pills. A higher resolution transmission spectrum of the pill in the 312 μm long well is shown in Figure 5-48b along with a copy of the spectrum which was already seen in Figure 5-43a. As seen many times before, the oscillation with a period on the order of 3 nm is the Fabry-Perot resonance of the 300 μm long pill. The longer period oscillation is consistent with the mode interference that was seen in the transmission spectra of the isolated 300 μm long pills.

The one significant difference between the measured spectrum for the pill in the 312 μm long well and the isolated pill of Figure 5-35, (see the comparison in Figure 5-49 is the long wavelength to short wavelength peak transmitted power ratio. This ratio is significantly higher for the integrated pill. This is partly due to the difference

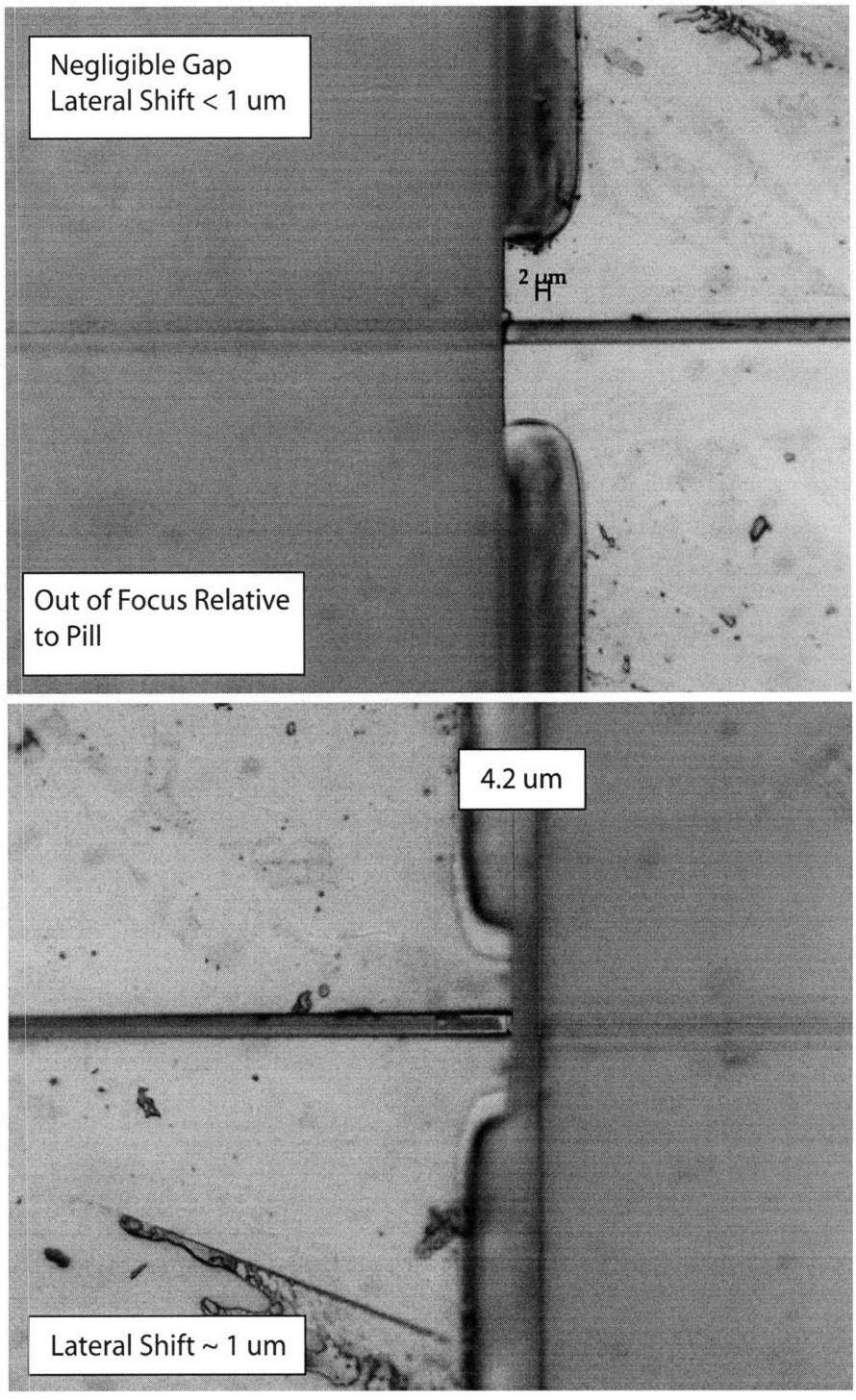

Figure 5-46: (a) Left and (b) Right facets of the pill integrated in the 311 μm long well. Notice that the waveguide stack is out of focus, more so than in Figure 5-45. It is believed that the very weak transmission through this pill was the result of vertical misalignment, as implied by the waveguide stack being out of focus.

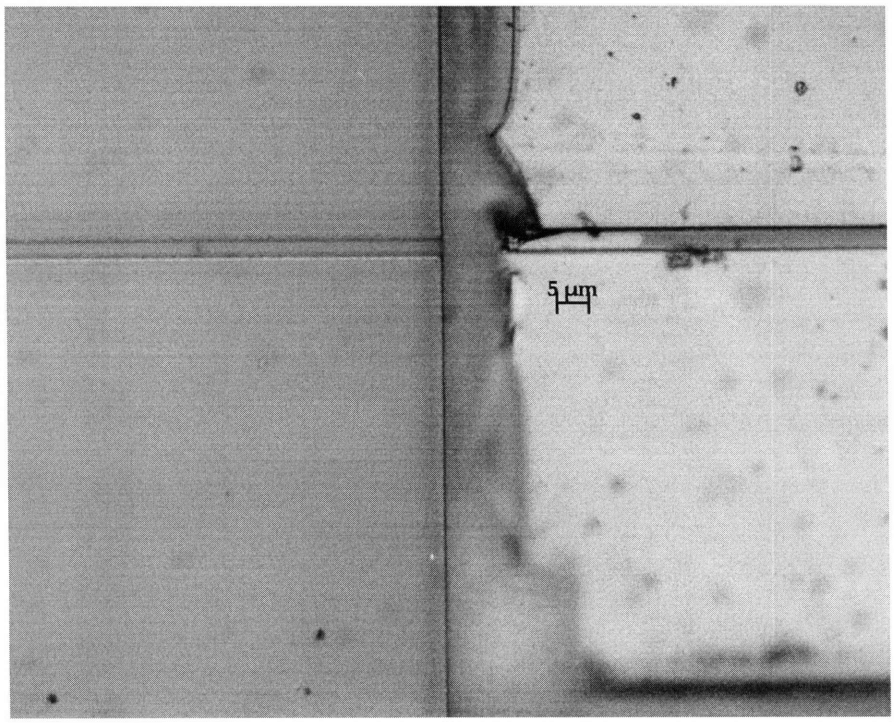

Figure 5-47: Left facet was broken during handling. The undetectable signal is clearly a result of facet scattering loss.

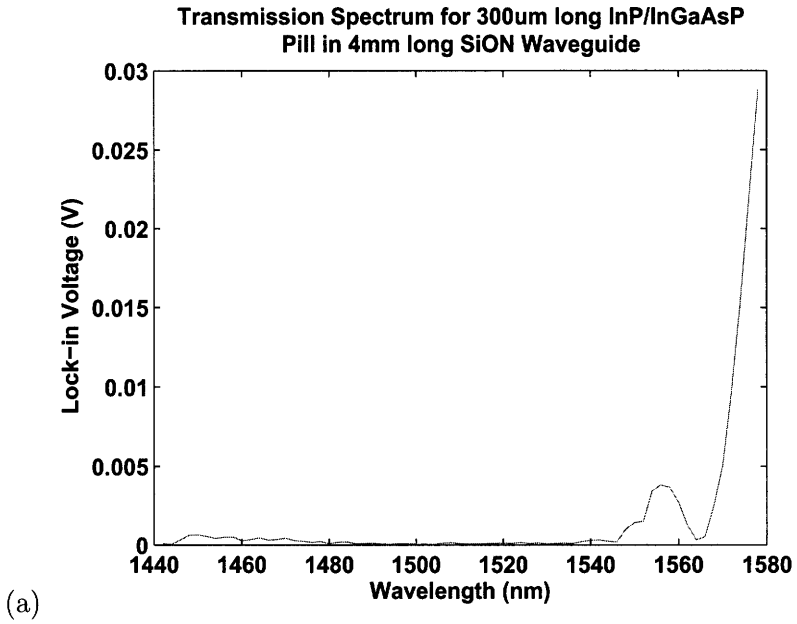

(a)

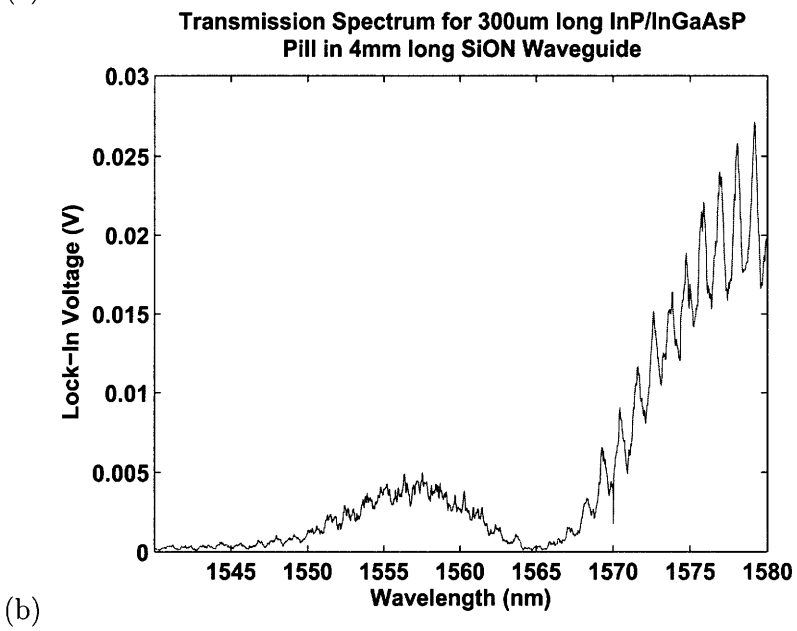

(b)

Figure 5-48: Best transmission results for an integrated pill: (a) Broad spectrum, (b) Detail of the longer wavelength portion of the spectrum.

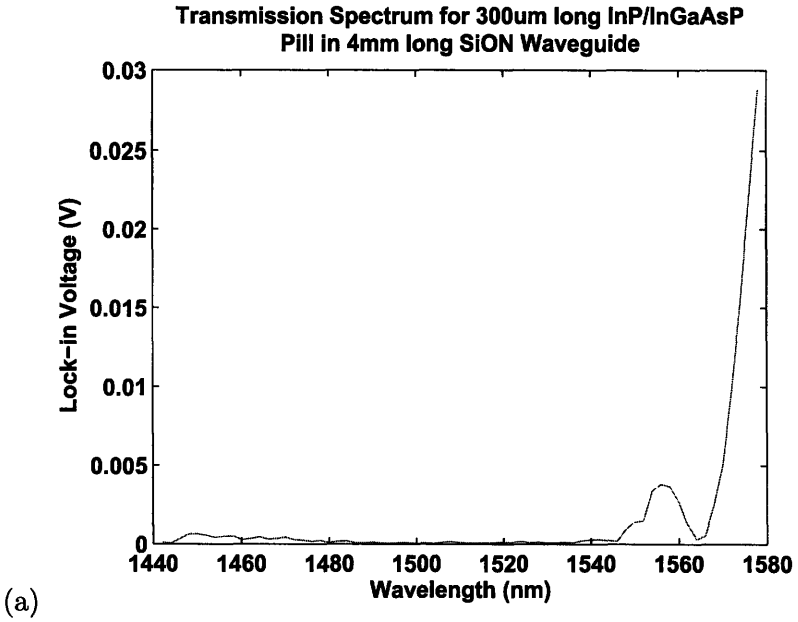

(a)

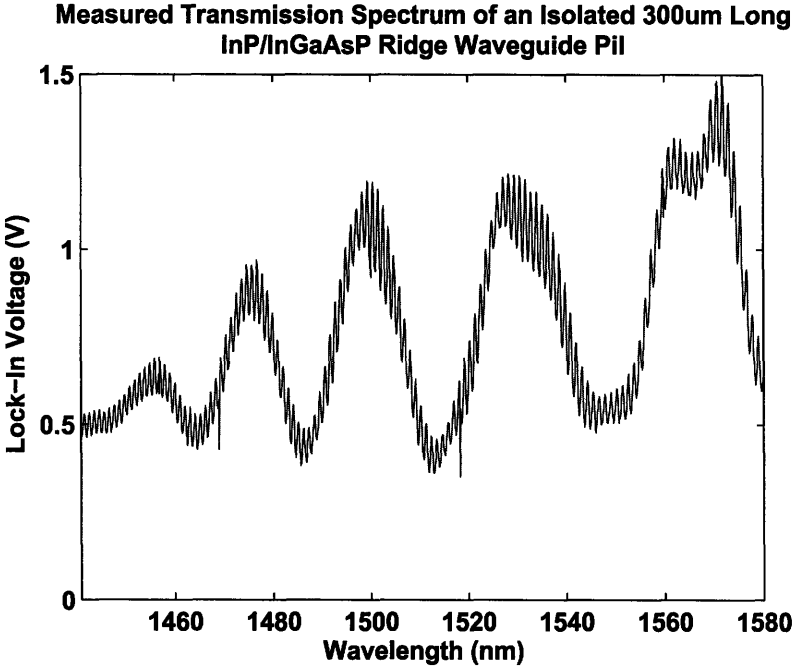

(b)

Figure 5-49: Comparison between the measured transmission spectrum for (a) the pill integrated in the 312 μm long well and (b) an isolated 300 μm long InP/InGaAsP ridge waveguide pill.

in the profile of the wave that is incident on the front of the isolated pill and the wave incident on the front of the integrated pill. Recall, of course, that the isolated pill was measured with the input fiber and the output fiber right next to the input and output facets of the pill. The lateral wave profile of the input lensed fiber is certainly different than the profile of the wave emitted from the etched facet of the interconnect waveguide at the edge of the well. Given the larger profile of the lensed fiber relative to the interconnect waveguide facet, more of the cladding modes (the loss of which is less wavelength dependent than the core modes) would be excited for the isolated pill than the integrated pill. This would be consistent with the higher long wavelength transmission to short wavelength transmission ratio for the integrated pill.

Polarization Sensitivity

Another effect that should be taken into consideration is the polarization dependent loss for the interconnect waveguides and the InP/InGaAsP ridge waveguides. In all of the transmission measurements, the polarization controller[9] was adjusted to maximize the transmission. That is, each time the interconnect waveguides or the isolated pills were measured, the polarization controller was adjusted until the voltage on the lock-in amplifier was maximized. This was always done at or near a wavelength of 1580 nm. It is likely that the polarization for maximum interconnect waveguide transmissivity is different from the polarization at which the transmissivity is a maximum for the InP/InGaAsP ridge waveguides. The result would be that even for perfect coupling between the interconnect waveguide and the integrated pill, the measured transmission loss would be higher than what would be expected based on the measurements for the isolated interconnect waveguide and the isolated pill.

To investigate this effect, transmission spectra were taken for polarizations coinciding with maximum and minimum transmission for the interconnect waveguides (Figure 5-50), the isolated 300 μm long pills (Figure 5-52), and for the pill integrated in the 312 μm long well (Figure 5-52). Notice that for the polarization corresponding

[9]The polarization controller is a series of three paddles through which a fiber is run. By rotating the paddles stress is placed on the fiber, altering the polarization of the emitted light.

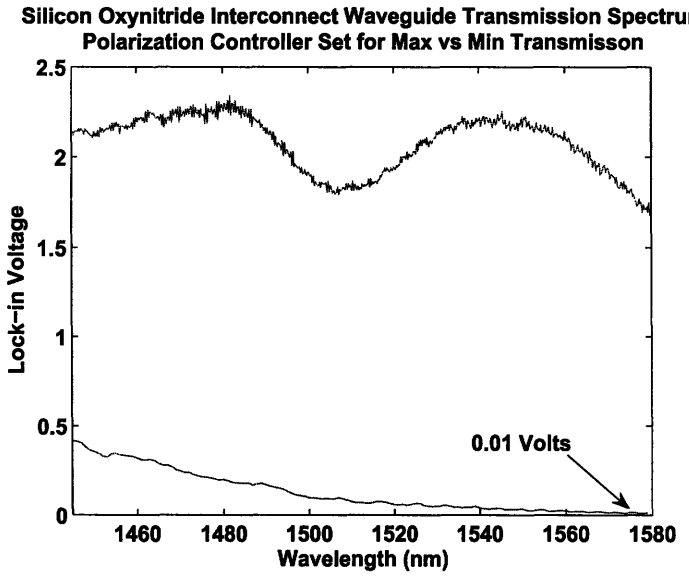

Figure 5-50: Interconnect waveguide transmission spectra. Comparison between the transmission spectrum for a polarization corresponding with maximum transmission and the transmission spectrum for a polarization corresponding with minimum transmission.

with minimum transmission at a wavelength of 1580 nm in Figure 5-52, the transmission is higher at the shorter wavelengths than it is for the polarization corresponding with maximum transmission at 1580 nm. In fact, for the mid wavelength range (1460 - 1540 nm) the spectrum for polarization for minimum transmission at 1580 nm resembles the transmission spectrum for the isolated pill (Figure 5-35). In Figure 5-53, these two spectra are compared, where the isolated pill spectrum has been scaled for a better comparison and it has been shifted[10] by approximately 10 nm.

It would seem from this figure that the polarization that gave the highest transmission for the integrated pill at a wavelength of 1580 nm, was a polarization for which the polarization dependent loss in the surrounding interconnect waveguides was higher in the mid wavelength range than the higher wavelength range. It appears that neither of the spectra in Figure 5-50 for the interconnect waveguides has

[10]When the spectrum is dominated by multimode interference, shifting the spectrum by about 10 nm corresponds to shortening or lengthening the pill by 1.5 μm. As the integrated pill and the isolated pill were not the same length and could have easily differed by 1.5 μm, this shifting is justified.

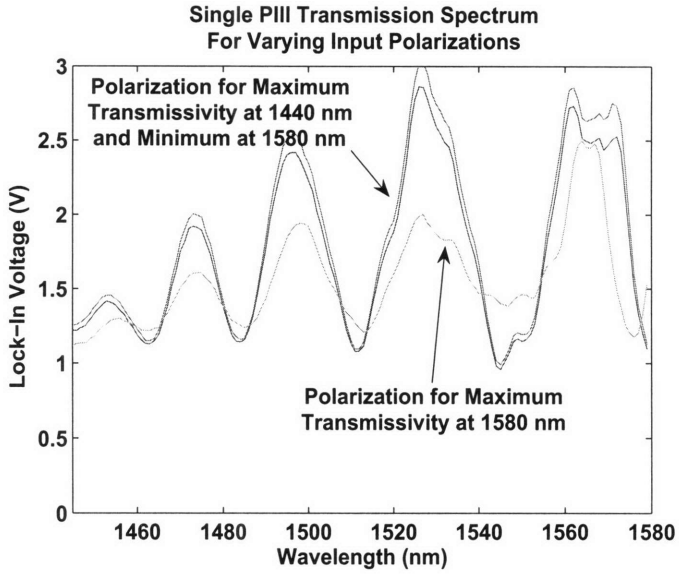

Figure 5-51: Transmission spectra for essentially two different polarizations. One polarization maximizes the transmissivity at 1580 nm, the other polarization results in the minimum transmission at 1580 nm. The polarization for maximum transmissivity at 1440 nm is essentially the same as the polarization for minimum transmissivity at 1580 nm and vice versa (as shown in the plot).

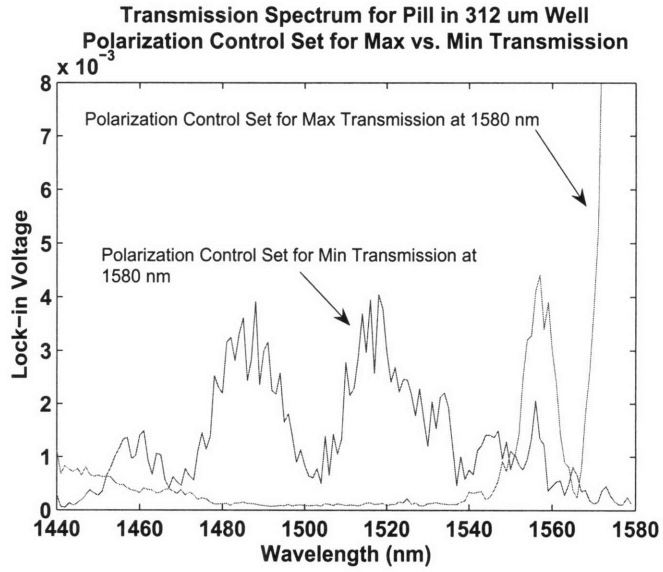

Figure 5-52: Transmission spectrum for the pill in the 312 μm long well with the polarization set for minimum transmission at 1580 nm compared with the spectrum with the polarization set for maximum transmission at 1580 nm.

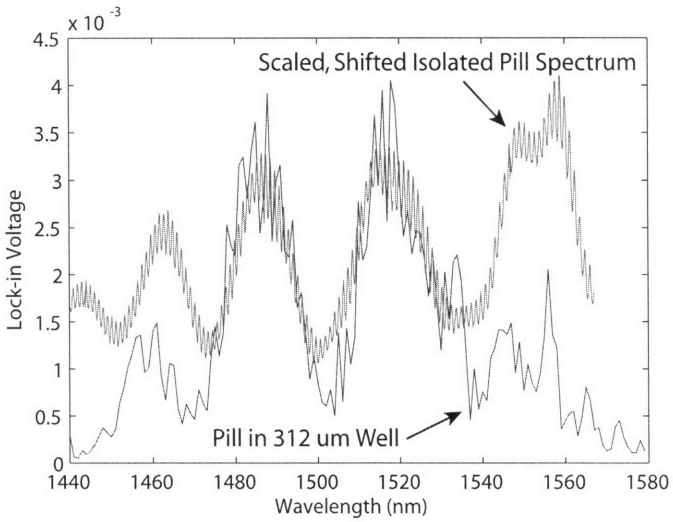

Figure 5-53: Transmission spectrum for the pill in the 312 μm long well with the polarization control set to a minimum, compared with the shifted, and scaled transmission spectrum of the isolated 300 μm long pill.

this characteristic. However, it is possible that for some other polarization, the spectra for the interconnect waveguides would have this characteristic. Based on the small change in the spectrum for the isolated pill for the two polarizations (Figure 5-51, it seems more likely that polarization dependent loss in the interconnect waveguides resulted in the discrepancy between the integrated pill spectrum and the isolated pill spectrum.

Coupling Loss Calculation and Comparison with FDTD Simulation Results

One of the ultimate goals of this thesis was to demonstrate coupling between the silicon oxynitride interconnect waveguides and the integrated InP/InGaAsP ridge waveguide pill structures. The data in this last section has shown that this was achieved for 3 of the 6 integrated pills. After determining why the transmission for some pills was higher than for others and why the spectra are shaped the way they are, the final step is to estimate the interface coupling loss.

In the transmission spectrum of the pill integrated in the 312 μm long well shown

in Figure 5-48, the maximum voltage measured on the lock-in amplifier was 27 mV. Recall that this was the integrated pill with the highest measured transmission. This value will now be used to estimate the interface coupling loss for this integrated pill by comparing it with the peak measured lock-in voltage for similar silicon oxynitride waveguides with no integrated pill. For the same input power, the average measured voltage on the lock-in amplifier for the interconnect waveguides without wells taken from the same chip was 1.25 V. Assuming no propagation loss in the pill, a worst-case coupling loss is computed as $10log_{10}(1.25/.027) = 16$ dB. That implies an average facet loss of 8 dB[11]. This is consistent with the FDTD simulations of Chapter 3 given the measured gap lengths and lateral misalignment of the pill in the 312 μm long well. The FDTD data originally shown in Figure 3-18 is shown again in Figure 5-54 with a linear fit so that the coupling loss at a separation of 7.9 μm can be extrapolated. Notice that the loss is approximately 9.5 dB/facet. Recall from Figure 5-44 that the right facet gap for the integrated pill was less than 1 μm. This would mean a loss of about 4 dB for this facet. The lateral shift of the right facet was minimal, but the left facet was shifted about 2 μm. This contributes approximately 3 dB of additional loss. The facet scattering loss was about 0.5 dB/facet, or 1 dB total. Finally, recall that the angled etch added a total of 1 dB (0.5 dB/facet). The total simulated loss is about 18.5 dB.

This simulated result is actually higher than the measured loss of 16 dB. The difference is most likely a result of the fact that the measurements do not only detect light that is coupled into the fundamental mode of both the pill and the interconnect waveguides. Recall that there was nonzero transmission through the isolated pill at the shorter wavelengths where most of the core guided modes would have been filtered out. In fact, this accounted for approximately 1/3 (1.75 dB) of the total measured power at the peak near 1580 nm. Adding this to the measured value of 16 dB yields a total loss of 17.75 dB. This differs by 0.75 dB from the simulated results.

[11]This is a safe assumption. If one assumes 10 dB/cm loss in the pill, which is consistent with the measurements in the first section of this chapter, then the propagation loss over the length of the pill is 10 dB/cm * 0.03 cm, or 0.3 dB. Of course, the interconnect waveguide would have had a loss of approximately 7 dB/cm, or 0.021 dB total. Clearly, the propagation loss is not dominating the overall loss and need not be considered in the calculation of the interface coupling loss.

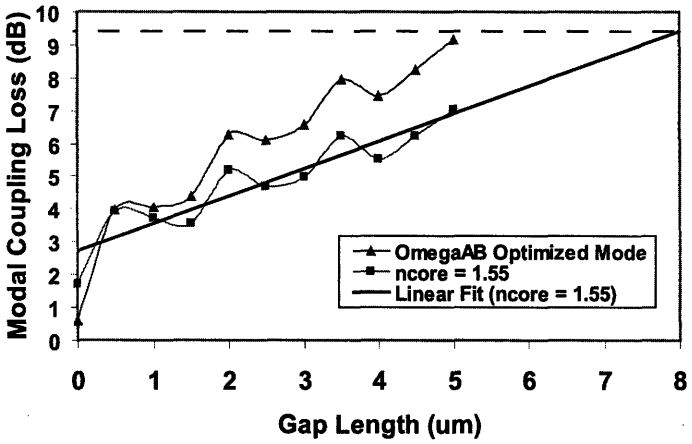

Figure 5-54: FDTD simulation results for interface coupling loss. Linear fit added to extrapolate out to 7.9 μm.

5.6 Summary

In the first section of this chapter, the propagation losses were determined by applying the Fabry-Perot propagation loss measurement technique for the silicon oxynitride waveguides. It was determined that fora width of 1.7 μm and a thickness of 0.7 μm, the average propagation loss was 7.3 dB/cm. In the second section, the propagation loss was approximated for the fundamental mode of the InP/InGaAsP ridge waveguide structures with the full substrate. This required a consideration of the multimode behavior of the waveguides. Based on the evaluation of the equation for the transmissivity for a waveguide with two interfering modes, the propagation loss was approximated at 9.6 dB/cm.

Etched gaps were measured and a model based on T-matrices for a multimode waveguide structure, the gap loss was extracted. It was shown that a high index gap fill material improves the coupling across that gap. Loss due to scattering at the rough interface was determined to be on the order of 0.5 dB/facet.

Transmission measurements were taken for isolated pill structures and six integrated pill structures. By comparing the spectra for the isolated and integrated

pills, it appears that polarization dependent loss in the two structures was limiting the maximum attainable transmitted power for the integrated pill. By comparing the highest measured transmitted power for an integrated pill with the transmitted power for waveguides with no pill and by removing the portion of the measured power attributable to cladding modes, the total coupling loss was found to be 17.75 dB. This is slightly lower than the FDTD simulated transmission loss of 18.75 dB. For two other of the six integrated pills, the transmission was measurable and that coupling loss was about 3 dB higher, or 20.75 dB. For the remaining three integrated pills, the lack of a measurable transmitted power was due to vertical misalignment (pill not sitting in the well) and a broken facet.

Chapter 6

Conclusion

There have been many accomplishments in this work, and yet a great deal remains to be done. This chapter summarizes the accomplishments and offers suggestions for the direction of future work.

6.1 Summary of Findings and Accomplishments

In this thesis, the design, fabrication, and characterization of a passive silicon-based photonics substrate was developed for the integration of InP/InGaAsP multi-quantum well ridge waveguide structures. These structures were assembled on the passive photonics substrate in wells etched into the silicon oxynitride waveguide stack. The silicon oxynitride waveguides, the InP/InGaAsP ridge waveguide structures, and the integrated system as a whole were characterized.

Silicon Oxynitride Waveguides

Silicon oxynitride core, silicon dioxide cladding waveguides were designed, fabricated, and characterized. The average propagation loss of the waveguides with optimum dimensions was measured as 7.3 dB/cm, which is consistent with the propagation loss of similar waveguides reported in the literature. The determination of the exact dimensions and index of refraction of the core for the waveguide was based on the optimization of coupling between the silicon oxynitride waveguides and the InP/InGaAsP

ridge waveguides found through Finite Difference Time Domain (FDTD) simulations. These simulations accounted for expected variations in the alignment of the integrated ridge waveguide pill structures.

Deep Waveguide Stack Etch

A process based on a polysilicon/silicon dioxide double hard mask design was developed for the etching of the thick (> 7 μm) waveguide stack. While the development of MEMS and MOEMS (Micro Opto-Electro-Mechanical Systems) technology has made the processing of thick layers more common, the etching of a silicon dioxide layer of this thickness is not a standard processing step. The success was the result of the double hard mask step and the proper etching chemistry and chamber conditions as discussed in Section 4.2.2.

Measurement Setup, Gap Measurements, and Modeling

For the measurements in this thesis, a waveguide measurement setup was refurbished and custom chucks and mounts were designed and machined. A technique was developed for the measurement of gap losses in which the transmission spectra of waveguides with varying numbers of etched gaps were compared to extract the loss incurred in coupling across a gap etched into the waveguide stack. Matlab scripts were written to model the gaps using T-matrices and multimode interference, with good qualitative agreement. Based on comparisons with FDTD simulations, scattering from the etched facets contributes approximately 0.5 dB per facet. It was also shown that as theorized, filling the gap with a material (other than air) and, in particular, with a refractive index of 2.2, the gap losses could be reduced.

Integration and Measurement of InP/InGaAsP Ridge Waveguide Pill Structures

InP/InGaAsP ridge waveguide pill structures were characterized and integrated in the wells etched into the silicon oxynitride/silicon dioxide waveguide stack. Coupling was measured for fifty percent of the pills that were integrated. For the best case,

the coupling loss was determined to be 17.75 dB. This is comparable to the 18.5 dB figure obtained from FDTD simulations.

6.2 Recommendations

While much was accomplished by the work presented in this thesis, there is much that still remains to be done in order to achieve the final goal of active III-V optoelectronic devices integrated with waveguides on silicon. Some recommendations for achieving this goal are given in this section. In addition, it is shown that the coupling loss for integrated InP/InGaAsP ridge waveguide devices could be significantly improved with only better pill alignment. Also, it is shown that the optimum waveguide design given better alignment yields an even lower coupling loss than the current waveguide design given this same better alignment.

Device Assembly

The device assembly method used in this thesis was rather rudimentary. It worked well for proof of concept, but continued work would necessitate some improvements. First, there should be a way to mount the pill and hold it in place. Either the pill needs to be bonded in place while it is being held down, or the spacing between the edges of the pill and the edges of the well need to be reduced so that the pill is not able to move much when the micropipette is removed. The reduction of the spacing requires vertical sidewalls for the edges of the pills (something currently being explored) and vertical sidewalls for the deep well etch. The latter could be achieved with a metal hardmask and an inductively coupled plasma (ICP) etcher, a combination that was not available in the labs used for the work in this thesis.

Improved Coupling

Improvements in the device assembly would drastically improve the coupling. Recall from the results and discussion in Section 5.5.2 that the best aligned facet had a gap length less than 1 μm. There is no fundamental reason for why the left and

right gap lengths for integrated pills could not both be less than 1 μm. Given the current waveguide design, a vertical sidewall well etch as discussed above, and lateral misalignment for both facets equal to the best measured value (less than 1 μm) the coupling loss for a pill with both gaps no greater than 1 μm would be on the order of 8.5 dB less than the measured value of 17.75 dB, or 9.25 dB. The use of an index matching material (like BCB) could reduce the scattering loss due to the etched facet roughness by as much as 0.5 dB/facet, lowering the total loss to 8.25 dB. While this exact loss value may not be achieved with these improvements, this analysis does demonstrate that reasonable and feasible improvements could cut the coupling loss in half.

Given the demonstrated shortest gap length on the order of 1 μm for well sidewalls with an 80^o angle, it is likely that this shortest gap length would be reduced for the case of a vertical sidewall well etch. Given that left and right gap lengths both less than 1 μm could be achieved and shown to be repeatable, the optimum waveguide design would correspondingly need to be changed. Recall that the original waveguide design in Section 3.2.3 was for coupling without a gap. It was shown that for no gap, the optimum design given a silicon oxynitride cladding was for a waveguide core with an index of 2.0, which is the refractive index of the material silicon nitride (which can be deposited using the same PECVD deposition system used to deposit the silicon oxynitride in this work) and a thickness of 0.3 μm. Simulations based on a 0.5 μm long gap with this waveguide design show coupling losses lowered by 2.5 dB per facet, reducing the total loss to 3.25 dB. Of course, this design places stricter tolerances on the vertical and lateral misalignment, and the issue of fabricating smaller waveguides to maintain single mode operation would need to be addressed, but it shows again that reasonable improvements could significantly reduce the coupling loss and that it is the alignment technique, not something fundamental, that limits the achievable coupling efficiency.

System Level Consideration

If the integrated pill were to be operated as a semiconductor optical amplifier (SOA), the gain of the SOA could be improved by choosing an operating wavelength at the peak of the gain curve for a structure and material that gives the highest known optical gain. For instance, it is possible that a larger gain relative to that achieved with the InP material system could be achieved with the GaAs material system operating at a wavelength of 850 nm. The 1550 nm wavelength used in this thesis was based on the minimum fiber dispersion requirements of long haul telecommunications networks. For the shorter interconnect lengths involved in chip-to-chip interconnects, the minimization of the losses in coupling between the on-chip waveguides and the printed circuit board (PCB) waveguides and the minimization of propagation loss in the PCB waveguides are more crucial than dispersion minimization.

Optimum Pill Shape

Another possible area for improvement is the shape of the integrated pill. Currently, the basic shape of the pill when viewed from above as shown in the microscope images in Section 5.5.2 is rectangular. As illustrated in Figure 6-1, a wedge shape, for instance, would force the pill into perfect lateral alignment. Even if the pill or the well was slightly over or under etched, as long as the angle was well controlled (which is typically the case as this is a function of the well controlled wafer and stage alignment of stepper photolithography systems) the pill would still be well aligned laterally.

The Future

While it is unknown if optical interconnects will ever be a viable technology for chip-to-chip communication, there is reason to believe that the advancement of integrated photonics in general will benefit from the integration of multiple materials on a single substrate, as many of the material requirements for the various photonic devices are orthogonal, requiring more than a single material. Towards that end, the work in

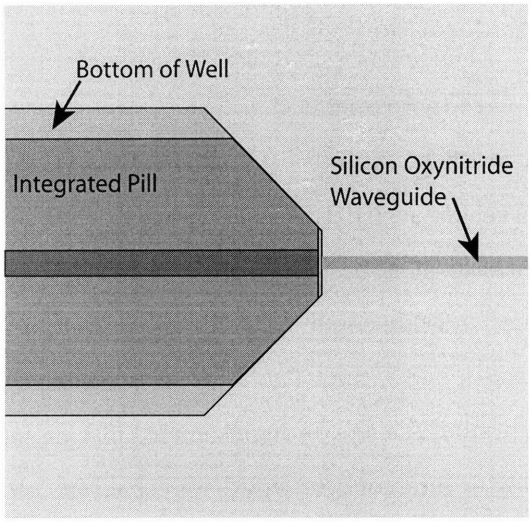

Figure 6-1: Shapes other than rectangular could improve the alignment of the pill in the well. A wedge shape shown here would greatly improve the lateral misalignment.

this thesis provides the foundation for understanding the issues involved with multiple material integration for in-plane photonics applications.

Appendix A

Transmission Measurements

Aside from visual inspection, the most frequently used measurement technique for this work is the on-chip waveguide optical transmission spectrum. This spectrum gives insight into both the coupling efficiency and the waveguide loss. This appendix details this measurement technique and how the data from these measurements can be used to characterize the devices and quantify the coupling efficiency. It also details the T-matrix, which, for the purpose of this work, is a mathematical description of either an interface between dielectric materials of differing refractive index, or a dielectric segment of some length and some propagation loss.

A.1 Transmission Spectrum Measurement Setup

Transmission spectrum measurements were used repeatedly throughout this work to provide a quantitative assessment of the device fabrication and integration. As such, it is a vital part of this work. These measurements involve coupling monochromatic light of a known wavelength from a tuneable laser[1] into one end of an on-chip waveguide via a lensed fiber[2] The light emitted from the other end of the waveguide is coupled

[1]The laser used for this work is an HP 8168F with emission in the range of 1430-1590nm. The wavelength can be stepped by 1 picometer.

[2]A lensed fiber is a fiber with a lensed tip. The lens is created either by polishing or melting the end of the fiber into a lens shape. In the case of melting, the tip is heated via a high voltage arc to the point of reflow. Surface tension pulls the surface into a spherical shape. Manufacturers can actually control the radius of curvature of the surface in order to set the working distance and spot

into a second fiber and sent to a photodetector. The optical power measured by the photodetector is recorded. The laser emission wavelength is stepped over some range of values, and the optical power measured by the photodetector is recorded for each wavelength. In order to remove the effects of photodetector dark current and stray light that is coupled into the output fiber, a lock-in amplifier is used[3]. A schematic of the complete measurement setup[4] is shown in Figure A-1. The positioning stages that hold the input and output fibers are three axis piezoelectric stages with position controlling feedback circuitry to reduce the effects of mechanical drift. The IR laser and the lock-in amplifier are connected via a GPIB interface to a computer running LabView. The computer is able to set and step the laser wavelength and store the lock-in amplifier voltage.

The final component in the measurement setup is a polarization controller. The polarization controller consists of input and output fiber ports and three paddles through which the fiber is run. When the paddles are rotated, the fiber is distorted inducing a shift in the polarization of the propagating light. This is an important

size of the emitted light.

[3]A lock-in amplifier reduces the influence of noise and dark current on the measured signal by locking in to the part of the photodetector current that is solely in response to the light coming from the input IR laser. The other parts of the photocurrent are filtered out. This works as follows. The chopper modulates the input light from the fiber with a square wave of some frequency f_{chop} (typically in the hundreds of Hz to a few kHz range). The photodetector generates a current that is the summation of the dark current, current due to stray light, and current due to light from the IR laser. This total current is sent to the lock-in amplifier as signal A. Signal A has a dc component due to the dark current and unmodulated stray light, a component at frequency f_{chop}, and components at other frequencies due to other optical and electrical noise sources. In addition to signal A, the square wave signal that corresponds to the chopper square wave modulation is also sent to the lock-in amplifier as signal B. The lock-in amplifier multiplies signal A by signal B. The signal generated by the multiplication of two signals with frequencies f_1 and f_2 is a signal with new frequency components at the sum, $f_1 + f_2$, and difference, $f_1 - f_2$, of the original frequencies. Both signal A and signal B have a component at f_{chop}, so when they are multiplied, the resulting signal, AB, has a dc component due to the difference. The signal AB is then sent through a low pass filter to remove the influence of all other components. The voltage level of this filtered signal is sent to the lock-in amplifier display. It is this voltage that is recorded in these transmission spectrum measurements.

[4]Notice that in addition to the IR tunable laser, light from a red laser is also coupled into the on-chip waveguides. This is done solely for the purpose of vertically aligning the input lensed fiber for optimum coupling. The microscope can of course be used for in-plane alignment, but it is difficult to tell if the fiber is emitting light just above, right on, or just below the waveguide. In the case of coupling into the silicon oxynitride waveguides, the red light also provides verification that the light is actually being guided by the waveguide, as opposed to simply being coupled into cladding or substrate modes.

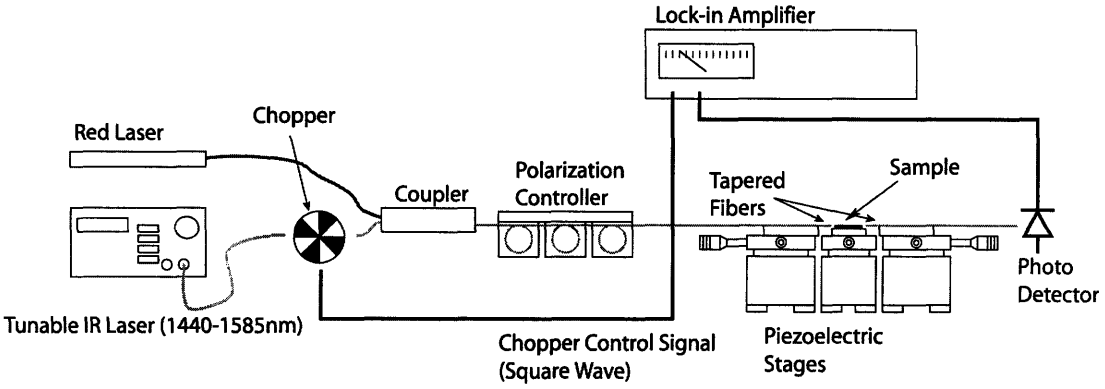

Figure A-1: On-chip waveguide transmission measurement setup.

components because both the silicon oxynitride waveguides and the InP/InGaAsP waveguides have polarization dependent loss ratios as high as 20dB.

A.1.1 Waveguide Loss Measurements

There are two techniques that can be used to measure waveguide propagation loss with the type of measurement setup described above. The first is commonly referred to as the cutback technique. It involves coupling light into waveguides of varying lengths and measuring the light coupled out of each of the waveguides. The propagation loss can be extracted from a plot of the measured light out versus waveguide length. The second approach, called the Fabry-Perot loss measurement, is essentially a measurement of the quality factor of a Fabry-Perot cavity. A waveguide with cleaved facets forms a lossy Fabry-Perot cavity, and knowledge of the effective index and length of the waveguide together with a measured transmission spectrum (as described above) can be used to calculate the waveguide propagation loss.

Cutback Technique

With the cutback technique, the transmission through waveguides of varying lengths is measured and used to extract the waveguide propagation loss. This technique is named for the method originally used to achieve different waveguide lengths. A waveguide is cleaved to a certain length and then measured. The waveguide is then

cleaved to a shorter length and measured again, etc. The limitation to the accuracy of this technique arises from variations[5] in the fiber-to-waveguide and waveguide-to-fiber coupling for the measurements made at the different lengths. It is important that the change in measured light out from the measurement at one waveguide length to the next be dominated by differences in the waveguide length (and loss therefore), not by variations in the facet quality.

A technique commonly used to minimize the variation in facet quality with the cutback technique is to vary the length of the waveguides by laying them out with bends and varying the length of the waveguide between the bends. Often called the "paperclip" method, this technique requires just two cleaves (one on each end of the waveguides). Each waveguide is designed with an equal number of bends so that the loss from the bends is the same for each waveguide. For the silicon oxynitride waveguides in this work, a bend radius of 250μm was used for the paperclip waveguides.

A.2 The Fabry-Perot Technique

The Fabry-Perot technique has the advantage that the measurement is not dependent on the fiber-to-waveguide and waveguide-to-fiber coupling. This technique is based on the extraction of the waveguide propagation loss from the transmission spectrum for the waveguide. The peak/valley ratio, along with the facet reflectivity and the waveguide length are used to calculate the propagation loss. The reflectivity is approximated using the fresnel reflection equation,

$$R = \left(\frac{n-1}{n+1}\right)^2 \tag{A.1}$$

where the value used for, n, the refractive index, is the effective index of the waveguide fundamental mode[6]

[5]These fiber-to-waveguide and waveguide-to-fiber coupling variations are due to variations in the quality of the waveguide end facets.

[6]The Fabry-Perot method works best for single-mode waveguides. Its application to multimode waveguides is useful only in gaining an approximate value for the loss of the various modes.

A.2.1 Fabry-Perot Technique Loss Equation

The equation for the propagation loss can be derived from the T-matrix for a Fabry-Perot cavity, which can be calculated from the T-matrix for a material segment with absorption loss situated between two dielectric interfaces. The T-matrices for a dielectric interface and a material segment with complex propagation vector are

$$T_{int} = \frac{1}{t}\begin{bmatrix} 1 & r \\ r & 1 \end{bmatrix} \tag{A.2}$$

$$T_{mat} = e^{-i\beta L}\begin{bmatrix} 1 & 0 \\ 0 & 1 \end{bmatrix} \tag{A.3}$$

$$T_{FP} = T_{int1}T_{mat}T_{int2} \tag{A.4}$$

$$T_{FP} = \frac{e^{-i\beta L}}{t^2}\begin{bmatrix} 1 & -r \\ -r & 1 \end{bmatrix}\begin{bmatrix} 1 & 0 \\ 0 & 1 \end{bmatrix}\begin{bmatrix} 1 & r \\ r & 1 \end{bmatrix} \tag{A.5}$$

$$T_{FP} = \frac{e^{-i\beta L}}{t^2}\begin{bmatrix} 1-r^2 & 0 \\ 0 & -r^2+1 \end{bmatrix} \tag{A.6}$$

Solving for the transmission coefficient for the total Fabry-Perot cavity, A_2/A_1 yields

$$\frac{A_2}{A_1} = \frac{t^2 e^{i\underline{\beta}L}}{1 - r^2 e^{2i\underline{\beta}L}} \tag{A.7}$$

Where r is the reflection coefficient corresponding to incidence on the facets from inside the cavity,

$$r = \frac{n_{eff} - 1}{n_{eff} + 1} \tag{A.8}$$

assuming air outside the cavity. L is the length of the cavity and $\underline{\beta}$ is the complex propagation coefficient,

$$\underline{\beta} = \frac{2\pi n_{eff}}{\lambda} + i\alpha \tag{A.9}$$

where α is the field absorption coefficient. As previously described, the transmission spectrum measurement measures power, not field magnitude. An equation for the

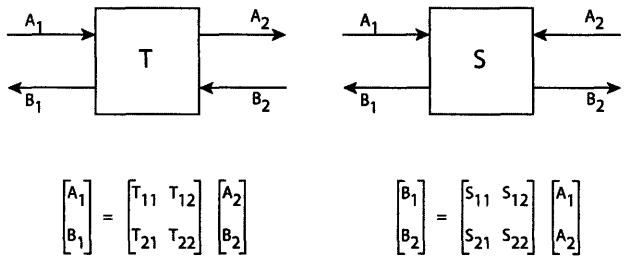

Figure A-2: T and S matrices.

power transmission spectrum can be found by squaring the magnitude of A_2/A_1.

$$T_{FP} = \left|\frac{A_2}{A_1}\right|^2 = \frac{t^4}{2 - 2r^2\cos(2\beta L)} \tag{A.10}$$

Solving for the maximum, I_{max}, and minimum I_{min} in the above equation and taking the ratio gives the desired final equation:

$$\alpha = \frac{-1}{2L} ln\left[\frac{1}{R}\frac{\sqrt{\frac{I_{max}}{I_{min}}} - 1}{\sqrt{\frac{I_{max}}{I_{min}}} + 1}\right] \tag{A.11}$$

A.3 Transmission Matrix

An optical transmission matrix (T-matrix for short) is a matrix that can be used to determine the transmission spectrum for a structure of arbitrary complexity. It relates incident and reflected field magnitudes on the right side of a structure, to the incident and reflected field magnitudes on the left side of the structure. The T-matrix is similar to the Scattering matrix which is composed of the more frequently used S-parameters of a structure. A T-matrix and the S-matrix are shown in Figure A-2. The difference is that the arrangement of the values of the T-matrix allows for T-matrices of two connected structures to be multiplied together to get the T-matrix for the combination of the two structures (see Figure A-3). In this way, the T-matrix for a complex structure can be determined by breaking it down into its fundamental elements, each of which has an easily determined T-matrix. The fundamental elements are a dielectric interface and a medium with a given length

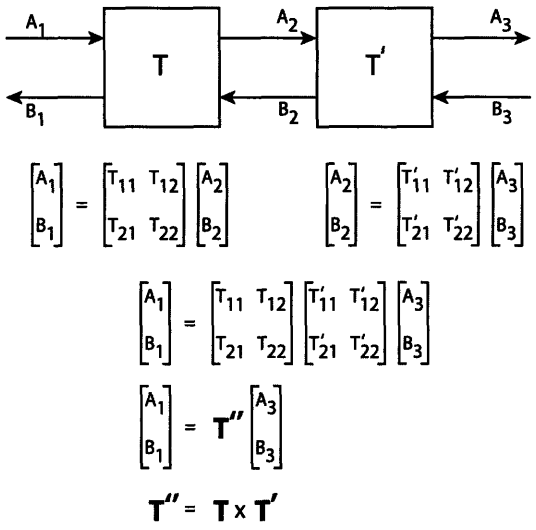

Figure A-3: T matrices for adjacent elements in a structure, T and T', may be multiplied to get one T-matrix, T'', for the combined structure.

and refractive index.

A.3.1 Dielectric Interface T-matrix

The T-matrix parameters for a dielectric interface can be found by starting with the matrix equations.

$$A_1 = A_2 T_{11} + B_2 T_{12} \tag{A.12}$$

$$B_1 = A_2 T_{12} + B_2 T_{22} \tag{A.13}$$

It is straightforward to express A_2 and B_1, the reflected field vectors, in terms of the incident field vectors and the interface reflection and transmission coefficients.

$$A_2 = t_1 A_1 + r_2 B_2 \tag{A.14}$$

$$B_1 = r_1 A_1 + t_2 B_2 \tag{A.15}$$

Rearranging equation A.14 yields

$$A_1 = \frac{1}{t_1} A_2 + \frac{r_1}{t_1} B_2 \tag{A.16}$$

Substituting this expression for A_1 in equation A.15 yields

$$B_1 = \frac{r_1}{t_1} A_2 + \frac{1}{t_1} B_2 \tag{A.17}$$

In equations A.16 and A.17 the following was used

$$t_1 = t_2 = t \tag{A.18}$$

$$r_1 = -r_2 \tag{A.19}$$

$$r_1^2 + t_1^2 = 1 \tag{A.20}$$

Hence the T-matrix for a dielectric interface is

$$T_{int} = \frac{1}{t} \begin{bmatrix} 1 & r_1 \\ r_1 & 1 \end{bmatrix} \tag{A.21}$$

Appendix B

Determination of Tmode for TE End-Fire Coupling

The goal of this Appendix is to find the transmissivity for two TE modes at an interface between two end-fire coupled slab waveguides with perfect alignment. Refer to Figure B-1 for this derivation. A mode is propagating in waveguide 1 from the left and is transmitted into waveguide 2 on the right.

The following equation gives the coupled power between two slab modes and is taken from page 604 of Reference [49]:

$$P_{1,2} = \frac{1}{4}\int \left(E_1(x) \times H_2^*(x) + E_2^*(x) \times H_1(x)\right) dx \tag{B.1}$$

where E is the electric field in the y direction and H is the magnetic field in the x direction. The subscripts refer to waveguides 1 and 2 shown in Figure B-1. A normalization factor, A can be applied so that the power for each mode is unity. Writing out the full normalized electric and magnetic fields in the y and x directions respectively for the components travelling to the right (positive z direction):

$$E_1 = A_1 Ep_1(x) e^{i\beta_1 z}\hat{y} \tag{B.2}$$

$$E_2 = A_2 Ep_2(x) e^{i\beta_2 z}\hat{y} \tag{B.3}$$

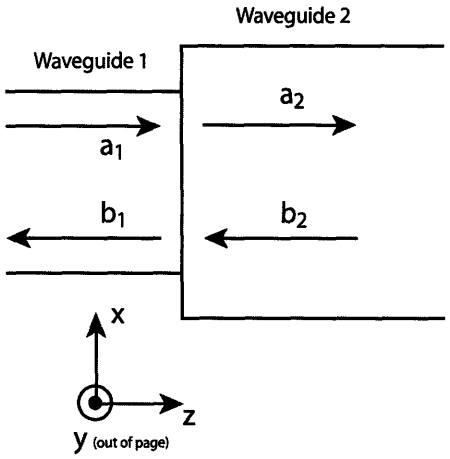

Figure B-1: Two end-fire coupled slab waveguides with left and right travelling field coefficients a and b.

$$H_1 = \frac{-\beta_1}{\mu\omega} A_1 Ep_1(x) e^{i\beta_1 z} \hat{x} \tag{B.4}$$

$$H_2 = \frac{-\beta_2}{\mu\omega} A_2 Ep_2(x) e^{i\beta_2 z} \hat{x} \tag{B.5}$$

where Ep_m is the mode profile for mode m, β_m is the propagation vector for mode m, μ is the permeability of the dielectric materials, and ω is the angular frequency of the electromagnetic wave. The normalization is found by setting the following condition:

$$P_m = \frac{1}{2} Re\left\{ \int (E_m \times H_m^*)\, dx \right\} = 1 \tag{B.6}$$

Applying this normalization yields the following:

$$A_m = \sqrt{\frac{2\mu\omega}{\beta_m \int (Ep_m(x))^2\, dx}} \tag{B.7}$$

Referring to Figure B-1, the following equations can be written:

$$a_2 = k_{11} a_1 + k_{12} b_1 \tag{B.8}$$

$$b_2 = k_{21} a_1 + k_{22} b_1 \tag{B.9}$$

The desired value is the ratio a_2/a_1, which is t, the transmission coefficient (it is actually T, the transmissivity that is desired, but that is found by squaring t). From the previous two equations:

$$t = \frac{a_2}{a_1} = k_{11} - \frac{k_{12}k_{21}}{k_{22}} \tag{B.10}$$

Applying Equation B.1 for the mode overlap power:

$$k_{22} = k_{11} = \frac{1}{4}\int \left(E_1(x) \times H_2^*(x) + E_2^*(x) \times H_1(x)\right) dx \tag{B.11}$$

$$k_{22} = k_{11} = \frac{1}{4}\int \left(E_1(x) \times H_2^*(x) - E_2^*(x) \times H_1(x)\right) dx \tag{B.12}$$

The minus sign is a result of the fact that k_{22} and k_{11} are for the overlap of waves propagating in opposite direction. Solving these equations and substituting the results into Equation B.10 yields:

$$t = T_{Fresnel}\frac{\int Ep_1(x)Ep_2(x)dx}{\sqrt{\int \left(Ep_1(x)\right)^2 dx \int \left(Ep_2(x)\right)^2 dx}} \tag{B.13}$$

where $T_{fresnel}$ is just the Fresnel transmission coefficient where,

$$T_{Fresnel} = 1 - R_{Fresnel} \tag{B.14}$$

and

$$R_{Fresnel} = \left[\frac{\beta_1 - \beta_2}{\beta_1 + \beta_2}\right]^2 \tag{B.15}$$

Appendix C

Process Recipes

This appendix contains all of the process recipes that were used to fabricate the waveguides and the etched wells. The waveguide and well etch processes are first shown as a series of steps. Following this section, the details of the individual steps are given.

C.1 Process Steps

Waveguide Deposition and Etch Process:

Step Name	Description/Details	Tool
1. RCA Clean	Basic Wafer Clean	rca-ICL
2. Oxide Dep	0.5 μm of oxide on front of wafer to protect wafer during backside deposition	DCVD
3. Oxide Dep	3 μm of oxide on back of wafer (lower cladding stress compensation layer)	DCVD
4. OxyNitride Dep	0.7 μm of silicon oxynitride on back of wafer (core stress compensation layer) using recipe *SiON RI = 1.6*	DCVD
5. Oxide Dep	0.5 μm of oxide on back of wafer (sacrificial layer)	DCVD
6. BOE Etch	Wet etch of 0.5 μm of oxide from front and back of wafer	oxEtch-BOE
7. RCA Clean	Basic Wafer Clean	rca-ICL
8. Oxide Dep	3 μm of oxide on front of wafer (lower cladding)	DCVD
9. OxyNitride Dep	0.7 μm of silicon oxynitride on front of wafer (core) using recipe *SiON RI = 1.6*	DCVD
10. Waveguide Anneal	4 hr anneal at 1050 (removes adsorbed hydrogen from deposited layers)	5B-Anneal
11. Waveguide Patterning	Photoresist spin-on, expose, and develop using *Ed B Waveguide* mask	i-stepper and coater6
12. Waveguide Etch	Etch of 0.7 μm core into waveguides	AME5000
13. Resist Ash	O_2 plasma removal of photoresist	asher-ICL
14. Piranha Clean	Double piranha clean	premetal-Piranha

Waveguide Deposition and Etch Process (Cont.):

Step Name	Description/Details	Tool
15. RCA Clean	Basic Wafer Clean	rca-ICL
16. Oxide Dep	3 μm of oxide on front of wafer (upper cladding)	DCVD
17. Oxide Dep	3 μm of oxide on back of wafer (upper cladding stress compensation layer)	DCVD
18. RCA Clean	Basic Wafer Clean	rca-ICL
19. Waveguide Anneal	4 hr anneal at 1050 (removes adsorbed hydrogen from deposited layers)	5B-Anneal

Deep Well Etch Process:

Step Name	Description/Details	Tool
1. RCA Clean	Basic Wafer Clean	rca-ICL
2. Poly Dep	LPCVD deposition of 1.5 μm of polysilicon hardmask layer	6B-Poly
3. RCA Clean	Basic Wafer Clean	rca-ICL
4. Oxide Dep	0.5 μm of oxide on front of wafer (second hardmask layer)	DCVD
5. Well Patterning	Photoresist spin-on, expose, and develop using *Ed B Well* mask	i-stepper and coater6
6. Oxide Etch	Etch of 0.5 μm oxide hardmask using same recipe as *Waveguide Etch* step above	AME5000
7. Poly Etch	Etch of 1.5 μm poly hardmask	AME5000
8. Deep Etch	Etch of 6.7 μm of waveguide stack	AME5000
9. Resist Ash	O_2 plasma removal of photoresist	asher-ICL

C.2 Step Recipes

Waveguide Etch (also Oxide Etch) on MTL Tool AME5000 (Stored Recipe "ED B WG"):

Step Name	Parameters/Details	Time (sec)
1. STAB	Pressure = 200mTorr; Gases = O_2 @ 30 sccm; RF = 0 W; MF = 50 Gauss;	30
2. DESCUM	Pressure = 200mTorr; Gases = O_2 @ 30 sccm; RF = 100 W; MF = 50 Gauss;	30
3. STAB	Pressure = 200mTorr; Gases = CF_4 @ 30 sccm, CHF_3 @ 30 sccm, Ar @ 100 sccm; RF = 0 W; MF = 50 Gauss;	20
4. ETCH	Pressure = 200mTorr; Gases = CF_4 @ 30 sccm, CHF_3 @ 30 sccm, Ar @ 100 sccm; RF = 600 W; MF = 50 Gauss;	160 for Waveguide Etch, 100 for Oxide Etch

Deep Etch on MTL Tool AME5000 (Stored Recipe "EB THK OX"):

Step Name	Parameters/Details	Time (sec)
1. ETCH	Pressure = 200mTorr; Gases = CF_4 @ 15 sccm, CHF_3 @ 45 sccm, Ar @ 100 sccm; RF = 600 W; MF = 30 Gauss;	300
2. COOL	Pressure = 200mTorr; No Gases, Throttle Fully Open; MF = 30 Gauss;	120

Poly Etch on MTL Tool AME5000 (Stored Recipe "5000: CH B STI"):

Step Name	Parameters/Details	Time (sec)
1. ETCH	Pressure = 200mTorr; Gases = CL_2 @ 60 sccm, HBR_3 @ 20 sccm; RF = 400 W; MF = 30 Gauss;	600

Appendix D

Modeling Software

This appendix contains the code for four of the more significant Matlab programs that were written and used for the modeling and data analysis in this thesis. The first program called *getMmulti* takes as the input, the information about a series of waveguide segments and output a matrix that is used by the second program *serialfpmulti.* This program calculates the transmission spectrum for a series of dielectric materials for the case of more than one mode. The third program calculates the period of the resonance for the transmission spectrum of a Fabry-Perot cavity. The fourth program calculates the propagation loss in dB/cm for a waveguide from the peak/valley ratio of the measured transmission spectrum, the length of the waveguide, and the effective index of the mode.

D.1 getMmulti.m

```
%  Edward R. Barkley    7/12/05
%
%  The purpose of this function is to calculate the material matrix, M, for
%  use in the script 'serialfp'.  This function can be used for the case of
%  normal incidence plane wave propagation.  The reflection and
%  transmission coefficients are calculated from the refractive index of
%  the materials.
```

```
%
%  Input:
%
%       nr:     an Nx3xm matrix where nr(n,1,m) is the refractive index of the
%               mth mode in the nth material, nr(n,2,m) is the modal loss
%               (or negative of the gain)
%               of the material in dB/cm, and nr(n,3,m) is the length of the
%               material segment in cm. The first and last material segments
%               are assumed to be semi-infinite in extent and are not included
%               in this array.  For example, if you want to find T for a
%               high-index segment of length 2mm embedded in a polymer,
%               then N=1.  N is the number of finite material segments.
%
%       n1:     the index of the leading semi-infinite material
%       nf:     the index of the trailing semi-inifinite material
%
%  Output:
%
%       M:      The M matrix detailed in the code for 'serialfp'
%
%
%

function[M] = getMmulti(nr,n1,nf)

len = length(nr(:,1,1));
m = length(nr(1,1,:));
M = ones(len,8,m);

for mm = 1:m,
```

```
    for ii = 1:len,
        if ii==1,
            nprev = n1;
        else
            nprev = nr(ii-1,1,mm);
        end
        r12 = (nprev - nr(ii,1,mm))/(nprev + nr(ii,1,mm));
        r21 = -r12;
        t12 = sqrt(1 - r12*r12);
        t21 = t12;
        M(2*ii - 1,:,mm) = [0 r12 r21 t12 t21 0 0 0];
        M(2*ii,:,mm) = [1 0 0 0 0 nr(ii,2,mm) nr(ii,3,mm) nr(ii,1,mm)];
    end

    r12 = (nr(ii,1,mm) - nf)/(nr(ii,1,mm) + nf);
    r21 = -r12;
    t12 = sqrt(1 - r12*r12);
    t21 = t12;
    M(2*ii + 1,:,mm) = [0 r12 r21 t12 t21 0 0 0 ];
end
```

D.2 serialfpmulti.m

```
%
%  This script is used to find the wavelength dependent transmissivity of a
%  series of fabry perots which may contain lossy elements.
%
%  Input:
%       Mirrors Matrix M:       An Nx8xm matrix where M(N,1,:) is an element
%                               type indicator.  A 0 means that the element
```

```
%                               is an interface.  A 1 means that the
%                               element is a material with some length. If
%                               the element is an interface, then M(N,2,:) is
%                               the reflection coefficient for the Nth
%                               interface referenced from the input side
%                               (meaning that it will be positive when
%                               going from a higher index to a lower
%                               index). Looking at the diagram below, this
%                               would typically be called r_12.  M(N,3,:) is
%                               the reflection coefficient r_21 of the Nth
%                               interface. M(N,4,:) is the transmission
%                               coefficient t_12 of the Nth interface.
%                               M(N,5,:) is the transmission coefficient t_21
%                               of the Nth interface. If the element is a
%                               material segment, then M(N,6,:) is the loss
%                               in dB/cm, and M(N,7,:) is the length of the
%                               segment in cm.  M(N,8,:) is the effective
%                               index of the segment.  m is the number of
%                               modes.
%       lam:                    Vector with the wavelengths in nm for which
%                               the transmissivity of the structure is to
%                               be computed.
%       show:                   plots T vs. L when show = 1, no plot when
%                               show = 0.
%       mag:                    A vector of length m with the magnitude
%                               coefficient for each mode.
%
%       The T matrices are defined as follows:
%
%                               -------------
```

```
%              A_n ----------> |             | ----------> A_n+1
%                              |      T      |
%                              |             |
%              B_n <---------- |_____________| <---------- B_n+1
%
%       The input (light in) side is the left, the output is on the right.
%       However the inputs to the T-matrix are A2 and B2.  This is because
%       while A1 is known, B1 is not.  But we can set A2 = 1 and B2 = 0.
%       We find A1 from the T-matrix and the transmission coefficient for
%       the matrix is then 1/A1. The calculation proceeds as follows:
%       Conceptually, the elements are in a line from left to right.  The
%       T-matrix for the rightmost element is calculated and multiplies the
%       input vector to the T-matrix [A_N B_N] where N is the number of
%       elements.  The resulting vector is then multiplied by the T-matrix
%       of the second to rightmost element.  This continues until A_1 is
%       found.  The transmission coefficient is then 1/A1. Matlab matrix
%       multiplication is written in the opposite of the conventional
%       orientation: i.e. Vector*Matrix as opposed to the way it is
%       normally written: Matrix*Vector.  For more on T-matrices, see the
%       text by Coldren and Corzine.
%
%   Modifications:
%
%   ERB:12-22-05:   Now outputs Reflectivity as well as Transmissivity.
%   ERB:08-28-06:   Changed the name of the function to serialfpmulti and
%                   to add multimode functionality.

function[Tran Refl] = serialfpmulti(M,lam,show,mag)

N = length(M(:,1,1));                          % N as defined above
```

```
N_L = length(lam);
lam = lam*1E-7;
m = length(M(1,1,:))
Tran = zeros(N_L,1);
Refl = zeros(N_L,1);

for mm = 1:m,
    for ii = 1:N_L;
        Vector = [1 0]; % Initialize the Input Vector [A(N+1) B(N+1)]
        for jj=N:-1:1,
            if(M(jj,1,mm))
                alpha = M(jj,6,mm)/(20*log10(exp(1)));
                beta = (2*pi*M(jj,8,mm)/lam(ii)) + i*alpha;
                T(1,1,jj) = exp(-i*beta*M(jj,7,mm));
                T(1,2,jj) = 0;
                T(2,1,jj) = 0;
                T(2,2,jj) = exp(i*beta*M(jj,7,mm));
            else
                r_12 = M(jj,2,mm);
                r_21 = M(jj,3,mm);
                t_12 = M(jj,4,mm);
                t_21 = M(jj,5,mm);
                T(1,1,jj) = 1/t_12;
                T(1,2,jj) = -r_21/t_12;
                T(2,1,jj) = r_12/t_12;
                T(2,2,jj) = (t_12*t_21 - r_12*r_21)/t_12;
            end
            Vector = Vector*T(:,:,jj);
        end
%        Tran(ii) = abs(1/Vector(1))^2;
```

```
%        Refl(ii) = (abs(Vector(2)/Vector(1)))^2;
        Tran(ii) = Tran(ii) + (sqrt(mag(mm)))*(1/Vector(1));
%        Refl(ii) = Refl(ii) + (Vector(2)/Vector(1));
    end
end
Tran = (abs(Tran)).^2;
%Refl = (abs(Refl)).^2;


if (nargin > 2)
    if (show == 1)
%        figure;
        plot(lam*1E7,10*Tran,'r');
    end
end
ratio = min(Tran)/max(Tran);
```

D.3 fabryperiod.m

```
%
% This function returns the period (dlam) in nanometers for a fabry perot cavity
% of length L (cm) and refractive index n at the wavelength lam (nm).

function[dlam] = fabry_period(lam,L,n)

L = L*1E7;
N = 2*L*n/lam;
lam2 = 2*L*n/(N-1);
dlam = lam2 - lam;
```

D.4 fpalpha.m

```
%
% This script finds the loss in dB/cm given the cavity length, R, and
% contrast ratio for a Fabry Perot waveguide loss experiment.  A positive
% result for alpha implies loss.
%
% Written by Edward Barkley 9/22/2005
%
% Inputs:
%
%   L: cavity length in cm
%   R: cavity mirror reflectivity
%   ratio: Imax/Imin
%
% Edits:
%
%   1.0:    On 7-07-06 changed line 25 from -10* ... to -20* ... Alpha as
%   calculated before was the loss in dB/cm of the field strength, not the
%   power.  As corrected, it is now the power loss in dB/cm.

function[alpha] = fpalpha(L,R,ratio)

k1 = sqrt(ratio);
k2 = k1 - 1;
k3 = k1 + 1;
k4 = k2/k3;
k5 = k4/R;
k6 = log(k5);
alpha = -20*log10(exp(1))*k6/(2*L);
```

```
k7 = k3/k2;
k8 = k7/R;
k9 = log(k8);
alpha2 = -10*log10(exp(1))*k9/(2*L);
```

Bibliography

[1] Stephen D. Senturia. *Microsystem design.* Kluwer Academic Publishers, Boston, 2001.

[2] J. M. Johnson, J. Castle, P. Garrett-Engele, Z. Kan, P. M. Loerch, C. D. Armour, R. Santos, E. E. Schadt, R. Stoughton, and D. D. Shoemaker. "Genome-wide survey of human alternative pre-mRNA splicing with exon junction microarrays". *Science*, 302(5653):2141–2144, 2003.

[3] Peter L. Hagelstein, Stephen D. Senturia, and Terry P. Orlando. *Introductory applied quantum and statistical mechanics.* Wiley-Interscience, Hoboken, N.J., 2004.

[4] H. Rong, R. Jones, A. Liu, O. Cohen, D. Hak, A. Fang, and M. Paniccia. "A continuous-wave Raman silicon laser". *Nature*, 433(7027):725–728, 2005.

[5] HAYASHI I, PANISH MB, FOY PW, and SUMSKI S. "Junction lasers which operate continuously at room temperature". 17(3):109–11, 1970.

[6] R. Droopad, J. Curless, Z. Yu, D. Jordan, Y. Liang, C. Overgaard, H. Li, T. Eschrich, J. Ramdani, L. Hilt, B. Craigo, K. Eisenbeiser, J. Kulik, P. Fejes, J. Finder, X. Hu, Y. Wei, J. Edwards, K. Moore, M. O'Steen, and O. Baklenov. GaAs on silicon using an oxide buffer layer. In *Compound Semiconductors 2002 - Proceedings of the Twenty-Ninth International Symposium on Compound Semiconductors, Oct 7-10 2002*, volume 174 of *Institute of Physics Conference Series*, pages 1–8, 2003.

[7] K. Eisenbeiser, R. Droopad, and J. Finder. "New research yields epitaxially grown GaAs on Si". *Solid State Technology*, 45(7):61–62, 2002.

[8] M. Forbes, J. Gourlay, and M. Desmulliez. "Optically interconnected electronic chips: A tutorial and review of the technology". *Electronics and Communication Engineering Journal*, 13(5):221–223, 2001.

[9] S. Koehl and M. Paniccia. "The quest to siliconize photonics". *Photonics Spectra*, 39(11):53–60, 2005.

[10] J. W. Goodman, F. J. Leonberger, S. Kung, and R. A. Athale. "Optical interconnections for VLSI systems". *Proceedings of the IEEE*, 72(7):850–866, 1984.

[11] H. Cho, P. Kapur, and K. C. Saraswat. "Power comparison between high-speed electrical and optical interconnects for interchip communication". *Journal of Lightwave Technology*, 22(9):2021–2033, 2004.

[12] L. A. Coldren and S. W. Corzine. *Diode lasers and photonic integrated circuits.* Wiley, New York, 1995.

[13] Amnon Yariv, Pocji Yeh, and Amnon Yariv. *Photonics : optical electronics in modern communications.* Oxford University Press, New York, 2007.

[14] R. A. Soref and B. R. Bennett. "Electrooptical effects in silicon". *IEEE Journal of Quantum Electronics*, QE-23(1):123–129, 1987.

[15] D. Samara-Rubio, U. D. Keil, L. Liao, T. Franck, A. Liu, D. W. Hodge, D. Rubin, and R. Cohen. "Customized drive electronics to extend silicon optical modulators to 4 Gb/s". *Journal of Lightwave Technology*, 23(12):4305–4314, 2005.

[16] L. Liao, D. Samara-Rubio, M. Morse, A. Liu, D. Hodge, D. Rubin, U. D. Keil, and T. Franck. "High speed silicon Mach-Zehnder modulator". *Optics Express*, 13(8):3129–3135, 2005.

[17] F. Xia, V. M. Menon, and S. R. Forrest. "Photonic integration using asymmetric twin-waveguide (ATG) technology: Part I - concepts and theory". *IEEE Journal on Selected Topics in Quantum Electronics*, 11(1):17–29, 2005.

[18] V. M. Menon, F. Xia, and S. R. Forrest. "Photonic integration using asymmetric twin-waveguide (ATG) technology: Part II-devices". *IEEE Journal on Selected Topics in Quantum Electronics*, 11(1):30–42, 2005.

[19] P. J. Williams, P. M. Charles, I. Griffith, L. Considine, and A. C. Carter. "High performance buried ridge DFB lasers monolithically integrated with butt coupled strip loaded passive waveguides for OEIC". *Electronics Letters*, 26(2):142–143, 1990.

[20] X. Yan, M. L. Masanovic, E. J. Skogen, Z. Hu, D. J. Blumenthal, and L. A. Coldren. "Optical mode converter integration with InP-InGaAsP active and passive waveguides using a single regrowth process". *IEEE Photonics Technology Letters*, 14(9):1249–1251, 2002.

[21] M. L. Masanovic, V. Lal, J. S. Barton, E. J. Skogen, L. A. Coldren, and D. J. Blumenthal. "Monolithically integrated Mach-Zehnder interferometer wavelength converter and widely tunable laser in InP". *IEEE Photonics Technology Letters*, 15(8):1117–1119, 2003.

[22] H. Kunzel, S. Ebert, R. Gibis, R. Kaiser, H. Kizuki, S. Malchow, and G. Urmann. "Selective MOMBE growth of InP-based waveguide/laser butt-joints". *Journal of Crystal Growth*, 192(1-2):56–62, 1998.

[23] J. Wallin, G. Landgren, K. Strubel, S. Nilsson, and M. Oberg. Selective area regrowth of butt-joint coupled waveguides in multi-section dbr lasers. In *Metalorganic Vapor Phase Epitaxy 1992. Sixth International Conference, 8-11 June 1992*, volume 124 of *J. Cryst. Growth (Netherlands)*, pages 741–6, Cambridge, MA, USA, 11/ 1992. Swedish Inst. of Microelectron., Kista, Sweden.

[24] O. Kayser, B. Opitz, R. Westphalen, U. Niggebrugge, K. Schneider, and P. Balk. Selective embedded growth of gainas by low pressure movpe. In *Fifth International Conference on Metalorganic Vapor Phase Epitaxy and Workshop on MOMBE, CBE, GSMBE, and Related Techniques, 18-22 June 1990*, volume 107 of *J. Cryst. Growth (Netherlands)*, pages 141–6, Aachen, West Germany, 01/01 1991. Inst. of Semicond. Electron., Tech. Univ., Aachen, West Germany.

[25] K. Shimoyama, M. Katoh, M. Noguchi, Y. Inoue, H. Gotoh, Y. Suzuki, and T. Satoh. Transverse junction buried heterostructure (tj-bh) laser diode grown by movpe. In *Fourth International Conference on Metalorganic Vapor Phase Epitaxy, 16-20 May 1988*, volume 93 of *J. Cryst. Growth (Netherlands)*, pages 803–8, Hakone, Japan, 11/ 1988. Thin Film Lab., Mitsubishi Chem. Ind., Ibaraki, Japan.

[26] K. Shimoyama, Y. Inoue, M. Katoh, H. Gotoh, Y. Suzuki, and H. Yajima. A new selective movpe regrowth process utilizing in-situ vapor phase etching for opto-electronic integrated circuits. In *Fifth International Conference on Metalorganic Vapor Phase Epitaxy and Workshop on MOMBE, CBE, GSMBE, and Related Techniques, 18-22 June 1990*, volume 107 of *J. Cryst. Growth (Netherlands)*, pages 767–71, Aachen, West Germany, 01/01 1991. Thin-Films Lab., Mitsubishi Kasei Co., Ibaraki, Japan.

[27] F. Xia, S. Datta, and S. R. Forrest. "A monolithically integrated optical heterodyne receiver". *IEEE Photonics Technology Letters*, 17(8):1716–1718, 2005.

[28] http://www.asipinc.com/pr_072605.asp Accessed in September, 2006.

[29] C. Gunn. 10gb/s cmos photonics technology. In *Silicon Photonics, Jan 25-26 2006*, volume 6125 of *Proceedings of SPIE - The International Society for Optical Engineering*, page 612501, San Jose, CA, United States, 2006. Luxtera Inc., Carlsbad, CA, United States, International Society for Optical Engineering, Bellingham WA, WA 98227-0010, United States.

[30] Y. Suzaki, H. Yasaka, H. Mawatari, K. Yoshino, Y. Kawaguchi, S. Oku, R. Iga, and H. Okamoto. "Monolithically integrated eight-channel WDM modulator with narrow channel spacing and high throughput". *IEEE Journal on Selected Topics in Quantum Electronics*, 11(1):43–48, 2005.

[31] http://www.luxtera.com/index.htm Accessed in September, 2006.

[32] D. W. Vernooy, A. M. Benzoni, H. A. Blauvelt, and J. S. Paslaski. Surface mount photonics as a platform for optoelectronic packaging. In *2003 IEEE LEOS Annual Meeting Conference Proceedings, Oct 26-30 2003*, volume 1 of *Conference Proceedings - Lasers and Electro-Optics Society Annual Meeting-LEOS*, pages 370–371, TUCSON, AZ, United States, 2003. Xponent Photonics Inc., Monrovia, CA 91016, United States, Institute of Electrical and Electronics Engineers Inc.

[33] D. W. Vernooy, J. S. Paslaski, H. A. Blauvelt, R. B. Lee, and K. J. Vahala. "Alignment-insensitive coupling for PLC-based surface mount photonics". *IEEE Photonics Technology Letters*, 16(1):269–271, 2004.

[34] http://www.xponentinc.com/technology/index.htm Accessed in September, 2006.

[35] H. Bae, H. Lee, K. Kim, S. Lee, O. Beom-Hoan, S. Park, and E. Lee. A triplexer optical transceiver module using cascaded directional couplers. In *Optoelectronic Integrated Circuits VIII, Jan 23-25 2006*, volume 6124 of *Proceedings of SPIE - The International Society for Optical Engineering*, page 61241, 2006.

[36] A. W. Fang, H. Park, R. Jones, O. Cohen, M. J. Paniccia, and J. E. Bowers. Heterogeneous integration of silicon and algainas for a silicon evanescent laser. In *Novel In-Plane Semiconductor Lasers V, Jan 23-26 2006*, volume 6133 of *Proceedings of SPIE - The International Society for Optical Engineering*, page 61330, San Jose, CA, United States, 2006. University of California Santa Barbara, ECE Department, Santa Barbara, CA 93106, United States, International Society for Optical Engineering, Bellingham WA, WA 98227-0010, United States.

[37] H. Park, A. W. Fang, S. Kodama, and J. E. Bowers. "Hybrid silicon evanescent laser fabricated with a silicon waveguide and III-V offset quantum wells". *Optics Express*, 13(23):9460–9464, 2005.

[38] E. Barkley and C. G. Fonstad Jr. "The impact of CMP and underlying back-end topographical features on losses in deposited dielectric waveguides". *IEEE Journal of Quantum Electronics*, 40(12):1709, 2004.

[39] M. Grabherr, M. Miller, R. Jaeger, R. Michalzik, U. Martin, H. J. Unold, and K. J. Ebeling. "High-power VCSEL's: single devices and densely packed 2-D-arrays". *IEEE Journal on Selected Topics in Quantum Electronics*, 5(3):495–502, 1999.

[40] W. K. Loke, S. F. Yoon, H. Q. Zheng, and C. G. Fonstad. Epitaxial growth of gaas in deep dielectric windows using solid source molecular beam epitaxy. In *Microphotonics - Materials, Physics and Applications, Nov 27-29 2000*, volume 637 of *Materials Research Society Symposium - Proceedings*, pages 5111–5116, Boston, MA, 2001. School of Elec. and Electronic Eng., Nanyang Technological University, Singapore 639798, Singapore, Materials Research Society.

[41] B. R. Singh. Silica based planar lightwave circuits on silicon platform. In *IWPSD-99: The 10th International Workshop on the Physics of Semiconductor Devices, Dec 14-Dec 18 1999*, volume 3975 (I of *Proceedings of SPIE - The International Society for Optical Engineering*, pages 319–326, New Delhi, India, 2000. CEERI, Rajasthan, India, Society of Photo-Optical Instrumentation Engineers, Bellingham, WA, USA.

[42] Dietrich Marcuse. *Light transmission optics.* Van Nostrand Reinhold, New York, 1972. Bibliography: p. 432-437.

[43] Gins Lifante. *Integrated photonics : fundamentals.* J. Wiley, Hoboken, NJ, 2003.

[44] D. O. Ouma, D. S. Boning, J. E. Chung, W. G. Easter, V. Saxena, S. Misra, and A. Crevasse. "Characterization and modeling of oxide chemical-mechanical

polishing using planarization length and pattern density concepts". *IEEE Transactions on Semiconductor Manufacturing*, 15(2):232–244, 2002.

[45] B. E. Stine, D. O. Ouma, R. R. Divecha, D. S. Boning, J. E. Chung, D. L. Hetherington, C. R. Harwood, O. S. Nakagawa, and S. Oh. "Rapid characterization and modeling of pattern-dependent variation in chemical-mechanical polishing". *IEEE Transactions on Semiconductor Manufacturing*, 11(1):129–140, 1998.

[46] F. W. Preston. "The theory and design of plate glass polishing". *Society of Glass Technology - Journal*, 11(42):214–256, 1927.

[47] W. J. MINFORD, S. K. KOROTKY, and R. C. ALFERNESS. "Low-loss Ti:$LiNBO_3$ waveguide bends at $\lambda = 1.3$ μm". QE-18(10):1802–1806, 1982.

[48] G. Bona, R. Germann, and B. J. Offrein. "SiON high-refractive-index waveguide and planar lightwave circuits". *IBM Journal of Research and Development*, 47(2-3), 2003.

[49] Allan W. Snyder and John D. Love. *Optical waveguide theory*, volume 190. Chapman and Hall, London ; New York, 1983. Allan W. Snyder, John D. Love.; Includes bibliographical references and indexes.

[50] S. I. Najafi, T. Touam, R. Sara, M. P. Andrews, and M. A. Fardad. "Sol-gel glass waveguide and grating on silicon". *Journal of Lightwave Technology*, 16(9):1640–1646, 1998.

[51] K. Worhoff, R. M. de Ridder, P. V. Lambeck, and A. Driessen. Silicon oxynitride in integrated optics. In *Proceedings of the 1998 11th Annual Meeting IEEE Lasers and Electro-Optics Society, LEOS. Part 2 (of 2), Dec 1-4 1998*, volume 2 of *Conference Proceedings - Lasers and Electro-Optics Society Annual Meeting-LEOS*, pages 370–371, Orlando, FL, USA, 1998. Univ of Twente, Enschede, Neth, IEEE, Piscataway, NJ, USA.

[52] R. M. de Ridder, K. Worhoff, A. Driessen, P. V. Lambeck, and H. Albers. "Silicon oxynitride planar waveguiding structures for application in optical communica-

tion". *IEEE Journal on Selected Topics in Quantum Electronics*, 4(6):930–937, 1998.

[53] Y. Cho and Y. Kim. Fabrication of planar SiON optical waveguide and its characterization. In *2005 MRS Fall Meeting, Nov 28-Dec 1 2005*, volume 891 of *Materials Research Society Symposium Proceedings*, pages 327–330, 2006.

[54] C. K. Wong, H. Wong, C. W. Kok, and M. Chan. Silicon oxynitride prepared by chemical vapor deposition as optical waveguide materials. In *International Conference on Materials for Advanced Technologies, Jul 4-8 2005*, volume 288 of *Journal of Crystal Growth*, pages 171–175. Department of Electronic Engineering, City University of Hong Kong, Kowloon, Hong Kong, Elsevier, Amsterdam, 1000 AE, Netherlands, 2006.

[55] K. K. Lee, D. R. Lim, H. Luan, A. Agarwal, J. Foresi, and L. C. Kimerling. "Effect of size and roughness on light transmission in a Si/SiO2 waveguide: Experiments and model". *Applied Physics Letters*, 77(11):1617–1619, 2000.

[56] F. Gao, Y. Wang, G. Cao, X. Jia, and F. Zhang. "Reduction of sidewall roughness in silicon-on-insulator rib waveguides". *Applied Surface Science*, 252(14):5071–5075, 2006.

[57] F. P. Payne and J. P. R. Lacey. "Theoretical analysis of scattering loss from planar optical waveguides". *Optical and Quantum Electronics*, 26(10):977–986, 1994.

[58] G. N. de Brabander, J. T. Boyd, and H. E. Jackson. "Single polarization optical waveguide on silicon". *IEEE Journal of Quantum Electronics*, 27(3):575–579, 1991.

[59] W. C. Borland, D. E. Zelmon, C. J. Radens, J. T. Boyd, and H. E. Jackson. "Properties of four-layer planar optical waveguides near cutoff". *IEEE Journal of Quantum Electronics*, QE-23(7):1172–1179, 1987.

[60] W. Stutius and W. Streifer. "Silicon nitride films on silicon for optical waveguides". *Applied Optics*, 16(12):3218–3222, 1977.

[61] A. Zhang, K. T. Chan, M. S. Demokan, V. W. C. Chan, P. C. H. Chan, and A. H. P. Chan. "Annealing effects on the loss and birefringence of silicon oxynitride rectangular optical waveguides". *Applied Physics Letters*, 87(10):101105, 2005.

[62] T. Wu and H. Chang. "Guiding mode expansion of a TE and TM transverse-mode integral equation for dielectric slab waveguides with an abrupt termination". *Journal of the Optical Society of America A: Optics and Image Science, and Vision*, 18(11):2823–2832, 2001.

[63] Jin Au Kong. *Electromagnetic wave theory.* EMW Publishing, Cambridge, Mass. :, 2000. Jin Au Kong.; Includes bibliographical references (p. 959-980) and index.

[64] Dennis Michael Sullivan, IEEE Microwave Theory, and Techniques Society. *Electromagnetic simulation using the FDTD method.* IEEE Press, New York, 2000.

[65] Allen Taflove and Susan C. Hagness. *Computational electrodynamics : the finite-difference time-domain method.* Artech House, Boston, 2005.

[66] Stephen M. Rossnagel, J. J. Cuomo, and William D. Westwood. *Handbook of plasma processing technology : fundamentals, etching, deposition, and surface interactions.* Noyes Publications, Park Ridge, N.J., U.S.A., 1990. edited by Stephen M. Rossnagel, Jerome J. Cuomo, William D. Westwood.; Includes bibliographical references and index.

[67] A. Tarraf, J. Daleiden, S. Irmer, D. Prasai, and H. Hillmer. "Stress investigation of PECVD dielectric layers for advanced optical MEMS". *Journal of Micromechanics and Microengineering*, 14(3):317–323, 2004.

[68] D. Criado, M. I. Alayo, M. C. A. Fantini, and I. Pereyra. "Study of the mechanical and structural properties of silicon oxynitride films for optical applications". *Journal of Non-Crystalline Solids*, 352(23-25):2319–2323, 2006.

[69] C. A. Davis. "Simple model for the formation of compressive stress in thin films by ion bombardment". *Thin Solid Films*, 226(1):30–34, 1993.

[70] W. N. Ye, D. Xu, S. Janz, P. Cheben, M. Picard, B. Lamontagne, and N. G. Tarr. "Birefringence control using stress engineering in silicon-on-insulator (SOI) waveguides". *Journal of Lightwave Technology*, 23(3):1308–1318, 2005.

[71] D. Schalch, A. Scharmann, and R. Wolfrat. "Role of hydrogen in silicon nitride and silicon oxynitride films". *Thin Solid Films*, 124(3-4):301–308, 1984.

[72] V. Van, B. E. Little, S. T. Chu, and J. V. Hryniewicz. Micro-ring resonator filters. In *2004 IEEE LEOS Annual Meeting Conference Proceedings, LEOS 2004, Nov 7-11 2004*, volume 2 of *Conference Proceedings - Lasers and Electro-Optics Society Annual Meeting-LEOS*, pages 571–572, Rio Grande, Puerto Rico, 2004. Little Optics Inc., Annapolis Junction, MD 20701, United States, Institute of Electrical and Electronics Engineers Inc., Piscataway, NJ 08855-1331, United States.

[73] H. Albers, L. T. H. Hilderink, E. Szilagyi, F. Paszti, P. V. Lambeck, and T. J. A. Popma. Reduction of hydrogen induced losses in PECVD-SiOxNy optical waveguides in the near infrared. In *Proceedings of the 1995 8th Annual Meeting of the IEEE Lasers and Electro-Optics Society. Part 2 (of 2), Oct 30-Nov 2 1995*, volume 2 of *Conference Proceedings - Lasers and Electro-Optics Society Annual Meeting-LEOS*, pages 88–89, 1995.

[74] A. Nagy. Vertical oxide etching without inducing change in critical dimensions. In *Advanced Techniques for Integrated Circuit Processing, Oct 1-5 1990*, volume 1392 of *Proceedings of SPIE - The International Society for Optical Engineering*, pages 165–184, Santa Clara, CA, USA, 1991. MOTOROLA ATC, Mesa, AZ, USA, Publ by Int Soc for Optical Engineering, Bellingham, WA, USA.

[75] L. Rolland, M. C. Peignon, C. Cardinaud, and G. Turban. "SiO_2/Si selectivity in high density CHF_3/CH_4 plasmas: role of the fluorocarbon layer". *Microelectronic Engineering*, 53(1):375–379, 2000.

[76] Sorab Khushro Ghandhi. *VLSI fabrication principles : silicon and gallium arsenide.* J. Wiley, New York, 1994. Sorab K. Ghandhi.; "A Wiley-Interscience publication."; Includes bibliographical references and index.; Very large scale integration fabrication principles.

[77] K. Worhoff, L. T. H. Hilderink, A. Driessen, and P. V. Lambeck. "Silicon oxynitride. a versatile material for integrated optic applications". *Journal of the Electrochemical Society*, 149(8):85–91, 2002.

[78] J. Piprek, Y. Chiu, and J. E. Bowers. Analysis of multi-quantum well electroabsorption modulators. In *Physics and Simulation of Optoelectronic Devices X, Jan 21-25 2002*, volume 4646 of *Proceedings of SPIE - The International Society for Optical Engineering*, pages 609–617, San Jose, CA, United States, 2002. Electrical Engineering Department, University of California, Santa Barbara, CA 93106, United States, The International Society for Optical Engineering.